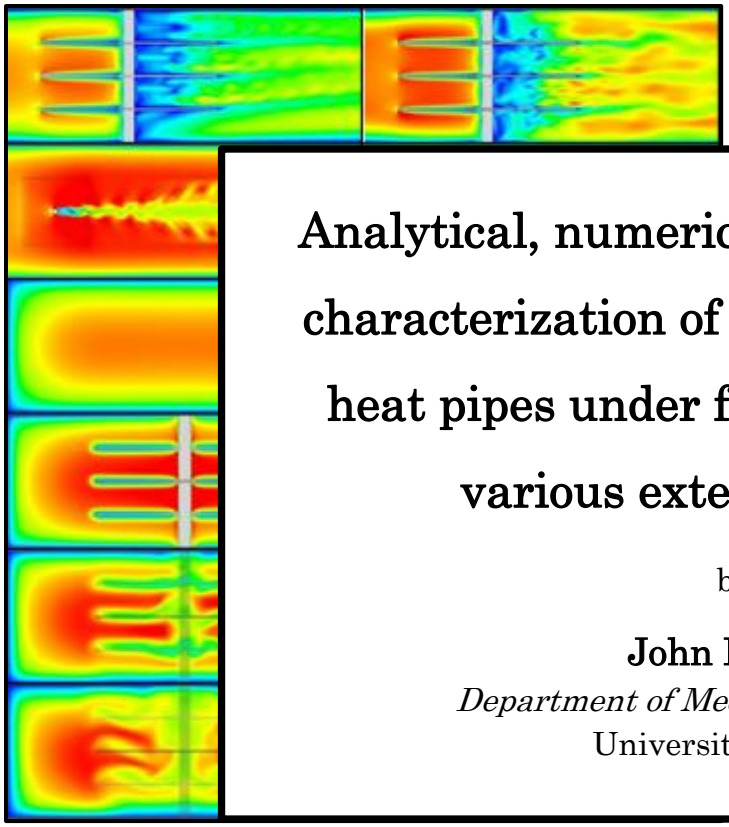

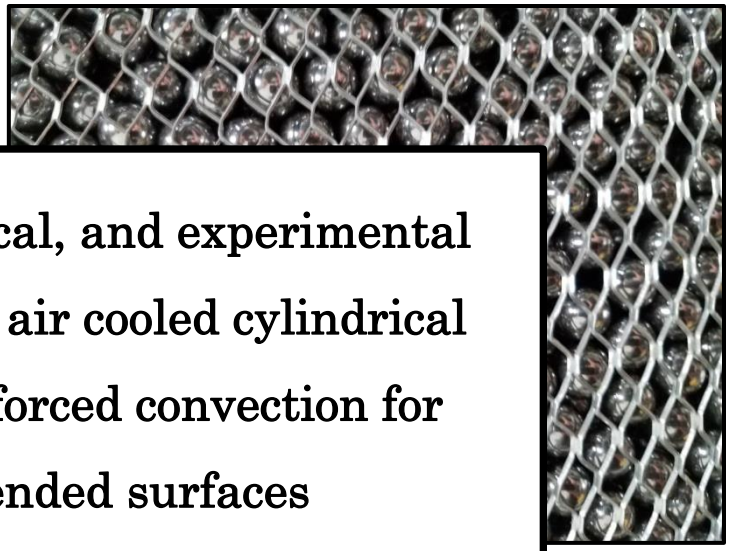

Analytical, numerical, and experimental characterization of air cooled cylindrical heat pipes under forced convection for various extended surfaces

by

John R. Stark

Department of Mechanical Engineering

University of Kansas

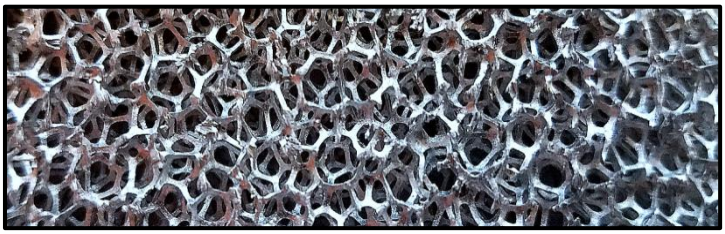

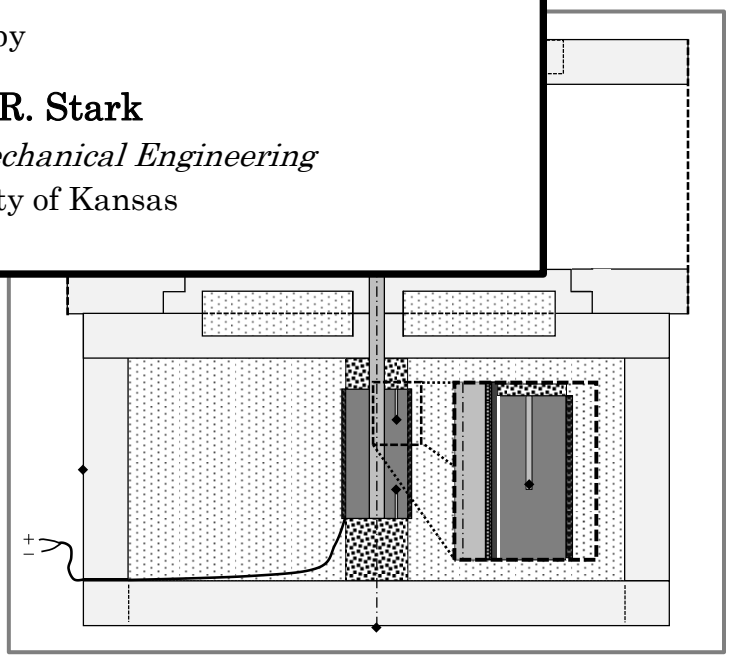

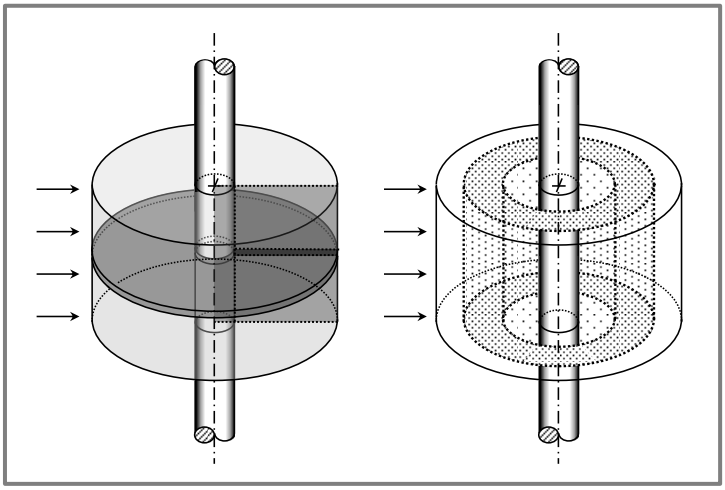

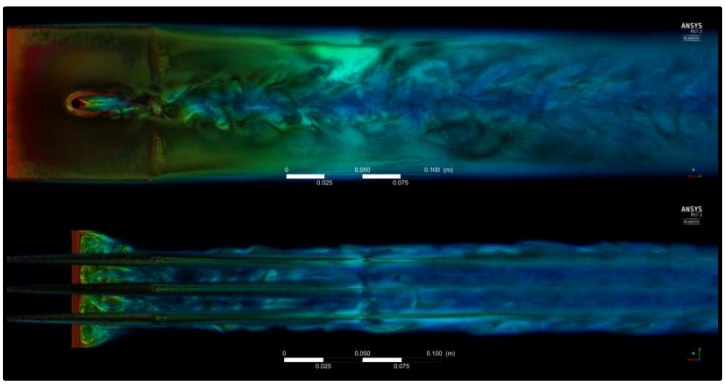

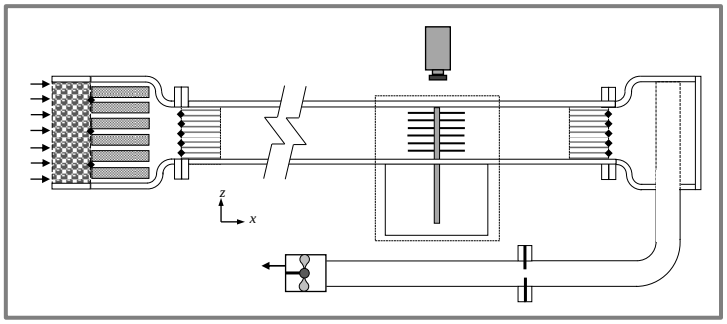

Analytical, numerical, and experimental characterization of air cooled cylindrical heat pipes under forced convection for various extended surfaces

by

John R. Stark

Submitted to the graduate degree program in Mechanical Engineering and the Graduate Faculty of the University of Kansas in partial fulfillment of the requirements for the degree of Doctor of Philosophy.

_____

Chairperson Professor **Theodore L. Bergman**
Dept. of Mechanical Engineering, University of Kansas

_____

Professor **Z.J. Wang**
Dept. of Aerospace Engineering, University of Kansas

_____

Associate Professor **Christopher Depcik**
Dept. of Mechanical Engineering, University of Kansas

_____

Assistant Professor **Xianglin Li**
Dept. of Mechanical Engineering, University of Kansas

_____

Assistant Professor **Huazhen Fang**
Dept. of Mechanical Engineering, University of Kansas

Date Defended: July 24th, 2017

University of Kansas
Department of Mechanical Engineering
Learned Hall 3165a, 1530 W. 15th Street
Lawrence, Kansas 66046

The Dissertation Committee for John Stark

certifies that this is the approved version of the following dissertation:

Analytical, numerical, and experimental characterization of air cooled cylindrical heat pipes under forced convection for various extended surfaces

Chairperson Professor **Theodore L. Bergman**
Dept. of Mechanical Engineering, University of Kansas

Date approved: July 27, 2017

Preface

This dissertation is submitted to the graduate degree program in Mechanical Engineering and the Graduate Faculty of the University of Kansas in partial fulfillment of the requirements for the degree of Doctor of Philosophy. The research that is detailed within was funded by the National Science Foundation under Grant Nos. 1435131 (University of Kansas) and 1435233 (University of Connecticut). The work was performed at the Department of Mechanical Engineering, at University of Kansas from September 2014 to June 2017 under the supervision of main supervisor Professor Theodore L. Bergman. Co-supervisors for this work are Professors Christopher Depcik, Xianglin Li, Huazhen Fang, and Ronald L. Dougherty of the Department of Mechancial Engineering and Professor Z.J. Wang of the Department of Aerospace Engineering.

First and foremost, I would like to thank my adviser, Dr. Bergman, for his guidance over the course of this research. Our detailed discussions were invaluable to my understanding of the material, and your careful revision of the resulting publications has improved my writing substantially. The phenomenal computational and experimental tools that you provided me greatly improved the quality of the work. Thank you for always being so welcoming to technical discussions, and for challenging me to know every aspect of what we have been working on. Thank you to my other committee members as well, as they each of have provided insight into this research.

To postdoctoral researcher Dr. Nourouddin Sharifi, your expertise on the experimental design and internal numerical modeling was invaluable to my work, but I appreciate your friendship to an even higher degree. Much of the experimental work in this dissertation was done with the help of undergraduate research assistants. Thank you to Will Libeer and Tom Dunn, whom were instrumental in the design and construction of the two flow channels employed. Thank you to Matt Zabel, Trey Fox, Raki Prasad, and Chadwick Sevart for their help in constructing the various arrays and performing data acquisition. I would also like to express my appreciation to those who I have met in my time at KU. Thank you to my officemate, John Liu,

for being someone with whom I could always share my difficulties and successes. It was very helpful to share an office with such a driven and positive individual.

To my Master's adviser, Dr. John Abraham, I thank you for always encouraging me and giving me the opportunity to work on such a wide range of projects. I would not have pursued my Master's if it were not for my interest in CFD that began in your fluid dynamics and heat transfer courses, and I would not have pursued a doctorate if it were not for research and teaching experiences that you provided me. Similarly, I thank Dr. Eph Sparrow for his mentoring, and for imparting to me his passion for heat transfer.

I would like to express my appreciation to my family, who have always been deeply supportive of my pursuits. To my sister Emily, it was nice to have a quick goodnight chat as I was leaving the office when you were just waking up in Germany. While it was nice to get to visit, it is wonderful to have you and your family back in the States. To my brothers Steve and Mikey, you are two of my best friends, and getting to see you both so often despite the distance has made an incredible difference. To my parents, it would be impossible to adequately express my appreciation for the multitude of ways in which you have supported me. You have given me life, purpose, and a shining example by which to live. Thank you.

Finally and most importantly, I'd like to thank my fiancé Kirsten for her continued love and support. You have been my best friend, confidant, and inspiration over these past 4 years. I am deeply grateful that you have stuck through the long distance with me, and I cannot wait to begin our lives together.

Abstract

The objective of this dissertation is to characterize heat transfer from cylindrical heat pipes (HPs) in cross flow with attached extended surfaces. The extended surfaces investigated include uniform thickness fins, open-cell highly porous metal foam, and an array consisting of periodic layers of metal fins and open-cell metal foam.

First, benchmark direct numerical simulations are used to compare existing analytical models for predicting convection heat transfer coefficients associated with a finned HP. The benchmark simulations are also used to identify the shear stress transport (SST) turbulence model as the preferred numerical model for the prediction of convection heat transfer from a finned HP. The SST external model is then coupled to a multiphase 2D internal HP model. Predictions from the resulting coupled numerical model are compared with experimental measurements for validation. A previously unreported phenomenon, localized depression of temperatures in the heat pipe wall, is identified.

A novel analytical model of annular foam-only arrays is subsequently developed, along with a generalized expression for the fin efficiency of square arrays based upon corresponding annular efficiencies. Numerically predicted thermal efficiencies compare favorably with predictions generated from the novel expressions for both the annular and square arrays. Comparison of experimentally measured heat rates and predicted heat rates found with the new expressions for a square metal foam array provides further validation.

Finally, novel expressions for the thermal resistance associated with annular composite fin-foam arrays are developed. Experimentally measured heat rates for such an array are compared to corresponding predictions generated with the new expressions to verify the model. A preliminary comparison of predicted heat transfer for the annular fin array, the foam-only annular array, and the new combined fin-foam array is generated, demonstrating the improved thermal performance associated with the metal foam-based configurations.

Publications

The following peer reviewed journal articles provide the basis for this dissertation.

P1: *J.R. Stark, T.L. Bergman, Prediction of convection from a finned cylinder in cross flow using direct simulation, turbulence modeling, and correlation-based methods, Numerical Heat Transfer, Part A: Applications 71 (3) (2017) 1-18.*

This work is aimed at ascertaining the best performing (*i*) turbulence model to employ in larger parametric studies by comparison to benchmark direct numerical simulations and (*ii*) analytical models to approximate the area averaged heat transfer coefficients associated with a finned heat pipe. My contributions comprise all of the analytical and numerical work detailed within.

P2*:* *J.R. Stark, N. Sharifi, T.L. Bergman, A. Faghri, An experimentally verified numerical model of finned heat pipes in crossflow, International Journal of Heat and Mass Transfer 97 (2016) 45-55.*

A novel, coupled numerical model is developed that is comprised of external flow simulations, similar to those of Paper **P1**, and simulations of the complex heat transfer mechanisms within the heat pipe (performed by post-doctoral researcher Nourouddin Sharifi). Predictions made via these models are then compared to experimental measurements. My contributions include all external numerical modeling, as well as assisting in the design, construction, and use of the experimental testing apparatus.

P3: *J.R. Stark, R. Prasad, T.L. Bergman, Experimentally validated analytical expressions for the thermal efficiencies and thermal resistances of porous metal foam-fins, International Journal of Heat and Mass Transfer 111 (2017) 1286-1295.*

Novel analytical models for open-cell, metal foams attached to a cylindrical base are developed for annular arrays, and are subsequently extended to square arrays. My contributions include generating the novel analytical models, performing all numerical modeling, overseeing experimental testing performed by an undergraduate student (Raki Prasad), and conducting all analyses within.

P4: *J.R. Stark, C.D. Sevart, T.L. Bergman, Experimentally validated analytical expressions for the thermal resistance of a novel composite fin-foam annular array, Applied Thermal Engineering (Submitted).*

An analytical model is developed for an array comprised of periodic layers of metal fins and open-cell, metal foam attached to a cylindrical base. Predictions generated with the novel model are compared to experimental measurements for validation. Additional comparisons are made between analytically predicted heat rates for a bare cylinder, a finned cylinder, a foam array, and a combined fin-foam array to assess relative performance. My contributions comprise all work detailed within, including oversight of an undergraduate student researcher (Chadwick Sevart).

P5: *N. Sharifi, J.R. Stark, T.L. Bergman, A. Faghri, The influence of thermal contact resistance on the relative performance of heat pipe-fin array systems, Applied Thermal Engineering 105 (2016) 46-55.*

The complex internal and external phenomena associated with the cooling of a finned HP described in Paper **P2** are reduced to a thermal resistance model. My contributions include performing numerical modeling of a conduction constriction resistance within the heat pipe wall, as well as identifying the newly described heat pipe limitation associated with the constriction of vapor condensation at the fin root. The majority of the work was performed by post-doctoral researcher Nourouddin Sharifi.

Table of Contents

Introduction 1

1.1. Background

Nearly all consumption of energy ends ultimately with the conversion to thermal energy in the form of waste heat. Efficient management of this thermal energy is necessary in a wide variety of applications, ranging from industrial processes to consumer goods. For example, the efficiency of all thermodynamic cycles increase as the thermal resistance associated with the dispersion of waste heat is reduced. Other applications, such as cooling of electronic devices, require low thermal resistances for the dissipation of waste heat to avoid excessive operating temperatures. These and other applications are discussed elsewhere [1]. Air and water are frequently used to remove heat from a process, as they (*i*) allow for the thermal energy to be carried by the movement of the material (as opposed to pure conduction) and (*ii*) are readily available. As a result, a multitude of designs for heat sinks [2] and heat exchangers [3] have been developed.

Novel heat exchanger designs centered on heat pipes (HPs) are one promising new technology that may allow for more efficient transfer of heat to the environment [4-10]. Heat pipes (and closely related thermosyphons) leverage the latent heat of vaporization to transport the thermal energy. A diagram of a typical HP and its working principles may be seen in Fig. 1(a). The working liquid (for example, water) is evaporated at the high temperature (or evaporator) section of the HP, after which the vapor flows through the hollow HP core to eventually condense on the low temperature (or condenser) section of the HP. This closed loop system is completed as the liquid working fluid returns to the evaporator section by capillary action in a wick and/or by gravitational forces.

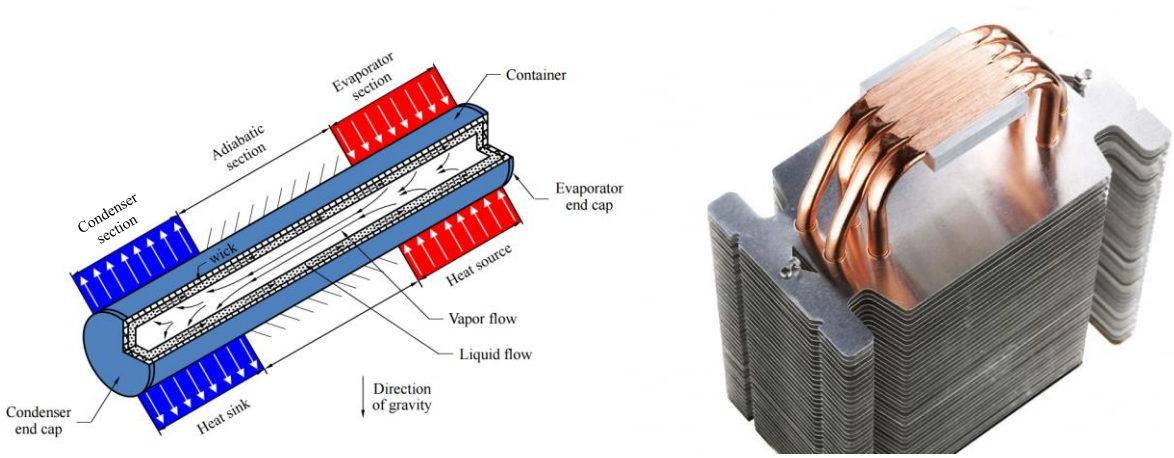

(a) (b)

Fig. 1. (a) Diagram of a HP [11] **(b)** Finned HP heat sink for a CPU [12].

As a result of the low thermal resistances associated with evaporation and condensation of the HP working fluid, HPs present incredibly low thermal resistances (corresponding to effective thermal conductivities greater than 100,000 W/mK in some cases [11, 13]). Of course, heat transfer to the evaporator section or from the condenser section of the HP must involve heat transfer from or to external sources or sinks. This transfer usually occurs by convection from (or to) an external fluid or fluids, and the flow of heat through such a heat pipe system may be dominated by the thermal resistances external to the HP. Hence, extended surfaces are typically attached externally to HPs in an effort to reduce the overall system resistance.

Currently, small scale HP heat exchangers with finned designs are used for cooling consumer electronics (as shown in Fig. 1(b)), but proposed designs including open-cell, high-porosity metal foams, and metal foam-fin systems are of interest since they may lead to relatively low overall system resistances. Due to the multiple material interfaces in a HP system, it is also necessary to have a quantitative understanding of how the thermal performance is influenced by potential contact resistances. Lastly, a clear understanding of how the external and internal heat transfer processes are coupled, and how the coupling affects the performance of the HP system, is necessary for the accurate prediction of overall system thermal behavior.

1.2. Scope of Dissertation

The objective of this dissertation is to investigate and/or generate predictive correlations and mathematical expressions describing heat transfer from a cylindrical heat pipe with attached extended surfaces consisting of (*i*) fins (Papers **P1**, **P2**, and **P5**), (*ii*) open-cell high-porosity metal foams (Paper **P3**), and (*iii*) combined fin and foam arrays (Paper **P4**). In Papers **P1** through **P4**, analytically (or empirically) predicted thermal performance is validated against numerically predicted and experimentally measured values. Further work investigating the interaction of internal (within the HP) and external (outside of the HP) thermal processes is also described (Papers **P2** and **P5**). The ultimate goal is to identify and create accurate correlations and expressions that represent the complex conductive and convective phenomena associated with the various types of extended surfaces applied externally to cylindrical HPs. Once developed, the correlations and expressions may be used to design various HP systems.

To accomplish the preceding goal, the performance of various steady-state turbulence models for the prediction of convective heat transfer from finned HPs or tubes in cross flow are first investigated (Paper **P1**). To reveal the underlying physical mechanisms and identify the preferred model(s), benchmark direct numerical simulations (DNS) predictions are performed. The benchmark predictions are based on a fully-elliptic, transient, incompressible, 3D numerical description of conservation of mass, energy, and momentum associated with the mixed (forced and free) convection about a finned cylinder. Once the preferred turbulence model is identified by comparison of its predictions with those of the DNS, both DNS and turbulence model predictions of time- and area-averaged heat transfer coefficients are compared to those calculated from correlations reported in the literature.

Following the investigation of the performance of the various predictions for the convective heat transfer from a finned HP, investigations of the combined internal and external performance of a finned HP are made (Papers **P2** and **P5**). The selected turbulence numerical model identified in Paper **P1** (a shear stress transport, or SST model) is employed to develop and demonstrate a novel computational methodology to couple 2D internal and 3D external simulations for a common configuration: a vertical HP with isothermal conditions at its lower evaporator section, and 3D convective conditions external to its upper finned condenser section.

This numerical model is validated by comparing its predictions against experimental results, and is used to examine the relationship between heat transfer internal and external to the finned HP.

The next extended surface considered is open-cell, high-porosity metal foam (Paper **P3**). For the investigation of metal foams, (*i*) a continuum-based, analytical description for conduction and forced convection heat transfer within an annular porous matrix attached concentrically to a circular tube, reported in terms of a thermal efficiency, is developed, (*ii*) a continuum-based numerical model is used to develop a semi-analytical expression for the thermal efficiency of a cubical porous block attached on-center to a circular tube, and (*iii*) the thermal behavior predicted with the semi-empirical expression is compared to experimental measurements conducted with convectively cooled foam blocks of square cross section attached on-center to a nearly isothermal warm cylinder (heat pipe) using a unique experimental setup.

Finally, an annular fin-foam array is modeled with a novel, continuum-based analytical description in a manner similar to that of the corresponding foam array (Paper **P4**). This model is validated through comparison with corresponding numerically predicted and experimentally measured heat transfer rates for a fin-foam array of square cross section. Quantification of the heat transfer performance of these extended surfaces enables future work to predict the relative performance of HP systems implementing the various designs.

The dissertation is presented in summary style, by first providing an overview of the published articles which constitute the dissertation. Chapters dedicated to the three extended surfaces of interest include a brief introduction, followed by a summary and discussion of key results. Note that the definitions of variables are consistent with those provided in the relevant papers.

The Finned Heat Pipe (Papers P1, P2, and P5) 2

2.1. Introduction and background

The analysis of finned heat pipes (HPs) is an example where accurate and efficient prediction of heat transfer coefficients is essential to ultimately create practical, system-level models. Because HPs have internal thermal resistances that can be orders of magnitude smaller than those associated with high thermal conductivity media of similar dimensions [13-14], accurate prediction of the convective heat transfer external to the HP is crucial in order to quantify the overall thermal resistance of convectively heated and/or cooled HPs. Papers **P1**, **P2**, and **P5** present models-for and predictions-of heat transfer for finned HPs. The focus will be on the convection processes external to the HP.

Numerical modeling has been used to analyze heat transfer processes both (*i*) within HPs (internal modeling) [15-30] and (*ii*) external to HPs (external modeling), such as those equipped with exterior fin arrays [25-27]. Both internal and external modeling employ simplifying assumptions. For example, interior modeling often includes accurate descriptions of the evaporation, condensation, and heat transfer processes within the HP itself, but is hampered by the specification of simplified external thermal boundary conditions at the HP evaporator and condenser sections. Alternatively, recently reported external modeling efforts provide detailed predictions of the external convective heat transfer processes, but typically treat heat transfer within the HP in a simplified manner [25-26]. A few recent studies involve development of overall HP system models that include detailed descriptions of both internal and external heat transfer processes. However, these models have been limited to 2D systems [25, 19-21]. For a finned HP subjected to 3D external forced convection, a unified and full 3D approach to solve both the internal and external heat transfer processes concurrently would be computationally

expensive. To the author's knowledge, full 3D predictions of heat transfer both internal and external to a HP have not been reported in the literature.

Paper **P1** presents a benchmarking study of various numerical modeling methodologies which have been developed to predict laminar, turbulent, and transitional convective heat transfer processes and rates as applied to heat transfer external to the finned HP. In addition to investigating the relative performance of the various models, Paper **P1** compares the predictive capability of multiple analytical models. Paper **P2** details a coupled numerical model that consists of (*i*) a 3D model of the flow external to the finned HP (using the preferred turbulence model identified in Paper **P1**) and (*ii*) a 2D model of the complex heat and mass transfer that occurs within the HP. Comparisons to experimental measurements are used to verify the relatively strong performance of the coupled HP model, despite the 2D treatment of the heat transfer and fluid flow internal to the HP.

2.2. External modeling benchmark problem

The benchmark study of Paper **P1** is performed for the computational domain of Fig. 2, which corresponds to air flow within a channel of an experimental testing apparatus employed in Paper **P2** (to be described in Section 2.4) as it passes over a HP with, in this case, three attached square fins. At one extreme of numerical modeling, direct numerical simulation (DNS) solves discretized forms of the governing equations that describe both spatially and temporally complex flows, providing detailed velocity and temperature distributions within the fluid. To capture relevant phenomena accurately, DNS simulations often require fine spatial resolution and small time steps. Hence, DNS typically requires significant computational resources to generate even a single set of predictions.

Many applications, such as those involving finned HPs, require simulations covering a range of operating conditions or entail large computational domains, and use of DNS may not be appropriate. To address the limitations of DNS, various turbulence models have been developed to predict the approximate average of the time-dependent variations within such flows [31-37]. Such models differ in their approximations, resulting in a multitude of predictions for a given physical situation [38-41], and the preferred model is sometimes case-dependent. At the other extreme, recourse to existing simple-to-use correlations may provide approximate, yet adequate

prediction of overall heat transfer rates or convection coefficients, which will be discussed in Section 2.4.

2.2.1. Direct Numerical Simulation

Direct modeling of the complex, time-dependent flow over the finned array of Fig. 2 is performed by solving transient conservation of energy,

$$\frac{\partial T}{\partial t}+u_x\frac{\partial T}{\partial x}+u_y\frac{\partial T}{\partial y}+u_z\frac{\partial T}{\partial z}=\alpha\left(\frac{\partial^2 T}{\partial x^2}+\frac{\partial^2 T}{\partial y^2}+\frac{\partial^2 T}{\partial z^2}\right) \tag{1}$$

continuity,

$$\frac{\partial u_x}{\partial x}+\frac{\partial u_y}{\partial y}+\frac{\partial u_z}{\partial z}=0 \tag{2}$$

and momentum equations in the *x*-, *y*-, and *z*-directions.

$$\frac{\partial u_x}{\partial t}+u_x\frac{\partial u_x}{\partial x}+u_y\frac{\partial u_x}{\partial y}+u_z\frac{\partial u_x}{\partial z}=-\frac{1}{\rho}\frac{\partial p}{\partial x}+\nu\left(\frac{\partial^2 u_x}{\partial x^2}+\frac{\partial^2 u_x}{\partial y^2}+\frac{\partial^2 u_x}{\partial z^2}\right) \tag{3a}$$

$$\frac{\partial u_y}{\partial t}+u_x\frac{\partial u_y}{\partial x}+u_y\frac{\partial u_y}{\partial y}+u_z\frac{\partial u_y}{\partial z}=-\frac{1}{\rho}\frac{\partial p}{\partial y}+\nu\left(\frac{\partial^2 u_y}{\partial x^2}+\frac{\partial^2 u_y}{\partial y^2}+\frac{\partial^2 u_y}{\partial z^2}\right) \tag{3b}$$

$$\frac{\partial u_z}{\partial t}+u_x\frac{\partial u_z}{\partial x}+u_y\frac{\partial u_z}{\partial y}+u_z\frac{\partial u_z}{\partial z}=-\frac{1}{\rho}\frac{\partial p}{\partial z}+\nu\left(\frac{\partial^2 u_z}{\partial x^2}+\frac{\partial^2 u_z}{\partial y^2}+\frac{\partial^2 u_z}{\partial z^2}\right)+\left[1-\beta\left(T-T_0\right)\right]g \tag{3c}$$

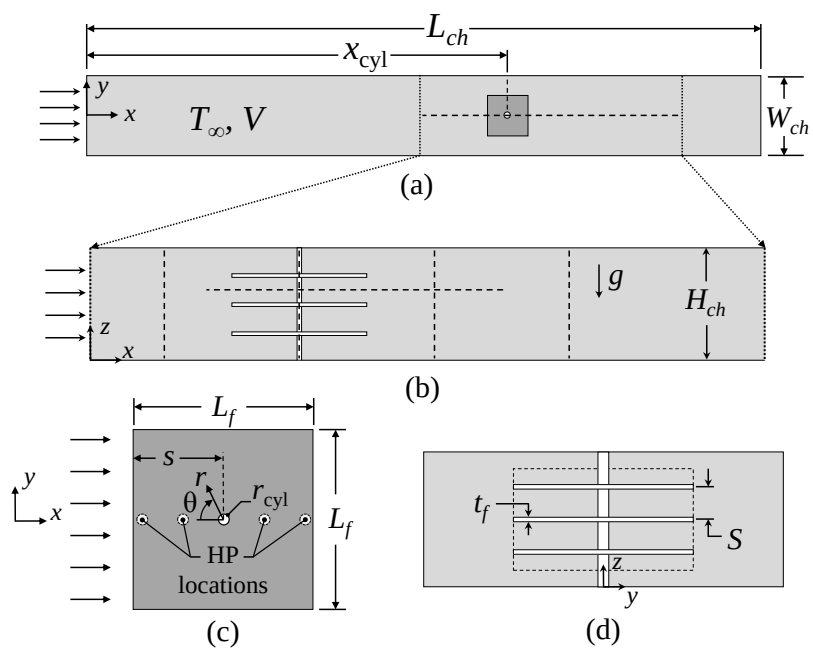

Fig. 2. Schematic of the computational domain. **(a)** Top view (*x*-*y* plane), **(b)** side view (*x*-*z* plane), **(c)** fin section (*x*-*y* plane), **(d)** flow direction (*y*-*z* plane), **[P1]**

Throughout this dissertation, the flow is assumed to be incompressible, and the fluid (air) is treated as a Boussinesq ideal gas [42] with properties evaluated at T_0 = 25°C and an absolute pressure of 1 atm. Initial conditions are a uniform fluid temperature of T_∞ and zero velocities throughout the domain.

2.2.2. Turbulence models

Five turbulence models, all of which employ additional equations to describe the transport of turbulence quantities and quantify turbulent (effective) transport, are considered. Two variations of Wilcox's κ-ω model, namely Menter's Shear Stress Transport model (SST) [31] and the Gamma-Theta transitional model (γ-Re$_\theta$ SST) [32-34], are investigated. Additional simulations using a classic κ-ε model [35], along with two common variations, the Re-Normalization Group model (RNG κ-ε) [36], and Explicit Algebraic Reynolds Stress model (κ-ε EARSM) [37], are performed. All five models are implemented in a consistent manner, and their predictions are compared to those of the DNS. The turbulence model simulations are performed for steady state conditions, governed by conservation of energy[1] (Eq. (4)), mass (Eq. (2)), as well as x-, y-, and z-momentum (Eqs. (5a) – (5c)).

$$u_x \frac{\partial T}{\partial x} + u_y \frac{\partial T}{\partial y} + u_z \frac{\partial T}{\partial z} = \left(\alpha + \alpha_{\text{turb}}\right)\left(\frac{\partial^2 T}{\partial x^2} + \frac{\partial^2 T}{\partial y^2} + \frac{\partial^2 T}{\partial z^2}\right) \tag{4}$$

$$u_x \frac{\partial u_x}{\partial x} + u_y \frac{\partial u_x}{\partial y} + u_z \frac{\partial u_x}{\partial z} = -\frac{1}{\rho}\frac{\partial p}{\partial x} + \left(\nu + \nu_{\text{turb}}\right)\left(\frac{\partial^2 u_x}{\partial x^2} + \frac{\partial^2 u_x}{\partial y^2} + \frac{\partial^2 u_x}{\partial z^2}\right) \tag{5a}$$

$$u_x \frac{\partial u_y}{\partial x} + u_y \frac{\partial u_y}{\partial y} + u_z \frac{\partial u_y}{\partial z} = -\frac{1}{\rho}\frac{\partial p}{\partial y} + \left(\nu + \nu_{\text{turb}}\right)\left(\frac{\partial^2 u_y}{\partial x^2} + \frac{\partial^2 u_y}{\partial y^2} + \frac{\partial^2 u_y}{\partial z^2}\right) \tag{5b}$$

$$u_x \frac{\partial u_z}{\partial x} + u_y \frac{\partial u_z}{\partial y} + u_z \frac{\partial u_z}{\partial z} = -\frac{1}{\rho}\frac{\partial p}{\partial z} + \left(\nu + \nu_{\text{turb}}\right)\left(\frac{\partial^2 u_z}{\partial x^2} + \frac{\partial^2 u_z}{\partial y^2} + \frac{\partial^2 u_z}{\partial z^2}\right) + \left[1 - \beta\left(T - T_o\right)\right]g \tag{5c}$$

Because the focus at this stage of the dissertation is on external convective effects, the cylinder and fin are considered to be isothermal. This restriction is relaxed starting with Paper **P2** (Section 2.4). Details of the additional governing turbulence equations and their corresponding boundary conditions may be found in Paper **P1**.

---

[1] Note that while it was inadvertently omitted in Paper **P1**, the turbulent thermal diffusivity, α_{turb}, is included in the conservation of thermal energy. Values of the turbulent Prandtl number (used to calculate α_{turb}) may be found elsewhere [43].

2.2.3. Benchmark numerical results

Simulations were run for low (0.5 m/s) and high (1.5 m/s) channel inlet velocities for the DNS and the five turbulence models. Samples of the results presented in Paper **P1** are as follows. Velocity distributions in the vertical mid-plane of the channel are shown in Fig. 3 with the mean flow traveling from left to right. The distributions of the steady-state SST and γ-Re_θ SST models are in qualitative agreement with those of the DNS. As in the DNS results, buoyancy effects are evident in the low velocity SST predictions but a similar buoyancy effect is not evident in the κ-ε, RNG κ-ε, or κ-ε EARSM predictions. For either the low- or high speed cases, the DNS and SST predictions show similar behavior immediately upstream and downstream of the vertical finned cylinder. In contrast, the three κ-ε models predict significantly larger velocities immediately downstream of the cylinder, relative to the benchmark DNS predictions. Predictions of the SST and γ-Re_θ SST models are nearly indistinguishable qualitatively.

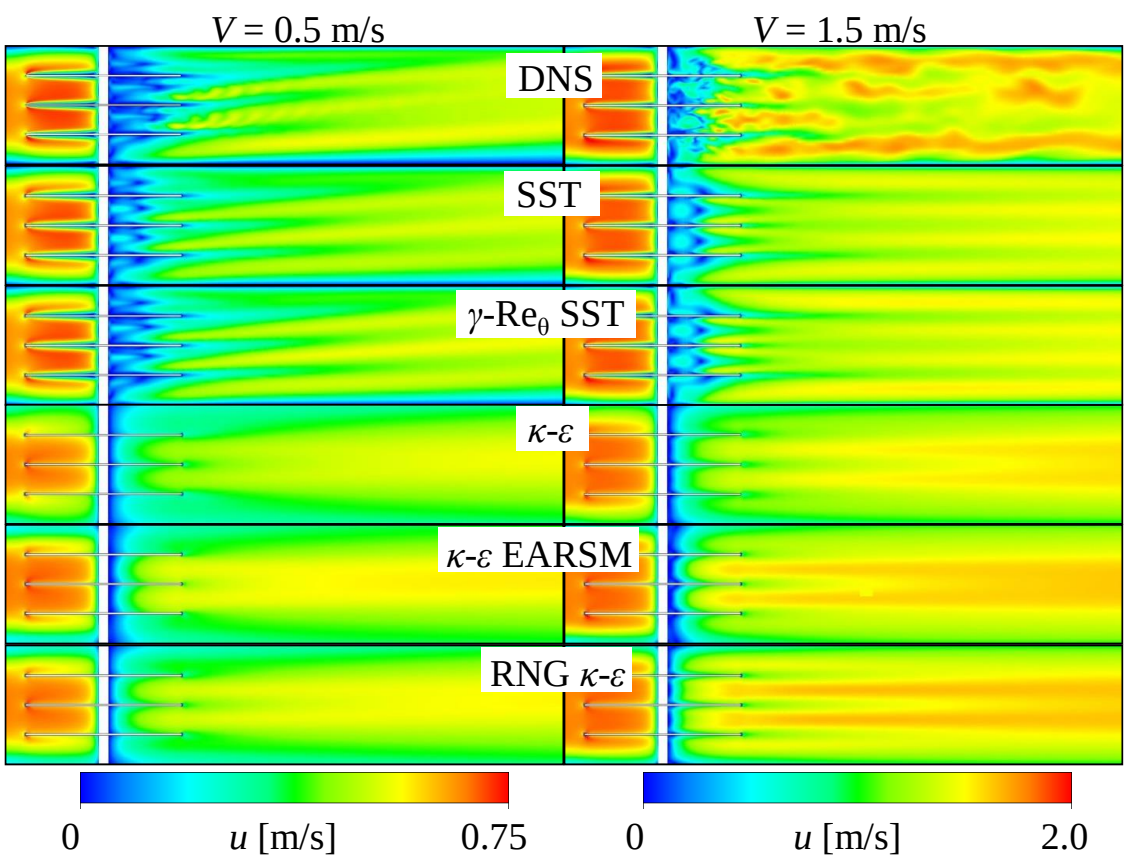

Fig. 3. Velocity distributions in the channel vertical centerplane (*x*-*z* plane). DNS predictions are shown at t = 1.75 s for both the low and high velocity cases. **[P1]**

Temperature distributions in the vertical mid-plane are displayed in Fig. 4. As discussed relative to Figs. 2 and 3, buoyancy effects are noted for the low inlet velocity case with warm air rising as it propagates downstream. The effects of buoyancy are not evident in the high velocity case. Overall, the predicted temperatures of the DNS, SST, and γ-Re_θ SST models are in qualitative agreement. The κ-ε, RNG κ-ε, and κ-ε EARSM models behave poorly, and only the κ-ε predictions are shown. From these qualitative results (as well as velocity and temperature distributions displayed midway between two fins as shown in Figs. 4 and 6, respectively, of **P1**), the poor performance of κ-ε predictions is readily apparent.

Comparisons of local heat transfer coefficients are made in Figs. 5 and 6. Note that, due to inability of the κ-ε models to even qualitatively predict the flow field, local convection coefficient predictions associated with these models are in poor quantitative agreement with DNS-predicted values, and are not reported here or in Paper **P1**. Instantaneous (DNS) and time-averaged (SST) local convection coefficient distributions for the cylinder are shown in Fig. 5. In general, the largest local coefficients are on the upstream portion of the cylinder (θ = 0°, Fig. 1c), and are smallest near θ = ±180°. Small local convection coefficients also exist in the vicinity of each fin because of the velocity reduction associated with boundary layer development on the fins. Overall, SST-predicted local heat transfer coefficients are substantially closer to the DNS benchmark predictions than those from the κ-ε models. Instantaneous (DNS) and time-averaged (SST) local heat transfer coefficients on the top surface of the middle fin are reported in Fig. 6. Whereas boundary layer development on the fins influences local heat fluxes on the cylinder (Fig. 5), flow around the cylinder influences local fluxes on the fins. The fin surface downstream of the cylinder experiences relatively high local coefficients associated with the shedding of vortices from the cylinder.

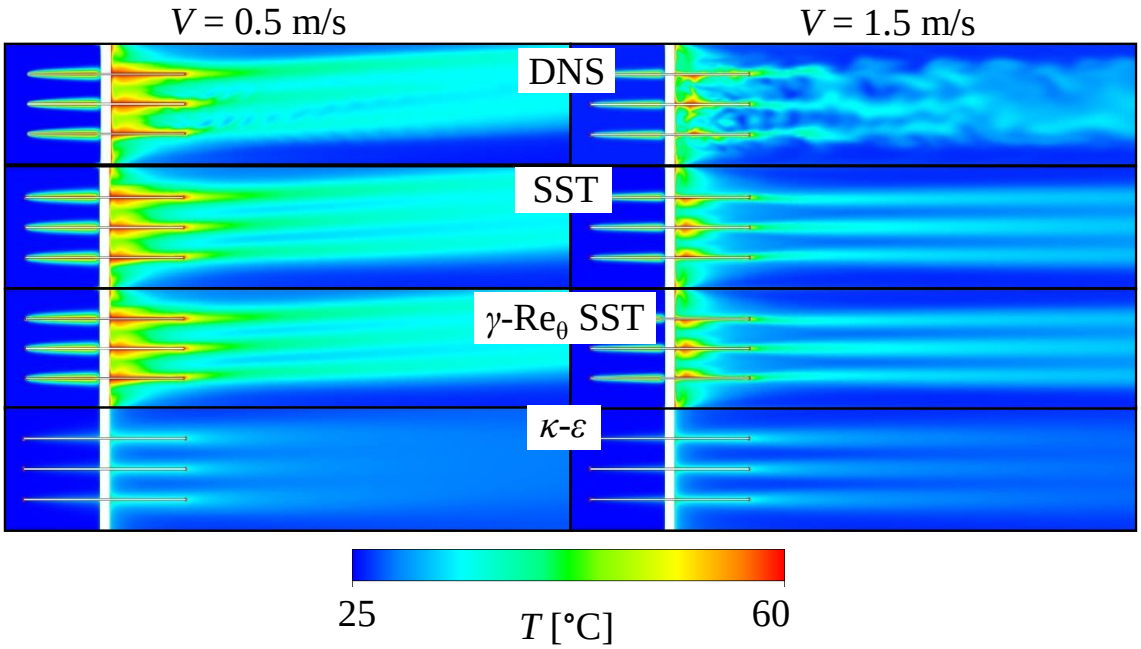

Fig. 4. Temperature distributions in the channel vertical centerplane (*x*-*z* plane). **[P1]**

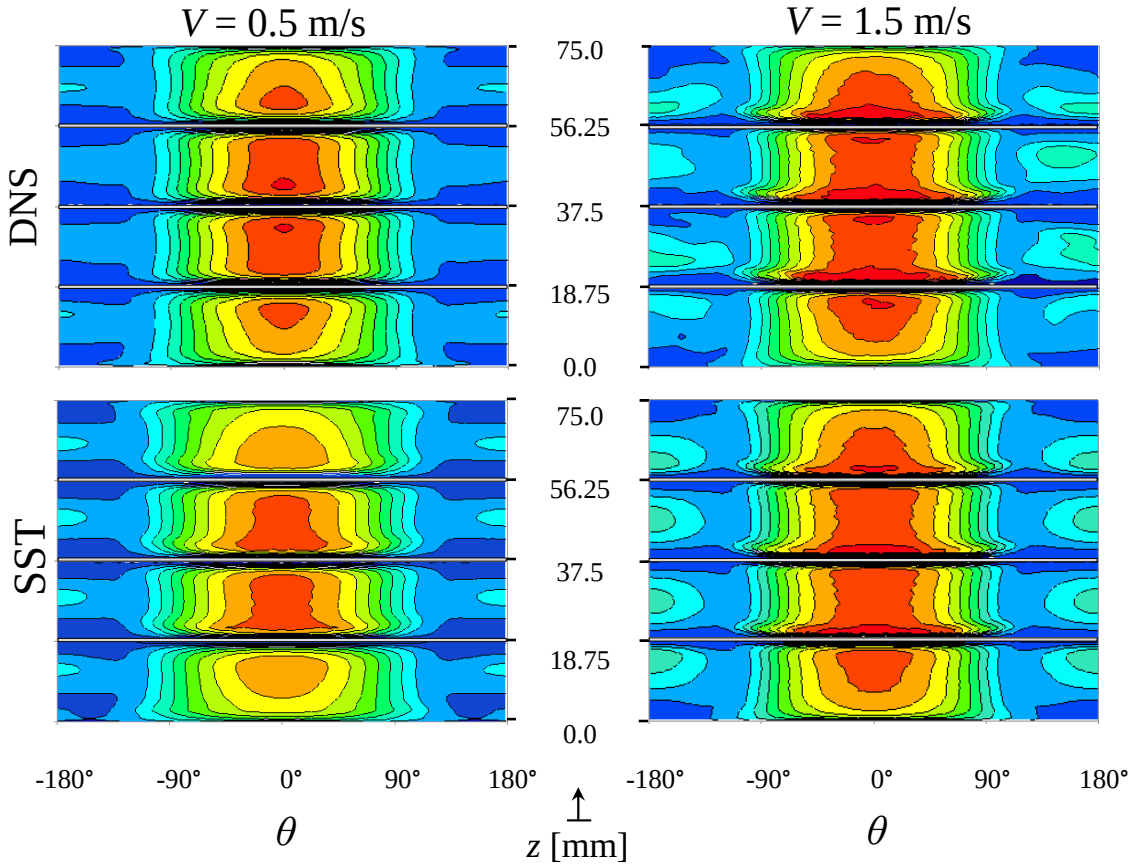

Fig. 5. Predicted transfer coefficient distributions on the cylinder. Coefficients range from h_{cyl} = 0 to 75 W/m^2 K and 0 to 150 W/m^2 K for the 0.5 and 1.5 m/s cases, respectively. Contour bands are plotted at intervals of 7.5 and 15 W/m^2 K for the two velocity cases. **[P1]**

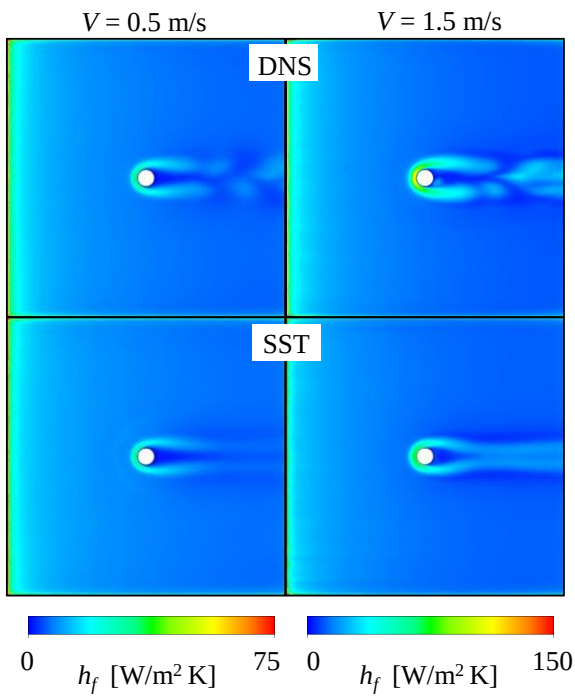

Fig. 6. Heat transfer coefficient distributions on the upper surface of the middle fin. Convection coefficients range from h_f = 0 to 75 W/m^2 K and 0 to 150 W/m^2 K for the V = 0.5 and 1.5 m/s cases, respectively. **[P1]**

Area- and time-averaged convection coefficients for the total exposed fin ($\overline{h_f}$) and exposed cylinder ($\overline{h_{\text{cyl}}}$) surfaces are determined during the quasi-steady state with the DNS model using Eqs. (13a) and (13c) of Paper **P1**. In both the high and low velocity cases, information at 150 distinct times (every fifth step over a time window of 0.75 s) were used to calculate the time average values. The values from the DNS were then compared with the area-averaged values of $\overline{h_f}$ and $\overline{h_{\text{cyl}}}$ obtained from steady state simulations, as defined by Eqs. (13b) and (13d) of Paper **P1**.

Comparison of the predicted convection coefficients, listed in Table 1, confirms the ability of the SST and γ-Re_θ SST models to closely replicate the benchmark DNS predictions. Specifically, the SST and γ-Re_θ SST values of $\overline{h_f}$ differ from the DNS model by 13% (V = 0.5 m/s case) to 18% (V = 1.5 m/s case). In contrast, the κ-ε, RNG κ-ε, and κ-ε EARSM predictions are in error by approximately 58% (V = 1.5 m/s case) and 70% (V = 0.5 m/s case). DNS, SST, and γ-Re_θ SST predictions of $\overline{h_{\text{cyl}}}$ are in agreement to within 4% for each case, while the κ-ε, RNG κ-ε, and κ-ε EARSM predictions exhibit errors between 41% and 65%.

	V = 0.5 m/s		V = 1.5 m/s	
	$\overline{h_f}$	$\overline{h_{\mathrm{cyl}}}$	$\overline{h_f}$	$\overline{h_{\mathrm{cyl}}}$
	W/m^2 K	W/m^2 K	W/m^2 K	W/m^2 K
DNS	12.9	28.9	23.2	50.9
SST	11.3	29.4	19.1	52.5
γ-Re$_\theta$ SST	11.4	29.5	19.2	52.9
κ-ε	4.84	13.4	9.76	30.0
RNG κ-ε	3.98	11.3	8.80	23.1
κ-ε EARSM	3.90	10.2	9.44	23.2

Table 1. Predicted time- and area-averaged fin and cylinder heat transfer coefficients predicted using various numerical models. **[P1]**

As a compromise between cost and accuracy, the SST model is used in the subsequent predictions of external convection simulations of Paper **P2** (Section 2.4).

2.3. Comparison of analytical models

Identifying analytical correlations that can approximate the thermal characteristics of the various extended and cylindrical (HP) surfaces analyzed for this dissertation is also desirable, as they allow for an expedient comparison of the relative performance of the fin arrays. To this end, the benchmark study was used as an opportunity to compare the accuracy of various correlations to predict the convective heat transfer coefficients associated with the fin and exposed HP surfaces.

The simplest correlation-based approach involves use of existing expressions for (*i*) cylinders in cross flow (Eqs. (14a) and (14b) of Table 2 of Paper **P1**) and (*ii*) flat plates in parallel flow (Eqs. (14c) to (14e) of Table 2 of Paper **P1**) to independently estimate $\overline{h_{\mathrm{cyl}}}$ and $\overline{h_f}$, neglecting all interaction and coupling between cylinder and fin boundary layer development. A more sophisticated approach involves utilization of numerical simulation-based correlations such as those of Romero-Mendez et al. [44] for convection from a finned tube, Eqs. (14f) and (14g) of Table 2 of Paper **P1**. (The +S correlation is affiliated with larger fin pitches.) Alternatively, an experimentally-derived correlation due to Sparrow and Samie [45] (Eq. (14h) of Table 2 of Paper **P1**) is tested.

Predicted area-averaged heat transfer coefficients for the fin and cylinder surfaces using the DNS, SST, κ-ε, and various analytical correlations for the V = 0.5 and 1.5 m/s cases are listed in Table 2. Predicted fin heat transfer coefficients, $\overline{h_f}$, using the three flat plate correlations are shown in rows 4 through 6 of Table 2. The Churchill and Bernstein correlation for a cylinder in cross flow yields results (see top $\overline{h_{\text{cyl}}}$ values in rows 4 through 6 of Table 2) that are within 5.5% and 1.4% of the SST predictions (see $\overline{h_{\text{cyl}}}$ values in row 2 of Table 2) for the V = 0.5 and 1.5 m/s cases, respectively. The Sparrow correlation for a cylinder in cross flow (see parenthetical $\overline{h_{\text{cyl}}}$ values in rows 4 through 6 of Table 2) yields results that are within 0.4% and 0.8% of the SST predictions for the V = 0.5 and 1.5 m/s cases, respectively. Both correlations exhibit excellent agreement with the DNS and SST predictions.

		V = 0.5 m/s			V = 1.5 m/s		
		$\overline{h_f}$ W/ m^2 K	$\overline{h_{\text{cyl}}}$ W/ m^2 K	$\overline{h_{\text{tot}}}$ W/ m^2 K	$\overline{h_f}$ W/ m^2 K	$\overline{h_{\text{cyl}}}$ W/ m^2 K	$\overline{h_{\text{tot}}}$ W/ m^2 K
Numerical	DNS	12.9	28.9	16.0	23.2	50.9	28.7
	SST	11.3	29.4	14.9	19.1	52.5	25.7
	κ-ε	4.8	13.4	6.5	9.8	30.0	13.8
Correlation-based	Flat Plate Laminar + Cylinder	8.72	31.0 (29.5)	9.20 (9.17)	15.1	53.2 (52.9)	15.9 (15.9)
	Flat Plate Turbulent + Cylinder	5.31	31.0 (29.5)	5.87 (5.84)	12.8	53.2 (52.9)	13.7 (13.7)
	Flat Plate Transition + Cylinder	8.43	31.0 (29.5)	8.92 (8.89)	16.1	53.2 (52.9)	16.9 (16.9)
	Romero-Méndez			8.01	-	-	14.1
	Romero-Méndez + S	-	-	8.35	-	-	14.5
	Sparrow and Samie	-	-	10.8	-	-	23.2

Table 2. Numerically- and correlation-predicted time- and area-averaged heat transfer coefficients for L_f = 100 mm. Predictions for $\overline{h_{\text{cyl}}}$ based on Eq. (14b) of Paper **P1** are shown parenthetically. **[P1]**

Predicted time- and area-averaged total array heat transfer coefficients, determined using $\overline{h_{\text{cyl}}}$ and $\overline{h_f}$, correspond to a weighted average of both the fin and heat pipe surface areas, $\overline{h_{\text{tot}}} = (\overline{h_f} A_f + \overline{h_{\text{cyl}}} A_{\text{cyl}}) / \left(A_f + A_{\text{cyl}} \right)$, and are in poor agreement with the benchmark DNS and SST values. The top and parenthetical values for $\overline{h_{\text{tot}}}$ are determined using the Eqs. (14a) (Churchill and Bernstein [1]) and (14b) (Sparrow et al. [46]) of Paper **P1**, respectively. Similarly, the Romero-Mendez based predictions are in poor agreement with the benchmark. Predictions generated with Eq. (14h) of Paper **P1** (Sparrow and Samie) show better agreement with the DNS and SST predictions, especially for the V = 1.5 m/s case. Therefore, if analytical expressions are to be used, the Sparrow and Samie correlation (Eq. (14h) of Paper **P1** correlation is recommended for fin array geometries and flow conditions similar to those discussed here. Note that Paper **P1** presents additional results assessing the impact of changes to the fin location and size on the ability of the analytical models.

2.4. Coupled internal and external numerical model of a finned heat pipe

2.4.1. Internal and external coupled simulations

With the SST numerical model identified as the best performing steady state simulation of the external airflow around the finned HP (as outlined in Paper **P1**), numerical simulations which additionally incorporate the heat transfer internal to the fins and HP were performed as outlined in Paper **P2**. A novel overall model, consisting of two coupled sub-models (one internal and one external), was used to predict the heat transfer performance of the array.

The internal sub-model describes axisymmetric, multiphase heat transfer and fluid flow within the HP. Details of the model, including the descriptive equations, are available in Sharifi et al. [28]. This model utilizes the thermal resistances external to the heat pipe, inferred from the second sub-model, as boundary conditions. In the second, external sub-model, the 3D single phase convection external to the HP condenser section is predicted using the SST modeling approach. Conduction within the fins and walls of the HP is included, and the transport of latent thermal energy via the complex phase change process associated with the HP working fluid is approximated by assigning an effective thermal conductivity to the vapor region of the HP in the external simulations. Further details of the external simulation may be found in Paper **P2**.

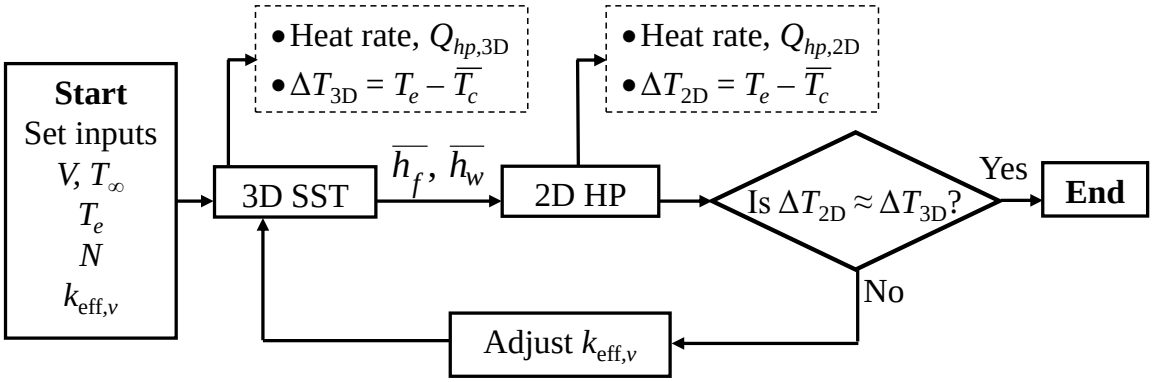

Fig. 7. Coupling of the internal (2D HP) and external (3D SST) numerical models. **[P2]**

The SST (external) and HP (internal) sub-models are coupled as diagrammed in Fig. 7. The overall simulation is initialized by first solving the steady-state, 3D, SST model. Upon convergence, the area-averaged convection heat transfer coefficients for the fins, $\overline{h_f}$, and the exposed HP condenser wall surfaces, $\overline{h_w}$, are determined from the predicted values of the SST model.

Step 1 of the iteration between the two sub-models involves prediction of the HP heat rate, $Q_{hp,3D}$, using the external SST model and an assumed value of $k_{eff,v}$. Predicted heat rates and temperature differences across the HP (ΔT) are saved for comparison to corresponding quantities predicted by the 2D internal HP model. In Step 2, values of $\overline{h_w}$ and $\overline{h_f}$ predicted by the 3D SST external model are used in the 2D internal HP model. Values of the heat rate, $Q_{hp,2D}$, and average temperature difference ΔT_{2D} are then obtained from the internal model. If $\Delta T_{2D} \approx \Delta T_{3D}$, a new value of effective thermal conductivity of the vapor is specified, and Steps 1 and 2 are repeated until $\left(\Delta T_{3D} - \Delta T_{2D}\right)/\Delta T_{2D} < 0.02$. A comparison of the final predicted values of the HP heat rates obtained by the 2D (internal) and 3D (external) models, $Q_{hp,2D}$ and $Q_{hp,3D}$ respectively, is used as a check of the overall modeling strategy.

2.4.2. Coupled model results

Comparisons of experimentally measured and numerically predicted (both 2D internal and 3D external) heat rates are reported in Table 3 for 8 cases consisting of all combinations of two velocities, two fin counts, and two excess temperatures. Also included in the table are the converged values of the effective vapor thermal conductivity and the heat transfer coefficients on the cylinder and fin surfaces.

Input parameters			Predicted values					
N	V	T_e	$k_{\mathrm{eff},v}$	$\overline{h_w}$	$\overline{h_f}$	$Q_{hp,3D}$	$Q_{hp,2D}$	Q_{exp}
	m/s	°C	W/m K	W/m^2 K	W/m^2 K	W	W	W
3	0.5	34.5	47,500	28.5	10.7	4.4	3.8	4.1
		60	52,000	28.5	10.7	15.9	14.8	15.4
	1.5	34.5	39,000	55.3	20.3	6.0	5.5	5.0
		60	63,000	55.3	20.3	23.1	20.7	19.3
6	0.5	34.5	35,000	26.3	11.0	7.6	6.9	5.9
		60	64,000	26.5	11.0	29.9	26.6	26.5
	1.5	34.5	32,000	51.2	19.5	10.4	9.2	7.3
		60	70,000	51.5	19.5	42.0	37.0	36.3

Table 3. Conditions (left) and predicted values (right) for parametric calculations. **[P2]**

the cylinder and fin surfaces. Predicted (2D and 3D) heat rates within 7 percent of the average of the two heat rates for all cases considered. Measured heat rates are consistently lower than predicted heat rates (an average discrepancy of 10 percent). This discrepancy may be attributed to contact resistances between the HP and the fins that are not accounted for in either (SST or HP) model.

Predicted (SST) and measured local fin temperatures (for the top surface of the upper square fin) are reported in Fig. 8 for a representative case. The minimum fin temperature shown for the measurements is $T_{\min} \approx 37.5$ºC and occurs at the outer leading edges of the square fin, while maximum temperatures ($T_{\max} \approx 56.0$ºC) occur at the fin root. The minimum and maximum SST-predicted temperatures occur at the same locations and are $T_{\min} = 37.7$ºC and $T_{\max} = 56.2$ºC, respectively. Advective effects are evident in both the measured and predicted temperature distributions, but regions closer to the fin root have a more uniform temperature distribution in the azimuthal direction. The nearly axisymmetric temperature distribution near the base of the fin gives further credence to the 2D modeling of the HP taken here.

Predicted temperature distributions along the length of the HP wall for both $N = 3$ and $N = 6$ fins ($T_e = 60$ºC, $V = 1.5$ m/s) are shown in Figs. 9(a) and 9(b), respectively, for both the 2D and 3D simulations of the coupled model. Both figures also include predicted temperature distributions for $N = 0$ for purposes of comparison. All simulations involve a HP evaporator temperature of 60ºC and an ambient air temperature of 25ºC. Significant temperature depressions

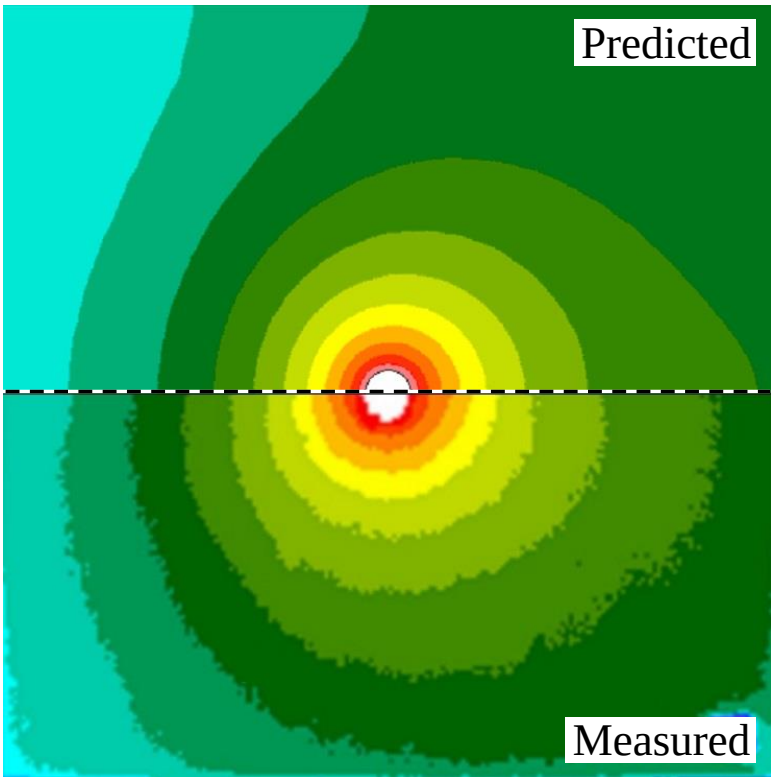

Fig. 8. Predicted (upper half) and measured (bottom half) fin top surface temperature distribution for V = 1.5 m/s (left to right): T_e = 60ºC, N = 6. See Section 4.2 of Paper **P2** for isotherm values. **[P2]**

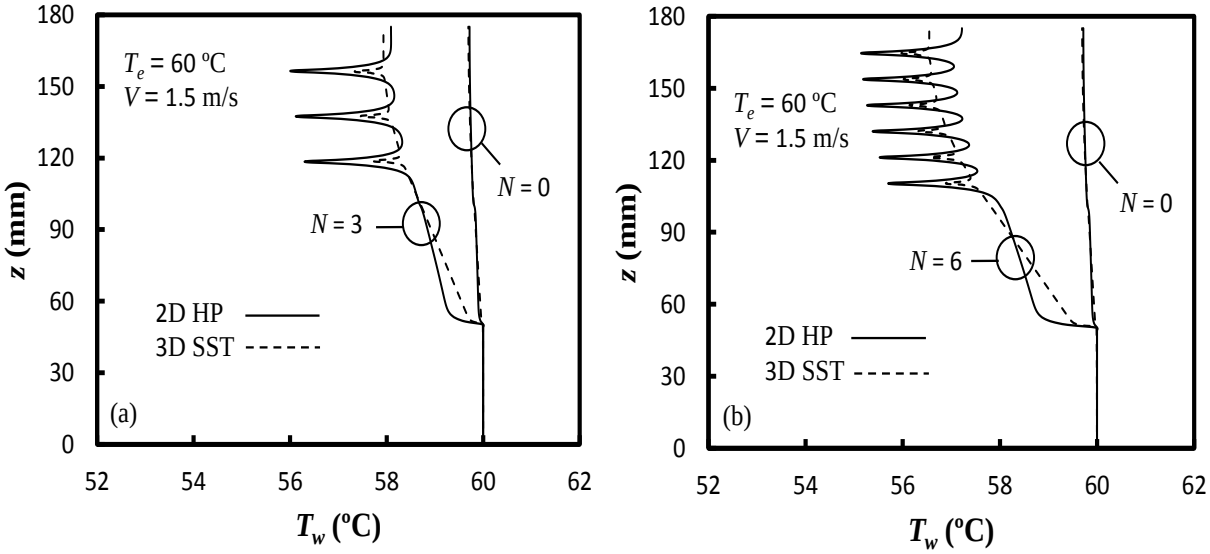

Fig. 9. Predicted HP wall temperature distributions ($r = r_{hp}$) for T_e = 60ºC. **(a)** N = 3, **(b)** N = 6. **[P2]**

exist within the HP wall adjacent to the fin roots. The depressions are a result of the interplay between the external convection processes, conduction within the fins, and multimode heat transfer within the HP. Depressions predicted by the 2D model are consistently larger than those for the 3D model. This may be attributed to the approximate treatment of the heat transfer within the HP vapor region in the 3D model which is unable to replicate, for example, variations in local condensation rates internal to the HP and, in turn, the correspondingly high local heat transfer rates adjacent to the fin roots. It is well known that increased constriction resistances are associated with large temperature depressions of the type noted here [1]. These resistances will increase the overall thermal resistance of the HP system, and reduce the HP heat rate predicted by the 2D model relative to those predicted by the 3D model, consistent with the results of Table 3. To the author's knowledge, this constriction resistance effect has not been previously reported in HP-related research.

2.4.3. Comparison to experimental measurements

Values of $Q_{hp,2D}$ and $Q_{hp,3D}$ determined from the coupled numerical model of Paper **P2** are compared to experimentally measured heat rates for validation. The experiments involve a copper-H_2O HP whose condenser fin array is cooled by forced convection of air, as shown in Figs. 3 and 4 of Paper **P2**. Heat rates predicted by the 2D HP and 3D SST models, along with measured heat rate values, are reported graphically in Fig. 10 for N = 3 and 6 fins, T_∞ = 25ºC, and a range of convective conditions. As evident, heat rates increase as N, T_e, and V are increased, with general agreement between the heat rates that are predicted and measured.

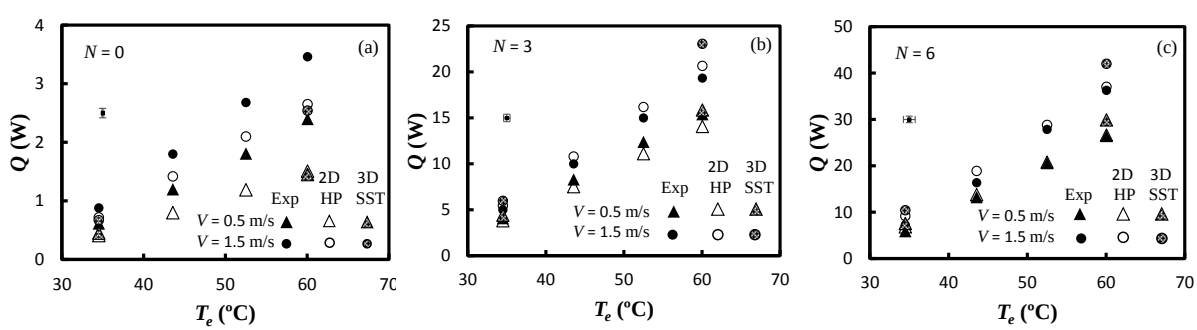

Fig. 10. Heat transfer rates versus HP exterior evaporator wall temperatures for different inlet air velocities. **(a)** N = 0, **(b)** N = 3, (c) N = 6. **[P2]**

2.5. Contact resistance and HP thermal resistance model

The complex interaction of local condenser section heat rates and the internal HP mechanics, described in conjunction with Fig. 9, are investigated further in Paper **P5**. The condenser section boundary conditions of the internal HP model of Paper **P2** are written to accommodate the potential thermal contact resistances at the fin-HP interface.

As discussed in the preceding section, the increase in local condensation rates at the HP wick adjacent to the fin roots leads to a (previously unreported) temperature depression in the HP wall. This temperature drop reflects a thermal constriction resistance. Paper **P5** compares heat transfer rates for (*i*) individual fin arrays and (*ii*) a finned HP-heat sink, which has additional base material concentrically attached to the HP. The hypothesis is that inclusion of a base material on the fin (the HP-heat sink) will reduce thermal depressions in the HP wall, making condensation rates more uniform within the HP, and extending the range of the operation of the HP by avoiding the *condensation limit* [20] beyond which local condensation rates cannot be increased.

For similar operating conditions, the HP-heat sink typically provides lower overall thermal resistances than the fin array without the heat-spreading base material. This is due to the mitigation of the constriction resistance by allowing for a larger amount of heat to reach the fin root by way of axial conduction. The impact of a thermal contact resistance between the HP and the two array designs is also investigated, finding that the plain fin array is more sensitive to a change in the thermal contact resistance than the fin with base array.

In addition to the numerical modeling, Paper **P5** presents a thermal resistance model of the HP. This model allows for the approximation of the HP thermal resistance, and was employed in the analysis of Papers **P3** and **P4**.

The metal foam array (Paper P3) 3

3.1. Introduction and background

As discussed in Section 1, open-cell high-porosity metal foams have many potential heat transfer applications, due to their extremely large surface areas per unit volume [47-49]. Large surface areas typically lead to low thermal resistances, making the prospect of metal foam (as opposed to metal fins) arrays attractive for application in HP systems. Heat transfer within a metal foam (depicted in Fig. 11) is complex, consisting of conduction within the metal component, convection between the metal and the saturating working fluid, and potentially radiation throughout the fluid domain.

Numerous efforts have been made to model the heat transfer processes using both multi-phase local, and continuum approaches. Local multi-phase analyses are often performed with the intent of informing continuum scale models through the quantification of effective thermal transport properties. Analytical [50-52] and numerical [53-59] models of idealized unit cells have been used to derive correlations describing foam properties that are necessary for continuum modeling [60-68].

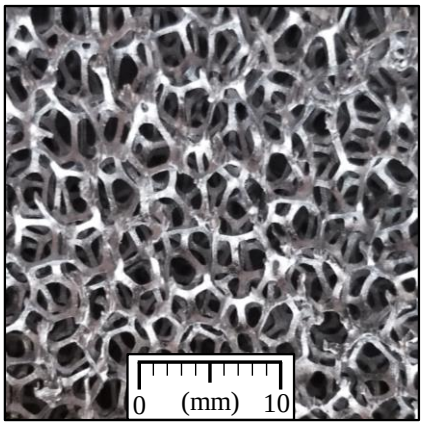

Fig. 11. Photograph of 10 PPI aluminum Duocel® foam. **[P3]**

In Paper **P3**, (*i*) a continuum-based, analytical description for conduction and forced convection heat transfer within an annular porous matrix attached concentrically to a circular tube, reported in terms of a thermal efficiency, is developed, (*ii*) a continuum-based numerical model is used to develop a semi-analytical expression for the thermal efficiency of a cubical porous block attached on-center to a circular tube, and (*iii*) the thermal behavior predicted with the semi-empirical expression is compared to experimental measurements.

3.2. Analytical model of annular porous array

Consider a cool, ambient fluid that is forced through an open-cell, annular metal foam block that is attached to the exterior of a hot cylindrical tube (or heat pipe), as illustrated in Fig. 12(a). Consistent with standard fin analyses [1], steady, one-dimensional conduction heat transfer in the radial direction is assumed. In addition, the block is taken to be isotropic with constant properties, and both (*i*) radiation heat transfer and (*ii*) heat transfer in the radial direction at $r = r_2$ are assumed to be negligible. The fluid flow within the porous material is assumed to provide a uniform convection coefficient between the fluid and solid phase, and is described by a characteristic temperature, that is either (*i*) that of the ambient fluid (as in the analysis below) or (*ii*) an appropriate log-mean temperature (as in a the comparison of model predictions with experimental results to be discussed later). Conduction within the gas can be shown to be negligible for the porous medium and fluid of interest here, and is neglected.

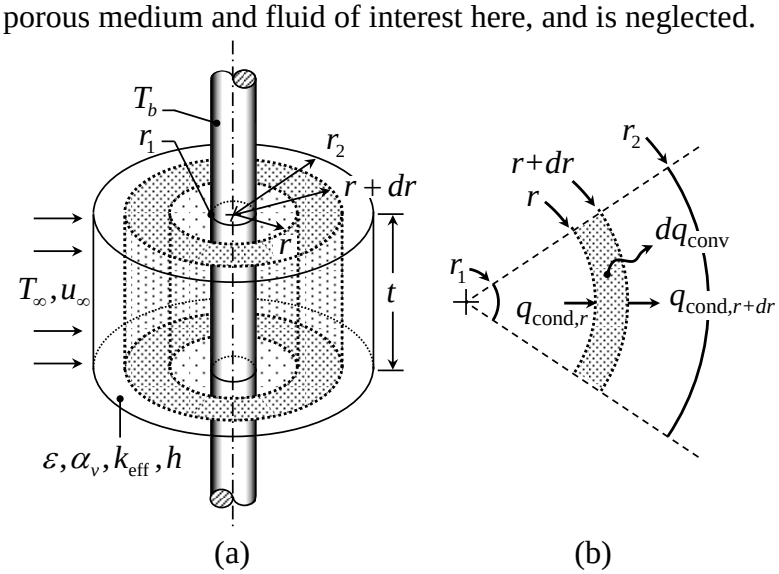

Fig. 12. Description of the 1D annular analytical domain. **(a)** overall domain, **(b)** annular control volume energy balance. **[P3]**

Applying conservation of thermal energy to a radial differential element within the porous cylindrical block, as illustrated in Fig. 12(b), ultimately yields

$$\frac{d^2\theta}{dr^2}+\frac{1}{r}\frac{d\theta}{dr}-m^2\theta=0 \qquad \text{where} \qquad m^2=\frac{\bar{h}\,\alpha_v}{k_{s,\text{eff}}} \tag{6}$$

Here, α_v is the specific surface area (surface area per unit volume) of the porous medium and $k_{s,\text{eff}}$ is the effective thermal conductivity of the solid phase. The heat transfer coefficient within the medium, $\bar{h}$, represents the spatially averaged value of the local heat transfer coefficient, h, at the metal-fluid interfaces. The excess temperature is $\theta(r) \equiv T(r) - T_\infty$. When solved under the boundary conditions of (*i*) constant base temperature, $\theta(r_1) = \theta_b$, and (*ii*) adiabatic behavior at the outer radius of the annular block, $\left(d\theta/dr\right)\big|_{r_2}=0$, expressions for the annular porous matrix heat rate and porous matrix efficiency for the annular block may be written as

$$q\left(r_1\right)=2\pi k_{s,\,\text{eff}}\,r_1 t\theta_b m\frac{K_1\left(mr_1\right)I_1\left(mr_2\right)-I_1(mr_1)K_1(mr_2)}{K_0\left(mr_1\right)I_1\left(mr_2\right)+I_0(mr_1)K_1(mr_2)} \tag{7}$$

and

$$\eta_a=\frac{\bar{\theta}}{\theta_b}=\frac{2r_1}{m\left(r_2^2-r_1^2\right)}\left[\frac{K_1\left(mr_1\right)I_1\left(mr_2\right)-I_1(mr_1)K_1(mr_2)}{K_0\left(mr_1\right)I_1\left(mr_2\right)+I_0(mr_1)K_1(mr_2)}\right] \tag{8}$$

respectively. The porous matrix efficiency, η_a, is analogous to the traditional fin efficiency [21] and leads to an expression for the equivalent thermal resistance associated with the combined conduction and convection processes within the foam,

$$R_{f,a}=\frac{\theta_b}{q\left(r_1\right)}=\frac{1}{A_s\eta_a\bar{h}}=\frac{1}{\alpha_v t\pi\left(r_2^2-r_1^2\right)\eta_a\bar{h}} \tag{9}$$

Correlations for determining α_v, $k_{s,\text{eff}}$, and $\bar{h}$ in open-cell metal foams are provided in Section 2.2 of Paper **P3**.

3.3. Numerical model for annular and square arrays

In order to extend the application range of the annular correlations of Section 3.2, numerical analysis of both annular and square array geometries were performed[2] using a

[2] Metal foams are commercially available in rectangular block forms with a square footprint, suggesting the relevance and importance of extending the preceding analysis for the annular block to square geometries.

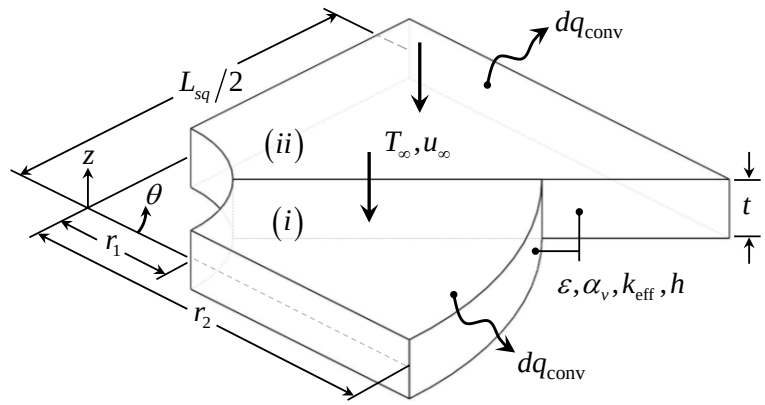

Fig. 13. Numerical domains for the (*i*) annular and (*ii*) square geometries. **[P3]**

consistent set of assumptions as described for the preceding analysis, with the exception that the numerical simulations include 3D effects. The predicted efficiencies associated with the two foam geometries of Fig. 13[3] were then compared over a range of square block lengths (L_{sq}), annular block radius ratios (r_2/r_1), and porous matrix constants (m) as defined in Eq. (6), in order to describe the square block behavior with expressions for the thermal efficiency and resistance.

Both geometries are described in terms of a common outer lateral dimension of $r_2 = L_{sq}/2$ and common thickness, t. Heat transfer within each domain is governed by a two-temperature porous model [69], which describes both the moving fluid (air) within the porous medium, and the solid component of the medium (aluminum). Heat transfer and fluid flow within the air are governed by conservation of energy, Eq. (10), conservation of mass, Eq. (11), and conservation of momentum, Eqs. (12a - 12c). Momentum conservation is described by the Brinkman-Forchheimer-extended Darcy model [69], which includes both pressure loss terms associated with the Darcy coefficient (K) and second order losses (K_{loss}), as calculated using the correlations provided by Calmidi [70].

[3] Symmetry is taken advantage of in the numerical modeling, resulting in the 45° computational domains for the (i) annular and (ii) square block cases of Fig. 13.

$$\varepsilon\rho_f c_{p,f}\left(u_x\frac{\partial T_f}{\partial x}+u_y\frac{\partial T_f}{\partial y}+u_z\frac{\partial T_f}{\partial z}\right)=k_{f,\text{eff}}\left(\frac{\partial^2 T_f}{\partial x^2}+\frac{\partial^2 T_f}{\partial y^2}+\frac{\partial^2 T_f}{\partial z^2}\right)+q_{sf} \tag{10}$$

$$\frac{\partial u_x}{\partial x}+\frac{\partial u_y}{\partial y}+\frac{\partial u_z}{\partial z}=0 \tag{11}$$

$$\frac{\rho_f}{\varepsilon}\left(u_x\frac{\partial u_x}{\partial x}+u_y\frac{\partial u_x}{\partial y}+u_z\frac{\partial u_x}{\partial z}\right)=-\frac{\partial p}{\partial x}+\frac{\mu}{\varepsilon}\left(\frac{\partial^2 u_x}{\partial x^2}+\frac{\partial^2 u_x}{\partial y^2}+\frac{\partial^2 u_x}{\partial z^2}\right)-\frac{\mu}{K}u_x-K_{\text{loss}}\frac{\rho_f\varepsilon}{2}|u|u_x \tag{12a}$$

$$\frac{\rho_f}{\varepsilon}\left(u_x\frac{\partial u_y}{\partial x}+u_y\frac{\partial u_y}{\partial y}+u_z\frac{\partial u_y}{\partial z}\right)=-\frac{\partial p}{\partial y}+\frac{\mu}{\varepsilon}\left(\frac{\partial^2 u_y}{\partial x^2}+\frac{\partial^2 u_y}{\partial y^2}+\frac{\partial^2 u_y}{\partial z^2}\right)-\frac{\mu}{K}u_y-K_{\text{loss}}\frac{\rho_f\varepsilon}{2}|u|u_y \tag{12b}$$

$$\frac{\rho_f}{\varepsilon}\left(u_x\frac{\partial u_z}{\partial x}+u_y\frac{\partial u_z}{\partial y}+u_z\frac{\partial u_z}{\partial z}\right)=-\frac{\partial p}{\partial z}+\frac{\mu}{\varepsilon}\left(\frac{\partial^2 u_z}{\partial x^2}+\frac{\partial^2 u_z}{\partial y^2}+\frac{\partial^2 u_z}{\partial z^2}\right)-\frac{\mu}{K}u_z-K_{\text{loss}}\frac{\rho_f\varepsilon}{2}|u|u_z \tag{12c}$$

Heat transfer in the solid domain is governed by conservation of energy

$$0=k_{s,\text{eff}}\left(\frac{\partial^2 T_s}{\partial x^2}+\frac{\partial^2 T_s}{\partial y^2}+\frac{\partial^2 T_s}{\partial z^2}\right)+q_{fs} \tag{13}$$

where the heat transferred between the two media is represented by

$$q_{sf}=-q_{fs}=\bar{h}\,\alpha_v\left(T_s-T_f\right) \tag{14}$$

The convection coefficient and the specific surface area (associated with the exposed surface area of the solid, shown in Fig. 11) are calculated as described in Section 2.2 of Paper **P3**.

Both the solid and gas domains are subject to a common base temperature of T_b at r_1. Adiabatic conditions are applied to both the solid and the gas at the outer edges of the two blocks in order to be consistent with the annular domain analysis, while symmetry conditions are assumed along the thin, vertical faces at θ = 0° and 45° (45° and 90°) for the annular (square) domain of Fig. 13. Additional boundary conditions are listed in Paper **P3**.

3.4. Experiments

Experiments were conducted to both validate and demonstrate usage of analytical expressions for the efficiency of a *square* porous matrix, to be developed in Section 3.5. A flow channel similar to the one described in Paper **P2** was used to generate benchmark data. An electrically heated heat pipe (HP) of cylindrical cross section is used to deliver thermal energy to the bases (at $r = r_1$) of four, stacked square porous block structures which surround the condenser section of the HP. The heat is ultimately transferred to cold air drawn through the channel and

porous metal blocks. The channel is similar to (but smaller than) that of Fig. 4 of Paper **P2**. Details of the experimental setup are provided in Paper **P3**.

Detailed information regarding measurement of local temperatures, local and average channel air velocities, as well as the calibration and validation procedures may be found in Paper **P2**. Measured heat rates are compared with predictions generated using the new expression for the thermal efficiency of the square foam block that is developed in Section 5.2 of Paper **P3**.

3.5. Results and discussion

3.5.1. Analytical versus numerical models

Numerically predicted porous matrix efficiencies for the annular porous block are first compared to the analytically derived efficiency provided in Eq. (8) for validation purposes over the ranges $0.001 \leq mL_c \leq 2.5$ and $1.2 \leq r_2/r_1 \leq 10$.

Analytically determined (lines) and numerically predicted values (circles) of the porous matrix efficiencies for the annular block are shown in Fig. 14(a). The efficiency decreases as either mL_c or r_2/r_1 increases, in a manner similar to the efficiency behavior of solid, annular fins [1]. Over the entire ranges of mL_c and r_2/r_1 used to generate Fig. 14(a), the mean difference between the analytically determined and numerically predicted efficiencies is less than 0.05%.

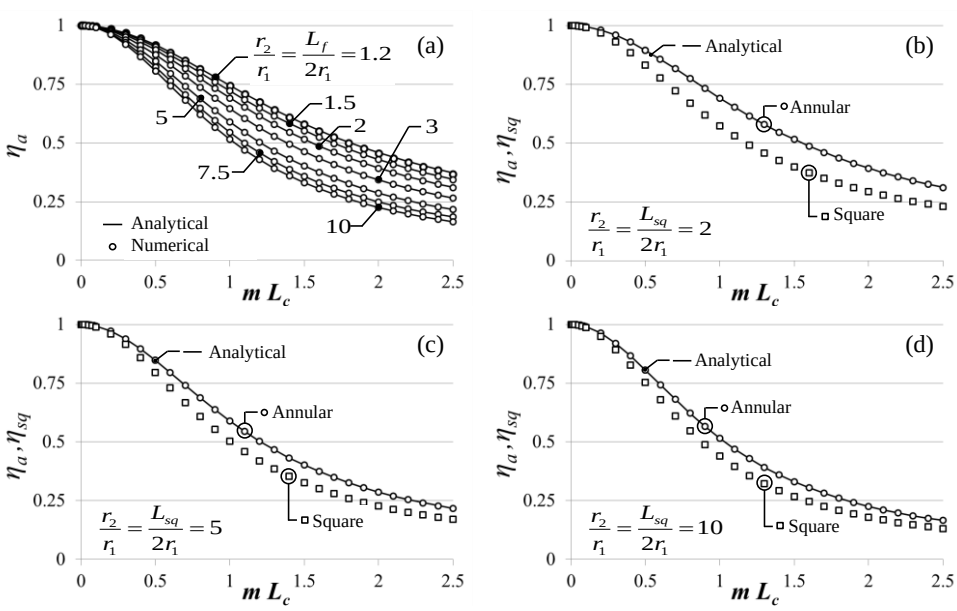

Fig. 14. Analytically- and numerically predicted porous matrix efficiencies versus mL_c. **(a)** annular analytical and numerical predictions for $r_2/r_1 = L_{sq}/(2r_1) =$ 1.2, 1.5, 2, 3, 5, 7.5, and 10, **(b)** predicted efficiencies for $r_2/r_1 = L_{sq}/(2r_1) = 2$, **(c)** predicted efficiencies for $r_2/r_1 = 5$, **(d)** predicted efficiencies for $r_2/r_1 = L_{sq}/(2r_1) = 10$. **[P3]**

Representative numerically predicted porous matrix efficiencies for annular and square blocks are shown in Figs. 14(b) through 14(d). The predictions were generated using the same mL_c and r_2/r_1 ranges as in Fig. 14(a), but with r_2 replaced by $L_{sq}/2$ when square blocks are considered. As evident, the annular block efficiencies are consistently higher than those of the square blocks at any given mL_c value. This is expected due to the relatively low local heat fluxes in the corner regions of the square block, reducing their efficiency relative to that of the annular blocks.

3.5.2. Extension to square arrays

One of the primary contributions of Paper **P3** is the development of an explicit mathematical expression for the efficiency of square foam blocks attached on center to circular tubes or HPs. The development involves extension of the analytical model. Annular and square results were compared for various r_2/r_1 (or $L_{sq}/(2r_1)$) over the range $0.001 \leq mL_c \leq 2.5$.

As noted in Fig. 15(a), $\eta_{sq}/\eta_a \rightarrow 1$ with both efficiencies approaching unity as $mL_c \rightarrow 0$. Conversely, as mL_c increases, the ratio of volume-weighted efficiencies (ηV) will approach unity (as shown in Fig. 15(b)), because the heat rates of the arrays converge as the additional material in the corners of the square array approaches the fluid temperature. This collapse of volume-weighted efficiencies to similar values for $mL_c \gtrsim 2.5$ is consistent with infinite fin behavior exhibited for $mL_c \gtrsim 2.5$ for traditional fins [1].

Since $\eta_{sq}/\eta_a \rightarrow 1$ at small mL_c, and $(\eta_{sq}V_{sq})/(\eta_a V_a) \rightarrow 1$ at large mL_c, analytical expressions for the annular porous block may be applied to the square block to determine the square block efficiency at small and large mL_c using η_{sq}/η_a and $(\eta_{sq}V_{sq})/(\eta_a V_a)$, respectively. In Paper **P3**, this limiting-case behavior was leveraged to create an expression which is valid over the *entire* range of mL_c by making use of a function that employs $K_0(mL_c)$ to appropriately weight the desirable behavior of the efficiency and the volume-weighted efficiency ratios, as shown in Fig. 15(c). The recommended analytical expressions, derived in detail in Paper **P3**, to determine the porous matrix efficiencies of both annular and square blocks are listed in Table 4. Also shown are the recommended ranges of application as well as the average and maximum discrepancies between the analytical values and numerical predictions. Analytically predicted efficiencies for the square array are compared to corresponding numerical predictions in Fig. 15(d), yielding errors of less than 1% for the investigated cases.

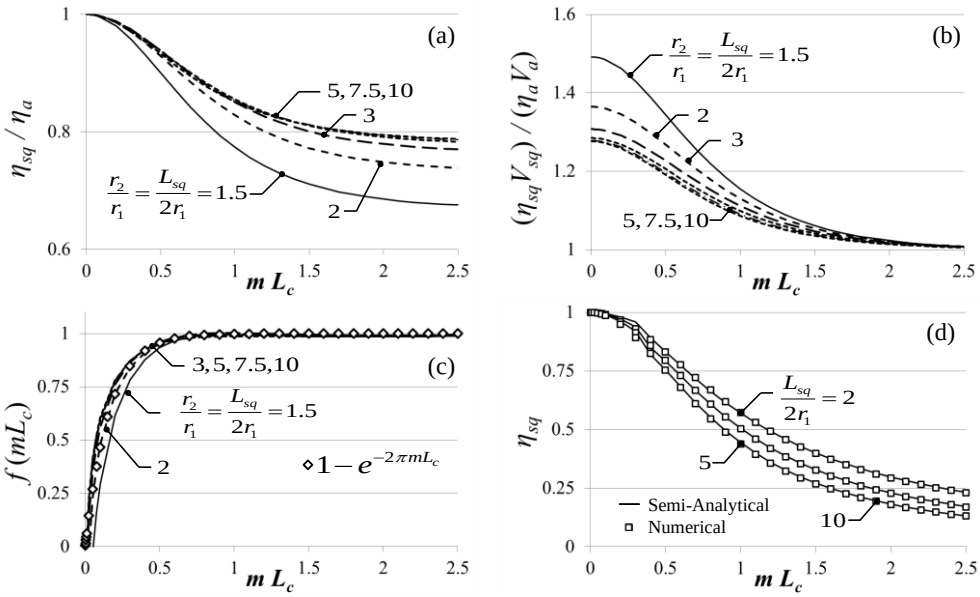

Fig. 15. Relationship of analytically- and numerically predicted porous matrix efficiencies versus mLc. **(a)** ratio of square to annular efficiencies, **(b)** ratio of square to annular volume-weighted efficiencies, **(c)** scaled Bessel function from Eq. (20) for various $r_2/r_1 = L_{sq}/(2r_1)$, **(d)** square semi-analytical and numerical predictions for $L_{sq}/(2r_1)$ = 1.2, 1.5, 2, 3, 5, 7.5, and 10. [**P3**]

	Recommended Expressions	Recommended Range	Avg. Error (Max. Error)	Eq.
Annular	$\eta_a = \frac{2r_1}{m\left(r_2^2-r_1^2\right)}\left[\frac{K_1(mr_1)I_1(mr_2)-I_1(mr_1)K_1(mr_2)}{K_0(mr_1)I_1(mr_2)+I_0(mr_1)K_1(mr_2)}\right]$	$0 \le mL_c \le \infty$ where $L_c = r_2 - r_1$	0.05% (0.59%) for $0 \le mL_c \le 2.5$	(5) of **[P3]**
Square	$\eta_{sq} \approx \frac{2r_1}{m\left[\left(L_{sq}/2\right)^2-r_1^2\right]}\left[\frac{K_1(mr_1)I_1(mL_{sq}/2)-I_1(mr_1)K_1(mL_{sq}/2)}{K_0(mr_1)I_1(mL_{sq}/2)+I_0(mr_1)K_1(mL_{sq}/2)}\right]$	$0 \le mL_c \le 0.4$ where $L_c = \frac{L_{sq}}{2} - r_1$	0.48% (4.7%) for $0 \le mL_c \le 0.4$	(5) of **[P3]**
	$\eta_{sq} = \frac{1-e^{-2\pi mL_{sq}}}{\frac{K_0(mL_{sq})}{\eta_a}+\left[1-K_0(mL_{sq})\right]\frac{V_{sq}}{(\eta_a V_a)}}$	$0.4 < mL_c \le \infty$ where $L_c = \frac{L_{sq}}{2} - r_1$	0.74% (4.7%) for $0.4 \le mL_c \le 2.5$	(20) of **[P3]**

Table 4. Recommended expressions for the porous matrix efficiencies of annular and square porous blocks; $1.5 \le r_2/r_1 = L_{sq}/(2r_1) \le 10$. **[P3]**

3.5.3. Comparison of predicted and measured heat rates

The expression for the square foam efficiency was also employed to predict corresponding experimentally measured heat rates. Predicted and measured heat transfer rates are reported in Fig. 16. The agreement between the predicted and measured heat rates is, on average, within 3%, and is considered to be excellent.

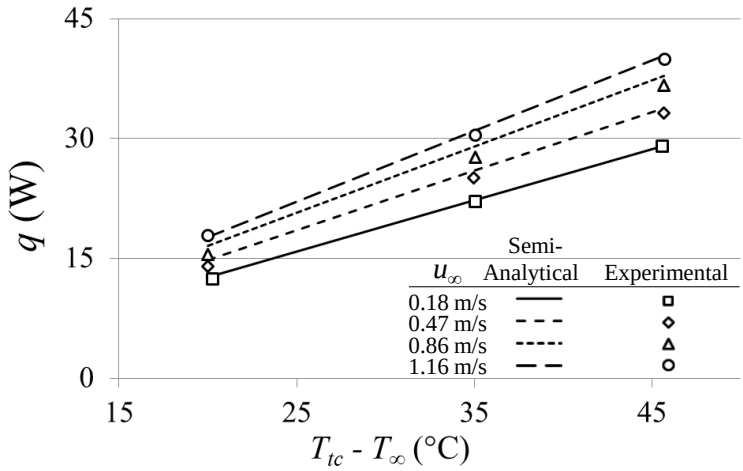

Fig. 16. Experimentally measured and semi-analytical predicted heat rates for a square porous matrix under various ambient velocity and thermal conditions. **[P3]**

Hence, the performance of (*i*) the novel annular continuum model for the foam efficiency and (*ii*) the subsequent extension to the square array are confirmed.

Importantly, because the forms of the governing one-dimensional heat equation (Eq. (6)) and boundary conditions for the annular foams considered here are identical to those of a thin, solid annular fin with an adiabatic tip available in undergraduate textbooks [1], the extension methodology developed in this study may also be applied to well-known expressions for the thermal efficiency of an annular thin fin [1] to thin fins of square shapes attached on-center to cylindrical tubes.

The combined fin-foam array (Paper P4) 4

4.1. Introduction and background

The low thermal resistances per unit volume associated with the open-cell, high-porosity metal foams discussed in Chapter 3 (due to the large surface area per unit volume) is beneficial for designing thermal systems. Several thermal management devices comprised of both metal foam and solid metal fins have been proposed [71-82].

A combination of the fin (Chapter 2) and the metal foam (Chapter 3) arrays is investigated in Paper **P4**, where it is sought to take advantage of the (*i*) low convective resistance of the foam and (*ii*) low radial conduction resistance of the fin. In doing so, a novel, approximate analytical model is developed and tested against corresponding experimental measurements.

4.2. Analytical model of combined fin-foam array

An approximate analytical model of the composite annular fin-foam array shown in Fig. 17(a) is developed to predict thermal efficiencies, resistances and heat rates when experiencing convective cooling (or heating) in a similar manner to the foam-only array of Paper **P3**. The model approximates the three-dimensional conduction and convection heat transfer in a manner that builds upon a standard annular fin analysis [1].

The analysis is performed for a representative axial segment of a composite fin-foam array, of characteristic unit pitch S, as shown in Fig. 17(a). A number of assumptions, consistent with those of Paper **P3** are employed, and are the same as those listed in Section 3.2 unless otherwise noted.

Assuming one-dimensional conditions in the radial direction, application of conservation of thermal energy to a differential radial element, shown within the fin (of thickness t) of Fig. 17(b) yields (see Paper **P4** for further detail)

$$\frac{d^2\theta_{fn}}{dr^2}+\frac{1}{r}\frac{d\theta_{fn}}{dr}-m_{fn}^2\theta_{fn}=0 \qquad \text{where} \qquad m_{fn}^2=\frac{2U}{k_{fn,\text{eff}}t} \tag{15}$$

where the excess fin temperature is $\theta_{fn}\equiv T_{fn}(r)-T_\infty$. An effective fin thermal conductivity, $k_{fn,\text{eff}} > k_{fn}$ (where k_{fn} is the molecular thermal conductivity of the fin material), and overall heat transfer coefficient, U, are used in Eq. (15). As detailed in Section 2.2 of Paper **P4**, $k_{fn,\text{eff}}$ is applied to the fin of thickness t, but accounts for radial conduction in both the solid fin and solid foam matrix. In a similar manner, the overall coefficient, U, accounts for (*i*) convection from the portions of the fin surface that are exposed directly to the fluid and (*ii*) conduction from the surface of the fin to the solid foam through a potential thermal contact resistance. Heat transfer to the solid foam by conduction from the fin is ultimately transferred to the fluid by convection.

Applying radial boundary conditions of (*i*) constant base temperature, $\theta(r_1)=\theta_b$, and (*ii*) adiabatic behavior at the outer radius of the array, $(d\theta/dr)\big|_{r_2}=0$, to Eq. (15) leads to expressions for the fin efficiency

$$\eta_{fn}=\frac{2r_1}{m_{fn}\left(r_2^2-r_1^2\right)}\left[\frac{K_1(m_{fn}r_1)I_1(m_{fn}r_2)-I_1(m_{fn}r_1)K_1(m_{fn}r_2)}{K_0(m_{fn}r_1)I_1(m_{fn}r_2)+I_0(m_{fn}r_1)K_1(m_{fn}r_2)}\right] \tag{16}$$

and the thermal resistance of the fin

$$R_{fn}=\frac{\theta_b}{q_{fn}(r_1)}=\frac{1}{A_{fn}\eta_{fn}U}=\frac{1}{2\pi\left(r_2^2-r_1^2\right)\eta_{fn}U} \tag{17}$$

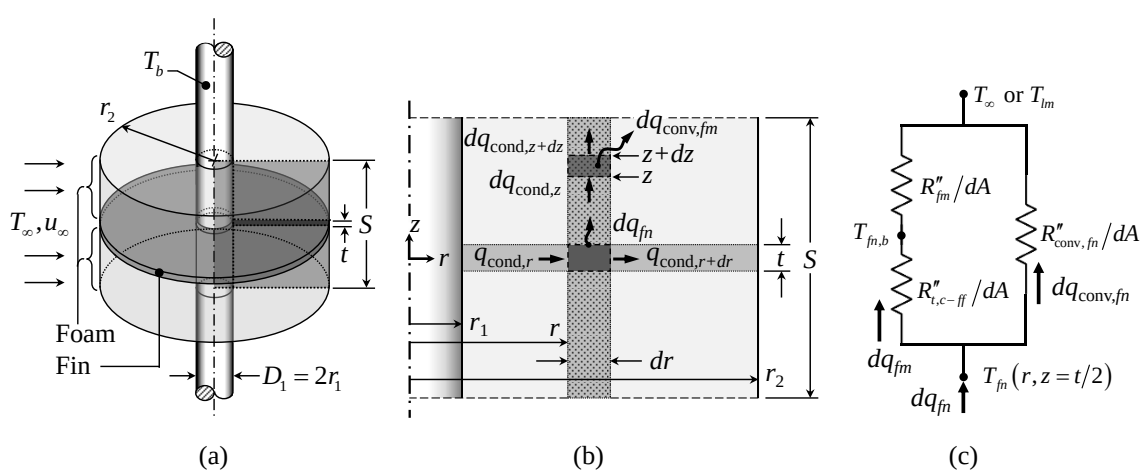

Fig. 17. Description of the annular analytical domain. **(a)** overall domain, **(b)** annular control volume energy balance, **(c)** thermal resistance network for overall heat transfer coefficient.

Heat transfer by convection also occurs at the exposed surface of the cylinder ($r = r_1$) that is not in contact with the solid foam matrix and is represented as

$$R_{\text{conv,cyl}} = \frac{1}{\varepsilon A_{\text{cyl}} \bar{h}_{\text{cyl}}} = \frac{1}{\varepsilon 2\pi r_1 \left(S - t\right) \bar{h}_{\text{cyl}}} \tag{18}$$

where the convection heat transfer coefficient is determined as discussed in Section 2.4 of Paper **P4**. The overall resistance to heat transfer in the radial direction at $r = r_1$ for a representative unit pitch of the array is therefore given by

$$R_{ff,S} = \left(R_{fn}^{-1} + R_{\text{conv,cyl}}^{-1}\right)^{-1} \tag{19}$$

or, for an array with N number of repeating pitches

$$R_{ff} = \left[N\left(R_{fn}^{-1} + R_{\text{conv,cyl}}^{-1}\right)\right]^{-1} \tag{20}$$

In order to employ this model as a predictive tool, several sub-calculations must be performed. Correlations for the determination of the surface area per volume (α_v), the contact resistances between the foam and either fin ($R''_{t,c-ff}$) or base of the fin ($R''_{t,c-b}$), as well as the convection heat transfer coefficients associated with the exposed foam ($\bar{h}_{fm}$), fin ($\bar{h}_{fn}$), and cylinder ($\bar{h}_{\text{cyl}}$) surfaces are provided in Section 2.4 of Paper **P4**. The effective thermal conductivity of the fin, $k_{fn,\text{eff}}$, is determined by equating its corresponding radial thermal resistance to the radial thermal resistance posed by conduction in the fin and foam as detailed in Section 2.2 of Paper **P4**.

The overall fin heat transfer coefficient, U, is defined in Section 2.3 of Paper **P4** to account for heat transfer at the upper and lower fin surfaces, which occurs by (*i*) conduction to the solid phase of the foam (after passing through a potential contact resistance) and (*ii*) direct convection to the fluid, as diagramed in Fig. 17(c). Heat transfer into the foam by conduction is then passed to the fluid by convection from the exposed surface area of the metal foam. The axial conduction and convection within the foam is approximated as if it were a Cartesian extended surface (of thickness dr and length $(S\text{-}t)/2$) attached to the fin as shown in the dark shaded region of Fig. 17(b). This treatment is similar to that of Paper **P3**, and has been taken elsewhere [61-63]. Detailed, explicit instructions for implementing of Eqs. (19) or (20) are provided in Section 2.5 of Paper **P4**.

4.3. Results and discussion

4.3.1. Comparison of predicted and measured heat transfer rates

Experiments were performed to validate the novel approximate analytical model of the combined fin-foam array. The experimental apparatus is identical to the one used in Paper **P3**, except for the addition of $N = 2$ aluminum fins (same as those used in the experiments of Paper **P2**). The electrically heated heat pipe (HP) of cylindrical cross section is used to deliver thermal energy to the bases of two equal fin-foam unit-pitches, as shown in Fig. 2(a) of Paper **P4**. The heat is dissipated to the air drawn through the channel and fin-foam array. Further details of the experimental setup are provided in Papers **P2** and **P3**.

Predictions using Eq. (20) and the methodology of Section 2.5 of Paper **P4** are modified to account for one (*i*) the expected temperature rise of the channel air through a LMTD analysis and (*ii*) the square outer dimension of the array by the extension detailed in Section 3.5.2. A detailed description of these modifications and the resulting expression for predicted heat rate may be found in Section 3.2 of Paper **P4**. Predictions using the detailed, step-by-step procedure of Section 3.2 of Paper **P4** were compared with experimentally measured heat rates for three average velocities and four excess temperatures, as displayed in Fig. 18. The relatively good agreement between the measurements and predictions confirms the efficacy of the proposed analytical model for the conditions considered here.

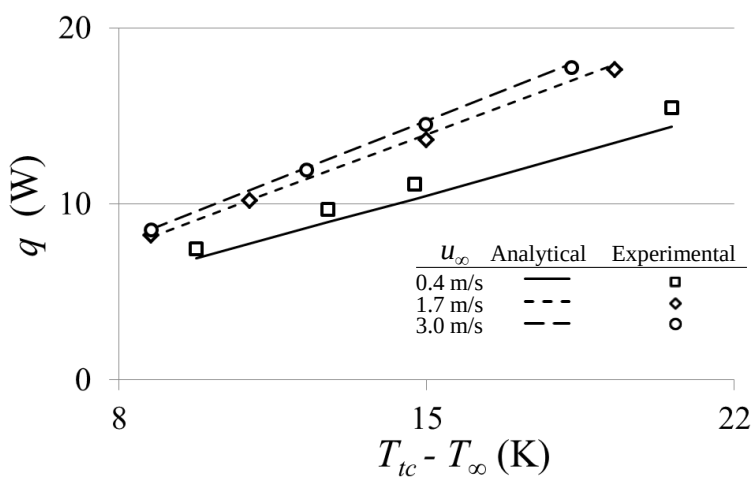

Fig. 18. Experimentally measured and predicted heat rates for a square fin-foam array under various ambient velocity and thermal conditions. Error bars on the experimental data points are of approximately the same size as the symbols and are not shown.

4.3.2. Parametric simulations

Once validated through comparison with experimental measurements, the model was exercised to determine the dependence of predicted heat rates to key parameters. Discussions of the sensitivity of the combined array to the thermal contact resistances ($R''_{t,c-ff}$ and $R''_{t,c-b}$), array radius (r_2/r_1), and the fin thickness (t) may be found in Sections 4.2.1, 4.2.2, and 4.2.3 of Paper **P4**, respectively. These investigations yield results which are consistent with physical expectations, further demonstrating the capability of the newly developed model.

Conclusions and recommendations 5

5.1. Comparison of fin, foam, and composite fin-foam arrays

With the successful identification and development of expressions for the determination of thermal resistances of the three types of extended surfaces established, the primary objective of this dissertation has been met. While the scope of this research is focused on obtaining correlations describing the heat transfer performance of the (*i*) fin (Chapter 2, Paper **P1**), (*ii*) foam (Chapter 3, Paper **P3**), and (*iii*) combined fin-foam (Chapter 4, Paper **P4**) arrays, it is desirable to generate preliminary comparisons of the relative thermal performance for systems involving the various extended surfaces. In this discussion, the dimensions, materials, and temperatures of Section 4.2 of Paper **P4** are employed, but with the fin replaced by foam for the foam-only case, and with the foam removed for the fin array case. Heat transfer from the bare cylinder, corresponding to convection from a cylinder in cross flow where the convection heat transfer coefficient is determined using the correlation of Sparrow et al. [45], is also considered. Analytical predictions for the finned HP are made in a manner consistent with those presented in Section 2.3 (Paper **P1**). Predicted heat rates for the foam-only case are made using the methodology described in Section 3.2 (Paper **P3**).

Predicted heat transfer rates corresponding to a base temperature of 60ºC and ambient temperature of 25ºC are reported in Fig. 19(a) (and in more detail in Fig. 19(b)) for the velocity range $0.1 \leq u_\infty \leq 10$ m/s. Heat rates are highest for the combined fin-foam foam array, followed by those of the foam-only and then the fin arrays, respectively. The smallest heat rates correspond to the bare cylinder, as expected. A comparison of the relative performance of the two foam-based configurations when normalized to those of the fin array case is made in Fig. 20(a). For the velocity range $0.1 \leq u_\infty \leq 10$ m/s, the predicted heat rates for the combined fin-foam array (foam array) are, on average, 4.8 (3.8) times larger than those associated with the fin

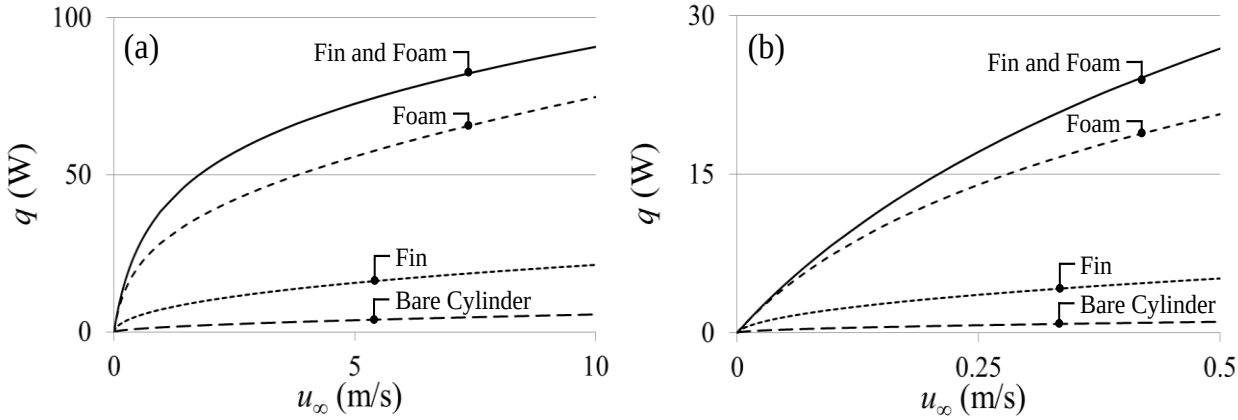

Fig. 19. Predicted heat rates for equal lengths of a (*i*) bare cylinder, (*ii*) finned cylinder, (*iii*) foam array, and (*iv*) composite fin-foam array versus u_∞. **(a)** for $0 \le u_\infty \le 10$ m/s, **(b)** for $0 \le u_\infty \le 0.5$ m/s.

array. Alternatively, the thermal resistances associated with the various configurations may be normalized relative to those of the fin array and are reported in Fig. 20(b) where each resistance is defined as $(T_b - T_{lm})/q$.

It is clear from the preliminary comparison of the arrays that improved thermal performance may be attained using either the foam or the combined fin-foam arrays as compared to traditional fins. However, the improvement in thermal performance is likely associated with appreciable increases in the fan power needed to drive the cooling air flow through the foam. The ultimate choice of which extended surface configuration to employ in a HP system will require a more nuanced investigation than presented here.

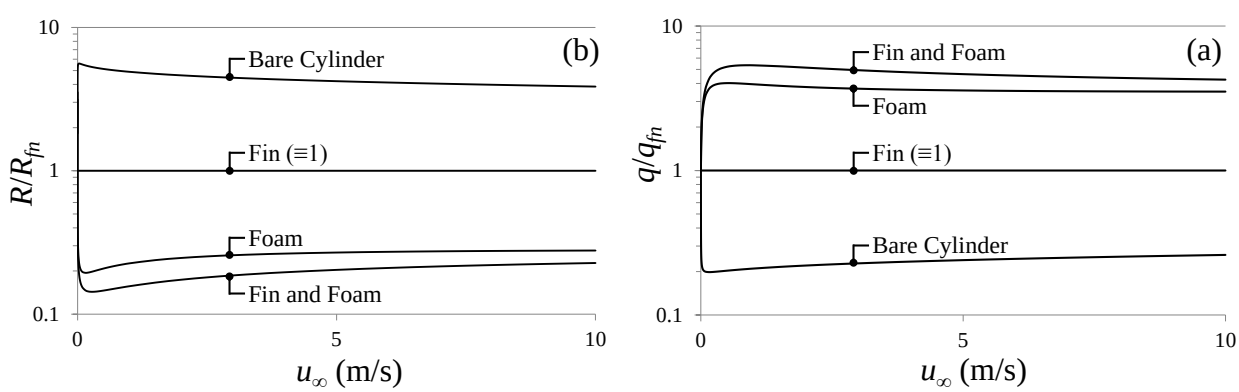

Fig. 20. Predicted heat transfer rates and thermal resistances normalized to the fin array case. **(a)** heat rate ratios for $0 \le u_\infty \le 10$ m/s, **(b)** thermal resistance ratios for $0 \le u_\infty \le 10$ m/s.

5.2. Conclusions and recommendations

Over the five published articles that constitute this dissertation, several key contributions to the field are identified. The major outcomes of this research effort include:

- Through the use of the benchmark DNS study of Paper **P1**, the SST turbulence model and the Sparrow and Samie [45] analytical model are shown to be the perferred turbulence and analytical models, respectively, for the prediction of convection heat transfer associated with a finned cylinder. Adding this information to the literature will allow future practitioners and researchers to choose the appropriate models with confidence.
- The coupled numerical model of Paper **P2** details a novel numerical solution for the prediction of heat transfer from a finned HP which incorporates (for the first time) descriptions of the detailed internal and external heat transfer processes. Again, this may be leveraged by practitioners and researchers who seek to accurately model such systems. Experimental validation of the numerical model confirms its performance.
- A constriction resistance that affects local condensation rates within a HP at the wick (adjacent from fin roots) is, for the first time, identified in Paper **P2**, and investigated further in Paper **P5**. Designing HP-based thermal systems requires knowledge of physical HP operational limits, making the identification of a previously unreported limiting behavior valuable.
- Novel expressions for the thermal resistances associated with foam (Paper **P3**) and combined fin-foam (Paper **P4**) arrays have been developed. These expressions will allow for a broader study on the relative performance of the various extended surfaces and enable practitioners to design novel thermal management devices.
- A correlation for the thermal efficiency of a foam array of square outer bounds is developed in Paper **P3.** Importantly, this expression, which allows results generated for annular fins attached to a cylindrical HP or tube to be extended to fins of square planform, may also be employed for uniform-thickness fins or composite fin-foam arrays.

During the course of meeting the objectives of this dissertation, several topics for future investigation have been identified.

While Paper **P1** determined the preferred correlation for the prediction of heat transfer from a finned cylinder, even the best performing expression still yielded an error of more than 10% in comparison to the benchmarks. Further numerical or experimental work to develop an improved correlation for convective heat transfer from a finned cylinder would be valuable. This dissertation does not investigate vortex generating fin surfaces, which may allow for improved thermal performance in fin arrays. Also, characterization of multi-row thermal systems may yield differing performance results, and may be considered in possible HP system designs. The coupled model of Paper **P2** produces excellent agreement with experimental results, but may possibly be limited by approximating the internal heat transfer as 2D. Axisymmetric phenomena, such as tilting to off-vertical configurations [83], has been shown to impact thermal performance, and accordingly, it may be beneficial to develop a finned HP numerical model consisting of 3D internal and external modeling to account for such complexities.

The developed expressions describing heat transfer for foam and the fin-foam arrays were compared to a selection of numerical and experimental results for validation; however, an investigation into the performance of these models over a much larger array of parameters would be of great value. Clearly identifying the range of application for various parameters would allow practitioners and researchers to employ the correlations with a greater degree of confidence.

Finally, there is much more research that could be carried out toward the relative performance of the fins, foam, and combined fin-foam arrays. The ultimate objective for this dissertation is the development of the expressions which allow for the comparison of thermal performance, but there are a multitude of considerations which may impact the relative array performance for each individual case. Future research comparing the performance of various geometries, flow conditions, and excess temperatures for the various extended surfaces may be necessary, as it is unknown if the relative array performance will be consistent throughout such changes. Further, use of these arrays in real world applications requires considerations beyond just thermal performance. The larger pressure drops (and resulting fan powers) and capital costs associated with metal foams must be considered. Ideally, hydrodynamic and economic models could be employed in unison with the thermal models developed herein to produce a more complete analysis of the benefits and tradeoffs of each type of array.

References 6

[1] T.L. Bergman, A.S. Lavine, Fundamentals of Heat and Mass Transfer, Eighth ed., Wiley, Hoboken, 2017.

[2] A.D. Kraus, A. Bar-Cohen, Design and Analysis of Heat Sinks, 1st ed., Wiley, New York, 1995.

[3] R.K. Shah, D.P. Sekulic, Fundamentals of Heat Exchanger Design, 1st ed., Wiley, New York, 2003.

[4] S.P. Benn, L.M. Poplaski, A. Faghri, T.L. Bergman, Analysis of thermosyphon/heat pipe integration for feasibility of dry cooling for thermoelectric power generation, Applied Thermal Engineering 104 (2016) 358-374.

[5] H. Shabgard, M.J. Allen, N. Sharifi, S.P. Benn, A. Faghri, T.L. Bergman, Heat pipe heat exchangers and heat sinks: opportunities, challenges, applications, analysis, and state of the art, International Journal of Heat and Mass Transfer 89 (2015) 138-158.

[6] W. Srimuang, P. Amatachaya, A review of the applications of heat pipe heat exchangers for heat recovery, Renewable Sustainable Energy Reviews 16 (2012) 4303–4315.

[7] K.S. Ong, Review of heat pipe heat exchangers for enhanced dehumidification and cooling in air conditioning systems, International Journal of Low-Carbon Technologies 0 (2014) 1-8.

[8] A. Mardiana-Idayu, S.B. Riffat, Review on heat recovery technologies for building applications, Renewable and Sustainable Energy Reviews 16 (2) (2012) 1241-255.

[9] M.S. Naghavi, K.S. Ong, M. Mehrali, I.S. Badruddin, H.S.C. Metselaar, A state-of-the-art review on hybrid heat pipe latent heat storage systems, Energy Conversion and Management 105 (2015) 1178-1204.

[10] A. Faghri, Heat pipes: review, opportunities and challenges, Frontiers in Heat Pipes 5 (1) (2014).

[11] A. Faghri, Heat Pipe Science and Technology, Second ed., Global Digital Press, 2016.

[12] Cooler Master Hyper 212 Evo, Cooler Master (2017).

[13] J.R. Stark, N. Sharifi, T.L. Bergman, A. Faghri, An experimentally verified numerical model of finned heat pipes in crossflow, International Journal of Heat and Mass Transfer 97 (2016) 45-55.

[14] A.A. El-Nasr and S.M. El-Haggar, Effective Thermal Conductivity of Heat Pipes, Heat and Mass Transfer 32 (1-2) (1996) 97-101.

[15] N. Sharifi, T.L. Bergman, M.J. Allen, A. Faghri, Melting and solidification enhancement using a combined heat pipe, foil approach, International Journal of Heat and Mass Transfer 78 (2014) 930-941.
[16] M. Mahdavi, S. Qiu, S. Tiari, Numerical investigation of hydrodynamics and thermal performance of a specially configured heat pipe for high-temperature thermal energy storage systems, Applied Thermal Engineering 81 (2015) 325-337.
[17] Y. Cao, A. Faghri, Transient two-dimensional compressible analysis for high-temperature heat pipes with pulsed heat input, Numerical Heat Transfer Applications 18 (4) (1990) 483–502.
[18] N. Zhu, K. Vafai, Vapor and liquid flow in an asymmetrical flat plate heat pipe: a three-dimensional analytical and numerical investigation, International Journal of Heat and Mass Transfer 41 (1) (1998) 159-174.
[19] N. Sharifi, S. Wang, T.L. Bergman, A. Faghri, Heat pipe-assisted melting of a phase change material, International Journal of Heat and Mass Transfer 55 (13-14) (2012) 3458-3469.
[20] N. Sharifi, A. Faghri, T.L. Bergman, C.E. Andraka, Simulation of Heat Pipe-assisted Latent Heat Thermal Energy Storage with Simultaneous Charging and Discharging, International Journal of Heat and Mass Transfer 80 (2015): 170-179.
[21] H. Shabgard, A. Faghri, T.L. Bergman, C.E. Andraka, Numerical simulation of heat pipe-assisted latent heat thermal energy storage unit for dish-stirling systems, Journal of Solar Engineering 136 (2) (2014) 021025-1-021025-12.
[22] M. Mahdavi, S. Qui, Mathematical modeling and analysis of steady state performance of a heat pipe network, Applied Thermal Engineering 91 (2015) 556-573.
[23] B. Xiao, A. Faghri, A three-dimensional thermal–fluid analysis of flat heat pipes, International Journal of Heat and Mass Transfer 51 (11-12) (2008) 3113-3126.
[24] N. Zhu, K. Vafai, Numerical and analytical investigation of vapor flow in a disk-shaped heat pipe incorporating secondary flow, International Journal of Heat and Mass Transfer 40 (12) (1997) 2887-2900.
[25] K.A.R. Ismail, C.L.F. Avles, M.S. Modesto, Numerical and experimental study on the solidification of PCM around a vertical axially finned isothermal cylinder, Applied Thermal Engineering 21 (1) (2001) 53-77.
[26] S. Tiari, S. Qiu, Three-dimensional simulation of high temperature latent heat thermal energy storage system assisted by finned heat pipes, Energy Conversion and Management 105 (2015) 260–271.
[27] S. Tiari, S. Qiu, M. Mahdavi, Numerical study of finned heat pipe-assisted thermal energy storage system with high temperature phase change material, Energy Conversion and Management 89 (2015) 833–842.
[28] N. Sharifi, S. Wang, T.L. Bergman, A. Faghri, Heat pipe-assisted melting of a phase change material, International Journal of Heat and Mass Transfer 55 (13-14) (2012) 3458-3469.

[29] N. Sharifi, A. Faghri, T.L. Bergman, C.E. Andraka, Simulation of Heat Pipe-assisted Latent Heat Thermal Energy Storage with Simultaneous Charging and Discharging, International Journal of Heat and Mass Transfer 80 (2015) 170-179.
[30] H. Shabgard, A. Faghri, T.L. Bergman, C.E. Andraka, Numerical simulation of heat pipe-assisted latent heat thermal energy storage unit for dish-stirling systems, Journal of Solar Engineering 136 (2) (2014) 021025-1-021025-12.
[31] F.R. Menter, Two-equation eddy-viscosity turbulence models for engineering applications, AIAA Journal 32 (8) (1994) 1598-1605.
[32] F.R. Menter, R.B. Langtry, S.R. Likki, Y.B. Suzen, P.G. Huang, S. Völker, A correlation-based transition model using local variables part 1 – model formulation, Proceedings of the ASME Turbo Expo, Power for Land Sea and Air (June 14-17, 2004).
[33] F.R. Menter, R.B. Langtry, S. Volker, Transition modelling for general purpose CFD codes, Flow, Turbulence, and Combustion 77 (2006) 277-303.
[34] F. Menter, T. Esch, S. Kubacki, Transition modelling based on local variables, Fifth International Symposium on Engineering Turbulence Modeling and Measurements, Mallorca, Spain (2002).
[35] W.P. Jones, B.E. Launder, The prediction of laminarization with a two-equation model of turbulence, International Journal of Heat and Mass Transfer 15 (1972) 301-314.
[36] V. Yakhot, S.A. Orszag, S. Thangam, T.B. Gatski, C.G. Speziale, Development of turbulence models for shear flows by a double expansion technique, Physics of Fluids A 4 (70) (1992) 1510-1520.
[37] S. Wallin, A.V. Johansson, An explicit algebraic Reynolds stress model for incompressible and compressible turbulent flows, Journal of Fluid Mechanics 403 (2000) 89–132.
[38] H. Nemati, M. Moghimi, Numerical study of flow over annular-finned tube heat exchangers by different turbulent models, CFD Letters 6 (3) (2014) 101-112.
[39] Y. Mao. Y. Zhang, Evaluation of turbulent models for natural convection of compressible air in a tall cavity, Numerical Heat Transfer, Part B: Fundamentals 64 (5) (2013) 351-364.
[40] L.A. El-Gabry, D.A. Kaminski, Numerical investigation of jet impingement with cross flow - comparison of Yang-Shih and standard k–ϵ turbulence models, Numerical Heat Transfer, Part A: Applications 47 (5) (2005) 441-469.
[41] A. Keshmiri , J. Uribe, N. Shokri, Benchmarking of three different CFD codes in simulating natural, forced, and mixed convection flows, Numerical Heat Transfer, Part A: Applications 67 (12) (2015) 1324-1351.
[42] E.M. Sparrow, J.P. Abraham, A new buoyancy model replacing the standard pseudo-density difference for internal natural convection in gases, International Journal of Heat and Mass Transfer 46 (19) (2003) 3583-3591.
[43] ANSYS CFX-Solver Theory Guide, Release 17.1, ANSYS, Inc., 2016.
[44] R. Romero-Mendez, M. Sen, K.T. Yang, R. McClain, Effect of fin spacing on convection in plate fin and tube heat exchanger, International Journal of Heat and Mass Transfer 43 (1) (2000) 39-51.

[45] E.M. Sparrow, F. Samie, Heat transfer and pressure drop results for one- and two-row arrays of finned tubes, International Journal of Heat and Mass Transfer 28 (12) (1985) 2247-2259.
[46] E.M. Sparrow, J.P. Abraham, J.C.K. Tong, Archival correlations for average heat transfer coefficients for non-circular and circular cylinders and for spheres in crossflow, International Journal of Heat and Mass Transfer 47 (24) (2004) 5285-5296.
[47] C.Y. Zhao, Review on thermal transport in high porosity cellular metal foams with open cells, International Journal of Heat and Mass Transfer 55 (2012) 3618–3632.
[48] I. Ghosh, How good is open-cell metal foam as a heat transfer surface, ASME Journal of Heat Transfer 131 (2009) 101004-1-8.
[49] L. Tadrist, M. Miscevic, O. Rahli, F. Topin, About the use of fibrous materials in compact heat exchangers, Experimental Thermal and Fluid Science 28 (2004) 193-199.
[50] D.L. Koch, R.G. Cox, H. Brenner, J.F. Brady, The effect of order on dispersion in porous media, Journal of Fluid Mechanics 200 (1989) 173–188.
[51] T.J. Lu, H.A. Stone, M.F. Ashby, Heat transfer in open-cell metal foams, Acta Materialia 46 (10) (1998) 3619-3635.
[52] P. Du Plessis, A. Montillet, J. Comiti, J. Legrand, Pressure drop prediction for flow through high porosity metallic foams, Chemical Engineering Science 49 (21) (1994) 3545-3553.
[53] D. Weaire, R. Phelan, A counter-example to Kelvin's conjecture on minimal surfaces, Philosophical Magazine Letters 69 (1994) 107–110.
[54] K. Boomsma, D. Poulikakos, F. Zwick, Metal foams as compact high performance heat exchangers, Mechanics of Materials 35 (12) (2003) 1161-1176.
[55] A. Kopanidis, A. Theodorakakos, E. Gavaises, D. Bouris, 3D numerical simulation of flow and conjugate heat transfer through a pore scale model of high porosity open cell metal foam, International Journal of Heat and Mass Transfer 53 (11–12) (2010) 2539-2550.
[56] S. Krishnan, J.Y. Murthy, S.V. Garimella, Direct simulation of transport in open-cell metal foams, ASME Journal of Heat Transfer 128 (2006) 793-799.
[57] Lord Kelvin (Sir William Thomson), On the division of space with minimum partitional area, Philosophical Magazine 24 (151) (1887) 121-134.
[58] M. Iasiello, S. Cunsolo, M. Oliviero, W.M. Harris, N. Bianco, W.S.K. Chiu, V. Naso, Numerical analysis of heat transfer and pressure drop in metal foams for different morphological models, ASME Journal of Heat Transfer 136 (11) (2014) 112601:1-10.
[59] P. Ranut, E. Nobile, L. Mancini, Microtomography-based CFD analysis of transport in open-cell aluminum metal foams, Journal of Physics: Conference Series 501 (1) (2014) 1-11.
[60] D.Y. Lee, K. Vafai, Analytical characterization and conceptual assessment of solid and fluid temperature differentials in porous media, International Journal of Heat and Mass Transfer 42 (3) (1999) 423-435.
[61] V.V. Calmidi, R.L. Mahajan R.L., Forced convection in high porosity metal foams, ASME Journal of Heat Transfer 122 (3) (2000) 557-565.

[62] T. Dixit, I. Ghosh, An experimental study on open cell metal foam as extended heat transfer surface, Experimental Thermal and Fluid Science 77 (2016) 28-37.
[63] I. Ghosh, Heat transfer correlation for high-porosity open-cell foam, International Journal of Heat and Mass Transfer 52 (5–6) (2009) 1488-1494.
[64] S.H. Park, T.H. Kim, J.H. Jeong, Experimental investigation of the convective heat transfer coefficient for open-cell porous metal fins at low Reynolds numbers, International Journal of Heat and Mass Transfer 100 (2016) 608-614.
[65] P. De Jaeger, C. T'Joen, H. Huisseune, B. Ameel, S. De Schampheleire, M. De Paepe, Assessing the influence of four cutting methods on the thermal contact resistance of open-cell aluminum foam, International Journal of Heat and Mass Transfer 55 (21–22) (2012) 6142-6151.
[66] T.M. Jeng, S.C. Tzeng, Y.H. Hung, An analytical study of local thermal equilibrium in porous heat sinks using fin theory, International Journal of Heat and Mass Transfer (49) (11–12) (2006) 1907-1914.
[67] C.Y. Zhao, W. Lu, S.A. Tassou, Thermal analysis on metal-foam filled heat exchangers. Part II: Tube heat exchangers, International Journal of Heat and Mass Transfer 49 (15–16) (2006) 2762-2770.
[68] C. T'Joen, P. De Jaeger, H. Huisseune, S. Van Herzeele, N. Vorst, M. De Paepe, Thermo-hydraulic study of a single row heat exchanger consisting of metal foam covered round tubes, International Journal of Heat and Mass Transfer 53 (15–16) (2010) 3262-3274.
[69] K. Vafai, C.L. Tien, Boundary and inertia effects on flow and heat transfer in porous media, International Journal of Heat and Mass Transfer 24 (2) (1981) 195-203.
[70] V.V. Calamidi, Transport Phenomenon in High Porosity Fibrous Metal Foams, PhD thesis, University of Colorado, Boulder, CO, 1997.
[71] A.A. Bhattacharya, R.L. Mahajan, Finned metal foam heat sinks for electronics cooling in forced convection, ASME. Journal of Electronic Packaging 124 (3) (2002) 155-163.
[72] H. Pokharna, A.A. Bhattacharya, Enhanced Heat Exchanger, Intel Corporation, US Patent No. 6958912 B2, 2005.
[73] S.S. Feng, M. Shi, Y. Li, T.J. Lu, Pore-scale and volume-averaged numerical simulations of melting phase change heat transfer in finned metal foam, International Journal of Heat and Mass Transfer 90 (2015) 838-847.
[74] A. Andreozzi, N. Bianco, M. Iasiello, V. Naso, Numerical study of metal foam heat sinks under uniform impinging flow, Journal of Physics; Conference Series, 34th UIT Heat Transfer Conference 796 (1) (2016) 1-9.
[75] S.S. Feng, J.J. Kuang, T. Wen, T.J. Lu, K. Ichimiya, An experimental and numerical study of finned metal foam heat sinks under impinging air jet cooling, International Journal of Heat and Mass Transfer 77 (2014) 1063-1074.
[76] A.A. Bhattacharya, R.L. Mahajan, Metal foam and finned metal foam heat sinks for electronics cooling in buoyancy-induced convection, ASME Journal of Electronic Packaging 128 (3) (2005) 259-266.

[77] C.T. DeGroot, D. Gateman, A.G. Straatman, The effect of thermal contact resistance at porous-solid interfaces in finned metal foam heat sinks, ASME Journal of Electronic Packaging 132 (4) (2010) 041007-041007-7.
[78] H. Seyf, M. Layeghi, Numerical analysis of convective heat transfer from an elliptic pin fin heat sink with and without metal foam insert, ASME Journal of Heat Transfer 132 (7) (2010) 071401-071401-9.
[79] D. Hernon, A. Lyons, S. Krishnan, M. Hodes, Al. O'Loughlin, Monolithic Structurally Complex Heat Sink Designs, Alcatel-Lucent USA Inc., US Patent No. 0299148, 2013.
[80] H. Kim, Heat Transfer Fin for Heat Exchanger, US Patent Application No. 0296008, 2005.
[81] D. Berukhim, A. Leishman, V. Avanessian, Mixed Carbon Foam/Metallic Heat Exchanger, Boeing, US Patent No. 9279626, 2012.
[82] M. Odabee, K. Hooman, H. Gurgenci, Metal foam heat exchangers for heat transfer augmentation from a cylinder in cross-flow, Transport in Porous Media 86 (3) (2011) 911-923.
[83] M.J. Allen, N. Sharifi, A. Faghri, T.L. Bergman, Effect of inclination angle during melting and solidification of a phase change material using a combined heat pipe-metal foam or foil configuration, International Journal of Heat and Mass Transfer 80 (2015) 767-780.

Publications 7

Paper P1

Title:

Prediction of convection from a finned cylinder in cross flow using direct simulation, turbulence modeling, and correlation-based methods

Authors:

John R. Stark

Theodore L. Bergman

Journal:

Numerical Heat Transfer, Part A: Applications

NUMERICAL HEAT TRANSFER, PART A
http://dx.doi.org/10.1080/10407782.2016.1277929

Prediction of convection from a finned cylinder in cross flow using direct simulation, turbulence modeling, and correlation-based methods

John R. Stark and Theodore L. Bergman

Department of Mechanical Engineering, The University of Kansas, Lawrence, KS, USA

ABSTRACT
Direct numerical simulation (DNS), two shear-stress transport (SST) turbulence models, and three k-ε models are used to predict mixed convection associated with air in cross flow over an isothermal, finned cylinder. The DNS predictions reveal complex time-variation in the flow field. Convection heat transfer coefficients predicted by the SST models are in good agreement with those generated by DNS, whereas the k-ε models do not accurately predict heat fluxes. Correlation-based predictions of heat transfer coefficients are, in general, in poor agreement with the DNS and SST predictions. The impact of various geometrical modifications on convection coefficients is also presented.

ARTICLE HISTORY
Received 3 August 2016
Accepted 28 November 2016

1. Introduction

Various methodologies have been developed to predict laminar, turbulent, and transitional convective heat transfer processes and rates. At one extreme, direct numerical simulation (DNS) solves discretized forms of the governing equations that describe both spatially and temporally complex flows, providing detailed velocity and temperature distributions within the fluid. To capture relevant phenomena accurately, DNS simulations often require fine spatial resolution and small time steps. Hence, DNS typically requires significant computational resources to generate even a single set of predictions.

Many applications require simulations covering a range of operating conditions or entail large computational domains, and use of DNS may not be appropriate. Various turbulence models have been developed to predict the approximate average of the time-dependent variations within such flows [3–9]. Such models differ in their approximations, resulting in a multitude of predictions for a given physical situation [10–14], and the preferred model is sometimes case-dependent. At the other extreme, recourse to existing correlations may provide approximate, yet adequate prediction of the overall heat transfer rates or convection coefficients.

The analysis of finned heat pipes (HPs) is an example where accurate and efficient prediction of heat transfer coefficients is essential to ultimately create practical, system-level models. For example, HP-enabled dry cooling of thermal electric power plants [15–18] is of contemporary interest. Recently [19], numerical models describing the heat transfer, liquid-vapor phase change, and fluid flow inside an HP were coupled to models of the external convection about the HP to achieve accurate predictions of the overall thermal resistance of a finned HP. Because HPs have internal thermal resistances that can be orders of magnitude smaller than those associated with high thermal conductivity media of similar dimensions [22, 23], accurate prediction of the convective heat transfer external to the HP is crucial in order to quantify the overall thermal resistance of convectively heated and/or cooled HPs.

CONTACT John R. Stark John.Robert.Stark@gmail.com Department of Mechanical Engineering, The University of Kansas, 1530 W. 15th Street, Lawrence, KS 66045, USA.
Color versions of one or more of the figures in the article can be found online at www.tandfonline.com/unht.

Nomenclature

A	area (m^2)
$C_{1\varepsilon}$, $C_{2\varepsilon}$, $C_{3\varepsilon}$	κ-ε model constants
$C^*_{2\varepsilon}$, C_μ	κ-ε model constants
D	diameter of cylinder (m)
$E_{\gamma 1}$, $E_{\gamma 2}$	SST transitional production term (kg/ m s^3)
F_1, F_2	SST blending functions
g	gravitational acceleration (m/s^2)
Gr	Grashof number
h	convection coefficient (W/m^2 K)
H	height (m)
k	thermal conductivity (W/m K)
L	length (m)
n	surface normal
p	pressure (Pa)
P_κ, P_b	SST and κ-ε production terms (kg/ m s^3)
$P_{\gamma 1}$, $P_{\gamma 2}$, $P_{\theta t}$	SST transitional production term (kg/ m s^3)
q''	heat flux (W/m^2)
Re	Reynolds number
$\widetilde{Re}_{\theta t}$	transitional momentum thickness Reynolds number
r, z, θ	coordinate directions
s	separation distance (m)
S	fin pitch (m), turbulent strain rate (s^{-1})
t	time (s), thickness (m)
T	temperature (°C)
u	velocity (m/s)
V	average air velocity (m/s)
W	width (m)
x, y, z	coordinate directions
α	thermal diffusivity (m^2/s)
α_1, β_1, β_2	SST model constants
β	thermal expansion coefficient (K^{-1})
ε	specific rate of turbulence dissipation (s^{-1})
γ	turbulence intermittency
θ	reduced temperature T - T_∞ (°C), angular direction
κ	turbulent kinetic energy (m^2/s^2)
μ	dynamic viscosity (kg/m s)
ν	kinematic viscosity (m^2/s)
ρ	density (kg/m^3)
σ_κ, σ_ω, $\sigma_{\omega 2}$	SST model constants
σ_f, $\sigma_{\theta t}$	SST transitional model constants
σ_κ, σ_ε	κ-ε model constants
T	normalized time (s)
ω	specific rate of turbulence dissipation (s^{-1})
Subscripts	
0	reference
ch	channel
cyl	cylinder
f	fin
surf	surface
tot	total
turb	turbulent
x, y, z	coordinate directions
∞	inlet
Superscripts	
–	average

Similarly, single-phase convective heat transfer from finned tubes has been studied extensively using experimental [24–31] and numerical [32–34] approaches. Be it externally finned tubes or HPs, the external flow is often highly three-dimensional, and characterized by (*i*) the formation of horseshoe vortices in the vicinity of fin–tube interfaces [29–31] and (*ii*) vortex shedding from the HP or tube [31] that can interfere with boundary-layer development on the fin surfaces. The flow complexity makes the development of general correlations encompassing a wide range of conditions particularly challenging.

The primary objective of this study is to assess the performance of various steady-state turbulence models for the prediction of convective heat transfer from finned HPs or tubes in cross flow. To identify the preferred model(s), benchmark DNS predictions are first generated. The benchmarks are based on a fully elliptic, transient, 3D numerical description of conservation of mass, energy, and momentum associated with the mixed (forced and free) convection about a finned cylinder. As will become evident, the DNS-generated flow fields are highly complex.

Once the preferred turbulence model is identified by comparison of its predictions with those of the DNS, both DNS and turbulence model predictions of time- and area-averaged heat transfer coefficients will be compared to those calculated from correlations reported in the literature.

2. Benchmark problem

The benchmark problem is associated with the computational domain of Figure 1, which is based upon experimental work reported by Stark et al. [19] involving a finned, cylindrical HP in cross flow. Consistent with [19], air at atmospheric pressure flows through a channel of height $H_{ch} = 75$ mm, width $W_{ch} = 200$ mm, and length $L_{ch} = 2.75$ m. To focus on the heat transfer external to a finned

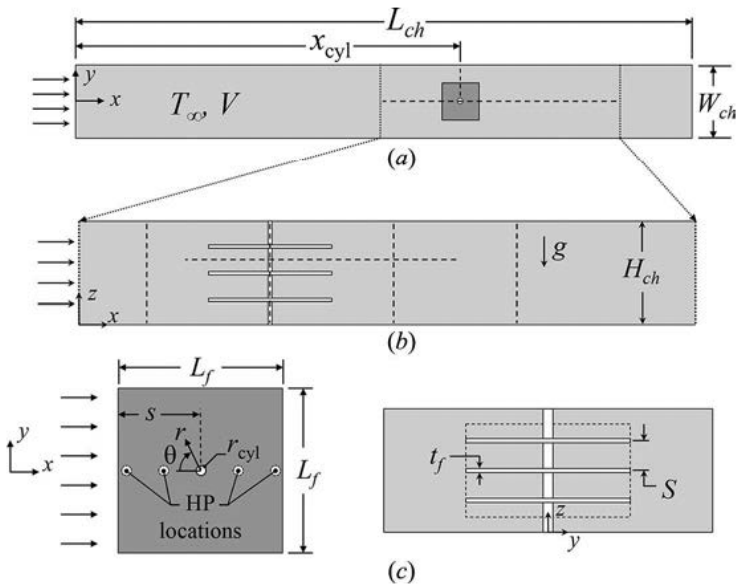

Figure 1. Schematic of the computational domain. (*a*) Top view (*x*–*y* plane), (*b*) side view (*x*–*z* plane), (*c*) fin section (*x*–*y* plane), and (*d*) flow direction (*y*–*z* plane).

HP that penetrates the bottom channel wall (in contrast to the heat transfer within the HP), the square fins and HP are specified to be isothermal (experimentally, the HP exhibits nearly isothermal conditions [19]). Simplification of the finned HP in this manner more readily reveals convective phenomena and yields results that are pertinent to convection from a finned tube.

A vertical, hot cylinder (diameter $D_{cyl} = 6$ mm) is centered in the width of the channel ($y_{cyl} = 0$) as shown in Figure 1. The diameter of the cylinder was chosen to allow for comparison with existing HP work [19, 21, 35, 36]. As in [19], the cylinder is located at $x_{cyl} = 1.33$ m downstream from the channel inlet, and has three square fins of dimension $L_f = 100$ mm and thickness $t_f = 0.97$ mm evenly spaced over the height of the channel (fin pitch $S = 18.75$ mm). Uniform inlet velocities of $V = 0.5$ and 1.5 m/s are specified at $x = 0$, as is a uniform temperature of $T_\infty = 25°C$. The cylinder and fin surfaces are at $T_{cyl} = T_f = 60°C$, and the channel walls are taken to be adiabatic. The channel outlet, located at $x = L_{ch}$, is assigned a zero relative pressure with zero second spatial derivatives of temperature in the x-direction. All solid surfaces are subject to no-slip velocity conditions.

3. Numerical models

3.1. Direct simulation

Flow and heat transfer are governed by the conservation of thermal energy (Eq. (1)), mass (Eq. (2)), and momentum (Eqs. (3*a*)–(3*c*)). The flow is assumed to be incompressible, and the fluid (air) is treated as a Boussinesq ideal gas [37] with properties evaluated at $T_0 = 25°C$ and an absolute pressure of 1 atm.

$$\frac{\partial T}{\partial t} + u_x \frac{\partial T}{\partial x} + u_y \frac{\partial T}{\partial y} + u_z \frac{\partial T}{\partial z} = \alpha\left(\frac{\partial^2 T}{\partial x^2} + \frac{\partial^2 T}{\partial y^2} + \frac{\partial^2 T}{\partial z^2}\right) \tag{1}$$

$$\frac{\partial u_x}{\partial x} + \frac{\partial u_y}{\partial y} + \frac{\partial u_z}{\partial z} = 0 \tag{2}$$

$$\frac{\partial u_x}{\partial t} + u_x \frac{\partial u_x}{\partial x} + u_y \frac{\partial u_x}{\partial y} + u_z \frac{\partial u_x}{\partial z} = -\frac{1}{\rho}\frac{\partial p}{\partial x} + \nu\left(\frac{\partial^2 u_x}{\partial x^2} + \frac{\partial^2 u_x}{\partial y^2} + \frac{\partial^2 u_x}{\partial z^2}\right) \tag{3a}$$

$$\frac{\partial u_y}{\partial t} + u_x\frac{\partial u_y}{\partial x} + u_y\frac{\partial u_y}{\partial y} + u_z\frac{\partial u_y}{\partial z} = -\frac{1}{\rho}\frac{\partial p}{\partial y} + \nu\left(\frac{\partial^2 u_y}{\partial x^2} + \frac{\partial^2 u_y}{\partial y^2} + \frac{\partial^2 u_y}{\partial z^2}\right) \tag{3b}$$

$$\frac{\partial u_z}{\partial t} + u_x\frac{\partial u_z}{\partial x} + u_y\frac{\partial u_z}{\partial y} + u_z\frac{\partial u_z}{\partial z} = -\frac{1}{\rho}\frac{\partial p}{\partial z} + \nu\left(\frac{\partial^2 u_z}{\partial x^2} + \frac{\partial^2 u_z}{\partial y^2} + \frac{\partial^2 u_z}{\partial z^2}\right) + [1-\beta(T-T_o)]g \tag{3c}$$

Initial conditions are a uniform temperature of T_∞ and zero velocities throughout the domain. Details of the DNS simulation, along with time- and grid-dependence information, may be found in [19]. At each time step, a convergence criterion applied to the residual mean squares (RMS) of all dependent variables (less than 10^{-5}) is met. In short, the computational mesh for the finite-volume DNS simulation comprises 36.1×10^6 elements, and a total real time of 10 s is simulated using a time step of 10^{-3} s. The DNS predications were generated using Ansys CFX v16.0, with each simulation requiring several weeks using 96 GB RAM on a dedicated Dell Precision T7600.

3.2. Turbulence models

Five turbulence models, all of which employ additional equations to describe the transport of turbulence, are considered. Two variations of Wilcox's κ-ω model, namely Menter's shear-stress transport (SST) model [3] and the Gamma-Theta transitional model (γ-Re_θSST) [4–6], are investigated. Additional simulations using a classic κ-ε model [7], along with two common variations, the Re-Normalization Group model (RNG κ-ε) [8] and the Explicit Algebraic Reynolds Stress model (κ-ε EARSM) [9], are performed. All five models are implemented in a consistent manner, and their predictions are compared to those of the DNS.

3.2.1. SST turbulence model

Menter's [3] modification of Wilcox's κ-ω turbulence model has been shown to produce accurate predictions of velocity fields and the associated convective heat transfer when compared with experimental and direct simulation techniques [10, 38–42]. Momentum and thermal transport are governed by the conservation of energy (Eq. (4)), mass (Eq. (2)), as well as x-, y-, and z-momentum (Eqs. (5a)–(5c)).

$$u_x\frac{\partial T}{\partial x} + u_y\frac{\partial T}{\partial y} + u_z\frac{\partial T}{\partial z} = \alpha\left(\frac{\partial^2 T}{\partial x^2} + \frac{\partial^2 T}{\partial y^2} + \frac{\partial^2 T}{\partial z^2}\right) \tag{4}$$

$$u_x\frac{\partial u_x}{\partial x} + u_y\frac{\partial u_x}{\partial y} + u_z\frac{\partial u_x}{\partial z} = -\frac{1}{\rho}\frac{\partial p}{\partial x} + (\nu+\nu_{\text{turb}})\left(\frac{\partial^2 u_x}{\partial x^2} + \frac{\partial^2 u_x}{\partial y^2} + \frac{\partial^2 u_x}{\partial z^2}\right) \tag{5a}$$

$$u_x\frac{\partial u_y}{\partial x} + u_y\frac{\partial u_y}{\partial y} + u_z\frac{\partial u_y}{\partial z} = -\frac{1}{\rho}\frac{\partial p}{\partial y} + (\nu+\nu_{\text{turb}})\left(\frac{\partial^2 u_y}{\partial x^2} + \frac{\partial^2 u_y}{\partial y^2} + \frac{\partial^2 u_y}{\partial z^2}\right) \tag{5b}$$

$$u_x\frac{\partial u_z}{\partial x} + u_y\frac{\partial u_z}{\partial y} + u_z\frac{\partial u_z}{\partial z} = -\frac{1}{\rho}\frac{\partial p}{\partial z} + (\nu+\nu_{\text{turb}})\left(\frac{\partial^2 u_z}{\partial x^2} + \frac{\partial^2 u_z}{\partial y^2} + \frac{\partial^2 u_z}{\partial z^2}\right) + [1-\beta(T-T_o)]g \tag{5c}$$

Additional equations describing the transport of turbulent kinetic energy κ (Eq. (6a)) and the specific rate of turbulence dissipation ω (Eq. (6b)) are employed. Turbulent viscosity and the production term, P_κ, are included in Eqs. 7(a) and 7(b), respectively, while the remaining coefficients are reported in [3].

$$\begin{aligned}\rho\left(\frac{\partial(u_x\kappa)}{\partial x} + \frac{\partial(u_y\kappa)}{\partial y} + \frac{\partial(u_z\kappa)}{\partial z}\right) &= P_\kappa - \beta_1\rho\kappa\omega + \frac{\partial}{\partial x}\left[(\mu+\sigma_\kappa\mu_{\text{turb}})\frac{\partial\kappa}{\partial x}\right] \\ &+ \frac{\partial}{\partial y}\left[(\mu+\sigma_\kappa\mu_{\text{turb}})\frac{\partial\kappa}{\partial y}\right] + \frac{\partial}{\partial z}\left[(\mu+\sigma_\kappa\mu_{\text{turb}})\frac{\partial\kappa}{\partial z}\right]\end{aligned} \tag{6a}$$

$$\rho\left(\frac{\partial(u_x\omega)}{\partial x}+\frac{\partial(u_y\omega)}{\partial y}+\frac{\partial(u_z\omega)}{\partial z}\right)=\frac{\alpha_1}{\nu_{\text{turb}}}P_\kappa-\beta_2\rho\,\omega^2+\frac{\partial}{\partial x}\left[(\mu+\sigma_\omega\mu_{\text{turb}})\frac{\partial\omega}{\partial x}\right]$$
$$+\frac{\partial}{\partial y}\left[(\mu+\sigma_\omega\,\mu_{\text{turb}})\frac{\partial\omega}{\partial y}\right]+\frac{\partial}{\partial z}\left[(\mu+\sigma_\omega\,\mu_{\text{turb}})\frac{\partial\omega}{\partial z}\right]+2(1-F_1)\frac{\rho\sigma_{\omega 2}}{\omega}\left(\frac{\partial\kappa\partial\omega}{\partial x^2}+\frac{\partial\kappa\partial\omega}{\partial y^2}+\frac{\partial\kappa\partial\omega}{\partial z^2}\right) \tag{6b}$$

$$\mu_{\text{turb}}=\rho\nu_{\text{turb}}=\frac{\rho\alpha_1\kappa}{\max(\alpha_1\omega,SF_2)} \tag{7a}$$

$$P_\kappa=\mu S^2 \tag{7b}$$

Boundary conditions associated with Eqs. (2), (4), and (5*a*)–(5*c*) are identical to those described earlier. In addition, the turbulence intensity at $x=0$ is assumed to be 5%, which determines the values of κ and ω at that location [3]. While turbulence intensity has been shown by Minkowycz et al. [43] to affect the predicted laminar to turbulent transition and the resulting momentum transfer, an investigation into the effects on the predicted heat transfer is outside of the scope of this work. The second spatial derivatives of κ and ω are set to zero at the channel outlet, and the spatial derivatives of κ and ω normal to all solid surfaces are set to zero. A convergence criterion applied to the RMS values for all dependent variables of 10^{-6} is enforced. A grid dependence study was carried out in a manner similar to that described in Appendix A of [19]; the final mesh contained 56.3×10^6 elements. The simulations required ~4 h to achieve a converged, grid-independent solution on the same computational hardware used for the DNS.

3.2.2. γ-Re_θ SST

A more recent SST model version that includes prediction of the intermittency of the turbulence is also investigated. This two-equation intermittency model was developed by Mentor [4, 5], with the goal of improving the accuracy of predictions in the laminar–turbulent transitional range. In addition to the equations of the previous section, two additional transport equations and associated parameters are defined. The intermittency of the turbulence γ (Eq. (8*a*)) is coupled with an equation governing the transitional momentum thickness Reynolds number $\widetilde{Re}_{\theta t}$ (Eq. (8*b*)):

$$\rho\left(\frac{\partial(u_x\gamma)}{\partial x}+\frac{\partial(u_y\gamma)}{\partial y}+\frac{\partial(u_z\gamma)}{\partial z}\right)=\frac{\partial}{\partial x}\left[\left(\mu+\frac{\mu_{\text{turb}}}{\sigma_f}\right)\frac{\partial\gamma}{\partial x}\right]$$
$$+\frac{\partial}{\partial y}\left[\left(\mu+\frac{\mu_{\text{turb}}}{\sigma_f}\right)\frac{\partial\gamma}{\partial y}\right]+\frac{\partial}{\partial z}\left[\left(\mu+\frac{\mu_{\text{turb}}}{\sigma_f}\right)\frac{\partial\gamma}{\partial z}\right]+P_{\gamma1}-E_{\gamma1}+P_{\gamma2}-E_{\gamma2} \tag{8a}$$

$$\rho\left(\frac{\partial(u_x\widetilde{Re}_{\theta t})}{\partial x}+\frac{\partial(u_y\widetilde{Re}_{\theta t})}{\partial y}+\frac{\partial(u_z\widetilde{Re}_{\theta t})}{\partial z}\right)=P_{\theta t}+\frac{\partial}{\partial x}\left[\sigma_{\theta t}(\mu+\mu_{\text{turb}})\frac{\partial\widetilde{Re}_{\theta t}}{\partial x}\right]$$
$$+\frac{\partial}{\partial y}\left[\sigma_{\theta t}(\mu+\mu_{\text{turb}})\frac{\partial\widetilde{Re}_{\theta t}}{\partial y}\right]+\frac{\partial}{\partial z}\left[\sigma_{\theta t}(\mu+\mu_{\text{turb}})\frac{\partial\widetilde{Re}_{\theta t}}{\partial z}\right] \tag{8b}$$

The terms $P_{\gamma1}$ and $E_{\gamma1}$ describe the sources of transition, while $P_{\gamma2}$ and $E_{\gamma2}$ are affiliated with destruction/relaminarization sources within the flow. Definitions of these source terms, the source term $P_{\theta t}$ (in Eq. (8*b*)), and the values of σ_f and $\sigma_{\theta t}$ may be found in [5]. The γ-Re_θ SST model employs the same definition of μ_{turb} as the original SST model (Eq. (7*a*)). Boundary conditions for T, u_x, u_y, u_z, κ, and ω are the same as listed in Section 3.2.1. In addition, the first spatial derivatives of γ and $\widetilde{Re}_{\theta t}$ normal to the solid surfaces are set to zero. Inlet boundary conditions for these two variables are quantified by the inlet turbulence intensity [5], and the second spatial derivatives of both variables normal to the outlet are set to zero. Simulations using the γ-Re_θ SST model were performed using the same convergence criterion as for the SST simulations. Grid independence was achieved, and the resulting simulations required ~5 h (20% longer than the corresponding SST simulations).

3.2.3. κ-ε turbulence model

In addition to the preceding SST models, three variations of the well-established κ-ε turbulence model [7] are also considered. The problem is still governed by the conservation of energy (Eq. (4)), mass (Eq. (2)), as well as x-, y-, and z-momentum (Eqs. (5a)–(5c)). The turbulent kinetic energy, κ, and the rate of dissipation of turbulent kinetic energy, ε, are governed by Eqs. (9a) and (9b), respectively [7].

$$\rho\left(\frac{\partial(u_x\kappa)}{\partial x}+\frac{\partial(u_y\kappa)}{\partial y}+\frac{\partial(u_z\kappa)}{\partial z}\right)=\frac{\partial}{\partial x}\left[\left(\mu+\frac{\mu_{\text{turb}}}{\sigma_\kappa}\right)\frac{\partial\kappa}{\partial x}\right]+\frac{\partial}{\partial y}\left[\left(\mu+\frac{\mu_{\text{turb}}}{\sigma_\kappa}\right)\frac{\partial\kappa}{\partial y}\right]+\frac{\partial}{\partial z}\left[\left(\mu+\frac{\mu_{\text{turb}}}{\sigma_\kappa}\right)\frac{\partial\kappa}{\partial z}\right]+P_\kappa+P_b-\rho\varepsilon \tag{9a}$$

$$\rho\left(\frac{\partial(u_x\varepsilon)}{\partial x}+\frac{\partial(u_y\varepsilon)}{\partial y}+\frac{\partial(u_z\varepsilon)}{\partial z}\right)=\frac{\partial}{\partial x}\left[\left(\mu+\frac{\mu_{\text{turb}}}{\sigma_\varepsilon}\right)\frac{\partial\varepsilon}{\partial x}\right]+\frac{\partial}{\partial y}\left[\left(\mu+\frac{\mu_{\text{turb}}}{\sigma_\varepsilon}\right)\frac{\partial\varepsilon}{\partial y}\right]+\frac{\partial}{\partial z}\left[\left(\mu+\frac{\mu_{\text{turb}}}{\sigma_\kappa}\right)\frac{\partial\varepsilon}{\partial z}\right]+C_{1\varepsilon}\frac{\varepsilon}{\kappa}(P_\kappa+C_{3\varepsilon}P_b)-C_{2\varepsilon}\rho\frac{\varepsilon^2}{\kappa} \tag{9b}$$

$$\mu_{\text{turb}}=\rho\nu_{\text{turb}}=\rho C_\mu\frac{\kappa^2}{\varepsilon} \tag{10}$$

The definition of the production term P_κ is consistent with that of the SST model (Eq. (7b)), but the turbulent viscosity μ_{turb} (Eq. (10)) is different from that of the SST model (Eq. (7a)). Values for σ_κ, σ_ε, $C_{1\varepsilon}$, $C_{2\varepsilon}$, and $C_{3\varepsilon}$ are provided in [7]. The boundary conditions governing T, u_x, u_y, u_z, and κ are the same as for the SST model, whereas the value of ε at the inlet boundary condition is determined by the turbulence intensity. Both the first spatial derivative of ε normal to all solid surfaces and the second spatial derivative of ε normal to the outlet are set to zero. The convergence criterion and grid dependence for the κ-ε model are handled in a manner similar to the SST model of Section 3.2.1. Using a final mesh of 72.1×10^6 elements, each simulation required a computation time of ~5 h.

3.2.4. RNG κ-ε

In an attempt to improve the performance of the κ-ε model, a new governing equation for ε (Eq. (11)) was developed [8] with the aim of accounting for the different scales of eddies by altering the production terms.

$$\rho\left(\frac{\partial(u_x\varepsilon)}{\partial x}+\frac{\partial(u_y\varepsilon)}{\partial y}+\frac{\partial(u_z\varepsilon)}{\partial z}\right)=\frac{\partial}{\partial x}\left[\left(\mu+\frac{\mu_{\text{turb}}}{\sigma_\varepsilon}\right)\frac{\partial\varepsilon}{\partial x}\right]+\frac{\partial}{\partial y}\left[\left(\mu+\frac{\mu_{\text{turb}}}{\sigma_\varepsilon}\right)\frac{\partial\varepsilon}{\partial y}\right]+\frac{\partial}{\partial z}\left[\left(\mu+\frac{\mu_{\text{turb}}}{\sigma_\kappa}\right)\frac{\partial\varepsilon}{\partial z}\right]+C_{1\varepsilon}\frac{\varepsilon}{\kappa}(P_\kappa+C_{3\varepsilon}P_b)-C^*_{2\varepsilon}\rho\frac{\varepsilon^2}{\kappa} \tag{11}$$

All other governing equations are the same as those used in the κ-ε model (Eqs. (2), (4), (5a)–(5c), and (9a)). The values of σ_κ, σ_ε, $C_{1\varepsilon}$, $C^*_{2\varepsilon}$, and $C_{3\varepsilon}$ differ slightly from those used in the κ-ε model, and may be found in [8]. All boundary conditions for the RNG κ-ε equations are identical to those used in the κ-ε model. The convergence, grid dependence, and computational requirements are consistent with the standard κ-ε model of Section 3.2.3.

3.2.5. κ-ε EARSM

The final variation of the κ-ε model investigated, κ-ε EASRM [9], makes further alterations to the governing equation for ε.

$$\rho\left(\frac{\partial(u_x\varepsilon)}{\partial x}+\frac{\partial(u_y\varepsilon)}{\partial y}+\frac{\partial(u_z\varepsilon)}{\partial z}\right)=\frac{\partial}{\partial x}\left[\left(\mu+\frac{\mu_{\text{turb}}}{\sigma_\varepsilon}\right)\frac{\partial\varepsilon}{\partial x}\right]+\frac{\partial}{\partial y}\left[\left(\mu+\frac{\mu_{\text{turb}}}{\sigma_\varepsilon}\right)\frac{\partial\varepsilon}{\partial y}\right]+\frac{\partial}{\partial z}\left[\left(\mu+\frac{\mu_{\text{turb}}}{\sigma_\kappa}\right)\frac{\partial\varepsilon}{\partial z}\right]+\rho C_1S\varepsilon-\rho C_1\frac{\varepsilon^2}{\kappa+\sqrt{\nu\varepsilon}}+C_{1\varepsilon}\frac{\varepsilon}{\kappa}\,C_{3\varepsilon}\,P_b \tag{12}$$

As in the RNG κ-ε model, all other governing equations remain the same as those used by the κ-ε model (Eqs. (2), (4), (5*a*)–(5*c*), and (9*a*)), and the values of σ_κ, σ_ε, $C_{2\varepsilon}$, and $C_{3\varepsilon}$ again deviate from the κ-ε and RNG κ-ε models, and may be found in [9]. Boundary conditions for the κ-ε EARSM equations are identical to those used in the κ-ε simulations. The convergence, grid dependence, and computational requirements are again consistent with the standard κ-ε model.

4. Results and discussion

4.1. Benchmark DNS predictions

The DNS model predicts the transient, 3D velocity and temperature distributions throughout the domain of Figure 1. The predictions illustrate the complexity of the flow, and are used to (*i*) evaluate heat transfer coefficients for the cylinder and fins, and (*ii*) serve as the benchmark against which the predictions of the turbulence models will be compared. Representative velocity distributions are shown in Figure 2 for the $V = 0.5$ m/s (left) and $V = 1.5$ m/s (right) cases at a single, arbitrary time after a quasi-steady state has been achieved (Appendix A). Velocity distributions in a vertical mid-plane of the channel (a subsection of the horizontal dashed line in Figure 1*a*) are shown in Figure 2*a* in which air flows from left to right, creating a complex wake region downstream of the finned cylinder.

4.1.1. Low-velocity case

For $V = 0.5$ m/s, air velocities are reduced immediately downstream of the finned cylinder, and the heated air rises as it flows from the left to the right. The importance of buoyancy forces is anticipated

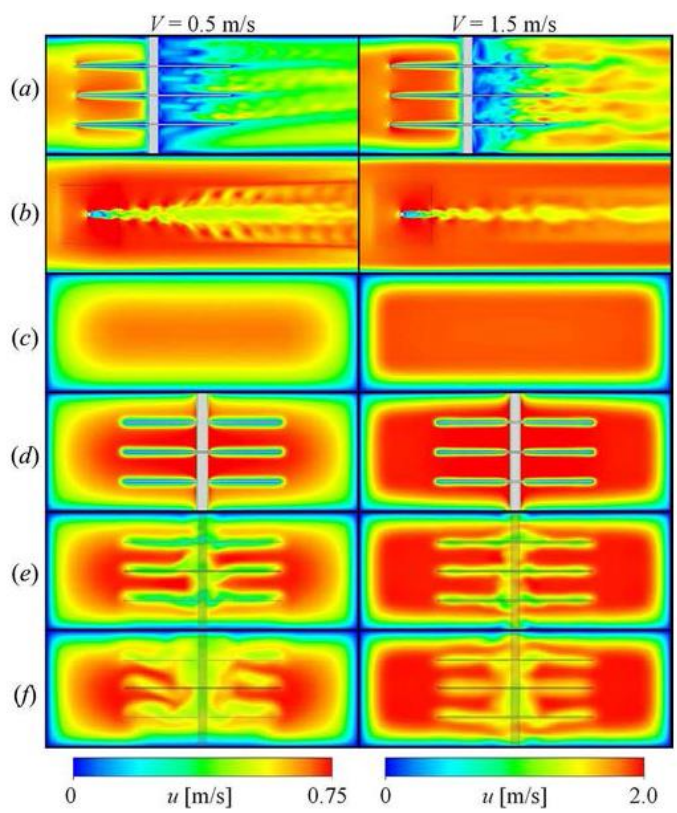

Figure 2. DNS-predicted instantaneous velocity distributions for $V = 0.5$ m/s, $t = 1.75$ s (left) and 1.5 m/s, $t = 1.75$ s (right) cases. (*a*) Side view (*x*–*z* plane), (*b*) midway between fins (*x*–*y* plane), (*c*) flow direction at $x_{cyl} - L_f$ (*y*–*z* plane), (*d*) flow direction at x_{cyl}, (*e*) flow direction at $x_{cyl} + L_f$, and (*f*) flow direction at $x_{cyl} + 2L_f$.

since $Gr_{H_{ch}}/Re^2_{H_{ch}} = 0.33$. Velocity distributions in a horizontal plane located midway between the top and middle fins (Figure 2*b*); the dashed horizontal line in Figure 1*b* reveals an expanding wake region downstream of the finned structure as vortices are shed from the cylinder. The flow is highly time-varying, and is not symmetric about $y = 0$.

Velocity distributions in a series of planes normal to the main flow direction (identified by the four dashed vertical lines in Figure 1*b*) are shown in Figure 2(*c–f*). For the low-velocity case, Figure 2*c* shows the development of isothermal, steady, viscous flow in the rectangular channel located one fin length upstream of the cylinder centerline ($x_{cyl} - L_f$). The flow slows in the immediate vicinity of the finned structure, as is evident in Figure 2*d* ($x = x_{cyl}$), and accelerates as is acceleration of the flow between the fins (and between the fins and channel walls). The thickness of the velocity boundary layer about the cylinder is substantially less than that of the boundary layers adjacent to the fins, reflecting the initiation of fin boundary layers at $x = x_{cyl} - L_f/2$. Velocities downstream of the finned structure are shown in Figures 2*e* ($x_{cyl} + L_f$) and 2f ($x_{cyl} + 2L_f$). As expected, the flow exhibits asymmetry about $y = 0$, and upon close inspection the slower, warm fluid is seen to rise as it propagates downstream. The velocity distribution becomes more uniform further downstream of the finned structure.

4.1.2. High-velocity case

Velocity distributions for the $V = 1.5$ m/s case show enhanced mixing relative to the low-velocity case. Flow downstream of the finned cylinder is less organized (Figure 2*a*) for the $V = 1.5$ m/s case, and the effects of buoyancy are not as evident as in the low-velocity situation since $Gr_{H_{ch}}/Re^2_{H_{ch}} = 0.037 \approx 0$. The robust shedding of structured vortices evident in the low-velocity case is not as pronounced for the $V = 1.5$ m/s situation (Figure 2*b*). Velocity boundary layers along the upstream channel walls (Figure 2*c*) as well as those adjacent to the cylinder and fins (Figure 2*d*) are thinner than those corresponding to $V = 0.5$ m/s, as expected. As for the $V = 0.5$ m/s case, flow downstream of the finned structure (Figures 2*e* and *f*) is not symmetric about $y = 0$, and becomes more uniform downstream as fluid mixing occurs. DNS-predicted temperature distributions corresponding to the conditions of Figure 2 are reported in Figure 5 and will be discussed shortly.

4.2. Turbulence model velocity and temperature predictions

Velocity distributions in the vertical mid-plane of the channel, corresponding to those of Figure 2*a*, are reported in Figure 3. (The DNS results have been expanded lengthwise relative to the distributions

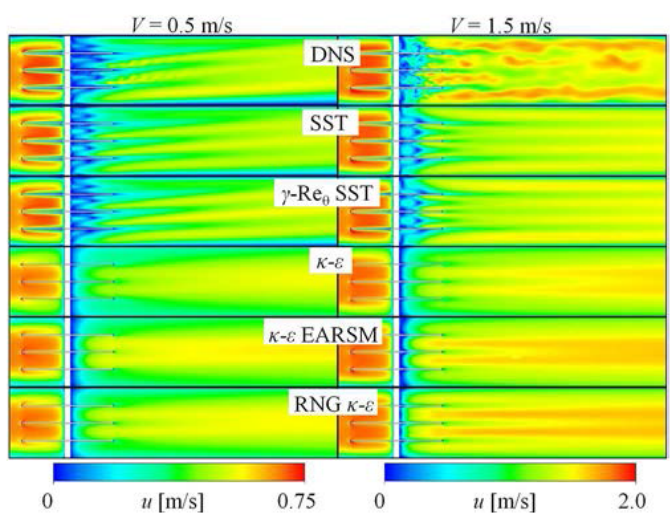

Figure 3. Velocity distributions in the channel vertical centerplane (*x–z* plane). DNS predictions are shown at $t = 1.75$ s for both the low- and high-velocity cases.

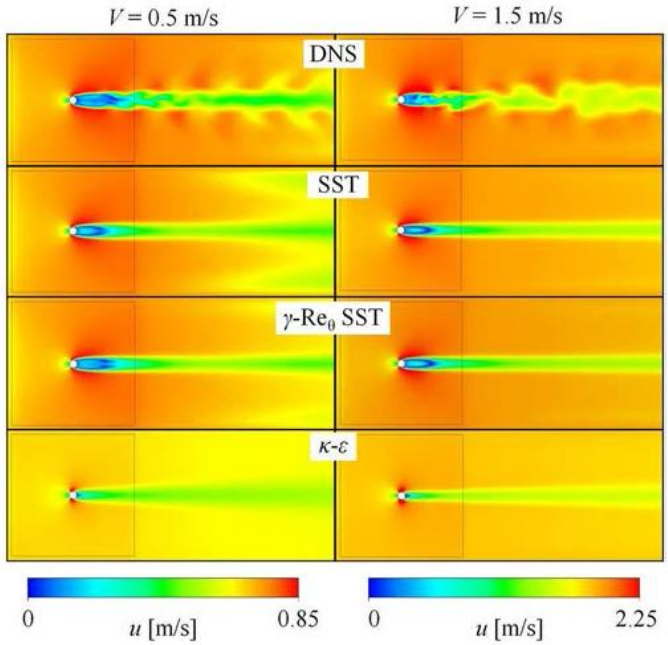

Figure 4. Velocity distributions in the x–y plane midway between the top two fins.

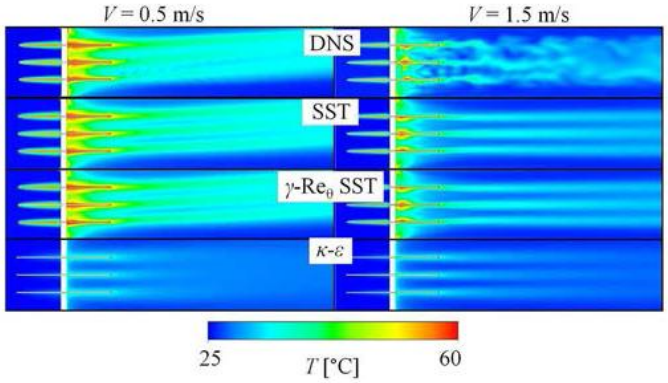

Figure 5. Temperature distributions in the channel vertical centerplane (x–z plane).

of Figure 2*a*.) The distributions of the steady-state SST and γ-Re_θ SST models are in qualitative agreement with those of the DNS. As in the DNS results, buoyancy effects are evident in the low velocity-SST predictions, but a similar buoyancy effect is not evident in the κ-ε, RNG κ-ε, or κ-ε EARSM predictions. For either the low- or high-speed cases, the DNS and SST predictions show similar behavior immediately upstream and downstream of the vertical cylinder. In contrast, the three κ-ε models predict significantly larger velocities immediately downstream of the cylinder, relative to the benchmark DNS predictions. Predictions of the SST and γ-Re_θ SST models are nearly indistinguishable qualitatively.

Velocity distributions midway between the top and middle fins (corresponding to those shown in Figure 2*b*) predicted by the DNS and SST methodologies are reported in Figure 4. (The DNS predictions have been magnified from the otherwise identical results of Figure 2*b*.) As in Figure 3, all three κ-ε-based models fail to replicate even the qualitative features of the DNS predictions, and their predictions are similar to one another. Therefore, only the κ-ε predictions are reported in Figure 4. Since the SST turbulence models are steady-state, vortex shedding is not predicted, and

symmetric time-averaged behavior about $y = 0$ is observed. Modest differences are noted between the SST and γ-Re_θ SST model predictions for the low-velocity case, with buoyancy effects more pronounced in the SST predictions, relative to those of the DNS or γ-Re_θ SST model.

Temperature distributions in the vertical mid-plane are displayed in Figure 5. As discussed relative to Figures 2 and 3, the buoyancy effects are noted for the low inlet velocity case with warm air rising as it propagates downstream. The effects of buoyancy are absent in the high-velocity case, also as expected. Overall, the predicted temperatures of the DNS, SST, and γ-Re_θ SST models are in qualitative agreement. The κ-ε, RNG κ-ε, and κ-ε EARSM models behave poorly, and only the κ-ε predictions are shown.

Air-temperature distributions in the horizontal plane midway between the top and middle fins, as predicted by the various numerical models, are reported in Figure 6. Again, the two SST models qualitatively replicate the DNS predictions and are in good agreement with each other. Moreover, time-averaged DNS and SST predictions of the widths of the thermal wakes downstream of the cylinder compare favorably to the experimentally measured widths [19], further validating the SST model's ability to capture the time-average of transient phenomena. Again, the κ-ε, RNG κ-ε, and κ-ε EARSM model predictions deviate substantially from those of the DNS and only the κ-ε results are shown.

4.3. Local convection coefficients

Values of the local convection coefficients both on the fin and on the cylinder surfaces (h_f and h_{cyl}) are determined on a per unit area basis; $h \equiv q''_{surf}/(T_{f,cyl} - T_\infty) = -\kappa \partial T/\partial n|_{surf}/(T_{f,cyl} - T_\infty)$. In the following discussion, both (*i*) instantaneous and (*ii*) time-averaged local coefficients will be reported; the distinction will be made clear in the context of the discussion. Also, due to inability of the κ-ε models to even qualitatively predict the flow field, local convection coefficient predictions associated with these models are in poor quantitative agreement with the DNS-predicted values, and will not be reported.

Instantaneous (DNS) and time-averaged (SST) local convection coefficient distributions for the cylinder are shown in Figure 7. In general, the largest local coefficients are on the upstream portion of the cylinder ($\theta = 0°$, Figure 1*c*), and are the smallest near $\theta = \pm 180°$. Small local convection coefficients also exist in the vicinity of each fin because of the velocity reduction associated with

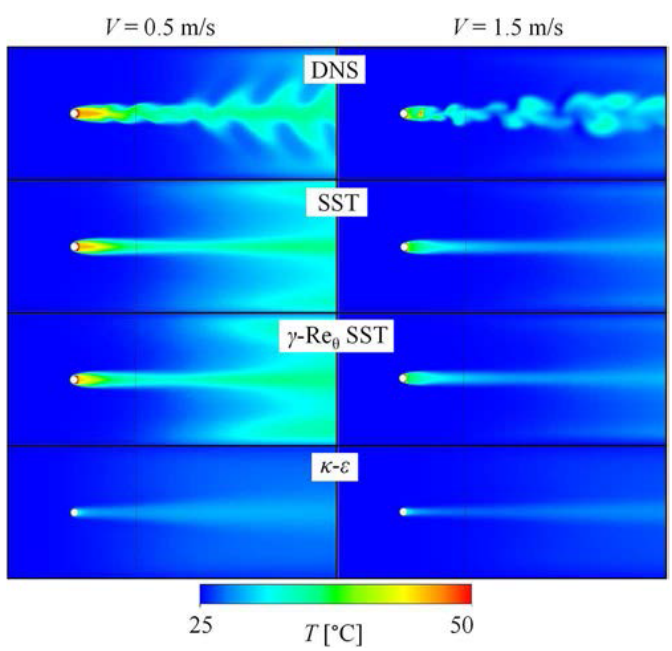

Figure 6. Temperature distributions in the horizontal plane midway between the top two fins (*x*–*y* plane).

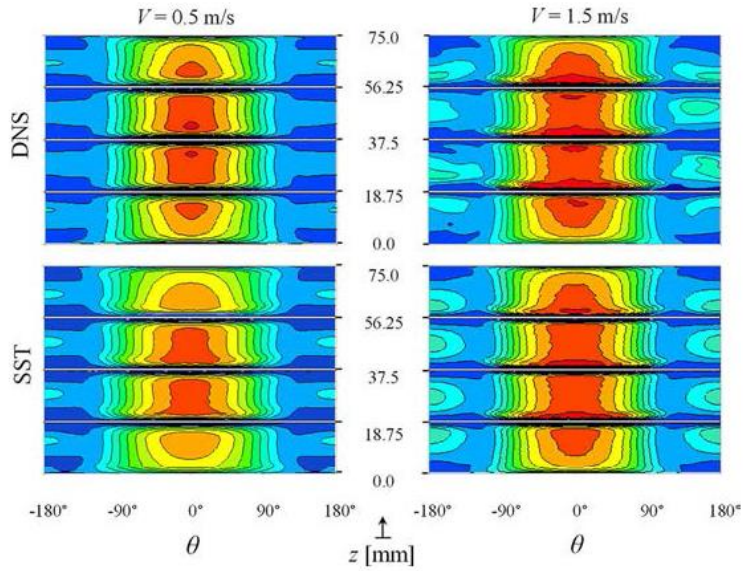

Figure 7. Predicted transfer coefficient distributions on the cylinder. Coefficients range from $h_{cyl} = 0$ to 75 W/m^2 K and 0 to 150 W/m^2 K for the 0.5 and 1.5 m/s cases, respectively. Contour bands are plotted at intervals of 7.5 and 15 W/m^2 K for the two velocity cases.

boundary-layer development on the fins. A similar reduction in local heat fluxes is attributed to boundary layers forming on the bottom and top channel walls at $z \approx 0$ and H_{ch}. Overall, there is good agreement between the local heat transfer coefficients predicted by the SST and DNS models. Note that SST simulations were also performed for a cylinder with no fins, yielding local heat transfer coefficient distributions similar to those for a plain cylinder in cross flow.

Instantaneous (DNS) and time-averaged (SST) local heat transfer coefficients on the top surface of the middle fin are reported in Figure 8. Whereas boundary-layer development on the fins influences

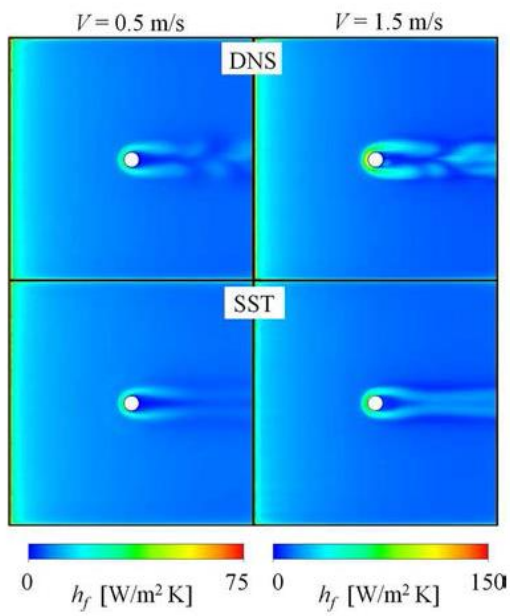

Figure 8. Heat transfer coefficient distributions on the upper surface of the middle fin. Convection coefficients range from $h_f = 0$ to 75 W/m^2 K and 0 to 150 W/m^2 K for the $V = 0.5$ and 1.5 m/s cases, respectively.

local heat fluxes on the cylinder (Figure 7), flow around the cylinder influences local fluxes on the fins. More specifically, an arc of high local heat transfer coefficients wraps around the cylinder, caused by horseshoe vortices, a commonly reported flow phenomenon for finned tubes [29–31]. The fin surface downstream of the cylinder experiences relatively high local coefficients associated with the shedding of vortices from the cylinder. This effect is especially pronounced in the DNS predictions, which are presented for an arbitrary time after quasi-steady state has been achieved. The steady-state SST predictions also indicate relatively high local heat transfer coefficients downstream of the cylinder.

4.4. Area-averaged convection coefficients

Area- and time-averaged convections for the total exposed fin ($\overline{h_f}$) and exposed cylinder ($\overline{h_{\text{cyl}}}$) surfaces are determined during the quasi-steady state with the DNS model using Eqs. (13*a*) and (13*c*), respectively. In both the high- and low-velocity cases, information at 150 distinct times (every fifth step over a time window of 0.75 s) was used to calculate the time average values. The values from the DNS were then compared with the area-averaged values of $\overline{h_f}$ and $\overline{h_{\text{cyl}}}$ obtained from steady-state simulations, as defined by Eqs. (13*b*) and (13*d*), respectively. Note that the fin area includes the top, bottom, and edge surfaces.

$$\overline{h_{\text{cyl}}} = \frac{\int_t^{t+T(t)} \left[\int_{A_w} q''(z, r = r_{\text{cyl}}, \theta, t)\, dA_{\text{cyl}} \right] dt}{A_{\text{cyl}}(T_{\text{cyl}} - T_\infty)T(t)} \text{ or } \frac{\int_{A_w} q''\,(z, r = r_{\text{cyl}}, \theta)\, dA_{\text{cyl}}}{A_{\text{cyl}}\,(T_{\text{cyl}} - T_\infty)} \tag{13a; 13b}$$

$$\overline{h_f} = \frac{\int_t^{t+T(t)} \left[\int_{A_w} q''\,(z, r, \theta,\ t)\, dA_f \right] dt}{A_f(T_f - T_\infty)T(t)} \text{ or } \frac{\int_{A_w} q''\,(z, r, \theta)\, dA_f}{A_f(T_f - T_\infty)} \tag{13c; 13d}$$

Comparison of the predicted convection coefficients, listed in Table 1, confirms the ability of the SST and γ-Re_θ SST models to closely replicate the benchmark DNS predictions. Specifically, the SST and γ-Re_θ SST values of $\overline{h_f}$ differ from the DNS model by 13% ($V = 0.5$ m/s case) to 18% ($V = 1.5$ m/s case). In contrast, the κ-ε, RNG κ-ε, and κ-ε EARSM predictions are in error by approximately 58% ($V = 1.5$ m/s case) and 70% ($V = 0.5$ m/s case). DNS, SST, and γ-Re_θ SST predictions of $\overline{h_{\text{cyl}}}$ are in agreement to within 4% for each case, whereas the κ-ε, RNG κ-ε, and κ-ε EARSM predictions exhibit errors between 41% and 65%.

4.5. Correlation-based predictions

As evident from the preceding discussion, convection processes at the fin and cylinder surfaces are coupled, with each influencing the other. In addition, the SST predictions of area-averaged heat transfer coefficients are in reasonable agreement with the DNS benchmark information. However,

Table 1. Predicted time- and area-averaged fin and cylinder heat transfer coefficients predicted using various numerical models.

	$V = 0.5$ m/s		$V = 1.5$ m/s	
	$\overline{h_f}$ W/m^2 K	$\overline{h_{\text{cyl}}}$ W/m^2 K	$\overline{h_f}$ W/m^2 K	$\overline{h_{\text{cyl}}}$ W/m^2 K
DNS	12.9	28.9	23.2	50.9
SST	11.3	29.4	19.1	52.5
γ-Re_θ SST	11.4	29.5	19.2	52.9
κ-ε	4.84	13.4	9.76	30.0
RNG κ-ε	3.98	11.3	8.80	23.1
κ-ε EARSM	3.90	10.2	9.44	23.2

to rapidly estimate the convection heat loss from the entire structure, it might be desirable to employ analytical, experimental-, or numerical-based correlations. Since correlations that apply to mixed (free and forced) convection are often of high uncertainty and of limited availability [44], the correlations considered next were developed for situations involving negligible buoyancy effects.

The simplest correlation-based approach involves the use of existing expressions for (*i*) cylinders in cross flow and (*ii*) flat plates in parallel flow to independently estimate $\overline{h_{cyl}}$ and $\overline{h_f}$, neglecting all coupling between cylinder and fin boundary-layer development. Here, Churchill and Bernstein's [44] correlation for a cylinder in cross flow, Eq. (14*a*) of Table 2, is used to predict $\overline{h_{cyl}}$. An updated correlation for a cylinder in cross flow provided by Sparrow et al. [45], Eq. (14*b*) of Table 2, is also used. The area-averaged coefficient, $\overline{h_f}$, is estimated by assuming each fin is a two-dimensional flat plate of negligible thickness. The value of $\overline{h_f}$ may then be calculated using correlations for laminar, turbulent, or transitional flow as provided in Eqs. (14*c*), (14*d*), and (14*e*) of Table 2, respectively. The Reynolds number associated with the fin length is$Re_{L_f} = VL_f/\nu = 3{,}236$ and 9,708 for the low- and high-velocity cases, respectively, suggesting that laminar flow would exist over the entire fin if the effects of (*i*) the cylinder and (*ii*) the finite fin thickness were neglected [34]. Here, transition from laminar to turbulent flow will be assumed to be triggered either by (*i*) the leading flat edge of the nonzero thickness fin located at $x = x_{cyl}$ - $L_f/2$ resulting in turbulent flow over the entire fin (Eq. (14*d*)), or (*ii*) by the cylinder at $x = x_{cyl}$ (Eq. (14*e*)).

A more sophisticated approach involves the utilization of numerical simulation-based correlations such as those of Romero-Méndez et al. [33] for convection from a finned tube, Eqs. (14*f*) and (14*g*) of Table 2. (The + S correlation is affiliated with larger fin pitches.) Alternatively, an experimentally derived correlation due to Sparrow and Samie [26] is tested; this correlation, Eq. (14*h*) of Table 2, uses a Reynolds number defined in terms of a mean velocity corresponding to the smallest cross-sectional area of the flow. The value of u_m is calculated using the SST-predicted velocities for the transverse plane, defined by the dashed lines in Figure 1*d*.

Predicted area-averaged heat transfer coefficients for the fin and cylinder surfaces using the DNS, SST, κ-ε, and various analytical correlations for the $V = 0.5$ and 1.5 m/s cases are listed in Table 3. The Churchill and Bernstein correlation for a cylinder in cross flow yields results that are within 7.3% (5.5%) and 4.5% (1.4%) of the DNS (SST) predictions for the $V = 0.5$ and 1.5 m/s cases, respectively. The Sparrow correlation for a cylinder in cross flow (listed in parentheses) yields results that are within 2% (0.4%) and 4% (0.8%) of the DNS (SST) predictions for the $V = 0.5$ and 1.5 m/s cases, respectively. Both correlations exhibit excellent agreement with the DNS and SST predictions. The *k*-ε predictions are in poor agreement with all of the other predictions for the cylinder. Area-averaged heat transfer coefficients for the fins, predicted using Eqs. (14*c*) through (14*e*), are consistent with

Table 2. Correlations used to predict time- and area-averaged fin and cylinder heat transfer coefficients.

Equation No.	Correlation	Equation
(14a)	Cylinder (Churchill and Bernstein [44])	$\overline{Nu}_D = \frac{\overline{h_{cyl}}D}{k} = 0.3 + \frac{0.62 Re_D^{1/2} Pr^{1/3}}{\left[1+(0.4/Pr)^{2/3}\right]^{1/4}}\left[1+\left(\frac{Re_D}{282{,}000}\right)^{5/8}\right]^{4/5}$
(14b)	Cylinder (Sparrow et al. [45])	$\overline{Nu}_D = \frac{\overline{h_{cyl}}D}{k} = 0.25 + \left(0.4 Re_D^{1/2} + 0.06 Re_D^{2/3}\right) Pr^{0.37}\left(\frac{\mu}{\mu_{surf}}\right)^{1/4}$
(14c)	Flat plate laminar [41]	$\overline{Nu}_{L_f} = \frac{\overline{h_f}L_f}{k} = 0.664\ Re_{L_f}^{1/2} Pr^{1/3}$
(14d)	Flat plate turbulent [41]	$\overline{Nu}_{L_f} = \frac{\overline{h_f}L_f}{k} = 0.037\ Re_{L_f}^{4/5}\ Pr^{1/3}$
(14e)	Flat plate transition [41]	$\overline{Nu}_{L_f} = \frac{\overline{h_f}L_f}{k} = \left[0.037\left(Re_{L_f}^{4/5} - Re_s^{4/5}\right) + 0.664\ Re_s^{1/2}\right]\ Pr^{1/3}$
(14f)	Romero-Méndez [33]	$\overline{Nu}_D = \frac{\overline{h_{tot}}D}{k} = Re_D Pr \frac{W_f S}{A_f + \pi S D^2}\left[1 - \exp\left(-\frac{1.32 Pr^{4/3} L_f^{1/2} D^{1/2}}{Re_D^{1/2} S}\right)\right]$
(14g)	Romero-Méndez + S [33]	$\overline{Nu}_D = \frac{\overline{h_{tot}}D}{k} = 1.32\ \frac{Pr^{7/3}\ L_f^{1/2}\ D^{1/2} Re_D^{1/2}\ W_f D^{1/2}}{A_f + \pi S D}$
(14h)	Sparrow [26]	$\overline{Nu}_m = \frac{\overline{h_{tot}}D}{k} = 0.0529\ Re_m^{0.704}$ where $Re_m = \frac{\rho u_m D}{\mu}$

Table 3. Numerically- and correlation-predicted time- and area-averaged heat transfer coefficients for $L_f = 100$ mm. Predictions based on Eq. (14*b*) are shown parenthetically.

		$V = 0.5$ m/s			$V = 1.5$ m/s		
		$\overline{h_f}$ W/m^2 K	$\overline{h_{cyl}}$ W/m^2 K	$\overline{h_{tot}}$ W/m^2 K	$\overline{h_f}$ W/m^2 K	$\overline{h_{cyl}}$ W/m^2 K	$\overline{h_{tot}}$ W/m^2 K
Numerical	DNS	12.9	28.9	16.0	23.2	50.9	28.7
	SST	11.3	29.4	14.9	19.1	52.5	25.7
	κ-ε	4.8	13.4	6.50	9.80	30.0	13.8
Correlation-based	Flat Plate Laminar + Cylinder	8.72	31.0 (29.5)	9.20 (9.17)	15.1	53.2 (52.9)	15.9 (15.9)
	Flat plate turbulent + cylinder	5.31	31.0 (29.5)	5.87 (5.84)	12.8	53.2 (52.9)	13.7 (13.7)
	Flat plate transition + cylinder	8.43	31.0 (29.5)	8.92 (8.89)	16.1	53.2 (52.9)	16.9 (16.9)
	Romero-Méndez			8.01	–	–	14.1
	Romero-Méndez + S	–	–	8.35	–	–	14.5
	Sparrow	–	–	10.8	–	–	23.2

each other, but significantly underpredict the heat transfer enhancement due to horseshoe vortex formation and vortex shedding as captured by the DNS and SST simulations. In contrast, the correlation-based predictions significantly exceed the k-ε values. Specifically, the laminar and transitional flat plate correlations perform the best, and deviate from the DNS predictions by a maximum of 18%.

Predicted time- and area-averaged heat transfer coefficients from the two correlations provided by Romero-Méndez [33] correspond to a weighted average of both the fin and HP surface areas, $\overline{h_{tot}} = (\overline{h_f}A_f + \overline{h_{cyl}}A_{cyl})/(A_f + A_{cyl})$, and are in poor agreement with the benchmark DNS and SST values. Predictions generated with Eq. (14*h*) show especially good agreement with the DNS and SST predictions for the $V = 1.5$ m/s case.

4.6. Effect of fin array geometry

The results shown in Figures 7 and 8 suggest that the interplay between flow over the cylinder and fin surfaces might be exploited to modify the time- and area-averaged heat transfer coefficients. The following analyses consider the effects of modifications to the finned cylinder geometry using the validated SST turbulence model.

4.6.1. Effect of fin size

SST predictions of the local heat transfer coefficient distribution on a smaller square fin ($L_f = 25$ mm) are compared to the distributions on the corresponding region of the $L_f = 100$ mm fin in Figure 9. The high local convection coefficients at the leading edge of the smaller fin are evident, and the effect of the cylinder on the local values of h_f is qualitatively similar for both fin sizes. As expected from Figure 9, the SST-predicted values of $\overline{h_f}$ are larger for the small fins ($\overline{h_f} = 20.2$ and 34.5 W/m^2 K) than those associated with the large fins ($\overline{h_f} = 11.3$ and 19.1 W/m^2 K) for the low- and high-velocity cases, respectively. The values of $\overline{h_{cyl}}$ are similar for the small fin geometry ($\overline{h_{cyl}} = 29.9$ and 51.3 W/m^2 K) and for the large fin configuration ($\overline{h_{cyl}} = 29.4$ and 52.5 W/m^2 K) for the $V = 0.5$ and 1.5 m/s cases, respectively. Ultimately, the values of $\overline{h_{tot}}$ are larger for the small fin geometry ($\overline{h_{tot}} = 27.7$ and 47.6 W/m^2 K) than for that of the larger fin case ($\overline{h_{tot}} = 14.9$ and 25.7 W/m^2 K) for the low- and high-air-velocity cases, respectively.

In general, the correlations again performed poorly, with a combination of Eqs. (14*b*) and (14*c*) providing the best value of $\overline{h_{tot}}$ (20.5 W/m^2 K) for the low-velocity case, which is within 25% of the SST value (27.7 W/m^2 K). The same combination performed best for the high-velocity case, yielding $\overline{h_{tot}} = 36.1$ W/m^2 K, again within 25% of the SST value (47.6 W/m^2 K). The Romero-Méndez, Romero-Méndez + S, and Sparrow correlations predicted values of $\overline{h_{tot}}$ to be only 11.3, 11.5, and 11.2 W/m^2 K, respectively, for the low-velocity case. The corresponding values for the high-velocity case were only 19.7, 19.9, and 23.5 W/m^2 K.

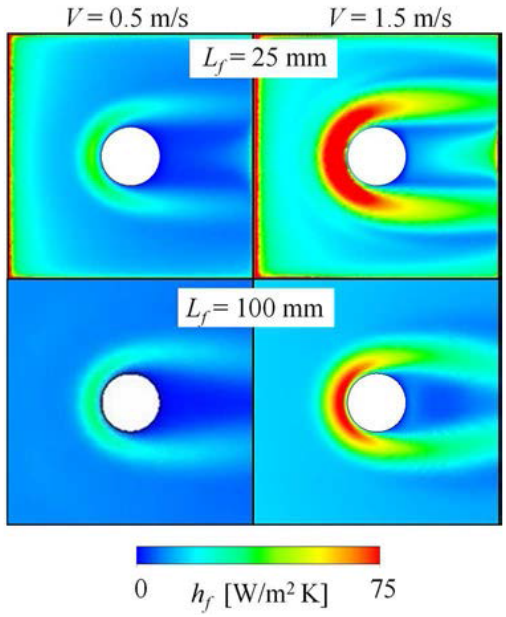

Figure 9. SST-predicted local heat transfer coefficient on the upper surface of the middle fin for $L_f = 25$ mm (top) and an enlarged view of the $L_f = 100$ mm fin (bottom). Convection coefficients range from $h_f = 0$ to 75 W/m^2 K.

4.6.2. Effect of the cylinder location

From Figure 8, it might be anticipated that shifting the cylinder upstream or downstream could influence the horseshoe and trailing cylinder vortices and, in turn, the values of $\overline{h_f}$ and $\overline{h_{tot}}$. Similarly, shifting the cylinder location would expose it to different air temperatures and velocities, potentially modifying the value of $\overline{h_{cyl}}$. A series of SST simulations were performed with $L_f = 100$ mm fins, with the cylinder placed at $s/L_f = 0.04$, 0.25, 0.75, and 0.96. SST-predicted heat transfer coefficients were all found to be within $\overline{h_f} = 11.4 \pm 0.1$ W/m^2 K and 19.2 ± 0.3 W/m^2 K for the low- and high-velocity cases, respectively, suggesting no meaningful influence of the cylinder placement on the overall fin heat transfer rate since the variations are all within the grid dependence, which is estimated to be $\pm 0.35\%$ for area-averaged quantities [19].

In contrast, the cylinder heat transfer coefficients were calculated to be $\overline{h_{cyl}} = 28.9 \pm 0.9$ W/m^2 K and 52.8 ± 0.3 W/m^2 K for the low- and high-velocity cases, respectively. The variation for the low-velocity case is modest (but not attributable to grid dependence), with a reduction in $\overline{h_{cyl}}$ observed as the cylinder is repositioned downstream. The influence of cylinder placement is less pronounced for the high-velocity case due to the thinner plate thermal and hydrodynamic boundary layers. Specifically, the values of $\overline{h_{tot}}$ were predicted to be 11.8 ± 0.1 W/m^2 K and 19.9 ± 0.2 W/m^2 K for the low- and high-velocity cases, respectively, with higher coefficients associated with the cylinders placed upstream. The modest influence of the cylinder placement on the overall heat transfer coefficients is consistent with experimental and computational observations for similar geometries considered previously [29, 32].

5. Conclusions

A DNS, two SST, and three k-ε models have been used to predict mixed convection associated with air in forced cross flow over an isothermal, finned cylinder. The DNS predictions reveal complex, three-dimensional time variations in the flow field. Strong coupling is noted between flow over the fins and that past the cylinder. Specifically, horseshoe and shedding vortices induced by the cylinder modify

local heat fluxes on the fin surfaces, whereas the fins reduce local air velocities and convection heat fluxes on the exposed surface of the cylinder. Complex buoyancy effects are noted for the low-velocity case considered here.

Time- and area-averaged convection heat transfer coefficients predicted by the steady-state SST models are in good agreement with benchmark DNS predictions, but the k-ε models do not accurately predict local or overall heat fluxes. Correlation-based predictions of fin, cylinder, and overall time-averaged heat transfer coefficients are, in general, in poor agreement with those of the benchmark DNS and SST models. Therefore, of the various options available to predict convection heat transfer coefficients over the types of finned tubes considered here, the steady-state SST model is recommended. Furthermore, use of the k-ε models is discouraged and caution must be exercised if correlations are employed to predict convection heat transfer rates associated with geometries and operating conditions similar to those considered here.

To demonstrate its utility, the DNS-validated SST model was used to quantify the impact of various modifications to the finned tube geometry on the overall convection heat transfer rates and coefficients. The overall heat transfer coefficients show little sensitivity to the placement of the cylinder relative to the fins, and exhibit expected increases in value as the fin size is reduced. Using a robust model such as SST, future studies could be conducted to simulate complex forced convection in, for example, arrays of finned HPs where wakes are expected to be important. Arrays including thousands of finned HPs would be required in many applications [17, 18].

Funding

This material is based upon work supported by the National Science Foundation under Grant No. 1435131.

References

[1] D. C. Wilcox, *Turbulence Modeling for CFD*, 3rd ed., DCW Industries, La Canada, CA, 2010.
[2] M. A. R. Sharif and K. K. Mothe, Evaluation of Turbulence Models in the Prediction of Heat Transfer Due to Slot Jet Impingement on Plane and Concave Surfaces, *Numer. Heat Transfer, Part B*, vol. 55, no. 4, pp. 273–294, 2009.
[3] F. R. Menter, Two-Equation Eddy-Viscosity Turbulence Models for Engineering Applications, *AIAA J.*, vol. 32, no. 8, pp. 1598–1605, 1994.
[4] F. R. Menter, R. B. Langtry, S. R. Likki, Y. B. Suzen, P. G. Huang, and S. Völker, A Correlation-Based Transition Model Using Local Variables Part 1 – Model Formulation, ASME GT2004–53452, *Proc. ASME Turbo Expo, Power for Land Sea and Air*, June 14–17, Vienna, Austria, 2004.
[5] F. R. Menter, R. B. Langtry, and S. Volker, Transition Modelling for General Purpose CFD Codes, *Flow Turbul. Combust.*, vol. 77, pp. 277–303, 2006.
[6] F. Menter, T. Esch, and S. Kubacki, Transition Modelling based on Local Variables, Fifth *Int. Symp. Eng. Turbul. Model Meas.*, Mallorca, Spain, 2002.
[7] W. P. Jones and B. E. Launder, The Prediction of Laminarization with a Two-Equation Model of Turbulence, *Int. J. Heat Mass Transfer*, vol. 15, pp. 301–314, 1972.
[8] V. Yakhot, S. A. Orszag, S. Thangam, T. B. Gatski, and C. G. Speziale, Development of Turbulence Models for Shear Flows by a Double Expansion Technique, *Phys. Fluids A*, vol. 4, no. 7, pp. 1510–1520, 1992.
[9] S. Wallin and A. V. Johansson, An Explicit Algebraic Reynolds Stress Model for Incompressible and Compressible Turbulent Flows, *J. Fluid Mech.*, vol. 403, pp. 89–132, 2000.
[10] H. Nemati and M. Moghimi, Numerical Study of Flow over Annular-Finned Tube Heat Exchangers by Different Turbulent Models, *CFD Lett*, vol. 6, no. 3, pp. 101–112, 2014.
[11] Y. Mao and Y. Zhang, Evaluation of Turbulent Models for Natural Convection of Compressible Air in a Tall Cavity, *Numer. Heat Transfer, Part B Fundam.*, vol. 64, no. 5, pp. 351–364, 2013.
[12] L. A. El-Gabry, and D. A. Kaminski, Numerical Investigation of Jet Impingement with Cross Flow - Comparison of Yang-Shih, and Standard k–ε Turbulence Models, *Numer. Heat Transfer Part A Appl.*, vol. 47, no. 5, pp. 441–469, 2005.
[13] A. Keshmiri, J. Uribe, and N. Shokri, Benchmarking of Three Different CFD Codes in Simulating Natural, Forced, and Mixed Convection Flows, *Numer. Heat Transfer Part A Appl.*, vol. 67, no. 12, pp. 1324–1351, 2015.

[14] A. A. Igci and M. E. Arici, A Comparative Study of Four Low-Reynolds-Number k-ε Turbulence Models for Periodic Fully Developed Duct Flow, and Heat Transfer, *Numer. Heat Transfer, Part B Fundam.*, vol. 69, no. 3, pp. 234–248, 2016.
[15] L. Badr, G. Boardman, and J. Bigger, Review of Water use in U.S. Thermoelectric Power Plants, *J. Energy Eng.*, vol. 138, no. 4, pp. 246–257, 2012.
[16] H. Koch and S. Vögele, Dynamic Modelling of Water Demand, Water Availability and Adaptation Strategies for Power Plants to Global Change, *Ecol. Econ.*, vol. 68, no. 7, pp. 2031–2039, 2009.
[17] H. Shabgard, M. J. Allen, N. Sharifi, S. P. Benn, A. Faghri, and T. L. Bergman, Heat Pipe Heat Exchangers, and Heat Sinks: Opportunities, Challenges, Applications, Analysis, and State of the Art, *Int. J. Heat Mass Transfer*, vol. 89, pp. 138–158, 2015.
[18] S. P. Benn, L. M. Poplaski, A. Faghri, and T. L. Bergman, Analysis of Thermosyphon/Heat Pipe Integration for Feasibility of Dry Cooling for Thermoelectric Power Generation, *Appl. Therm. Eng.*, vol. 104, pp. 358–374, 2016.
[19] J. R. Stark, N. Sharifi, T. L. Bergman, and A. Faghri, An Experimentally Verified Numerical Model of Finned Heat Pipes in Cross Flow, *Int. J. Heat Mass Transfer*, vol. 97, pp. 45–55, 2016.
[20] L. M. Poplaski, A. Faghri, and T. L. Bergman, Analysis of Internal and External Thermal Resistances of Heat Pipes including Fins using a Three-Dimensional Numerical Simulation, *Int. J. Heat Mass Transfer*, vol. 102, pp. 455–469, 2016.
[21] N. Sharifi, J. R. Stark, T. L. Bergman, and A. Faghri, The Influence of Thermal Contact Resistance on the Relative Performance of Heat Pipe-Fin Array Systems, *Appl. Therm. Eng.*, vol. 105, pp. 46–55, 2016.
[22] A. A. El-Nasr and S. M. El-Haggar, Effective Thermal Conductivity of Heat Pipes, *Heat Mass Transfer*, vol. 32, no. 1–2, pp. 97–101, 1996.
[23] A. Faghri *Heat Pipe Science and Technology*, Taylor & Francis, Washington, DC, 1995.
[24] S. P. Kearney and A. M. Jacobi *Local and Average Heat Transfer and Pressure Drop Characteristics of Annularly Finned Tube Heat Exchangers, ACRC TR-69*, University of Illinois, Urbana, IL, 1998.
[25] X. Hu and A. M. Jacobi, Local Heat Transfer Behavior, and its Impact on a Single-Row, Annularly Finned Tube Heat Exchanger, *ASME J. Heat Transfer*, vol. 115, no. 1, pp. 66–74, 1993.
[26] E. M. Sparrow and F. Samie, Heat Transfer and Pressure Drop results for One- and Two-Row Arrays of Finned Tubes, *Int. J. Heat Mass Transfer*, vol. 28, no. 12, pp. 2247–2259, 1985.
[27] F. E. M. Saboya and E. M. Sparrow, Local and Average Transfer Coefficients for One-Row Plate Fin and Tube Heat Exchanger Configurations, *ASME J. Heat Transfer*, vol. 96, pp. 265–272, 1974.
[28] S. M. Saboya and F. E. M. Saboya, Experiments on Elliptic Sections in One and Two Row Arrangements of Plate Fin and Tube Heat Exchangers, *Exp. Therm. Fluid Sci.*, vol. 24, pp. 67–75, 2001.
[29] F. E. M. Saboya and E. M. Sparrow, Effect of Tube Relocation on the Transfer Capabilities of a Fin and Tube Heat Exchanger, *ASME J. Heat Transfer*, vol. 96, pp. 421–422, 1974.
[30] C. J. Baker, The Laminar Horseshoe Vortex, *J. Fluid Mech.*, vol. 95, pp. 347–367, 1979.
[31] C. J. Baker, The Oscillation of Horseshoe Vortex Systems, *J. Fluids Eng.*, vol. 113, pp. 489–495, 1991.
[32] J. Yin, Z. He, F. Chen, and J. Ma, Effect of Tube Location Change on Heat Transfer Characteristics of Plain Plate Fin-and-Tube Heat Exchangers, *ASME J. Therm. Sci. Eng. Appl.*, vol. 6, no. 2, 021005, 2013.
[33] R. Romero-Mendez, M. Sen, K. T. Yang, and R. Mc Clain, Effect of Fin Spacing on Convection in Plate Fin and Tube Heat Exchanger, *Int. J. Heat Mass Transfer*, vol. 43, no. 1, pp. 39–51, 2000.
[34] R. Romero-Méndez, Study of External Heat Transfer Mechanisms in Single-Row Fin and Tube Heat Exchangers, Ph.D. dissertation, Department of Aerospace and Mechanical Engineering, University of Notre Dame, Notre Dame, IN 46556, USA, 1998
[35] M. J. Allen, T. L. Bergman, A. Faghri, and N. Sharifi, Robust Heat Transfer Enhancement During Melting and Solidification of a Phase Change Material Using a Combined Heat Pipe-Metal Foam or Foil Configuration, *ASME J. Heat Transfer*, vol. 137, no. 10, pp. 102301-1-102301–12, 2015
[36] N. Sharifi, T. L. Bergman, M. J. Allen, and A. Faghri, Melting, and Solidification Enhancement Using a Combined Heat Pipe, Foil Approach, *Int. J. Heat Mass Transfer*, vol. 78, pp. 930–941, 2014.
[37] E. M. Sparrow and J. P. Abraham, A new Buoyancy Model Replacing the Standard Pseudo-Density Difference for Internal Natural Convection in Gases, *Int. J. Heat Mass Transfer*, vol. 46, no. 19, pp. 3583–3591, 2003.
[38] J. P. Abraham, E. M. Sparrow, and J. C. K. Tong, Heat Transfer in all Pipe Flow Regimes - Laminar, Transitional/ Intermittent, and Turbulent, *Int. J. Heat Mass Transfer*, vol. 52, pp. 557–563, 2009.
[39] J. P. Abraham, E. M. Sparrow, and W. J. Minkowycz, Internal-Flow Nusselt Numbers for the Low-Reynolds-Number end of the Laminar-to-Turbulent Transition Regime, *Int. J. Heat Mass Transfer*, vol. 54, pp. 584–588, 2011.
[40] J. P. Abraham, E. M. Sparrow, J. C. K. Tong, and D. W. Bettenhausen, Internal Flows which Transist from Turbulent through Intermittent to Laminar, *Int. J. Therm. Sci.*, vol. 49, pp. 256–263, 2010.
[41] J. C. K. Tong, J. P. Abraham, J. M. Y. Tse, and E. M. Sparrow, Impact of Chamfer Contours to Reduce Column Drag, *Eng. Comput. Mech.*, vol. 168, pp. 79–88, 2015.
[42] J. C. K. Tong, J. P. Abraham, J. M. Y. Tse, W. J. Minkowycz, and E. M. Sparrow, New Archive of Heat Transfer Coefficients from Square and Chamfered Cylinders in Crossflow, *Int. J. Therm. Sci.*, vol. 105, pp. 218–223, 2016.

[43] W. J. Minkowycz, J. P. Abraham, and E. M. Sparrow, Numerical Simulation of Laminar Breakdown and Subsequent Intermittent and Turbulent Flow in Parallel-Plate Channels: Effects of Inlet Velocity Profile and Turbulence Intensity, *Int. J. Heat Mass Transfer*, vol. 52, no. 17–18, pp. 4040–4046, 2009.
[44] T. L. Bergman, A. S. Lavine, F. P. Incropera, and D. P. Dewitt *Fundamentals of Heat and Mass Transfer*, 7th ed., Wiley, Hoboken, 2011.
[45] E. M. Sparrow, J. P. Abraham, and J. C. K. Tong, Archival Correlations for Average Heat Transfer Coefficients for Non-Circular and Circular Cylinders and for Spheres in Crossflow, *Int. J. Heat Mass Transfer*, vol. 47, no. 24, pp. 5285–5296, 2004.

Appendix A. Quasi-steady state

DNS-predicted, instantaneous, area-averaged heat transfer coefficients for the benchmark problem are reported in Figure A1 over the time span $0 \leq t \leq 1.5$ s. A quasi-steady state is approached at $t \approx 0.25$ s for both the $V = 0.5$ and 1.5 m/s cases. Quasi-steady results are reported only for times greater than 0.5 s.

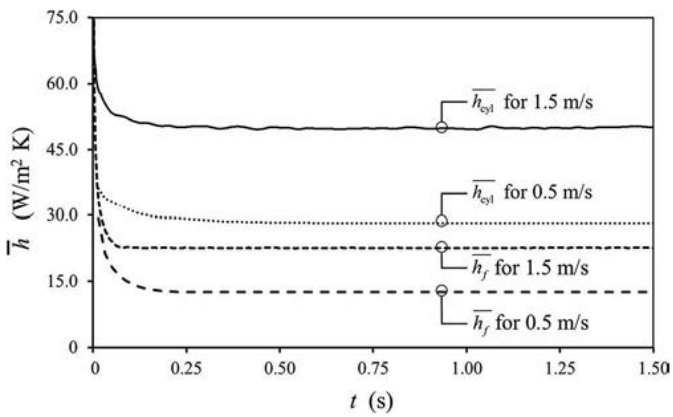

Figure A1. DNS predictions of $\overline{h_f}$ and $\overline{h_{cyl}}$ for the $V = 0.5$ m/s and 1.5 m/s cases with $L_f = 100$ mm *versus* time.

Paper P2

Title:

An experimentally verified numerical model of finned heat pipes in crossflow

Authors:

John R. Stark

Nourouddin Sharifi

Theodore L. Bergman

Amir Faghri

Journal:

International Journal of Heat and Mass Transfer

International Journal of Heat and Mass Transfer 97 (2016) 45–55

Contents lists available at ScienceDirect

International Journal of Heat and Mass Transfer

journal homepage: www.elsevier.com/locate/ijhmt

An experimentally verified numerical model of finned heat pipes in crossflow

John R. Stark [a,*], Nourouddin Sharifi [a], Theodore L. Bergman [a], Amir Faghri [b]

[a] Department of Mechanical Engineering, The University of Kansas, 1530 W. 15th Street 3138, Lawrence, KS 66045, USA
[b] Department of Mechanical Engineering, The University of Connecticut, 191 Auditorium Road, Storrs, CT 06269-3139, USA

ARTICLE INFO

Article history:
Received 3 December 2015
Received in revised form 20 January 2016
Accepted 21 January 2016

Keywords:
Heat pipe
Numerical modeling
Fins
Fin arrays

ABSTRACT

A numerical model is developed to predict heat rates associated with a heat pipe whose finned condenser section is subjected to external forced convection. Multiphase, conjugate heat transfer inside the heat pipe is predicted using a 2-dimensional model, while fluid flow and convection heat transfer within the fin array is described with a coupled 3-dimensional shear stress transport (SST) model. Predictions of local temperatures and overall heat rates are verified experimentally. The SST model is also validated with 3-dimensional direct simulations that show highly time-dependent, 3-dimensional phenomena in the fin array. A previously unreported phenomenon, localized depression of temperatures in the heat pipe wall, is presented and parametric simulations reveal the sensitivity of system performance to the number of fins and the air velocity in the fin array.

Published by Elsevier Ltd.

1. Introduction

As is well known, heat pipes (HPs) can pose thermal resistances that are orders of magnitude smaller than those associated with conduction within high thermal conductivity materials of similar dimension [1–3]. Recent reviews [4–13] have thoroughly described both HP applications and their principles of operation. Due to the remarkably small thermal resistances posed by HPs, the heat transfer capability of HP systems is often limited by, for example, convective resistances associated with external fluid flow about the HP condenser and/or evaporation sections. Hence, external fins or fin arrays are often employed to reduce the overall thermal resistances of such systems [14–22].

Numerical modeling has been used to analyze heat transfer processes both (*i*) within HPs [22–32] and (*ii*) external to HPs such as those equipped with exterior fin arrays [19–22]. Both approaches have employed simplifying assumptions. For example, interior modeling often employs accurate descriptions of the evaporation, condensation, and heat transfer processes within the HP itself, but is hampered by the specification of idealized external thermal boundary conditions at the HP evaporator and condensation sections. Alternatively, recently-reported simulations provide an accurate prediction of the external convective heat transfer processes, but typically treat heat transfer within the HP in a simplified manner [19–21]. Recent investigations describe advances that have been made by developing overall HP system models that include detailed descriptions of both internal and external heat transfer processes. However, these models have been limited to 2D systems [22,26–28].

For a finned HP subjected to 3D external forced convection, a unified and full 3D approach to solve both the internal and external heat transfer processes concurrently would be computationally expensive. Moreover, detailed 3D predictions of phenomena within the HP may not be needed in some cases due to the multiphase (evaporation and condensation) processes that are affiliated with relatively small thermal resistances. To the authors' knowledge, full 3D predictions of heat transfer within both the interior and exterior to a HP have not been reported in the literature.

The objective of this study is to develop and demonstrate a novel computational methodology to couple 2D internal and 3D external simulations for a common configuration; a vertical HP with isothermal conditions at its lower evaporator section, and unsteady 3D convective conditions external to its upper finned condenser section. The model is computationally less expensive than a full 3D simulation and, as will become evident, can satisfactorily replicate measurements of various heat transfer quantities.

2. Numerical model

As shown in Fig. 1a, an externally-finned HP of circular cross section and length $L_{hp} = L_e + L_a + L_c$ is oriented vertically, with an

* Corresponding author. Tel.: +1 515 291 4101.
E-mail address: John.Robert.Stark@gmail.com (J.R. Stark).

http://dx.doi.org/10.1016/j.ijheatmasstransfer.2016.01.051
0017-9310/Published by Elsevier Ltd.

Nomenclature

A	area (m^2)
D	diameter (m)
F_1, F_2	SST blending functions
g	gravitational acceleration (m/s^2)
Gr	Grashof number
h	convection coefficient (W/m^2 K)
H	height (m)
k	thermal conductivity (W/m K)
L	length (m)
m	fin constant
N	number of fins
p	pressure (Pa)
P_κ	SST production term (kg/m s^3)
q''	heat flux (W/m^2)
Q	heat rate (W)
R	thermal resistance (K/W)
Re	Reynolds number
r, z, θ	coordinate directions
S	fin pitch (m), turbulent strain rate (s^{-1})
St	Strouhal number
T	temperature (°C)
t	time (s), thickness (m)
u	velocity (m/s)
V	average air velocity (m/s)
W	width (m)
x, y, z	coordinate directions

Greek symbols

α	thermal diffusivity (m^2/s)
$\alpha_1, \beta_1, \beta_2$	SST model constants
β	thermal expansion coefficient (K^{-1})
θ	reduced temperature $T - T_\infty$ (°C), angular direction
κ	turbulent kinetic energy (m^2/s^2)
μ	dynamic viscosity (kg/m s)
ν	kinematic viscosity (m^2/s)
ρ	density (kg/m^3)
$\sigma_\kappa, \sigma_\omega, \sigma_{\omega 2}$	SST model constants
ω	specific rate of turbulence dissipation (s^{-1})

Superscripts

–	average

Subscripts

0	reference
2, 2c	fin radius, corrected fin radius
2D, 3D	2- or 3-dimensional
a	adiabatic, air
ag	aerogel
Al	aluminum
ar	Airloy
c	condenser
ch	channel
conv	convection
d	downstream
e	evaporator
eff	effective
exp	experimental
f	fin
hp	heat pipe
hs	heat spreader
i	case index
min, max	minimum, maximum
SST	shear stress transport
tot	total
tp	thermal paste
ts	top fin surface
turb	turbulent
u	upstream
v	heat pipe vapor
w	heat pipe wall
wi	heat pipe wick
∞	inlet

evaporator section of length L_e positioned beneath the adiabatic and air-cooled condenser sections of lengths L_a and L_c, respectively. The condenser section is finned, with air flowing through the fin array. The finned HP is shown installed in a flow channel in a manner consistent with an experimental setup described later.

A novel overall model, to be presented, consists of two coupled sub-models. The first describes axisymmetric, multiphase heat transfer and fluid flow within the HP. The second describes conduction processes within the HP and the 3D single phase convection external to the HP condenser section. The two sub-models are coupled as will be described shortly. Predictions of the overall model are verified with experimental data, and the model is used to parametrically investigate the HP system performance and reveal previously-unobserved thermal phenomena within the HP.

2.1. HP sub-model

A HP sub-model is used to solve the 2D, axisymmetric equations that govern the transient evaporation and condensation processes within an internally-wicked HP, as well as the fluid flow and heat transfer (vapor phase advection, and conduction) within the HP. Details of the model, including the descriptive equations, are available in Sharifi et al. [26]. Due to their length, they will not be repeated here.

The computational domain for the HP sub-model (shown in detail in Fig. 1 of [26] and in Fig. 1a) is comprised of the HP wall, wick, and vapor regions. The region ($0 \leqslant z \leqslant L_{hp}$; $0 < r \leqslant r_v$) contains the vapor phase of the HP working fluid. Heat transfer in this region is governed by conservation of mass, r- and z-momentum, and energy, as laid out in Eqs. (1)–(8) of [26]. The wick ($r_v < r \leqslant r_w$) is a porous metal that is assumed to be saturated with the liquid

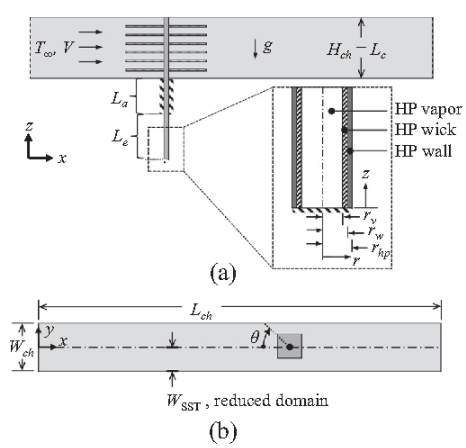

Fig. 1. Schematic of the physical system. (a) Test section, (b) flow channel. Two separate coordinate systems are shown.

phase of the HP working fluid. Following the approach of Cao and Faghri [24], the flow of liquid within the wick is neglected, and thermal equilibrium between the liquid and the wick material is assumed. The 2D energy equation applied to the wick requires specification of an effective thermal conductivity, as described in Eqs. (9)–(11) of [26] while conduction in the solid HP wall ($r_w < r \leqslant r_{hp}$) is described by Eq. (12) of the same reference. Radiation is neglected since all of the solid materials are opaque, temperatures are relatively low, and thermal resistances due to convection are relatively small. Potential thermal contact resistances are also neglected.

The top and bottom end cap surfaces of the HP ($z = 0$, L_{hp}) are adiabatic. The exterior surface of the evaporator section is of uniform and constant temperature T_e, while the exterior of the HP condenser section at $L_e + L_a < z \leqslant L_{hp}$, $r = r_{hp}$ experiences two distinct convection-related heat transfer processes; the first is direct convective cooling along the un-finned external surface of the HP condenser section

$$-k_w \frac{\partial T}{\partial r}\bigg|_{z,r=r_{hp}} = \overline{h_w}\left[T(z, r = r_{hp}) - T_\infty\right] = \overline{h_w}\theta(z, r = r_{hp}) \tag{1a}$$

where $\overline{h_w}$ is the time- and area-averaged convection heat transfer coefficient for the exposed (non-finned) portions of the HP condenser section that is determined as will be discussed in Section 2.3. The second process involves radial conduction to the roots of each of the N annular fins of thickness t_f and outer radius r_2. Fin analysis [33] is used to generate an effective heat transfer coefficient, which is applied to the fin roots (at $r = r_{hp}$) so that

$$\begin{aligned} -k_w \frac{\partial T}{\partial r}\bigg|_{z,r=r_{hp}} &= \overline{h_{\text{eff}}}\theta(z, r = r_{hp}) \\ &= \overline{h_f}\left[\frac{2}{t_f m} \times \frac{K_1(mr_{hp})I_1(mr_{2c}) - I_1(mr_{hp})K_1(mr_{2c})}{K_0(mr_{hp})I_1(mr_{2c}) + I_0(mr_{hp})K_1(mr_{2c})}\right]\theta(z, r = r_{hp}) \end{aligned} \tag{1b}$$

where $r_{2c} = r_2 + t_f/2$ is used to account for convection from all exposed fin surfaces, and $m = \sqrt{2\overline{h_f}/k_f t_f}$. The parameter $\overline{h_f}$ is the time- and area-averaged convection heat transfer coefficient associated with the top, bottom and tips of the fins (determined as discussed in Section 2.3), while I_0 (K_0) and I_1 (K_1) are modified, zero-order and first-order Bessel functions of the first (second) kind. Eqs. (1)–(12) of [26], specification of an initial, uniform temperature of 27 °C and zero velocities everywhere, along with the preceding boundary conditions complete the 2D HP model description. Note that, although the problem is steady in the mean, initial conditions are required as the HP code was originally developed to simulate transient conditions in other applications [26]. The governing equations are solved using a finite volume approach [26] with convergence at each time step assumed when residual mean square values $<10^{-6}$ exist across all dependent variables. The grid dependence of the solutions were checked, with a grid of 190×50 ($z \times r$) yielding heat rates within 0.8% of those produced with a grid of 240×70 ($z \times r$). Typical computation times ranged from 20 to 40 min.

2.2. Air side sub-model

The heat transfer coefficients $\overline{h_w}$ and $\overline{h_f}$ of Eq. (1) are associated with convection resistances that affect (and can dominate) the overall thermal resistance of this HP configuration, and their values are generally unknown. In this study, they are determined by simulating the complex 3D (air) flow through the fin array. Specifically, the convection coefficients are determined using the SST turbulence model, to be described shortly.

As previously discussed, the 3D, multiphase heat transfer within the HP is not modeled because of the expense of the computations. Instead, the vapor region of the HP is replaced in the 3D model by an artificial, stationary, high thermal conductivity medium that mimics the low thermal resistance associated with the evaporation, condensation, and advection processes in the HP vapor region ($0 < r \leqslant r_v$, $0 \leqslant z \leqslant L_{hp}$). The effective thermal conductivity $k_{\text{eff},v}$ of the artificial medium is determined through an iterative process, as described in the next sub-section.

Various approaches may be taken to quantify the 3D air side convection processes. Here, a 3D, transient, fully-elliptic direct numerical simulation (DNS) is first employed to accurately predict the air side convection processes. The predictions of the direct simulation are then used to validate a less expensive steady-state, 3D model that utilizes the shear stress transport (SST) approach. Buoyancy forces are accounted for through a Boussinesq approximation [34] in each model, and because the objective of the comparison is to test the ability of the SST model to predict time-averaged flow in this complex geometry, isothermal HP and fins are temporarily assumed.

Due to the expense of the direct simulation only a limited number of direct predictions are used to validate the 3D, steady-state model based on Menter's SST turbulence approach [35]. Predictions of both models will be compared with measurements of key heat transfer parameters. To further test the assumption of axisymmetry that is inherent in the 2D HP model, square fins of surface area equal to that of the annular fins of the HP model are considered in the direct and SST models as well as in the companion experiments.

2.2.1. Direct simulation

The computational domain includes (*i*) the isothermal HP and finned condenser section (Fig. 1a) and (*ii*) the entire air region within the flow channel of Fig. 1b. To capture the dynamics of the air side convection processes, symmetry about the vertical channel mid-plane is *not* assumed. Conservation of thermal energy is, therefore,

$$\frac{\partial T}{\partial t} + u_x\frac{\partial T}{\partial x} + u_y\frac{\partial T}{\partial y} + u_z\frac{\partial T}{\partial z} = \alpha\left(\frac{\partial^2 T}{\partial x^2} + \frac{\partial^2 T}{\partial y^2} + \frac{\partial^2 T}{\partial z^2}\right) \tag{2}$$

The air is assumed to be incompressible with constant properties, with a velocity distribution that is governed by conservation of mass (Eq. (3)) and momentum (Eqs. (4a)–(4c)). The reference state for all properties as well as the Boussinesq approximation [34] is taken to be a temperature of $T_0 = 25$ °C and pressure of 1 atm.

$$\frac{\partial u_x}{\partial x} + \frac{\partial u_y}{\partial y} + \frac{\partial u_z}{\partial z} = 0 \tag{3}$$

$$\frac{\partial u_x}{\partial t} + u_x\frac{\partial u_x}{\partial x} + u_y\frac{\partial u_x}{\partial y} + u_z\frac{\partial u_x}{\partial z} = -\frac{1}{\rho}\frac{\partial p}{\partial x} + \nu\left(\frac{\partial^2 u_x}{\partial x^2} + \frac{\partial^2 u_x}{\partial y^2} + \frac{\partial^2 u_x}{\partial z^2}\right) \tag{4a}$$

$$\frac{\partial u_y}{\partial t} + u_x\frac{\partial u_y}{\partial x} + u_y\frac{\partial u_y}{\partial y} + u_z\frac{\partial u_y}{\partial z} = -\frac{1}{\rho}\frac{\partial p}{\partial y} + \nu\left(\frac{\partial^2 u_y}{\partial x^2} + \frac{\partial^2 u_y}{\partial y^2} + \frac{\partial^2 u_y}{\partial z^2}\right) \tag{4b}$$

$$\frac{\partial u_z}{\partial t} + u_x\frac{\partial u_z}{\partial x} + u_y\frac{\partial u_z}{\partial y} + u_z\frac{\partial u_z}{\partial z} = -\frac{1}{\rho}\frac{\partial p}{\partial z} + \nu\left(\frac{\partial^2 u_z}{\partial x^2} + \frac{\partial^2 u_z}{\partial y^2} + \frac{\partial^2 u_z}{\partial z^2}\right) + [1 - \beta(T - T_o)]g \tag{4c}$$

Initial conditions used in the direct simulation are uniform temperatures of T_∞ and zero velocities everywhere. The velocity and temperature distributions at the channel inlet ($x = 0$, Fig. 1(b)) are assumed to be uniform. The reference pressure at $x = L_{ch}$ is set to

zero, and the second derivative of temperatures are also zero at the channel exit. No-slip conditions are applied at all solid surfaces and the channel walls are assumed to be adiabatic. The governing equations for the direct simulation are solved using a computational mesh of 36.1×10^6 elements and a time step of 0.001 s over an overall simulated duration of 10 s. Grid- and time-step independence is discussed in the Appendix A. The convergence criterion applied to each time step is for the residual mean squares of all variables to be less than 10^{-5}. Computation times of several weeks were typically required for each case, requiring 96 GB of RAM on a Dell Precision T7600.

2.2.2. SST turbulence model

Predictions generated from the direct simulation (along with experimental measurements) are used to validate the computationally-efficient, steady-state SST model applied to a reduced air side domain (channel half-width) shown in Fig. 1b. The SST model has been shown [36–40] to yield accurate results when employed in conjugate heat transfer applications where flow separation is likely to occur. This model is governed by conservation of energy

$$u_x\frac{\partial T_i}{\partial x}+u_y\frac{\partial T_i}{\partial y}+u_z\frac{\partial T_i}{\partial z}=\alpha_i\left(\frac{\partial^2 T_i}{\partial x^2}+\frac{\partial^2 T_i}{\partial y^2}+\frac{\partial^2 T_i}{\partial z^2}\right)\quad i=f,\ w,\ wi,\ v,\ \text{and}\ a \tag{5}$$

while fluid motion in the air is governed by conservation of mass (Eq. (3)) and conservation of x, y, and z momentum (Eqs. (6a)–(6c)). The air is again assumed to be incompressible with constant properties. The reference state for properties and the Boussinesq approximation is the same as for the direct simulation.

$$u_x\frac{\partial u_x}{\partial x}+u_y\frac{\partial u_x}{\partial y}+u_z\frac{\partial u_x}{\partial z}=-\frac{1}{\rho}\frac{\partial p}{\partial x}+(\nu+\nu_{\text{turb}})\left(\frac{\partial^2 u_x}{\partial x^2}+\frac{\partial^2 u_x}{\partial y^2}+\frac{\partial^2 u_x}{\partial z^2}\right) \tag{6a}$$

$$u_x\frac{\partial u_y}{\partial x}+u_y\frac{\partial u_y}{\partial y}+u_z\frac{\partial u_y}{\partial z}=-\frac{1}{\rho}\frac{\partial p}{\partial y}+(\nu+\nu_{\text{turb}})\left(\frac{\partial^2 u_y}{\partial x^2}+\frac{\partial^2 u_y}{\partial y^2}+\frac{\partial^2 u_y}{\partial z^2}\right) \tag{6b}$$

$$u_x\frac{\partial u_z}{\partial x}+u_y\frac{\partial u_z}{\partial y}+u_z\frac{\partial u_z}{\partial z}=-\frac{1}{\rho}\frac{\partial p}{\partial z}+(\nu+\nu_{\text{turb}})\left(\frac{\partial^2 u_z}{\partial x^2}+\frac{\partial^2 u_z}{\partial y^2}+\frac{\partial^2 u_z}{\partial z^2}\right)+[1-\beta(T-T_o)]g \tag{6c}$$

The remaining governing equations (Eqs. (7a) and (7b)) for the air side are from the SST turbulence model. Expressions for the turbulent viscosity and the production terms are included in Eqs. (8a) and (8b), respectively, and all remaining coefficients may be found in Menter [35].

$$\rho\left(\frac{\partial(u_x\kappa)}{\partial x}+\frac{\partial(u_y\kappa)}{\partial y}+\frac{\partial(u_z\kappa)}{\partial z}\right)=P_\kappa-\beta_1\rho\kappa\omega+\frac{\partial}{\partial x}\left[(\mu+\sigma_\kappa\mu_{\text{turb}})\frac{\partial\kappa}{\partial x}\right]+\frac{\partial}{\partial y}\left[(\mu+\sigma_\kappa\mu_{\text{turb}})\frac{\partial\kappa}{\partial y}\right]+\frac{\partial}{\partial z}\left[(\mu+\sigma_\kappa\mu_{\text{turb}})\frac{\partial\kappa}{\partial z}\right] \tag{7a}$$

$$\rho\left(\frac{\partial(u_x\omega)}{\partial x}+\frac{\partial(u_y\omega)}{\partial y}+\frac{\partial(u_z\omega)}{\partial z}\right)=\frac{\alpha_1}{\nu_{\text{turb}}}P_\kappa-\beta_2\rho\omega^2+\frac{\partial}{\partial x}\left[(\mu+\sigma_\omega\mu_{\text{turb}})\frac{\partial\omega}{\partial x}\right]+\frac{\partial}{\partial y}\left[(\mu+\sigma_\omega\mu_{\text{turb}})\frac{\partial\omega}{\partial y}\right]+\frac{\partial}{\partial z}\left[(\mu+\sigma_\omega\mu_{\text{turb}})\frac{\partial\omega}{\partial z}\right]2(1-F_1)\frac{\rho\sigma_{\omega 2}}{\omega}\left(\frac{\partial\kappa\partial\omega}{\partial x^2}+\frac{\partial\kappa\partial\omega}{\partial y^2}+\frac{\partial\kappa\partial\omega}{\partial z^2}\right) \tag{7b}$$

$$\mu_{\text{turb}}=\rho\nu_{\text{turb}}=\frac{\rho\alpha_1\kappa}{\max(\alpha_1\omega,SF_2)};\quad P_\kappa=\mu S^2 \tag{8a; 8b}$$

Time-averaged symmetry about the vertical channel mid-plane (and zero shear) is exploited to further reduce the computational expense of the air-side SST modeling. An assumed turbulence intensity of 5% is specified at $x = 0$, and the spatial second derivatives of κ, the turbulent kinetic energy, and ω, the specific rate of turbulent dissipation, are set to zero at the channel outlet. In addition, the spatial derivatives of κ and ω with respect to the outward surface normal of all air-side solid surfaces are set to zero. At the channel inlet, κ and ω are functions of the turbulence intensity, the definition of which is available from Menter [35]. Inlet conditions correspond to uniform channel air velocities and temperatures. The artificial stationary medium (which occupies the HP vapor phase region) is initially assigned an arbitrary, large value of $k_{\text{eff},v}$. Convergence of the SST model is assumed when residual mean squared (RMS) values < 10^{-6} are achieved for all dependent variables. Grid independence is discussed in the Appendix. The final computational grids contained 27.8×10^6, 100.5×10^6, and 127.2×10^6 elements for 0, 3, and 6 fin cases, respectively. A typical simulation time required for solving the SST model is 9 h (2.5 h) for the initial (coupled iteration) cases.

2.3. SST-HP sub-model coupling

The SST and HP sub-models are coupled as diagramed in Fig. 2. The overall simulation is initialized by first solving the steady-state, 3D, SST model. Upon convergence, the area-averaged convection heat transfer coefficients for the fins, $\overline{h_f}$, and the exposed HP condenser wall surfaces, $\overline{h_w}$, are determined using

$$\overline{h_w}=\frac{1}{A_w}\int_{A_w}\frac{q''(z,r=r_{hp},\theta)}{\theta_w}dA_w;\quad \overline{h_f}=\frac{1}{A_f}\int_{A_f}\frac{q''(z,r=r_{hp},\theta)}{\theta_f}dA_f \tag{9a; 9b}$$

where $\theta \equiv T - T_\infty$. Step 1 of the iteration between the two sub-models involves prediction of the HP heat rate, $Q_{hp,3D}$, and the calculated difference between the area-averaged temperatures of the HP evaporator and HP condenser. Predicted values of Q_{hp} and ΔT defined as

$$\Delta T_{2D\text{ or }3D}=T_e-\overline{T_c}=T_e-\frac{1}{A_c}\int_{A_c}TdA_c \tag{10}$$

are saved for comparison to corresponding quantities predicted by the 2D HP model.

In Step 2, values of $\overline{h_w}$ and $\overline{h_f}$ predicted by the 3D SST model are used in Eqs. (1a) and (1b) of the 2D HP model. Values of the heat rate, $Q_{hp,2D}$, and average temperature difference ΔT_{2D} are then obtained. If $\Delta T_{2D} \not\approx \Delta T_{3D}$, a new value of $k_{\text{eff},v}$ is specified, and Steps 1 and 2 are repeated until $(\Delta T_{3D} - \Delta T_{2D})/\Delta T_{2D} < 0.02$. A comparison of the final predicted values of the HP heat rates obtained by the 2D and 3D models, $Q_{hp,2D}$ and $Q_{hp,3D}$ respectively, is used as a check of the overall modeling strategy.

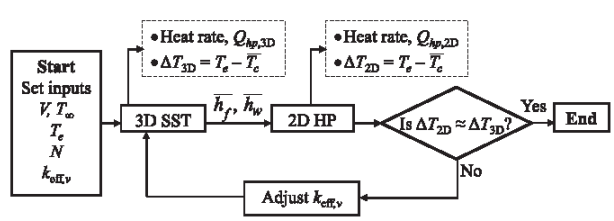

Fig. 2. Coupling of the internal (2D HP) and external (3D SST) numerical models.

3. Experiments

Experiments were conducted to validate the various models. They involve a copper–H_2O HP whose condenser fin array is cooled by forced convection of air, as shown in Figs. 3 and 4.

3.1. Heat pipe and fins

The vertically-oriented, copper–H_2O HP (Enertron HP-HD06DI17500BA) shown in Fig. 3 is of length L_{hp} = 175 mm and diameter D_{hp} = 6 mm. Wick and wall dimensions, as well as physical and effective properties, along with other HP characteristics are listed elsewhere [22]. The HP evaporator (condenser) section is of length L_e = 50.8 mm (L_c = 75 mm). The evaporator section is encapsulated by a cylindrical aluminum (Al 2024-T4; k_{hs} = 121 W/m K) heat spreader of length $L_{hs} = L_e$, outer diameter 25.4 mm, and inner diameter 6.05 mm. Thermal paste (Arctic Silver 5; k_{tp} = 8.7 W/m K) is packed within the gap between the HP and the spreader. The heat source is an adhesive-backed electrical patch heater (McMaster 35765K634) of dimensions 50.8 mm × 305 mm × 1.80 mm that is wrapped around the outer periphery of the heat spreader.

The temperature of the evaporator's exterior wall is deduced by (*i*) measuring temperatures at two axial locations within the heat spreader at r = 6.35 mm with 127 μm diameter K-type thermocouples, and (*ii*) using a conduction resistance analysis to bridge the thermal resistances posed by the aluminum and the thin layer of thermal paste. The maximum measured temperature difference between the two thermocouples is less than 0.1 °C, while the largest difference between the average temperature of the thermocouples and exterior surface of the HP evaporator is 2.1 °C, corresponding to the largest heat rate considered here.

The N square aluminum (AL 3003-h14; k_f = 159 W/m K) fins are of planar dimension $L_f = W_f$ = 100 mm and thickness t_f = 0.97 mm. The fins are evenly spaced, on center, over the condenser length with a pitch of $S = L_c/(N+1)$. The fins were first soldered onto the HP with Superior Flux AL27-33-75 solder paste using a standalone jig and oven setup.

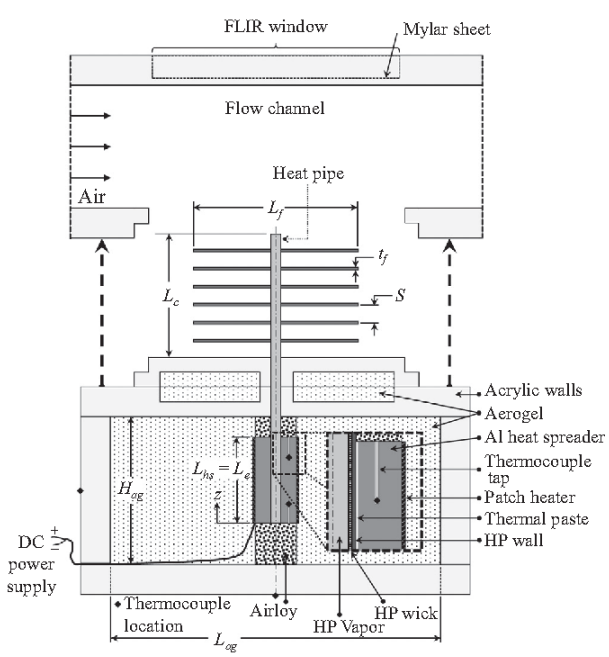

Fig. 3. Side view of the test section (finned HP, HP carrier, and flow channel).

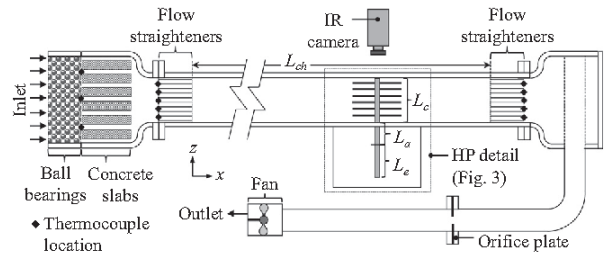

Fig. 4. Flow channel (side view).

3.2. HP carrier

Potential conjugate heat transfer effects, as well as parasitic heat losses, are addressed by carefully designing a HP carrier. To minimize outward radial heat losses from the heat spreader, it is embedded in a rectangular bed of aerogel powder (Lumira®; k_{ag} = 0.012 W/m K) of length L_{ag} = 100 mm, width W_{ag} = 80 mm, and height H_{ag} = 90 mm, contained by 18.7 mm thick acrylic walls. To minimize axial losses and to physically support the HP, cylinders were machined from solid aerogel sheets (Airloy® X103ML; k_{ar} = 0.029 W/m K) with radial dimensions equal to that of heat spreader. To minimize (*i*) axial losses to the overlying flow channel and (*ii*) radial losses from/gains to the HP adiabatic section, a cylindrical pocket of 40 mm height, 25.4 mm inner diameter, and 139.7 mm outer diameter was machined in the top acrylic assembly of the heat pipe carrier and filled with aerogel powder.

After being snapped into place, the top, circular surface of the HP carrier lies flush with the bottom surface of the flow channel. The carrier is secured to the flow channel with small (of diameter 6.35 mm), low thermal conductivity Nylon 12-12 screws to further minimize conjugate heat transfer effects. Overall heat losses are predicted to be less than 47% and 5% of the power delivered to the patch heater for the experiments involving the lowest (Q_{exp} = 0.61 W) and highest heat rates (Q_{exp} = 36.3 W), respectively.

3.3. Flow channel

The flow channel is shown schematically in Fig. 4, along with a second cartesian coordinate system whose origin is at the exit of the flow straightening section (x-direction), the mid-plane of the tunnel (y-direction), and at vertical elevation coincident with the bottom of the HP (z-direction). The interior dimensions of the flow channel are L_{ch} = 2.75 m, interior width of W_{ch} = 200 mm, and height H_{ch} = 75 mm. The centerline of the HP is located at x = 1.33 m, y = 0. The flow channel walls are constructed of 18.7 mm thick acrylic sheet.

The flow channel is operated in suction mode. The inlet air is thermally conditioned by passing it through an inlet plenum comprised of a 100 mm long packed bed of 12 mm stainless steel ball bearings followed by a bank of 40 mm thick, 194 mm × 260 mm concrete slabs. The slabs are separated by channels of height 3 mm. Flow conditioning is achieved with a bank of thin-walled, 5 mm diameter plastic cylinders (drinking straws) 197 mm long. Characterization of the flow channel yielded an isothermal temperature distribution in the y–z plane located at x = 1.28 m. The top wall of the flow channel houses a semitransparent, 0.23 mm thick Mylar sheet whose bottom surface is flush with the bottom surface of the top channel wall (Figs. 3 and 4). An infrared imaging system (FLIR A300) is mounted in a look-down configuration and used to measure the temperature distributions on the top surface of the top fin which was painted with a thin layer of Krylon 1602 ultra-flat paint of emissivity 0.96 in the spectral range of interest [41].

The semitransparent nature of the Mylar window was accounted for when interpreting the infrared temperature information, as discussed in the next section.

The air exits the flow channel through a second set of conditioners and a 100 mm diameter perforated tube positioned horizontally within the tunnel exit plenum. The air is driven by a fan whose flow rate could be manually adjusted by partially blocking the fan exit. Bulk flow rates were measured using an orifice plate situated in a long straight section of 100 mm tubing. The pressure drop across the orifice plate was calibrated to bulk flow rates that were inferred by spatially integrating the local velocity distributions within the tunnel. Locations of various 127 μm K-type thermocouples are identified in Fig. 4.

3.4. Instrumentation and data acquisition

The patch heater at the HP evaporator section is powered by a DC power supply (Dr. Meter HY3005F-3). A voltmeter (AMPROBE AM-510; accuracy ±0.8% of reading +1 LSD; resolution 10 mV) and ammeter (FLUKE 77 IV; accuracy ±1.5% of reading +2 LSD; resolution 1 mA) are used to measure the electric power dissipation within a maximum uncertainty of ±0.70 W (associated with the maximum power considered; 36.3 W). Thermocouple and pressure transducer (Omega PX653-01D5V, ±0.001 inch H_2O) voltages are collected by a data acquisition system (National Instruments cDAQ-9188 XT) at 2 s intervals using LabVIEW software. A hot wire probe (Anemomaster 6035-0E; accuracy ±3% of reading, resolution 0.01 m/s) was used to measure the local air velocities within the flow channel within a maximum uncertainty of ±0.046 m/s (associated with the velocity of 1.5 m/s). All of the welded thermocouples were constructed from the same spools of wire to minimize bias error when reporting temperature differences. The thermocouples were calibrated using the boiling and freezing points of distilled water within an estimated uncertainty ±0.1 °C. Temperatures indicated by the infrared camera (when viewing the HP assembly through the Mylar window) were corrected by developing and using an off-line calibration involving an aluminum heat exchanger of known temperature that was painted with Krylon 1602 and viewed through the Mylar window. The maximum uncertainty associated with reported infrared-measured temperatures is ±0.15 °C.

4. Results and discussion

4.1. DNS-SST comparison

DNS predictions were generated using the computational domain of Fig. 1b. These predictions were used to validate the SST model (applied to the channel half-width of Fig. 1b) for $N = 3$ fins, $T_\infty = 25$ °C and inlet velocities of $V = 0.5$ and 1.5 m/s. Since the DNS-SST comparison is meant only to check the ability of the SST model to accurately predict the 3D external flow, an isothermal HP assembly $T_{hp,f} = 60$ °C, was specified in order to reduce the cost of the comparison. The DNS and SST predictions are both deemed to be grid and time-step independent (Appendix A).

Air temperature distributions (at the vertical mid-plane of the channel) generated by the DNS model (at an arbitrary time after quasi-steady conditions are reached) and SST models (steady state) are reported in Fig. 5. For $V = 0.5$ m/s, the DNS (Fig. 5a) and SST predictions (Fig. 5c) are similar. Buoyancy forces drive three rising warm wakes that issue downstream from each of the three fins. Since $Gr_{H_{ch}}/Re^2_{H_{ch}} = 0.33$, inertial and buoyancy forces are expected to be of similar magnitude.

For $V = 1.5$ m/s (DNS, Fig. 5b; SST, Fig. 5d; $Gr_{H_{ch}}/Re^2_{H_{ch}} = 0.037$) the DNS predictions involve a complex, time-dependent structure. As expected, the time-averaged SST predictions (Fig. 5d) reveal steeper temperature gradients (higher heat transfer rates) near the solid surfaces, compared to those of Fig. 5c. Buoyancy effects are not evident in the higher velocity predictions.

Temperature distributions in a horizontal plane located midway between the middle and top fins are shown in Fig. 6. Vortex shedding from the vertical HP is evident in the DNS predictions for both the low (Fig. 6a) and high velocity (Fig. 6b) cases. Boundary layer development over the fins is affected by the vortices, with temperature distributions in a horizontal plane (not shown) immediately downstream of the top fin being affected by of the vortex shedding process. The interplay between the fin and HP convection processes, as well as the buoyancy effects of the smaller velocity case, makes specification of $\overline{h_w}$ and $\overline{h_f}$ using standard correlations prone to large uncertainty.

4.2. Comparison of DNS and SST predictions with experimental measurements

Local air temperatures were measured in the same horizontal planes as included in Fig. 6 using a butt-welded K-type thermocouple held taught and supported between small holes placed in the vertical channel walls. Analysis of air temperatures measured at approximately 3.0 and 6.3 HP diameters downstream of the HP centerline reveals St values of 0.176 and 0.193 for the low and high velocity cases, respectively. The measured values are in good agreement with St values for vortex shedding from a plain cylinder in cross flow [42].

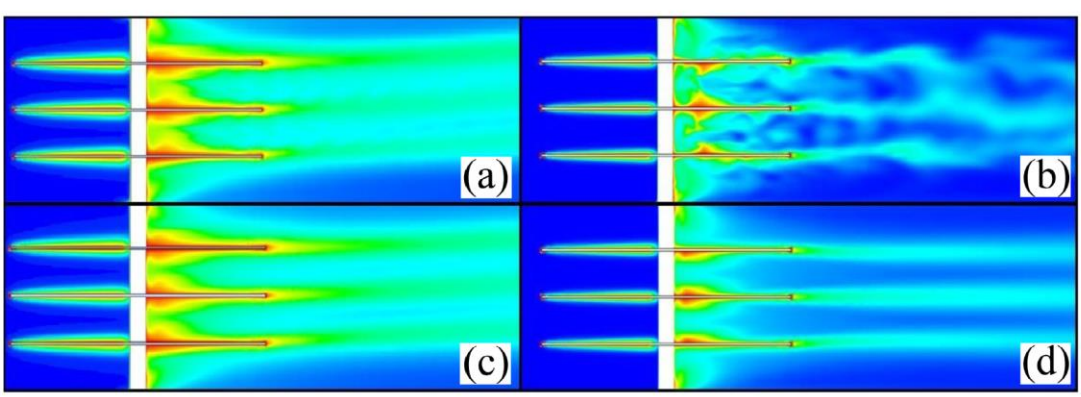

Fig. 5. Temperature distributions in the channel centerplane, $N = 3$, $T_e = T_{hp,f} = 60$ °C. (a) DNS ($V = 0.5$ m/s), (b) DNS ($V = 1.5$ m/s), (c) SST ($V = 0.5$ m/s), (d) SST ($V = 1.5$ m/s). Minimum and maximum temperatures are $T_{min} = 25$ °C and $T_{max} = 52$ °C.

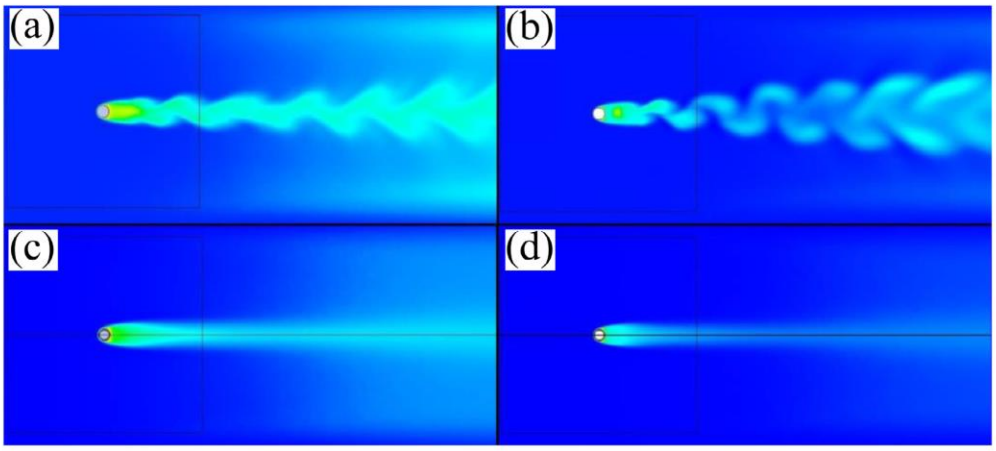

Fig. 6. Temperature distributions in horizontal plane midway between fins, $N = 3$, $T_e = T_{hp,f} = 60$ °C. (a) DNS ($V = 0.5$ m/s), (b) DNS ($V = 1.5$ m/s), (c) SST ($V = 0.5$ m/s), (d) SST ($V = 1.5$ m/s). Temperature scale same as Fig. 5.

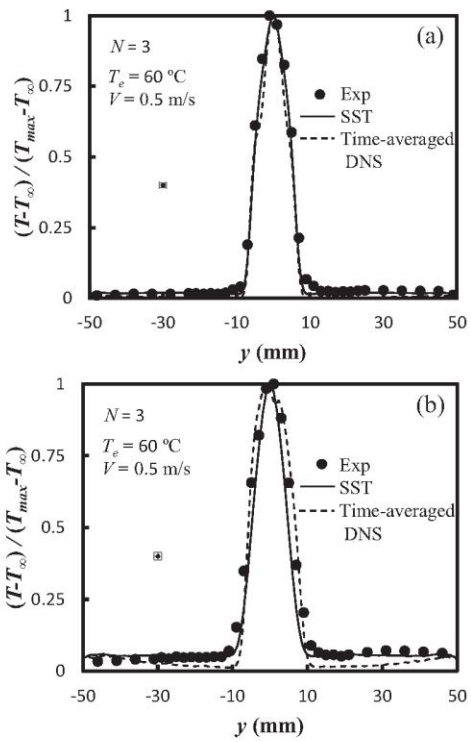

Fig. 7. Dimensionless DNS, SST, and experimental temperature distributions across thermal wakes, $N = 3$, $T_e = 60$ °C, $V = 0.5$ m/s. (a) 3.0 HP diameters downstream from the HP centerline (b) 6.3 HP diameters downstream from the HP centerline.

Since the experiments involve an operating HP and the DNS model employs the assumption of an isothermal HP-fin assembly, thermal conditions to which the air is exposed are different. Therefore, measured and predicted dimensional air temperatures are not expected to be in agreement. However, a comparison of measured and DNS-predicted dimensionless air temperatures is meaningful. Typical comparisons of time-averaged temperatures measured across the downstream wake averaged over 5 min are shown in Fig. 7a (thermocouple placed 3.0 HP diameters downstream of the HP centerline) and Fig. 7b (6.3 HP diameters downstream). Both the time-averaged DNS and steady-state SST predictions are in good agreement with time-averaged measured dimensionless temperatures, further validating the SST predictions. Predicted values of $\overline{h_w}$ and $\overline{h_f}$, obtained from the SST and DNS models, are reported in Table 1. The predictions of the two models are in agreement to within ± 6%.

Table 1
DNS and SST predicted heat transfer coefficients (W/m^2 K, $N = 3$, $T_e = 60$ °C).

Case	$V = 0.5$ m/s		$V = 1.5$ m/s	
	$\overline{h_f}$	$\overline{h_w}$	$\overline{h_f}$	$\overline{h_w}$
Time-averaged DNS	12.93	28.96	23.24	51.38
SST	13.83	31.13	25.40	58.68

4.3. Comparison of overall model predictions with experimental measurements

The results thus far are for an isothermal HP-fin array assembly. To ascertain the performance of the overall (coupled HP and SST) model described in Fig. 2, the isothermal HP assumption is now relaxed. Measured and predicated (both 2D and 3D) heat rates are reported in Table 2 for 8 cases. Also included in the table are the converged values of $k_{\mathrm{eff},v}$, $\overline{h_w}$, and $\overline{h_f}$.

Predicted (2D and 3D) heat rates are in good agreement (within 7% of the average of the two heat rates) for all cases considered here. Predicted 3D heat rates are consistently higher than their predicted 2D counterparts. This discrepancy may be attributed to non-uniform predicted temperatures in the wall of the HP condenser section, to be discussed shortly. Measured heat rates are consistently lower than predicted heat rates (an average discrepancy of 10%); this discrepancy may be attributed to thermal contact resistances between the HP and the fins that are not accounted for in either (SST or HP) model.

The convection heat transfer coefficients of Table 2 exhibit several expected trends. First, values of the convection coefficients increase as the air speed is increased. Second, heat transfer coefficients for the exposed HP walls are higher than those associated with the fins. Third, the predicted convection coefficients are nearly independent of the evaporator temperatures (for a given air velocity) since buoyancy effects do not dominate. The converged effective thermal conductivity used in the 3D SST model increases as the evaporator temperature increases, reflecting the

Table 2
Conditions (left) and predicted values (right) for parametric calculations.

Input parameters			Predicted values					
N	V m/s	T_e °C	$k_{eff,v}$ W/m K	$\overline{h_w}$ W/m^2 K	$\overline{h_f}$ W/m^2 K	$Q_{hp,3D}$ W	$Q_{hp,2D}$ W	Q_{exp} W
3	0.5	34.5	47,500	28.47	10.74	4.41	3.81	4.09
		60	52,000	28.46	10.74	15.86	14.07	15.40
	1.5	34.5	39,000	55.28	20.27	5.99	5.47	5.00
		60	63,000	55.29	20.27	23.06	20.66	19.34
6	0.5	34.5	35,000	26.29	11.02	7.56	6.86	5.92
		60	64,000	26.47	11.03	29.89	26.64	26.46
	1.5	34.5	32,000	51.24	19.47	10.42	9.19	7.27
		60	70,000	51.53	19.50	42.01	37.03	36.30

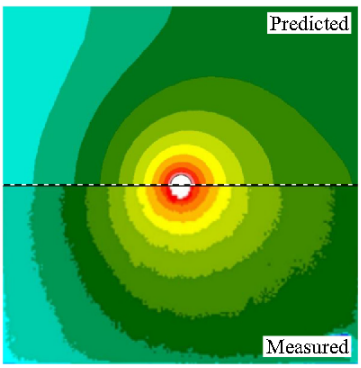

Fig. 8. Predicted (upper half) and measured (bottom half) fin top surface temperature distribution for $V = 1.5$ m/s (left to right): $T_e = 60$ °C, $N = 6$. See Section 4.2 for isotherm values.

more vigorous evaporation, condensation, and HP vapor advection associated with the larger overall HP temperature differences.

Predicted (SST) and measured local fin temperatures (for the top surface of the upper square fin) are reported in Fig. 8 for a representative case, $N = 6$, $T_e = 60$ °C, $T_\infty = 25$ °C, $V = 1.5$ m/s. Eleven isotherms are shown in Fig. 8, all separated by temperature differences of 1.68 °C. The minimum fin temperature shown for the measurements is $T_{min} \approx 37.5$ °C and occurs at the outer leading edges of the square fin, while maximum temperatures ($T_{max} \approx 56.0$ °C) occur at the fin root. The minimum and maximum SST-predicted temperatures occur at the same locations and are $T_{min} = 37.7$ °C and $T_{max} = 56.2$ °C. Advective effects are evident in both the measured and predicted temperature distributions, but regions closer to the fin root have a more uniform temperature distribution in the azimuth direction, θ, of Fig. 1b. The nearly axisymmetric temperature distribution near the base of the fin gives further credence to the 2D modeling of the HP taken here. Advective effects are also evident in Fig. 9, which reports measured (both spanwise and streamwise) temperature distributions on the top surface of the upper fin. The 3D SST predictions show similar advective effects as the measurements, while the 2D HP predictions show no dependence on θ, as required. In general the agreement between predicted (2D and 3D) and measured local fin temperatures is considered to be good.

4.4. Predicted HP wall temperatures

Predicted temperature distributions along the length of the HP wall ($r = r_{hp}$) for both $N = 3$ and $N = 6$ ($T_e = 60$ °C, $V = 1.5$ m/s) are shown in Fig. 10a and b, respectively, using the modeling approach of Fig. 2. Both figures also include predicted temperature distributions for $N = 0$ for purposes of comparison. Significant temperature depressions exist within the HP wall adjacent to the fin roots. The thermal depressions are a result of the interplay between the external convection processes, conduction within the fins, and multimode heat transfer within the HP. Depressions predicted by the 2D model are consistently larger than those for the 3D model. This may be attributed to the approximate treatment of the heat transfer within the HP vapor region in the 3D model which is unable to replicate, for example, variations in local condensation rates internal to the HP and, in turn, the correspondingly high local heat transfer rates adjacent to the fin roots. It is well known that increased constriction resistances are associated with large temperature depressions of the type noted here [33]. These resistances will increase the overall thermal resistance of the HP system, and reduce the HP heat rate predicted by the 2D model relative to those predicted by the 3D model, consistent with the results of Table 2.

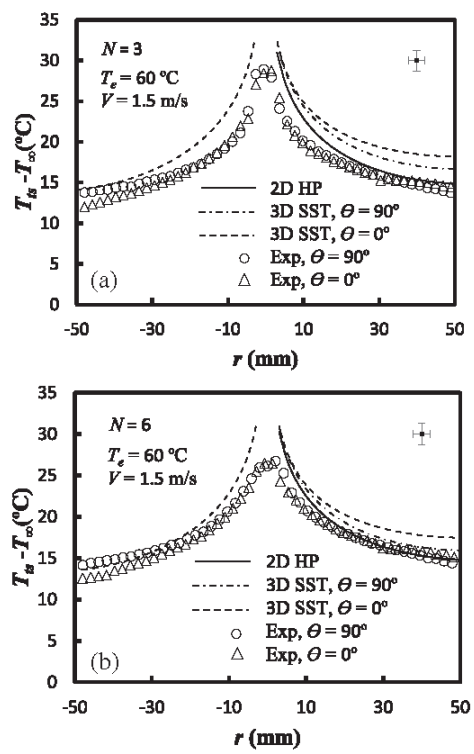

Fig. 9. Top surface temperature distributions for $V = 1.5$ m/s, $T_e = 60$ °C, and $\theta = 0$, 90°. (a) $N = 3$, (b) $N = 6$.

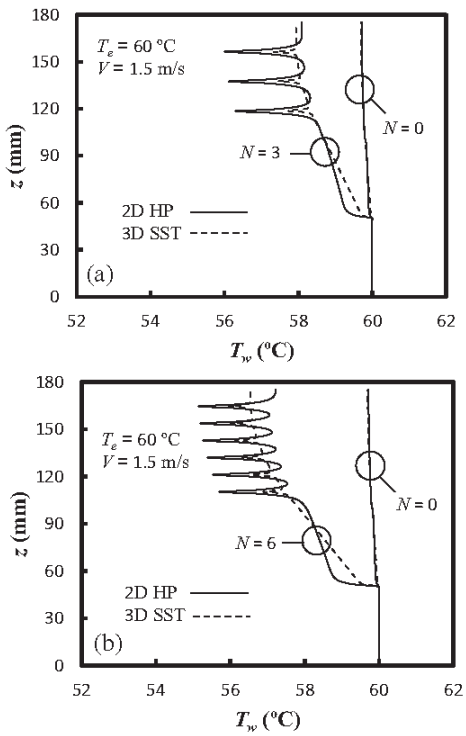

Fig. 10. Predicted HP wall temperature distributions ($r = r_{hp}$) for T_e = 60 °C. (a) N = 3, (b) N = 6.

To the authors' knowledge, this constriction resistance effect has not been previously reported in HP-related research.

4.5. Parametric simulations

Heat rates predicted by the 2D HP and 3D SST models, along with measured heat rate values, are reported graphically in Fig. 11 for N = 0, 3 and 6, T_∞ = 25 °C, and a range of convective conditions. As evident, heat rates increase as N, T_e, and V are increased, with general agreement between the heat rates that are predicted and measured.

4.6. Heat pipe and external thermal resistances

The detailed predictions of the coupled 2D and 3D models can be used to determine total, heat pipe, and external convection thermal resistances. The total and HP resistances are determined using the expressions $R_{tot} = (T_e - T_\infty)/Q_{hp}$ and $R_{hp} = (T_e - \bar{T}_c)/Q_{hp}$, respectively, while the external air convection resistances are calculated from $R_{conv} = R_{tot} - R_{hp}$. The HP and convection thermal resistances are assumed to act in series, and R_{conv} includes the effects of convection directly from the HP and through the external fin arrays. Note that the experimental total thermal resistances are calculated in the same manner as their predicted counterparts, except measured heat rates are used.

As evident from Table 3, predicted and measured total thermal resistances are in relatively good agreement. The total thermal resistances decrease as T_e, N, or V increase. In every case, the overall thermal resistance is dominated by the external thermal resistances, suggesting that significantly improved performance could be achieved with optimized external fin arrays.

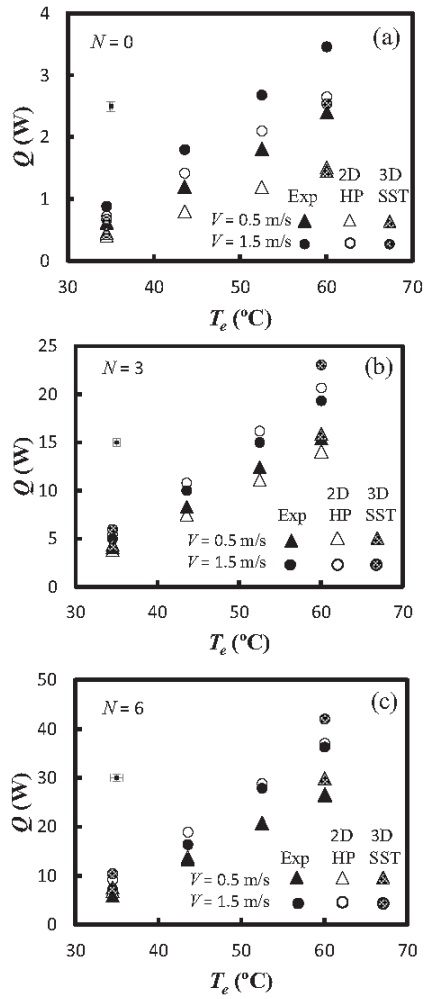

Fig. 11. Heat transfer rates versus HP exterior evaporator wall temperatures for different inlet air velocities. (a) N = 0, (b) N = 3, (c) N = 6.

4.7. Limitation of the stagnant HP core approach of the 3D SST model

As discussed, the 3D SST model incorporates an artificial stationary medium of high thermal conductivity in the HP vapor region to approximate the low thermal resistances inside the HP. Values of the effective core thermal conductivity, $k_{eff,v}$, are determined by employing the coupling strategy of Fig. 2. To estimate the possible influence of non-axisymmetric heat transfer in the HP, several 3D SST simulations were performed for extreme cases in which the stationary core is subdivided into upstream ($0 < \theta \leqslant \pi/2$) and downstream ($\pi/2 < \theta \leqslant \pi$) halves. To force highly-3D processes within the HP, the effective thermal conductivity of the upstream half is set to $k_{eff,v,u} = 2k_{eff,v}$ (or 0) while the conductivity of the downstream half is specified to be $k_{eff,v,d} = 0$ (or $2k_{eff,v}$).

Predicted temperature distributions on the top surface of the upper fin for the conditions of Fig. 8, using the extreme effective thermal conductivity values, are shown in Fig. 12. As expected, warmer temperatures are pushed upstream for the $k_{eff,v,d} = 0$ case, with the opposite behavior noted for $k_{eff,v,u} = 0$. The temperature distributions, obtained with $k_{eff,max}$ = 140,000 W/m K, bracket those of Fig. 8. The predicted heat rates are 40.31 W and 40.40 W for $k_{eff,v,d} = 0$ and $k_{eff,v,u} = 0$, respectively. These represent less than

Table 3
Conditions (left) and predicted thermal resistances (right) for parametric calculations.

Input parameters			Predicted values (2D)			Predicted values (3D)			Measured values
N	V m/s	T_e °C	R_{tot} K/W	R_{hp} K/W	R_{conv} K/W	R_{tot} K/W	R_{hp} K/W	R_{conv} K/W	R_{tot} K/W
3	0.5	34.5	2.50	0.11	2.39	2.15	0.10	2.05	2.32
		60	2.48	0.10	2.38	2.21	0.10	2.11	2.27
	1.5	34.5	1.74	0.14	1.60	1.58	0.12	1.46	1.90
		60	1.70	0.10	1.60	1.52	0.08	1.44	1.81
6	0.5	34.5	1.38	0.16	1.22	1.25	0.14	1.11	1.60
		60	1.31	0.09	1.22	1.17	0.08	1.09	1.32
	1.5	34.5	1.03	0.17	0.86	0.91	0.15	0.76	1.31
		60	0.94	0.08	0.86	0.83	0.07	0.76	0.96

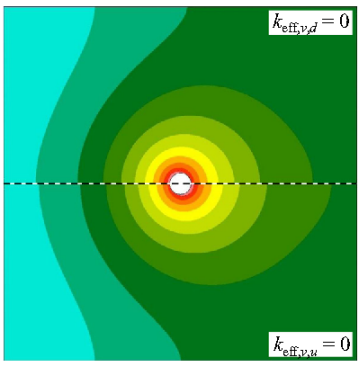

Fig. 12. Predicted fin top surface temperature distributions for $V = 1.5$ m/s, $T_e = 60$ °C, $N = 6$ for $k_{eff,v,d} = 0$ (top half) and $k_{eff,v,u} = 0$ (bottom half). The temperature scale is the same as for Fig. 8.

5% decrease from the nominal value of $Q_{hp} = 42.01$ W reported in Table 2. Similar percentage reductions were observed for the $N = 3$ case.

As evident, simply doubling the effective conductivity in one half of the HP vapor region (and setting the conductivity in the other half to zero) has little effect on the overall heat rate, but changes the predicted value of ΔT_{3D} by approximately 20%. Usage of the iteration process of Fig. 2 to hone the predictions yields heat rates of 41.67 and 41.68 W for the $k_{eff,v,d} = 0$ and $k_{eff,v,u} = 0$ cases, respectively, with $k_{eff,max} = 200{,}000$ W/m K predicted for both cases. Similar trends were observed for the $N = 3$ case.

From the preceding discussion, it is expected that highly asymmetric conditions within the HP have a minor effect on temperature distributions, and an insignificant effect on the predicted heat transfer rate in finned HP systems.

5. Conclusions

A novel modeling strategy, based upon an existing, multiphase 2D HP model that is coupled with a new 3D single-phase (external flow) model has been developed. The 3D external flow sub-model uses the shear stress transport (SST) approach. SST predictions have been validated through a comparison with both direct simulations and experimental measurements. Likewise, the overall model has been validated by comparing its predictions with experimental measurements of local temperatures and heat rates. The model has revealed temperature depressions in the HP wall that can affect the overall thermal resistance of the HP-fin array system. The model has also been used to quantify total heat rates and their sensitivity to external flow conditions and the number of fins in the array. With the overall modeling strategy verified, the model can be exercised to predict a wide array of system performance parameters including but not limited to overall thermal resistances, external flow pressure drops, as well as fan pumping requirements for various HP and of fin array designs.

Acknowledgments

This material is based upon work supported by the National Science Foundation under Grant Nos. 1435131 (University of Kansas) and 1435233 (University of Connecticut). The authors also wish to thank undergraduate research assistants Will Libeer and Thomas Dunn for their assistance in the construction and validation of the experimental apparatus.

Appendix A. Time step and grid-size independence

Predictions of the SST simulations, generated using the commercial software Ansys CFX (v16.0), for the $N = 0$, 3 and 6 fin configurations with $T_e = 60$ °C, $T_\infty = 25$ °C, and $V = 1.5$ m/s were evaluated for their grid dependence. The grid dependence study for $N = 3$, presented here, is representative of all cases. Details of the computational mesh (≈100 million elements) within the vertical mid-plane of the channel for the $N = 3$ case are shown in Fig. A-1. Predictions of the heat transfer rate $Q_{hp,3D}$, overall temperature difference, ΔT_{3D}, as well as the convection heat transfer coefficients, $\overline{h_f}$ and $\overline{h_w}$ are shown in Table 4. A grid refinement from 70.6 million to 96.6 million elements yielded a maximum of 0.36% change in any of parameters, at which point grid independence

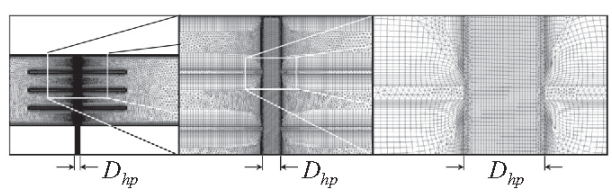

Fig. A-1. SST computational mesh for $N = 3$ determined by the grid independence study. Magnification is increased from left to right.

Table 4
Predicted values (right) as a function of the number of elements employed (left).

Nodes	Elements	$\overline{h_w}$ W/m^2 K	$\overline{h_f}$ W/m^2 K	$Q_{hp,3D}$ W	ΔT_{3D} K
1.2E+07	8.4E+06	82.0	36.6	26.3	1.75
2.2E+07	1.5E+07	82.7	36.7	26.4	1.75
2.3E+07	1.4E+07	71.0	25.1	22.3	1.48
3.4E+07	2.1E+07	78.7	23.8	22.8	1.51
1.0E+08	7.1E+07	55.3	20.3	23.3	1.53
1.4E+08	9.7E+07	55.3	20.2	23.3	1.54

was considered to be achieved. Adequate mesh sizes utilized for the $N = 0$ and 6 fin cases were determined in a similar manner and are 27.8 and 127.2 million elements, respectively.

The $N = 3$ DNS simulation with the same $T_e = T_{hp,f} = 60$ °C, T_∞, and V as for the SST cases, was evaluated for grid dependence in a similar manner. This process yielded a satisfactory mesh of 36.1 million elements within the air domain (less than 0.7% variation relative to predictions generated from a computational grid of 17.7 million elements). Additionally, time step dependence was investigated. Time-averaged DNS results changed by less than 0.1% when the time step was reduced from 0.005 s to 0.001 (which is the time-step used here).

References

[1] D.A. Reay, P.A. Kewm, R.J. McGlen, Heat Pipes: Theory, Design, and Applications, sixth ed., Elsevier, Oxford, 2014.
[2] Amir. Faghri, Heat Pipe Science and Technology, Taylor & Francis, Washington, DC, 1995.
[3] A.A. El-Nasr, S.M. El-Haggar, Effective thermal conductivity of heat pipes, Heat Mass Transfer 32 (1–2) (1996) 97–101.
[4] H. Shabgard, M.J. Allen, N. Sharifi, S.P. Benn, A. Faghri, T.L. Bergman, Heat pipe heat exchangers and heat sinks: opportunities, challenges, applications, analysis, and state of the art, Int. J. Heat Mass Transfer 89 (2015) 138–158.
[5] W. Srimuang, P. Amatachaya, A review of the applications of heat pipe heat exchangers for heat recovery, Renew. Sustain. Energy Rev. 16 (2012) 4303–4315.
[6] K.S. Ong, Review of heat pipe heat exchangers for enhanced dehumidification and cooling in air conditioning systems, Int. J. Low-Carbon Technol. (2014) 1–8.
[7] A. Mardiana-Idayu, S.B. Riffat, Review on heat recovery technologies for building applications, Renew. Sustain. Energy Rev. 16 (2) (2012) 1241–1255.
[8] M.S. Naghavi, K.S. Ong, M. Mehrali, I.S. Badruddin, H.S.C. Metselaar, A state-of-the-art review on hybrid heat pipe latent heat storage systems, Energy Convers. Manage. 105 (2015) 1178–1204.
[9] A. Faghri, Heat pipes: review, opportunities and challenges, Front. Heat Pipes 5 (1) (2014).
[10] M. Mochizuki, T. Nguyen, K. Mashiko, Y. Saito, T. Nguyen, V. Wuttijumnong, A review of heat pipe application including new opportunities, Front. Heat Pipes 2 (1) (2011).
[11] S. Liu, M. Sakr, A comprehensive review on passive heat transfer enhancements in pipe exchangers, Renew. Sustain. Energy Rev. 19 (2013) 64–81.
[12] H.N. Chaudhry, B.R. Hughes, S.A. Ghani, A review of heat pipe systems for heat recovery and renewable energy applications, Renew. Sustain. Energy Rev. 16 (4) (2012) 2249–2259.
[13] A. Faghri, Review and advances in heat pipe science and technology, J. Heat Transfer 134 (12) (2012) 123001.
[14] E. Okamoto, Y. Fukaya, M. Chikami, Heat Pipe Heat Exchanger, US Patent No. 4537247, 1985.
[15] N.N. Carpenter, Heat Pipe Heat Exchanger, Hudson Products Co., US Patent No. 5379831, 1995.
[16] A. Faghri, T.L. Bergman, N. Sharifi, M.J. Allen, H. Shabgard, J.S. Breit, Energy storage and thermal management using phase change materials in conjunction with heat pipes and foil, foams, or other porous media, US Patent Application No. 0284020 A1, 2014.
[17] K.S. Kim, M.H. Won, J.W. Kim, B.J. Back, Heat pipe cooling technology for desktop PC CPU, Appl. Therm. Eng. 23 (9) (2003) 1137–1144.
[18] M.A. Abd El-Baky, M.M. Mohamed, Heat pipe heat exchanger for heat recovery in air conditioning, Appl. Therm. Eng. 27 (4) (2007) 795–801.
[19] K.A.R. Ismail, C.L.F. Avles, M.S. Modesto, Numerical and experimental study on the solidification of PCM around a vertical axially finned isothermal cylinder, Appl. Therm. Eng. 21 (1) (2001) 53–77.
[20] S. Tiari, S. Qiu, Three-dimensional simulation of high temperature latent heat thermal energy storage system assisted by finned heat pipes, Energy Convers. Manage. 105 (2015) 260–271.
[21] S. Tiari, S. Qiu, M. Mahdavi, Numerical study of finned heat pipe-assisted thermal energy storage system with high temperature phase change material, Energy Convers. Manage. 89 (2015) 833–842.
[22] N. Sharifi, T.L. Bergman, M.J. Allen, A. Faghri, Melting and solidification enhancement using a combined heat pipe, foil approach, Int. J. Heat Mass Transfer 78 (2014) 930–941.
[23] M. Mahdavi, S. Qiu, S. Tiari, Numerical investigation of hydrodynamics and thermal performance of a specially configured heat pipe for high-temperature thermal energy storage systems, Appl. Therm. Eng. 81 (2015) 325–337.
[24] Y. Cao, A. Faghri, Transient two-dimensional compressible analysis for high-temperature heat pipes with pulsed heat input, Numer. Heat Transfer Appl. 18 (4) (1990) 483–502.
[25] N. Zhu, K. Vafai, Vapor and liquid flow in an asymmetrical flat plate heat pipe: a three-dimensional analytical and numerical investigation, Int. J. Heat Mass Transfer 41 (1) (1998) 159–174.
[26] N. Sharifi, S. Wang, T.L. Bergman, A. Faghri, Heat pipe-assisted melting of a phase change material, Int. J. Heat Mass Transfer 55 (13–14) (2012) 3458–3469.
[27] N. Sharifi, A. Faghri, T.L. Bergman, C.E. Andraka, Simulation of heat pipe-assisted latent heat thermal energy storage with simultaneous charging and discharging, Int. J. Heat Mass Transfer 80 (2015) 170–179.
[28] H. Shabgard, A. Faghri, T.L. Bergman, C.E. Andraka, Numerical simulation of heat pipe-assisted latent heat thermal energy storage unit for dish-stirling systems, J. Solar Eng. 136 (2) (2014) 021025-1–021025-12.
[29] N. Zhu, K. Vafai, Numerical and analytical investigation of vapor flow in a disk-shaped heat pipe incorporating secondary flow, Int. J. Heat Mass Transfer 40 (12) (1997) 2887–2900.
[30] M. Mahdavi, S. Qui, Mathematical modeling and analysis of steady state performance of a heat pipe network, Appl. Therm. Eng. 91 (2015) 556–573.
[31] B. Xiao, A. Faghri, A three-dimensional thermal–fluid analysis of flat heat pipes, Int. J. Heat Mass Transfer 51 (11–12) (2008) 3113–3126.
[32] J. Rice, A. Faghri, Analysis of porous wick heat pipes, including capillary dry-out limitations, J. Thermophys. Heat Transfer 21 (3) (2007) 475–486.
[33] T.L. Bergman, A.S. Lavine, F.P. Incropera, D.P. Dewitt, Fundamentals of Heat and Mass Transfer, seventh ed., Wiley, Hoboken, 2011.
[34] E.M. Sparrow, J.P. Abraham, A new buoyancy model replacing the standard pseudo-density difference for internal natural convection in gases, Int. J. Heat Mass Transfer 46 (19) (2003) 3583–3591.
[35] F.R. Menter, Two-equation eddy-viscosity turbulence models for engineering applications, AIAA J. 32 (8) (1994) 1598–1605.
[36] H. Nemati, M. Moghimi, Numerical study of flow over annular-finned tube heat exchangers by different turbulent models, CFD Lett. 6 (3) (2014) 101–112.
[37] J.P. Abraham, E.M. Sparrow, J.C.K. Tong, Heat transfer in all pipe flow regimes – Laminar, transitional/intermittent, and turbulent, Int. J. Heat Mass Transfer 52 (2009) 557–563.
[38] J.P. Abraham, E.M. Sparrow, W.J. Minkowycz, Internal-flow Nusselt numbers for the low-Reynolds-number end of the laminar-to-turbulent transition regime, Int. J. Heat Mass Transfer 54 (2011) 584–588.
[39] J.P. Abraham, E.M. Sparrow, J.C.K. Tong, D.W. Bettenhausen, Internal flows which transist from turbulent through intermittent to laminar, Int. J. Therm. Sci. 49 (2010) 256–263.
[40] J.C.K. Tong, J.P. Abraham, J.M.Y. Tse, E.M. Sparrow, Impact of chamfer contours to reduce column drag, Eng. Comput. Mech. 168 (2015) 79–88.
[41] Emissivity of Paint, NASA Jet Propulsion Laboratory, 26 Feb. 2012. <http://master.jpl.nasa.gov/reference/paints.htm>.
[42] R.D. Blevins, Flow-induced Vibration, Krieger Publishing Company, Malabar, FL, 1990.

Paper P3

Title:

Experimentally validated analytical expressions for the thermal efficiencies and thermal resistances of porous metal foam-fins

Authors:

John R. Stark

Raki Prasad

Theodore L. Bergman

Journal:

International Journal of Heat and Mass Transfer

International Journal of Heat and Mass Transfer 111 (2017) 1286–1295

Contents lists available at ScienceDirect

International Journal of Heat and Mass Transfer

journal homepage: www.elsevier.com/locate/ijhmt

Experimentally validated analytical expressions for the thermal efficiencies and thermal resistances of porous metal foam-fins

J.R. Stark *, R. Prasad, T.L. Bergman

Department of Mechanical Engineering, The University of Kansas, 1530 W. 15th Street 3138, Lawrence, KS 66045, USA

ARTICLE INFO

Article history:
Received 24 January 2017
Received in revised form 10 March 2017
Accepted 12 March 2017

Keywords:
Thermal efficiency
Metal foam
Porous media convection
Numerical modeling
Analytical modeling

ABSTRACT

Novel, analytical expressions are developed for the thermal efficiency and thermal resistance associated with forced convection and conduction within a cylindrically shaped, open porous medium that is attached concentrically to a circular tube. Using the new analytical expression in conjunction with a two-temperature porous medium numerical model, a companion semi-analytical expression for the thermal efficiency of a cubical foam block attached on-center to a circular tube is also developed. Heat rates predicted with the semi-analytical model are verified through comparison with experimentally measured heat transfer rates using open-cell metal foam. Foam thermal resistances are also quantified over a range of operating conditions. The recommended ranges of application of the analytical and experimentally verified semi-analytical expressions for the thermal efficiency of both annular and square-shaped foams are also presented.

1. Introduction

Owing to their extremely large surface areas per unit volume, open-cell high-porosity metal foams have many potential heat transfer applications [1–3]. Heat transfer within a metal foam (depicted in Fig. 1) is complex, consisting of conduction within the metal component, convection between the metal and the saturating working fluid, and potentially radiation throughout the fluid domain. Numerous efforts have been made to model the heat transfer processes using both multi-phase local, and continuum approaches. Local multi-phase analyses are often performed with the intent of informing continuum scale models through the quantification of effective thermal transport properties.

Extensive work has been carried out to generate an idealized solid phase structure for a typical unit cell within the foam, providing the geometrical information needed to develop the multi-phase local models and effective properties. The approximation of a general, disordered porous medium by using idealized unit cells was shown by Koch et al. [4] to be valid in ultimately predicting effective transport properties. Analytical modeling of the conduction and convection heat transfer within a linear cylinder lattice unit cell (characterized by a grid of uniform diameter cylinders that meet orthogonally) was first proposed by Lu et al. [5], who used cylinder-in-cross flow correlations to approximate the convective heat transfer processes. Du Plessis et al. [6] performed the first numerical analysis of the three-dimensional steady flow through a simple unit cell.

Conduction and convection within a more geometrically complex unit cell, which was first proposed by Weaire and Phalen [7], was numerically simulated by Boomsma et al. [8], Kopanidis et al. [9], and others, yielding reasonable predictions of experimentally measured pressure drops associated with flow through the foam structure. Krishman et al. [10] used a similar approach with a less complex Kelvin unit cell [11] while Iasiello et al. [12] compared predicted heat transfer rates and pressure drops associated with the Weaire-Phalen and Kelvin unit cells, showing that the more simplified Kelvin model is acceptable for the prediction of area-averaged convection coefficients and overall pressure loss characteristics. Numerical modeling of convection and conduction by Ranut et al. [13] utilized an experimentally determined foam geometry, with predictions showing good agreement with those associated with previous unit cell modeling efforts.

Continuum-based, analytical modeling of heat transfer within highly porous metal foams has also been conducted. Using a two-temperature (solid-fluid) approach, an analytical description of one-dimensional Cartesian conduction and convection within a porous medium was developed by Lee and Vafai [14]. Similar modeling of forced convection and conduction within open-cell, high-porosity metal foams has been achieved and described in terms of a thermal efficiency [15–20] similar to the traditional efficiency of thin solid fins [21]. In a related study, heat transfer within

* Corresponding author.
E-mail address: John.Robert.Stark@gmail.com (J.R. Stark).

http://dx.doi.org/10.1016/j.ijheatmasstransfer.2017.03.041
0017-9310/

Nomenclature

A	area (m^2)
r', $\tilde{r}$	geometric constants
c_p	specific heat at constant pressure (J/kg K)
D	diameter, unit cell length (m)
h	convection coefficient (W/m^2 K)
H	height (m)
k	thermal conductivity (W/m K)
K	permeability (m^2)
K_{loss}	loss coefficient (m^{-1})
L	length (m)
LMTD	log mean temperature difference (°C)
m	porous matrix constant (m^{-1})
$\dot{m}$	mass flow rate (kg/s)
Nu	Nusselt number
p	pressure (Pa)
Pr	Prandtl number
q	heat rate (W)
q'	heat rate per unit length (W/m)
r	radius (m)
r_1, r_2	inner radius, outer radius (m)
R	thermal resistance (K/W)
R'	length based thermal resistance (m K/W)
R''	area based thermal resistance (m^2 K/W)
Re	Reynolds number
T	temperature (°C)
t	thickness (m)
u	velocity (m/s)
V	volume (m^3)
W	width (m)
x, y, z	coordinate directions

Greek

α_v	surface area per unit volume (m^2/m^3)
ε	porosity
η	porous matrix efficiency
θ	excess temperature (°C)
μ	dynamic viscosity (Pa s)
ρ	density (kg/m^3)

Superscripts

–	average

Subscripts

0, 1	Bessel series order
a	annular
b	base, bottom
c	characteristic, condenser, contact, cross-section
ch	channel
$cond$	conduction
$conv$	convection
e	evaporator
eff	effective
f	fiber, fluid, foam
hp	heat pipe
hs	heat spreader
i	insulation
in	insert
lm	logarithmic mean
o	outlet
p	pore
r	radial
s	solid, surface
t	top
tc	thermocouple
tp	thermal paste
sq	square
tot	total
∞	ambient

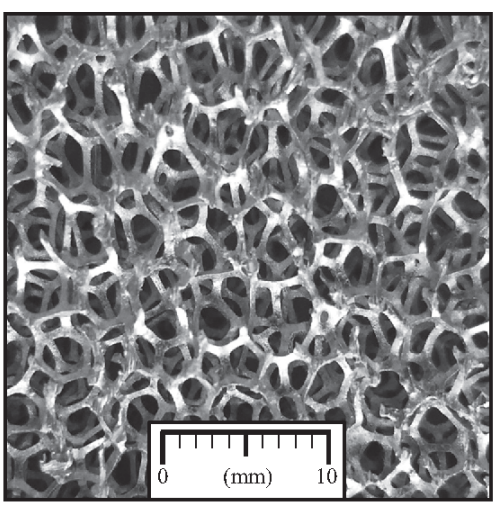

Fig. 1. Photograph of 10 PPI aluminum Duocel® foam.

annular porous media experiencing forced convection within a concentric tube heat exchanger that is filled with aluminum foam was analytically described by Zhao et al. [22]. Experimental and numerical investigations of a cylinder with an attached annular foam block have been performed by T'Joen et al. [23] and Odabaee et al. [24], respectively.

In this study, (i) a continuum-based, analytical description for conduction and forced convection heat transfer within an annular porous matrix attached concentrically to a circular tube, reported in terms of a thermal efficiency, will be developed, (ii) a continuum-based numerical model will be used to develop a semi-analytical expression for the thermal efficiency of a cubical porous block attached on-center to a circular tube, and (iii) the thermal behavior predicted with the semi-empirical expression will be compared to experimental measurements conducted with convectively cooled foam blocks of square cross section attached on-center to a nearly isothermal warm cylinder (heat pipe) using a unique experimental setup.

2. Analytical continuum model for annular, foam-based extended surfaces

Consider a cool, ambient fluid that is forced through an open-cell, annular metal foam block that is attached to the exterior of a hot cylindrical tube (or heat pipe), as illustrated in Fig. 2(a). Consistent with standard fin analyses [21], steady, one-dimensional conduction heat transfer in the radial direction is assumed. In addition, the block is taken to be isotropic with constant properties, and both (i) radiation heat transfer and (ii) heat transfer in the radial direction at $r = r_2$ are assumed to be negligible. The fluid flow

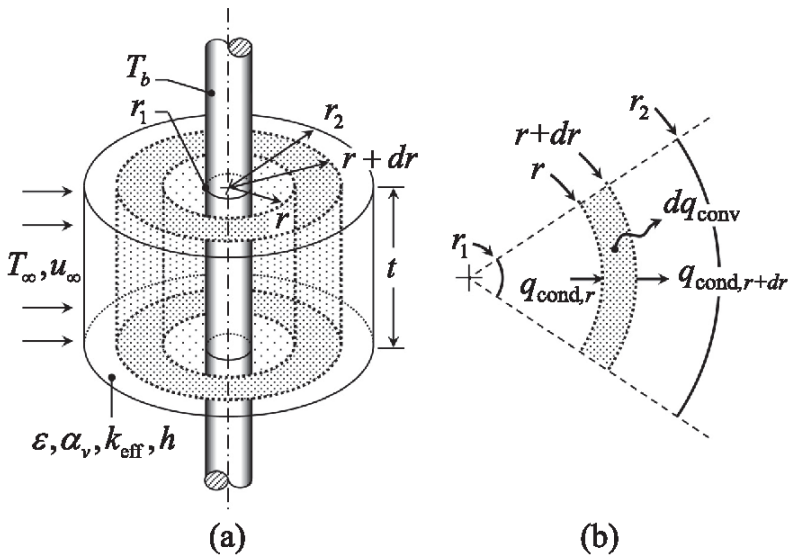

Fig. 2. Description of the 1D annular analytical domain. (a) Overall domain, (b) annular control volume energy balance.

within the porous material is assumed to provide a uniform convection coefficient between the fluid and solid phase, and is described by a characteristic temperature, that is either (i) that of the ambient fluid (as in the analysis below) or (ii) an appropriate log-mean temperature (as in the comparison of model predictions with experimental results to be discussed later). Conduction within the gas can be shown to be negligible for the porous medium and fluid of interest here, and is neglected.

2.1. Analysis

Applying conservation of thermal energy to a radial differential element within the porous cylindrical block, as illustrated in Fig. 2 (b), yields

$$\frac{d^2T}{dr^2}+\left(\frac{1}{A_{c,r}}\frac{dA_{c,r}}{dr}\right)\frac{dT}{dr}-\left(\frac{1}{A_{c,r}}\frac{\bar{h}}{k_{s,\text{eff}}}\frac{dA_s}{dr}\right)(T-T_\infty)=0 \tag{1}$$

where the first and second terms are associated with the radial conduction through the solid phase of the metal foam, and the third term represents the convection heat transfer from the solid phase to the fluid. The area normal to conduction in the radial direction and the differential surface area experiencing convection are

$$A_{c,r}=2\pi rt \quad \text{and} \quad dA_s=\alpha_v dV=\alpha_v d\left[t(r^2-r_1^2)\pi\right] \tag{2a, 2b}$$

respectively. Here, α_v is the specific surface area (surface area per unit volume) of the porous medium and $k_{s,\text{eff}}$ is the effective thermal conductivity of the solid phase. The heat transfer coefficient within the medium, $\bar{h}$, represents the spatially averaged value of the local heat transfer coefficient, h, at the metal-fluid interfaces. Defining an excess temperature, $\theta(r)\equiv T(r)-T_\infty$, Eq. (1) may be simplified to

$$\frac{d^2\theta}{dr^2}+\frac{1}{r}\frac{d\theta}{dr}-m^2\theta=0 \quad \text{where} \quad m^2=\frac{\bar{h}\,\alpha_v}{k_{s,\text{eff}}} \tag{3}$$

When solved under the boundary conditions of (i) constant base temperature, $\theta(r_1)=\theta_b$, and (ii) adiabatic behavior at the outer radius of the annular block, $(d\theta/dr)|_{r_2}=0$, expressions for the annular porous matrix heat rate and porous matrix efficiency for the annular block, $\eta_a\equiv q(r_1)/\left[\bar{h}\alpha_v t(r_2^2-r_1^2)\theta_b\right]$ may be written as

$$q(r_1)=2\pi k_{s,\text{eff}}r_1 t\theta_b m\frac{K_1(mr_1)I_1(mr_2)-I_1(mr_1)K_1(mr_2)}{K_0(mr_1)I_1(mr_2)+I_0(mr_1)K_1(mr_2)} \tag{4}$$

and

$$\eta_a=\frac{\bar{\theta}}{\theta_b}=\frac{2r_1}{m(r_2^2-r_1^2)}\left(\frac{K_1(mr_1)I_1(mr_2)-I_1(mr_1)K_1(mr_2)}{K_0(mr_1)I_1(mr_2)+I_0(mr_1)K_1(mr_2)}\right) \tag{5}$$

respectively. Note that the metal surface area at $r=r_2$ is small compared to the surface area within the porous array, justifying the use of the adiabatic tip condition. The porous matrix efficiency, η_a, is analogous to the traditional fin efficiency [21] and leads to an expression for the equivalent thermal resistance associated with the combined conduction and convection processes within the foam, which may be defined as

$$R_{f,a}=\frac{\theta_b}{q(r_1)}=\frac{1}{A_s\eta_a\bar{h}}=\frac{1}{\alpha_v t\pi(r_2^2-r_1^2)\eta_a\bar{h}} \tag{6}$$

The preceding thermal resistance may be utilized in resistance-based analyses of complex thermal systems such as those described in [21,25–27] In addition, a resistance per unit cylinder length may be defined as

$$R'_{f,a}=\frac{\theta_b}{q'(r_1)}=\frac{t}{A_s\eta_a\bar{h}}=\frac{1}{\alpha_v(r_2^2-r_1^2)\pi\eta_a\bar{h}} \tag{7}$$

2.2. Determination of α_v, $k_{s,\text{eff}}$, and $\bar{h}$

Implementation of the preceding analysis necessitates quantification of the relevant geometric and transport terms, α_v, $k_{s,\text{eff}}$, and $\bar{h}$. The values of the terms may be specified, or calculated using appropriate sub-models for specific types of foams and operating conditions. The porous medium used to demonstrate the application of the analytical solutions and in the experiments of Section 4 is an open-cell, aluminum foam (Duocel® Al 10-44) characterized by a measured porosity of $\varepsilon=0.941$ and a nominal pore size of 10 pores per inch (PPI). The methodology of Calmidi [28] is used to determine a characteristic pore size, D_p, based upon the pore density (expressed in PPI or pores per meter, PPM) and the porosity, ε, as in Eq. (8a) [28]. The characteristic metal fiber diameter of

the foam, D_f, is then the difference between the average unit cell length, D (that includes both pores and fibers), and D_p as expressed in Eq. (8b) [28].

$$D_p = \frac{1}{PPI(or\ PPM)}\left(1 - 2\sqrt{\frac{(1-\varepsilon)}{3\pi}}\right); \quad D_f = D - D_p \tag{8a; 8b}$$

The specific surface area is then determined from the values of D_f and D_p [28] as

$$\alpha_v = \frac{3\pi D_f}{D_p^2} \tag{9}$$

Many models for the effective thermal conductivity of aluminum foams have been reported, as recently reviewed by Wang and Li [29]. To be consistent with Eq. (1), an analytically derived correlation for the effective thermal conductivity within only the solid phase, $k_{s,\text{eff}}$ for Duocel® aluminum foams [30] is utilized

$$k_{s,\text{eff}} = \left[\frac{2}{\sqrt{3}}\left(\frac{r'\tilde{r}}{(1+\tilde{r})k_s} + \frac{(1-r')\tilde{r}}{\frac{2}{3}\tilde{r}k_s} + \frac{\frac{\sqrt{3}}{2}-\tilde{r}}{\frac{4r'}{3\sqrt{3}}\tilde{r}k_s}\right)\right]^{-1} \tag{10}$$

where $r' = 0.09$ and $\tilde{r}$ is a geometric parameter expressed as

$$\tilde{r} = \frac{-r' + \sqrt{r'^2 + 4(1-\varepsilon)\frac{\sqrt{3}}{6}\left[2 - r'\left(1+\frac{4}{\sqrt{3}}\right)\right]}}{\frac{2}{3}\left[2 - r'\left(1+\frac{4}{\sqrt{3}}\right)\right]} \tag{11}$$

Local (equal to area-averaged) heat transfer coefficients are calculated via an experimentally derived correlation provided by Park et al. [18], where the Nusselt and Reynolds numbers are based upon the metal fiber's characteristic diameter, D_f, and the Reynolds number, $Re_{D_f} = u_p D_f/\nu_f$, is a function of the average pore velocity ($u_p = u_\infty/\varepsilon$).

$$Nu_{D_f} = \frac{\bar{h}D_f}{k_f} = 0.039 Re_{D_f}^{0.8} Pr^{0.4} \tag{12}$$

3. Numerical model

Porous metal foams are commercially available in rectangular block forms with a square footprint, suggesting the relevance and importance of extending the preceding analysis for the annular block to square geometries. To do so, a series of numerical simulations involving either square or annular blocks is performed using a consistent set of assumptions as described for the preceding analysis, with the exception that the numerical simulations include three-dimensional effects. The predicted efficiencies associated with the two foam geometries of Fig. 3 are then compared over a range of square block lengths (L_{sq}), annular block radius ratios (r_2/r_1), and porous matrix constants (m) as defined in Eq. (3), in order to describe the square block behavior with expressions similar to Eq. (5).

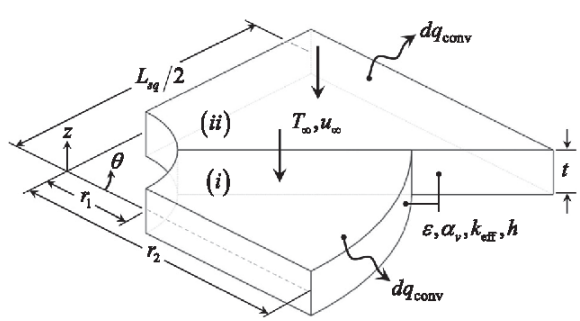

Fig. 3. Numerical domains for the (i) annular and (ii) square geometries.

The gas within the porous medium is assumed to be incompressible. Symmetry is taken advantage of to reduce computational expense, resulting in the 45° computational domains for the (i) annular and (ii) square block cases of Fig. 3. (The annular and square block domains of Fig. 3 are considered independently in the simulations. The 45° square domain represents the smallest possible for that geometry. The 45° annular domain was chosen to match the square domain.) Both geometries are described in terms of a common outer lateral dimension of $r_2 = L_{sq}/2$ and common thickness, t. Heat transfer within each domain is governed by a two-temperature porous model [31], which describes both the moving fluid (air) within the porous medium, and the solid component of the medium (aluminum). Heat transfer and fluid flow within the air are governed by conservation of energy, Eq. (13), conservation of mass, Eq. (14), and conservation of momentum, Eqs. (15a–15c). Momentum conservation is described by the Brinkman-Forchheimer-extended Darcy model [31,32], which includes both pressure loss terms associated with the Darcy coefficient (K) and second order losses (K_{loss}), as calculated using the correlations provided by Calmidi [28].

$$\varepsilon\rho_f c_{p,f}\left(u_x\frac{\partial T_f}{\partial x} + u_y\frac{\partial T_f}{\partial y} + u_z\frac{\partial T_f}{\partial z}\right) = k_{f,\text{eff}}\left(\frac{\partial^2 T_f}{\partial x^2} + \frac{\partial^2 T_f}{\partial y^2} + \frac{\partial^2 T_f}{\partial z^2}\right) + q_{sf} \tag{13}$$

$$\frac{\partial u_x}{\partial x} + \frac{\partial u_y}{\partial y} + \frac{\partial u_z}{\partial z} = 0 \tag{14}$$

$$\frac{\rho_f}{\varepsilon}\left(u_x\frac{\partial u_x}{\partial x} + u_y\frac{\partial u_x}{\partial y} + u_z\frac{\partial u_x}{\partial z}\right) = -\frac{\partial p}{\partial x} + \frac{\mu}{\varepsilon}\left(\frac{\partial^2 u_x}{\partial x^2} + \frac{\partial^2 u_x}{\partial y^2} + \frac{\partial^2 u_x}{\partial z^2}\right) - \frac{\mu}{K}u_x - \varepsilon K_{\text{loss}}\frac{\rho_f\varepsilon}{2}|u|u_x \tag{15a}$$

$$\frac{\rho_f}{\varepsilon}\left(u_x\frac{\partial u_y}{\partial x} + u_y\frac{\partial u_y}{\partial y} + u_z\frac{\partial u_y}{\partial z}\right) = -\frac{\partial p}{\partial y} + \frac{\mu}{\varepsilon}\left(\frac{\partial^2 u_y}{\partial x^2} + \frac{\partial^2 u_y}{\partial y^2} + \frac{\partial^2 u_y}{\partial z^2}\right) - \frac{\mu}{K}u_y - K_{\text{loss}}\frac{\rho_f\varepsilon}{2}|u|u_y \tag{15b}$$

$$\frac{\rho_f}{\varepsilon}\left(u_x\frac{\partial u_z}{\partial x} + u_y\frac{\partial u_z}{\partial y} + u_z\frac{\partial u_z}{\partial z}\right) = -\frac{\partial p}{\partial z} + \frac{\mu}{\varepsilon}\left(\frac{\partial^2 u_z}{\partial x^2} + \frac{\partial^2 u_z}{\partial y^2} + \frac{\partial^2 u_z}{\partial z^2}\right) - \frac{\mu}{K}u_z - K_{\text{loss}}\frac{\rho_f\varepsilon}{2}|u|u_z \tag{15c}$$

Heat transfer in the solid domain is governed by conservation of energy

$$0 = k_{s,\text{eff}}\left(\frac{\partial^2 T_s}{\partial x^2} + \frac{\partial^2 T_s}{\partial y^2} + \frac{\partial^2 T_s}{\partial z^2}\right) + q_{fs} \tag{16}$$

where the heat transferred between the two media is represented by

$$q_{sf} = -q_{fs} = \bar{h}\,\alpha_v(T_s - T_f) \tag{17}$$

The convection coefficient is calculated from Eq. (12) and the specific surface area (associated with the exposed surface area of the solid, shown in Fig. 1) is calculated from Eq. (9).

Both the solid and gas domains are subject to a common base temperature of T_b at r_1. Adiabatic conditions are applied to both the solid and the gas at the outer edges of the two blocks in order to be consistent with the annular domain analysis, while symmetry conditions are assumed along the thin, vertical faces at $\theta = 0°$ and

45° (45° and 90°) for the annular (square) domain of Fig. 3. Adiabatic boundary conditions are applied to the solid at the top and bottom surfaces ($z = \pm t/2$) of the domain. The gas enters the domain normal to the top surface ($z = +t/2$) at a specified ambient temperature and the gas exits the $z = -t/2$ surface at zero relative pressure and with a zero second spatial derivative of the fluid temperature in the z-direction. No-shear velocity conditions are applied at r_1 and r_2 ($L_{sq}/2$) for the annular (square) cases in an effort to maintain uniform flow in the numerical predictions to be consistent with the preceding analysis.

The computational mesh, which was assessed for grid-independence as described in the Appendix, consists of approximately 100,000 elements. Convergence is assumed once all RMS values of all dependent variables are below 10^{-7}. The results reported here entail a total of 476 simulations performed using Ansys CFX (17.1) on a Dell Precision T7600.

4. Experiments

Experiments were conducted to both validate and demonstrate usage of analytical expressions for the efficiency of a square porous matrix, to be developed in Section 5.2.

4.1. Experimental apparatus

A flow channel similar to the one described in Stark et al. [33] was used to generate benchmark data. An electrically heated heat pipe (HP) of cylindrical cross section is used to deliver thermal energy to the bases (at $r = r_1$) of four, stacked square porous block structures which surround the condenser section of the HP. The heat is ultimately transferred to cold air drawn through the channel and porous metal blocks. The channel is similar to (but smaller than) that of Fig. 4 of [33] with a length $L_{ch} = 1.3$ m and cross sectional width and height of $W_{ch} = 100$ mm and $H_{ch} = 120$ mm, respectively.

A copper-H_2O HP with a sintered copper wick (Enertron HP-HD06DI17500BA) is positioned vertically in a HP carrier that can be snapped into place through the bottom of the channel, as shown in Fig. 3a. The HP is of diameter $D_{hp} = 6$ mm and length $L_{hp} = 175$ mm; additional geometric dimensions as well as physical and effective properties are reported elsewhere [33–35]. Within the heavily insulated carrier is a cylindrical aluminum heat spreader (Al 2024-T4; $k_{hs} = 121$ W/m K) which surrounds the evaporator section of the HP of length $L_e = 50.8$ mm. The spreader has an inner (outer) diameter of 6.05 mm (25.4 mm) and a height of $L_{hs} = L_e$. The 0.05 mm gap between the HP and heat spreader is packed with thermal paste (Artic Silver 5; $k_{tp} = 8.7$ W/m K). Thermal energy is provided to the exterior of the heat spreader by an adhesive-backed electrical patch heater (McMaster 35765K634) [33] energized by a DC power supply (Dr. Meter HY3005F-3) and is transferred radially inward to the HP. The power dissipation (heat rate, q) is measured by an ammeter (FLUKE 77 IV; accuracy ±1.5% of reading +2 LSD; resolution 1 mA) and a voltmeter (AMPROBE AM-510; accuracy ±0.8% of reading +1 LSD; resolution 10 mV).

The condenser section of the HP is of length $L_c = 51$ mm and is placed at the centers of four, stacked blocks of high porosity aluminum foam (10 PPI Duocel® Al 10-44), each block with an outer dimension of $L_{sq} = 100$ mm and thickness 12.7 mm, as shown in Fig. 3b. The blocks have a measured average porosity of $\varepsilon = 0.941$. Each foam block is attached to a threaded aluminum insert fabricated of the same alloy as the heat spreader previously described. The solid inserts have inner diameters of 6.05 mm and outer threaded diameters of 25.4 mm with UNC 1-8 threads [36]. To minimize the thermal contact resistance between the foam blocks and the threaded solid inserts, an undersized hole (diameter 5 mm) is first drilled through the center of the foam's largest face, then the insert is screwed into the foam block, crushing the aluminum foam into the screw threads. The 0.05 mm gaps between the inserts and the HP are also packed with Artic Silver thermal paste. Closed-cell styrofoam blocks (100 mm × 100 mm, $L_{i,t} = 55$ mm and $L_{i,b} = 14.2$ mm, $k_i = 0.033$ W/m K) are installed above and below the metal foam blocks to reduce heat losses and ensure that the channel air is directed entirely through the foam matrices.

Detailed information regarding measurement of local temperatures, local and average channel air velocities, as well as the calibration and validation procedures may be found in [33].

4.2. Analysis of experimental measurements

The experiments are used to quantify the thermal resistance of the foam block, R_f, and to test a new expression for the thermal efficiency of the square foam block that is developed in Section 5.2.

Heat is transferred from the electric patch heater to the air within the foam (at either T_∞ or T_{lm}) through the thermal resistance network of Fig. 3c. A local temperature within the heat spreader, of value T_{tc}, is measured at a known radial location as shown in Fig. 3a. The conduction resistance between the location associated with T_c and the inner wall of the heat spreader is calculated to be $R_{hs} = 0.019$ K/W using a one-dimensional conduction analysis [21]. Heat is conducted through the thermal paste ($R_{tp,e} = 0.003$ K/W) to the exterior of the HP evaporator section at temperature $\overline{T_e}$. The complex, multi-phase conduction, convection, and phase change heat transfer mechanisms within the HP walls, wick and working fluid are modeled using the methodology of Sharifi et al. [35], who ultimately reported a thermal resistance of $R_{hp} \approx 0.22$ K/W for the HP used here operating under similar evaporator and condenser wall temperatures. Since the HP evaporator and condenser sections are of equal length, $R_{tp,c} = R_{tp,e}$ while the radial conduction resistance associated with the aluminum inserts is $R_{in,r} = 0.037$ K/W based on a one-dimensional conduction analysis and assuming an outer insert radius located midway between the crown and root of the threading. The contact resistance per unit area between the highly porous metal foam and the threaded aluminum insert is estimated to be $R''_{t,c} = 0.0246$ K m^2/W and is taken from the experimentally derived values reported by Sadeghi et al. [37] for the lowest contact pressure (0.5 MPa), which is applied to the total area of the threading. This yields a thermal resistance of $R_{t,c} = 0.38$ K/W. Note that parasitic heat losses were measured by removing the heat pipe/foam assembly, and were found to be small (approximately 5 percent of the electrical power). The parasitic losses were subtracted from the measured electrical power and the corrected heat transfer rates are used in Section 5.3.

The sum of the thermal resistances between the base of the foam and the location corresponding to T_{tc} is equal to 0.71 K/W. The lone remaining thermal resistance in the network, R_f, is associated with the conjugate heat transfer within the square metal foam. Its value will be determined via a new, semi-analytical expression for the efficiency of the square metal block, to be developed in Section 5.2.

5. Results

5.1. Analytical results and numerical predictions

5.1.1. Validation of the numerical model

Numerically predicted porous matrix efficiencies for the annular porous block, as calculated using Eq. (18), are first compared to the analytically derived efficiency provided in Eq. (5).

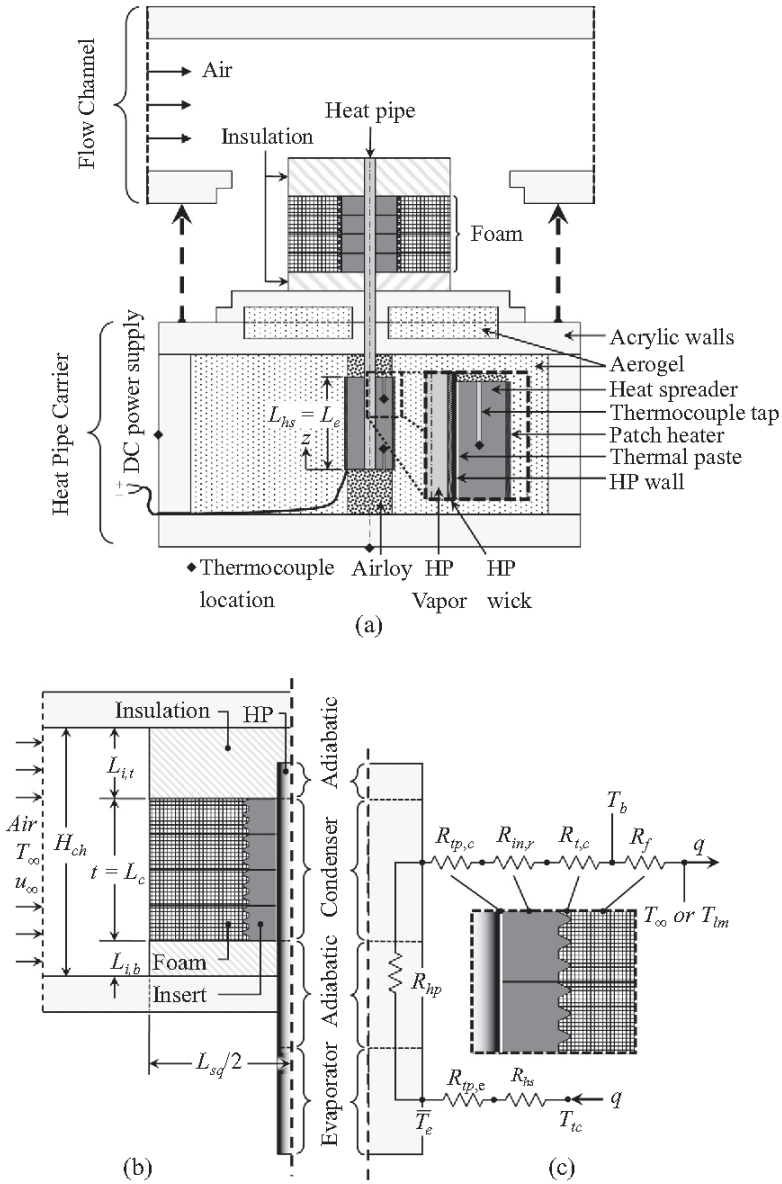

Fig. 4. Experimental setup. (a) Centerline view of the channel and heat pipe carrier, (b) detail of the heat pipe and foam, (c) thermal resistance network.

$$\eta_a \equiv \frac{\int_V \bar{h}\alpha_v[T(x,y,z) - T_\infty]dV}{\bar{h}\alpha_v(T_b - T_\infty)V} \tag{18}$$

For this comparison exercise, an annular block of thickness $t = 1$ mm, outer radius $r_2 = 50$ mm, and various inner radii, r_1, are specified. The base and ambient temperatures are set to $T_b = 60$ °C and $T_\infty = 25$ °C, respectively. The relatively small thickness of the computational domain, in conjunction with a relatively high ambient velocity, $u_\infty = 1$ m/s, limits the numerically predicted temperature rise of the air as it passes through the medium to $\Delta T \lesssim 0.3$ °C, consistent with the assumption of the gas temperature being at its ambient value in the development of Eq. (5). To achieve consistent values of mL_c for a range of inner radii (where $L_c = r_2 - r_1$) convection heat transfer coefficients ($\bar{h}$), specific areas (α_v), and effective solid phase thermal conductivities ($k_{s,\text{eff}}$) were parametrically varied. Specifically, predictions were generated over the ranges $0.001 \le mL_c \le 2.5$ and $1.2 \le r_2/r_1 \le 10$. Gas properties are evaluated at $p = 1$ atm and $T = 25$ °C, while $k_s = 218$ W/m K [38] yielding $k_{s,\text{eff}} = 4.62$ W/m K.

Analytically determined (lines) and numerically predicted values (circles) of the porous matrix efficiencies for the annular block are shown in Fig. 5a. The efficiency decreases as either mL_c or r_2/r_1 increases, in a manner similar to the efficiency behavior of solid, annular fins [21]. Over the entire ranges of mL_c and r_2/r_1 used to generate Fig. 5a, the mean difference between the analytically determined and numerically predicted efficiencies is less than 0.05%. Hence, the numerical model is deemed to be validated.

5.1.2. Numerically predicted efficiencies of annular and square foam blocks

Representative numerically predicted porous matrix efficiencies for annular and square blocks are shown in Fig. 5b–d. The predictions were generated using the same mL_c and r_2/r_1 ranges as in Fig. 5a, but with r_2 replaced by $L_{sq}/2$ when square blocks are con-

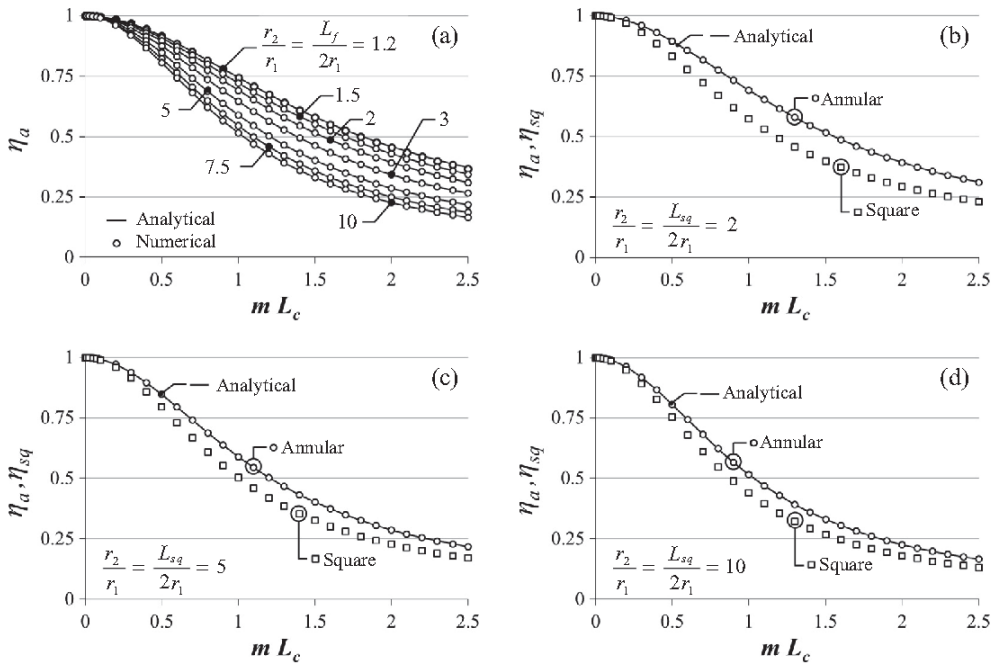

Fig. 5. Analytically- and numerically predicted porous matrix efficiencies versus mL_c. (a) Annular analytical and numerical predictions for $r_2/r_1 = L_{sq}/(2r_1) = 1.2, 1.5, 2, 3, 5, 7.5$, and 10, (b) predicted efficiencies for $r_2/r_1 = L_{sq}/(2r_1) = 2$, (c) predicted efficiencies for $r_2/r_1 = 5$, (d) predicted efficiencies for $r_2/r_1 = L_{sq}/(2r_1) = 10$.

sidered. As evident, the annular block efficiencies are consistently higher than those of the square blocks at any given mL_c value. This is expected due to the relatively low local heat fluxes in the corner regions of the square block, reducing their efficiency relative to that of the annular blocks.

5.2. Mathematical expressions for the efficiency of square foam blocks

The main objective of this investigation is to develop an explicit mathematical expression for the efficiency of square foam blocks attached on center to circular tubes or HPs. The development involves extension of the validated numerical model, and proceeds as follows.

The ratio η_{sq}/η_a, is shown in Fig. 6a for various r_2/r_1 (or $L_{sq}/(2r_1)$) over the range $0.001 \le mL_c \le 2.5$. As expected from Fig. 5, $\eta_{sq}/\eta_a \to 1$ with both efficiencies approaching unity as $mL_c \to 0$. Discrepancies between η_{sq} and η_a increase as the difference in volumes of the annular and square porous blocks increase (as r_2/r_1 decreases). This effect is most prevalent at small values of r_2/r_1; for the $r_2/r_1 = L_{sq}/(2r_1) = 1.2$ case, the square block has 89% more volume than the annular block (and $\eta_{sq}/\eta_a \sim 0.5$ at large mL_c). In contrast, for $r_2/r_1 = 10$ the square block has 28% more foam than the annular block (and $\eta_{sq}/\eta_a \sim 0.8$ at large mL_c).

With the effect of the foam geometry in mind, volume-weighted efficiencies (ηV) were also calculated and are reported in Fig. 6b. In contrast to the dependence of η_{sq}/η_a on mL_c noted in Fig. 6a, the ratio $(\eta_{sq}V_{sq})/(\eta_a V_a) \to 1$ as $mL_c \to \infty$, due to the diminishing involvement of the outermost foam regions in the overall heat transfer process, as the length or diameter of the porous block becomes large. This collapse of volume-weighted efficiencies to similar values for $mL_c \gtrsim 2.5$ is consistent with infinite fin behavior exhibited for $mL_c \gtrsim 2.5$ for traditional fins [21].

Since $\eta_{sq}/\eta_a \to 1$ at small mL_c, and $(\eta_{sq}V_{sq})/(\eta_a V_a) \to 1$ at large mL_c, analytical expressions for the annular porous block may be applied to the square block to determine the square block efficiency at small and large mL_c using η_{sq}/η_a and $(\eta_{sq}V_{sq})/(\eta_a V_a)$, respectively. However, a generalized correlation(s), valid over the entire range of mL_c is desired and is developed as follows.

Use of a function that employs $K_0(mL_c)$ (defined in Eq. (19) and shown in Fig. 6c) appropriately weights the desirable behavior of Fig. 6a evident at small mL_c, with that of Fig. 6b at large mL_c

$$f(mL_c) \equiv K_0(mL_c)\frac{\eta_{sq}}{\eta_a} + (1 - K_0(mL_c))\frac{(\eta_{sq}V_{sq})}{(\eta_a V_a)} \simeq 1 - e^{-2\pi mL_c} \tag{19}$$

and ultimately yields Eq. (20), which can be used to predict η_{sq} solely as a function of mL_c and η_a (as given in Eq. (5)).

$$\eta_{sq} = \frac{1 - e^{-2\pi mL_c}}{\frac{K_0(mL_c)}{\eta_a} + (1 - K_0(mL_c))\frac{V_{sq}}{(\eta_a V_a)}} \tag{20}$$

Square porous block efficiencies determined with (i) the analytically verified numerical model along with Eq. (19) and (ii) Eq. (20) are reported in Fig. 6d. Overall, the agreement between the numerically- and analytically determined efficiencies is good, with the larger discrepancies occurring at the smaller values of mL_c and $L_{sq}/(2r_1)$ (as can be seen upon close inspection of Fig. 6d). However, it should be noted that there exists a value of $L_{sq}/(2r_1)$ below which a single pore would occupy the entire lateral block dimension and use of either the analysis or numerical model of this study would be inappropriate. For the square foam and value of L_{sq} used here, the limit is $L_{sq}/(2r_1)_{,\min} = (L_{sq}/2 + D_p)/r_1 = 1.2$. In addition, since the efficiencies for either the annular or square foam are near unity at small values of mL_c, as evident in Fig. 5b–d, Eq. (5) performs better than Eq. (20) in predicting the efficiency of the square foam block.

The recommended analytical expressions to determine the porous matrix efficiencies of both annular and square blocks are listed in Table 1. Also shown are the recommended ranges of application as well as the average and maximum discrepancies between the analytical values and numerical predictions. Note that although discrepancies are reported for a limited range of mL_c, the analytical

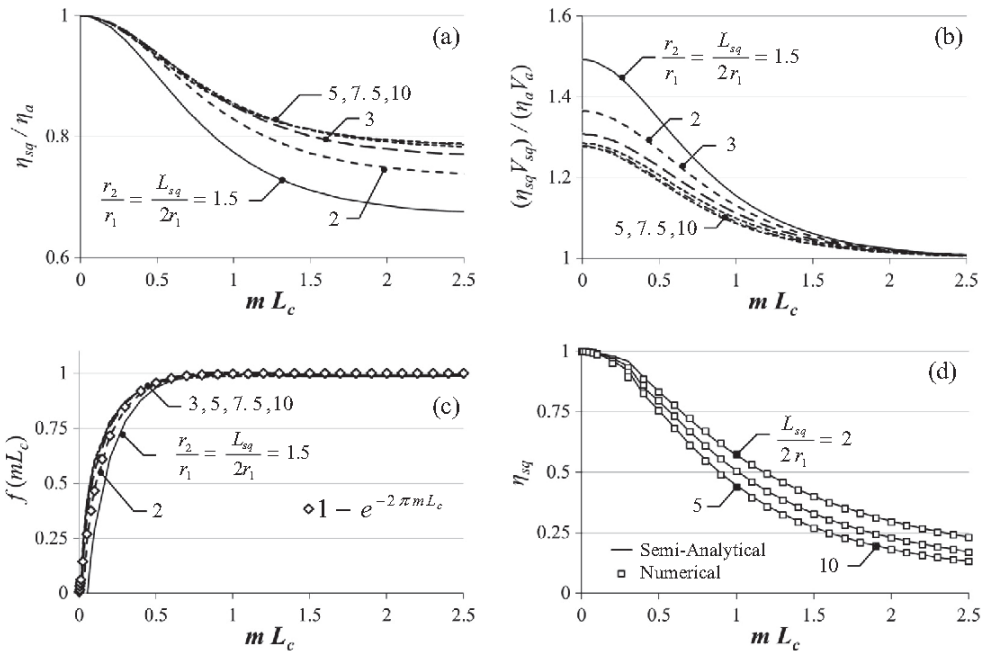

Fig. 6. Relationship of analytically- and numerically predicted porous matrix efficiencies versus mL_c. (a) Ratio of square to annular efficiencies, (b) ratio of square to annular volume-weighted efficiencies, (c) scaled Bessel function from Eq. (20) for various $r_2/r_1 = L_{sq}/(2r_1)$, (d) square semi-analytical and numerical predictions for $L_{sq}/(2r_1) = 1.2$, 1.5, 2, 3, 5, 7.5, and 10.

expressions may be applied to any value of mL_c as evident in Fig. 6c.

5.3. Comparison of predicted and measured heat transfer rates

Eq. (20) is now employed to predict the value of R_f and the experimentally measured heat transfer rates. Experiments were performed with four ambient velocities ($u_\infty = 0.18$, 0.47, 0.86, and 1.16 m/s) for $L_{sq}/(2r_1) = 3.9$. At each velocity three excess temperatures, $\theta = T_{tc} - T_\infty \approx 20$, 35, and 45 °C, were investigated experimentally.

An appreciable increase in the air temperature (defined here to be a maximum increase in its temperature relative to θ_b exceeding 5%) is anticipated for the experimental flow rates and thermal conditions used here, necessitating employment of a log mean temperature difference (LMTD) across the foam resistance of the thermal resistance network of Fig. 3c

$$q = \frac{\text{LMTD}}{R_{f,sq}} \tag{21}$$

where

$$\text{LMTD} = T_b - T_{lm} = \frac{(T_b - T_\infty) - (T_b - T_{f,o})}{\ln\left(\frac{T_b - T_\infty}{T_b - T_{f,o}}\right)} = \frac{T_{f,o} - T_\infty}{\ln\left(\frac{T_b - T_\infty}{T_b - T_{f,o}}\right)} \tag{22}$$

and

$$R_{f,sq} = \frac{1}{\alpha_v t (L_{sq}^2 - \pi r_1^2)\eta_{sq}\bar{h}} \tag{23}$$

where $T_{f,o}$ is the average air temperature at the outlet of the foam. Thermal energy passing from the heat spreader, at T_{tc}, to the base of the foam is

$$q = \frac{T_{tc} - T_b}{R_{\text{tot}-f,sq}} \tag{24}$$

and

$$q = \dot{m}c_{p,f}(T_{f,o} - T_\infty) \tag{25}$$

Eqs. (21) through (25) may be combined to yield

$$q = (T_{tc} - T_\infty)\frac{1 - e^{\frac{1}{\dot{m}c_{p,f}R_{f,sq}}}}{R_{\text{tot}-f,sq} - \left(R_{\text{tot}-f,sq} + \frac{1}{\dot{m}c_{p,f}}\right)e^{\frac{1}{\dot{m}c_{p,f}R_{f,sq}}}} \tag{26}$$

Table 1
Expressions for the porous matrix efficiencies of annular and square porous blocks; $1.5 < r_2/r_1 = L_{sq}/(2r_1) < 10$. Use with Eq. (6) or Eq. (23).

	Recommended expressions	Recommended range	Avg. error (Max. Error)	Eq.
Annular	$\eta_a = \frac{2r_1}{m(r_2^2 - r_1^2)}\left(\frac{K_1(mr_1)I_1(mr_2) - I_1(mr_1)K_1(mr_2)}{K_0(mr_1)I_1(mr_2) + I_0(mr_1)K_1(mr_2)}\right)$	$0 \leqslant mL_c \leqslant \infty$ where $L_c = r_2 - r_1$	0.05% (0.59%) for $0 \leqslant mL_c \leqslant 2.5$	(5)
Square	$\eta_{sq} \approx \frac{2r_1}{m((L_{sq}/2)^2 - r_1^2)}\left(\frac{K_1(mr_1)I_1(mL_{sq}/2) - I_1(mr_1)K_1(mL_{sq}/2)}{K_0(mr_1)I_1(mL_{sq}/2) + I_0(mr_1)K_1(mL_{sq}/2)}\right)$	$0 \leqslant mL_c \leqslant 0.4$ where $L_c = \frac{L_{sq}}{2} - r_1$	0.48% (4.7%) for $0 \leqslant mL_c \leqslant 0.4$	(5)
	$\eta_{sq} = \frac{1 - e^{2\pi m L_{sq}}}{\frac{K_0(mL_{sq})}{\eta_a} + (1 - K_0(mL_{sq}))\frac{V_{sq}}{(\eta_a V_a)}}$	$0.4 < mL_c \leqslant \infty$ where $L_c = \frac{L_{sq}}{2} - r_1$	0.74% (4.7%) for $0.4 \leqslant mL_c \leqslant 2.5$	(20)

where $\dot{m}$ is the mass flow rate of air and air properties are evaluated at $T = (T_b + T_{lm})/2$.

5.3.1. Predicted heat rates

Predicted and measured heat transfer rates are reported in Fig. 7. Note that the uncertainty in the heat rates is ±3% of the reported values, while the uncertainty in the reported values of the measured excess temperatures is ±1%.

The agreement between the predicted and measured heat rates is considered to be excellent. The values of $R_{f,sq}$, determined using Eq. (23), are 0.72, 0.58, 0.48, and 0.43 K/W for the $u_\infty = 0.18$, 0.47, 0.86, and 1.16 m/s cases, respectively.

5.3.2. Experimentally inferred porous matrix resistances

Measured values of $R_{f,sq}$ may be deduced from the experimentally determined heat rates and temperatures in conjunction with the thermal resistance network of Fig. 3c. The values $R_{f,sq}$ are 0.74 ± 0.04, 0.62 ± 0.03, 0.53 ± 0.02, and 0.41 ± 0.01 K/W for the $u_\infty = 0.18$, 0.47, 0.86, and 1.16 m/s cases, respectively, reflecting an average difference of approximately 6% from the values determined from Eq. (23) reported above.

It should be noted that the preceding predictions of q and the inferred values of $R_{f,sq}$ depend on the values of the remaining thermal resistances in the network of Fig. 3c. The resistance with the largest uncertainty is that of the contact between the insert and the foam. Increasing (decreasing) $R''_{t,c}$ by 10% decreases (increases) predicted values of q by approximately 3% and decreases (increases) $R_{f,sq}$ by approximately 7%.

6. Conclusions and recommendations

Novel, analytical expressions have been developed for the thermal efficiency and thermal resistance associated with convection and conduction within an open-cell metal foam (of cylindrical shape) that is attached to a circular tube. Using a two-temperature porous medium numerical model (validated by comparing its predictions to those of the analytical expression), a companion semi-analytical expression for the thermal efficiency of square-shaped, open-cell metal foam blocks attached on-center to a circular tube (Eq. (20)) was also developed. To demonstrate its usage, the semi-analytical model for square foam blocks was employed to predict experimentally measured heat transfer rates, as well as experimentally inferred values of the foam thermal resistances in a unique experimental setup. The new analytical and semi-analytical expressions for the thermal efficiency of both annular and square-shaped foams are summarized in Table 1, along with their broad recommended ranges of application and levels of uncertainty.

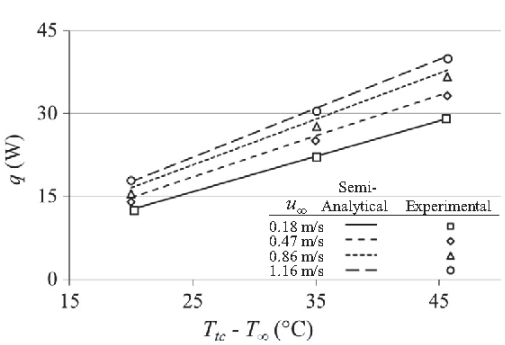

Fig. 7. Experimentally measured and semi-analytical predicted heat rates for a square porous matrix under various ambient velocity and thermal conditions.

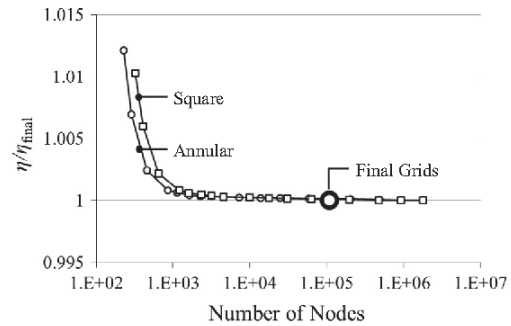

Fig. A1. Predicted efficiencies versus mesh count.

Because the forms of the governing one-dimensional heat equation and boundary conditions for the annular foams considered here are identical to those of a convectively heated or cooled thin, solid annular fin with an adiabatic tip [21], the extension methodology developed in this study may also be used to extend well-known expressions for the thermal efficiency of an annular thin fin [21] to thin fins of square shapes attached on-center to cylindrical tubes. As implied in the discussion of the experimental apparatus and experimental results, novel approaches are desirable to both more accurately quantify and minimize thermal contact resistances at the foam-tube interface.

Acknowledgments

This material is based upon work supported by the National Science Foundation under Grant Nos. 1435131 (University of Kansas) and 1435233 (University of Connecticut). The authors also wish to thank Will Libeer and Trey Fox, as well as Dr. Nourouddin Sharifi, for their assistance in the construction and validation of the experimental apparatus.

Appendix A. Grid independence

Simulations for the square and annular porous media geometries, as outlined in Section 3, were investigated for their grid dependence for the $r_2/r_1 = L_{sq}/(2r_1) = 1.5$ and 5, and 10 geometries and the $mL_c = 0.1$ and 2 cases. The grid dependence study discussed here (corresponding to $r_2/r_1 = L_{sq}/(2r_1) = 10$ and $mL_c = 2$) is representative of all geometries and cases. Results of the predicted efficiency, the volumetrically averaged temperature of the porous matrix, and the heat rate were compared for computational grids ranging from 560 (228) to 1.80 million (1.78 million) nodes for the annular (square) geometries. Convergence was assessed by normalizing the monitored quantities to results corresponding to the highest node count. Predictions for both the annular and square geometries were within 0.1% of the highest resolution results for grids greater than approximately 1200 nodes (e.g., predictions of the porous matrix efficiency are shown in Fig. A1). Grids consisting of of 110,960 and 122,056 nodes were employed for $r_2/r_1 = L_{sq}/(2r_1) = 10$, which produced results within 0.01% of those associated with the highest resolution grid. Similar grids were employed for all geometries and cases.

References

[1] C.Y. Zhao, Review on thermal transport in high porosity cellular metal foams with open cells, Int. J. Heat Mass Transf. 55 (2012) 3618–3632.
[2] I. Ghosh, How good is open-cell metal foam as a heat transfer surface, ASME J. Heat Transfer 131 (2009) 101004–1–8.
[3] L. Tadrist, M. Miscevic, O. Rahli, F. Topin, About the use of fibrous materials in compact heat exchangers, Exp. Thermal Fluid Sci. 28 (2004) 193–199.
[4] D.L. Koch, R.G. Cox, H. Brenner, J.F. Brady, The effect of order on dispersion in porous media, J. Fluid Mech. 200 (1989) 173–188.

[5] T.J. Lu, H.A. Stone, M.F. Ashby, Heat transfer in open-cell metal foams, Acta Mater. 46 (10) (1998) 3619–3635.
[6] P. Du Plessis, A. Montillet, J. Comiti, J. Legrand, Pressure drop prediction for flow through high porosity metallic foams, Chem. Eng. Sci. 49 (21) (1994) 3545–3553.
[7] D. Weaire, R. Phelan, A counter-example to Kelvin's conjecture on minimal surfaces, Philos. Mag. Lett. 69 (1994) 107–110.
[8] K. Boomsma, D. Poulikakos, F. Zwick, Metal foams as compact high performance heat exchangers, Mech. Mater. 35 (12) (2003) 1161–1176.
[9] A. Kopanidis, A. Theodorakakos, E. Gavaises, D. Bouris, 3D numerical simulation of flow and conjugate heat transfer through a pore scale model of high porosity open cell metal foam, Int. J. Heat Mass Transf. 53 (11–12) (2010) 2539–2550.
[10] S. Krishnan, J.Y. Murthy, S.V. Garimella, Direct simulation of transport in open-cell metal foams, ASME J. Heat Transfer 128 (2006) 793–799.
[11] Lord Kelvin (Sir William Thomson), On the division of space with minimum partitional area, Phil. Mag. 24 (151) (1887) 121–134.
[12] M. Iasiello, S. Cunsolo, M. Oliviero, W.M. Harris, N. Bianco, W.K.S. Chiu, V. Naso, Numerical analysis of heat transfer and pressure drop in metal foams for different morphological models, ASME Journal of Heat Transfer 136 (11) (2014) 112601:1–112610:10.
[13] P. Ranut, E. Nobile, L. Mancini, Microtomography-based CFD analysis of transport in open-cell aluminum metal foams, J. Phys: Conf. Ser. 501 (1) (2014) 1–11.
[14] D.Y. Lee, K. Vafai, Analytical characterization and conceptual assessment of solid and fluid temperature differentials in porous media, Int. J. Heat Mass Transf. 42 (3) (1999) 423–435.
[15] V.V. Calmidi, R.L. Mahajan, R.L., Forced convection in high porosity metal foams, ASME, J. Heat Transfer 122 (3) (2000) 557–565.
[16] T. Dixit, I. Ghosh, An experimental study on open cell metal foam as extended heat transfer surface, Exp. Thermal Fluid Sci. 77 (2016) 28–37.
[17] I. Ghosh, Heat transfer correlation for high-porosity open-cell foam, Int. J. Heat Mass Transf. 52 (5–6) (2009) 1488–1494.
[18] S.H. Park, T.H. Kim, J.H. Jeong, Experimental investigation of the convective heat transfer coefficient for open-cell porous metal fins at low Reynolds numbers, Int. J. Heat Mass Transf. 100 (2016) 608–614.
[19] P. De Jaeger, C. T'Joen, H. Huisseune, B. Ameel, S. De Schampheleire, M. De Paepe, Assessing the influence of four cutting methods on the thermal contact resistance of open-cell aluminum foam, Int. J. Heat Mass Transf. 55 (21–22) (2012) 6142–6151.
[20] T.M. Jeng, S.C. Tzeng, Y.H. Hung, An analytical study of local thermal equilibrium in porous heat sinks using fin theory, Int. J. Heat Mass Transf. 49 (11-12) (2006) 1907–1914.
[21] T.L. Bergman, A.S. Lavine, F.P. Incropera, D.P. Dewitt, Fundamentals of Heat and Mass Transfer, seventh ed., Wiley, Hoboken, 2011.
[22] C.Y. Zhao, W. Lu, S.A. Tassou, Thermal analysis on metal-foam filled heat exchangers. Part II: Tube heat exchangers, Int. J. Heat Mass Transf. 49 (15–16) (2006) 2762–2770.
[23] C. T'Joen, P. De Jaeger, H. Huisseune, S. Van Herzeele, N. Vorst, M. De Paepe, Thermo-hydraulic study of a single row heat exchanger consisting of metal foam covered round tubes, Int. J. Heat Mass Transf. 53 (15–16) (2010) 3262–3274.
[24] M. Odabee, K. Hooman, H. Gurgenci, Metal foam heat exchangers for heat transfer augmentation from a cylinder in cross-flow, Transp. Porous Media 86 (3) (2011) 911–923.
[25] S.P. Benn, L.M. Poplaski, A. Faghri, T.L. Bergman, Analysis of thermosyphon/heat pipe integration of dry cooling for thermoelectric power generation, Appl. Therm. Eng. 104 (2016) 358–374.
[26] H. Shabgard, T.L. Bergman, N. Sharifi, A. Faghri, High temperature latent heat thermal energy storage using heat pipes, Int. J. Heat Mass Transf. 53 (15–16) (2010) 2979–2988.
[27] H. Shabgard, M.J. Allen, N. Sharifi, S.P. Benn, A. Faghri, T.L. Bergman, Heat pipe heat exchangers and heat sinks: opportunities, challenges, applications, analysis, and state of the art, Int. J. Heat Mass Transf. 89 (2015) 138–158.
[28] V.V. Calamidi, Transport Phenomenon in High Porosity Fibrous Metal Foams PhD thesis, University of Colorado, Boulder, CO, 1997.
[29] F. Wang, X. Li, The stagnant thermal conductivity of porous media predicted by the random walk theory, Int. J. Heat Mass Transf. 107 (2017) 520–533.
[30] V.V. Calmidi, R.L. Mahajan, The effective thermal conductivity of high porosity fibrous metal foams, ASME J. Heat Transfer 121 (2) (1999) 466–471.
[31] K. Vafai, C.L. Tien, Boundary and inertia effects on flow and heat transfer in porous media, Int. J. Heat Mass Transf. 24 (2) (1981) 195–203.
[32] K. Vafai, S.J. Kim, Forced convection in a channel filled with a porous medium: an exact solution, ASME J. Heat Transfer 111 (4) (1989) 1103–1106.
[33] J.R. Stark, N. Sharifi, T.L. Bergman, A. Faghri, An experimentally verified numerical model of finned heat pipes in crossflow, Int. J. Heat Mass Transf. 97 (2016) 45–55.
[34] N. Sharifi, T.L. Bergman, M.J. Allen, A. Faghri, Melting and solidification enhancement using a combined heat pipe, foil approach, Int. J. Heat Mass Transf. 78 (2014) 930–941.
[35] N. Sharifi, J.R. Stark, T.L. Bergman, A. Faghri, The influence of thermal contact resistance on the relative performance of heat pipe-fin array systems, Appl. Therm. Eng. 105 (2016) 46–55.
[36] E. Oberg, Machinery's Handbook, 29th ed., Industrial Press, New York, 2012, pp. 1815–1867.
[37] E. Sadeghi, S. Hsieh, M. Bahrami, Thermal conductivity and contact resistance of metal foams, J. Phys. D Appl. Phys. 44 (12) (2011), 125406:1-7.
[38] Metals Handbook, 10th ed., v. 2, ASM Handbook Committee, American Society for Metals, USA, 1990.

Paper P4

Title:

Experimentally validated analytical expressions for the thermal resistance of a novel composite fin-foam annular array

Authors:

John R. Stark

Chadwick D. Sevart

Theodore L. Bergman

Journal:

Applied Thermal Engineering (Subitted)

Note: The publication is still in the review process, and as a result the submitted format is included here.

Abstract

Novel expressions are developed for the thermal resistance associated with an array consisting of periodic layers of metal fins and open-cell, high porosity metal foam attached annularly to a base cylinder. Predictions generated with the new expressions are verified by comparison with experimental measurements involving such an array and a cylindrical heat pipe. Parametric simulations are performed to assess the performance of the array over a range of geometric configurations, thermal contact resistances, and air velocities. Analytically predicted heat rates for an annular fin array, a foam-only annular array, and the new combined fin-foam array are compared, illustrating the improved thermal performance made possible by combining metal fins and foam into a composite array.

Keywords

Metal Foam; Porous Media Convection; Fin and Foam Array; Heat Pipe

Nomenclature

A	area (m^2)
c_p	specific heat at constant pressure (J/kg K)
D	diameter, unit cell length (m)
h	convection coefficient (W/m^2 K)
H	height (m)
k	thermal conductivity (W/m K)
L	length (m)
m_{fm}	porous matrix constant (m^{-1})
m_{fn}	fin constant (m^{-1})
$\dot{m}$	mass flow rate (kg/s)
N	number of unit pitches
Nu	Nusselt number
Pr	Prandtl number
PPI , PPM	pores per inch, pores per meter (m^{-1})
q	heat rate (W)
r, z	coordinate directions
r_1, r_2	inner radius, outer radius (m)
r', $\tilde{r}$	geometric constants
R	thermal resistance (K/W)
R''	area based thermal resistance (m^2 K/W)
Re	Reynolds number
S	unit pitch (m)
t	fin thickness (m)
T	temperature (°C)
u	velocity (m/s)
U	overall heat transfer coefficient (W/m^2 K)
W	width (m)
Greek	
α_v	surface area per unit volume (m^2/m^3)
ε	porosity

η	porous matrix efficiency
θ	excess temperature (˚C)

Superscripts

$\bar{}$	average

Subscripts

app	apparatus
b	base, bottom
c	cell, characteristic, condenser
ch	channel
cond	conduction
conv	convection
cyl	base cylinder
e	evaporator
eff	effective
f	fiber, fluid
ff	composite fin-foam
fm	foam
fn	fin
hp	heat pipe
hs	heat spreader
i	insulation
in	insert
lm	logarithmic mean
max	maximum
p	pore
r	radial
s	solid, surface
sq	square
S	per unit pitch

t	top
t,c	thermal contact
tc	thermocouple
tp	thermal paste
tot	total
∞	ambient

1. Introduction

Open-cell, high-porosity metal foams have many possible heat transfer applications due to their large surface area to volume ratios [1-4]. As a result, metal foams are generally associated with low thermal resistances per unit volume; however, they also exhibit low effective thermal conductivities due to their high porosities. When employed as an extended surface, these factors contribute to relatively large temperature gradients in the foam (and as a result, a lower thermal surface efficiency) when compared to traditional fins. In an effort to overcome this limitation, several thermal management devices comprised of both metal foam and solid metal fins have been proposed.

Heat sinks comprised of traditional linear fins of uniform thickness with metal foams filling the intermittent spaces were first proposed by Bhattacharya and Mahajan [5-6]. Subsequent numerical [7-9] and experimental [9-10] work assessed the performance of such arrays. The impact of thermal contact resistance between the fin and foam for this configuration was investigated by DeGroot et al. [11], who found the thermal performance of the array to exceed that of a corresponding traditional fin array, even if there is an infinitely large thermal contact resistance between the two media. Similar geometries for which a porous medium constructed of a 3D-printed solid matrix with a prescribed periodic unit cell geometry have been proposed by Hernon et al. [13]. Seyf and Layeghi [12] performed numerical analysis of a foam-filled pin fin array. Foam-filled flat plate heat exchangers, first proposed by Kim [14], have been proposed to include solid metal fins that penetrate into the foam to promote conduction into the foam [15].

Like metal foams, incorporation of heat pipes (HPs) can improve heat exchanger performance due to their low thermal resistances [16-17]. However, the overall resistance of thermal management systems incorporating HPs (or thermosyphons) is often dominated by

convective resistances external to the HP when air cooling is used [18-19]. Therefore, extended surfaces are routinely attached to HPs (which are typically of cylindrical cross section). Metal foam attached externally to a base cylinder have been modeled experimentally [20-23], numerically [23-24], and analytically [23].

Unlike annular foam or fin arrays, little research has been devoted to combined annular fin-foam arrays with a cylindrical base. Jeng and Tzeng [25] experimentally investigated an array consisting of an axially-finned cylinder, where the space between the longitudinal fins have attached metal foam, and the authors report up to a 78% reduction in the arrays thermal resistance. To the authors' knowledge, no studies have been undertaken to characterize a system where periodic fin-foam layers are attached orthogonally to a cylinder.

The objective of this study is to propose a novel, analytical model to quantify the thermal resistance and heat transfer from a combined fin-foam annular array. Model predictions will be compared to experimentally measured heat rates. Parametric simulations will be performed to assess the sensitivity of heat rates and thermal resistances to the array's geometrical configuration, thermal contact resistances, and the air velocity. Finally, comparisons are made between predicted heat rates for the combined fin-foam array, and those of (*i*) a bare cylinder, (*ii*) an annular fin array, and (*iii*) a foam-only annular array to demonstrate the advantages of combining solid fins and metal foam in an annular array configuration.

2. Analytical model of a composite annular fin and foam extended surface

An approximate analytical model of the composite annular fin-foam array shown in Fig. 1(a) is developed to predict thermal efficiencies, resistances and heat rates when experiencing convective cooling (or heating). The model approximates the complex, three-dimensional conduction and convection heat transfer in a manner that builds upon a standard annular fin analysis [26].

The analysis is performed for a representative axial segment of a composite fin-foam array, of characteristic unit pitch S, as shown in Fig. 1(a). A number of assumptions, consistent with those of Stark et al. [23], are employed. The open-cell foam is assumed to be geometrically isotropic with constant properties, and it is assumed that radiation heat transfer is negligible. Conduction within the fluid is neglected, as it can be shown to have a negligible impact on heat transfer for the materials and operating conditions considered here. Fluid flowing through the

foam is assumed to provide uniform convection coefficients between the solid foam and the fluid, as well as between exposed fin and cylinder surfaces and the fluid. The constant property, incompressible fluid is described by either (*i*) the ambient fluid temperature (as in the analysis below or for cases where the temperature variation of the fluid is negligible) or (*ii*) an appropriate log-mean temperature (as will be employed in the experimental analysis and the parametric simulations to be presented later). Additional assumptions are noted in the following discussion.

2.1. Annular composite fin-foam model

Assuming one-dimensional conditions in the radial direction, application of conservation of thermal energy to a differential radial element, shown within the fin (of thickness *t*) of Fig. 1(b), yields

$$\frac{d^2T_{fn}}{dr^2}+\frac{1}{r}\frac{dT_{fn}}{dr}-\frac{2U}{k_{fn,\mathrm{eff}}t}\left(T_{fn}-T_\infty\right)=0 \tag{1}$$

An effective fin thermal conductivity, $k_{fn,\mathrm{eff}} > k_{fn}$, and overall heat transfer coefficient, U, are introduced in Eq. (1). As detailed in Section 2.2, $k_{fn,\mathrm{eff}}$ is applied to the fin of thickness t, but accounts for radial conduction in both the solid fin and solid foam matrix. The overall coefficient accounts for (*i*) convection from the portions of the fin surface that are exposed directly to the fluid and (*ii*) conduction from the surface of the fin to the solid foam through a potential thermal contact resistance. Heat transfer to the solid foam by conduction from the fin is ultimately transferred to the fluid by convection.

By defining an excess fin temperature, $\theta_{fn}\equiv T_{fn}\left(r\right)-T_\infty$, Eq. (1) may be reduced to

$$\frac{d^2\theta_{fn}}{dr^2}+\frac{1}{r}\frac{d\theta_{fn}}{dr}-m_{fn}^2\theta_{fn}=0 \quad \text{where} \quad m_{fn}^2=\frac{2U}{k_{fn,\mathrm{eff}}t} \tag{2}$$

Applying radial boundary conditions of (*i*) constant base temperature, $\theta(r_1) = \theta_b$, and (*ii*) adiabatic behavior at the outer radius of the array, $\left(d\theta/dr\right)\big|_{r_2}=0$, to Eq. (2) leads to expressions for the fin efficiency

$$\eta_{fn}=\frac{2r_1}{m_{fn}\left(r_2^2-r_1^2\right)}\left(\frac{K_1\left(m_{fn}r_1\right)I_1\left(m_{fn}r_2\right)-I_1(m_{fn}r_1)K_1(m_{fn}r_2)}{K_0\left(m_{fn}r_1\right)I_1\left(m_{fn}r_2\right)+I_0(m_{fn}r_1)K_1(m_{fn}r_2)}\right) \tag{3}$$

and the thermal resistance of the fin

$$R_{fn} = \frac{\theta_b}{q_{fn}(r_1)} = \frac{1}{A_{fn}\eta_{fn}U} = \frac{1}{2\pi\left(r_2^2 - r_1^2\right)\eta_{fn}U} \tag{4}$$

Heat transfer by convection also occurs at the exposed surface of the cylinder ($r = r_1$) that is not in contact with the solid foam matrix and is represented as

$$R_{\text{conv,cyl}} = \frac{1}{\varepsilon A_{\text{cyl}}\bar{h}_{\text{cyl}}} = \frac{1}{\varepsilon 2\pi r_1 (S-t)\bar{h}_{\text{cyl}}} \tag{5}$$

where the convection heat transfer coefficient is determined as discussed in Section 2.4. The overall resistance to heat transfer in the radial direction at $r = r_1$ for a representative unit pitch of the array is therefore given by

$$R_{ff,S} = \left(R_{fn}^{-1} + R_{\text{conv,cyl}}^{-1}\right)^{-1} \tag{6}$$

or, for an array with N number of repeating pitches

$$R_{ff} = \left[N\left(R_{fn}^{-1} + R_{\text{conv,cyl}}^{-1}\right)\right]^{-1} \tag{7}$$

If a thermal contact resistance exists at the root of the fin and the solid phase of the foam, Eq. (6) may be modified to

$$R_{ff,S} = \left(R_{\text{conv,cyl}}^{-1} + \left(R_{fn} + R_{t,c-b}\right)^{-1}\right)^{-1} \quad \text{where} \quad R_{t,c-b} = R''_{t,c-b}/\left(2\pi r_1 S\right) \tag{8}$$

and Eq. (7) may be modified accordingly. The contact resistance is described further in Section 2.4.

2.2. Determination of $k_{fn,\text{eff}}$

The effective thermal conductivity of Eq. (1), $k_{fn,\text{eff}}$, is determined by equating its corresponding radial thermal resistance (for the fin of thickness t) to the radial thermal resistance posed by conduction in the fin and foam

$$\frac{1}{R_{\text{cond},fn,\text{eff}}} = \frac{1}{R_{\text{cond},fn}} + \frac{1}{R_{\text{cond},fm}} \quad \text{or} \quad \frac{2\pi t k_{fn,\text{eff}}}{\ln(r_2/r_1)} = \frac{2\pi t k_{fn}}{\ln(r_2/r_1)} + \frac{2\pi(S-t)k_{fm,\text{eff}}}{\ln(r_2/r_1)} \tag{9}$$

which may be simplified to

$$k_{fn,\text{eff}} = k_{fn} + \frac{S-t}{t}k_{fm,\text{eff}} \tag{10}$$

The effective thermal conductivity within the solid phase of the foam, $k_{fm,\mathrm{eff}}$, is taken from the analytically derived correlation of Calmidi and Mahajan [27]

$$k_{fm,\mathrm{eff}} = \left[\frac{2}{\sqrt{3}} \left(\frac{r'\tilde{r}}{\left(1+\tilde{r}\right)k_s} + \frac{\left(1-r'\right)\tilde{r}}{\frac{2}{3}\tilde{r}k_s} + \frac{\frac{\sqrt{3}}{2}-\tilde{r}}{\frac{4r'}{3\sqrt{3}}\tilde{r}k_s} \right) \right]^{-1} \tag{11}$$

where $r' = 0.09$, $\tilde{r}$ is a geometric parameter expressed as

$$\tilde{r} = \frac{-r' + \sqrt{r'^2 + 4\left(1-\varepsilon\right)\frac{\sqrt{3}}{6}\left[2 - r'\left(1+\frac{4}{\sqrt{3}}\right)\right]}}{\frac{2}{3}\left[2 - r'\left(1+\frac{4}{\sqrt{3}}\right)\right]} \tag{12}$$

and k_s is the thermal conductivity of the solid phase of the foam.

2.3. Determination of U

Heat transfer at the upper and lower fin surfaces occurs by (*i*) conduction to the solid phase of the foam (after passing through a potential contact resistance) and (*ii*) direct convection to the fluid. The two processes are represented by the thermal resistance network shown in Fig. 1(c).

Conduction to the foam is handled as if it were a Cartesian extended surface of thickness *dr* and length (*S*-*t*)/2, allowing a thermal efficiency to be defined in a manner similar to classical analysis of a fin with a uniform cross section [26]. A similar approach for modeling metal foams has been taken elsewhere [28-32]. An energy balance applied to the annular *dr* element illustrated in Fig. 1(b) yields

$$\frac{d^2T_{fm}}{dz^2} - \frac{\alpha_v \bar{h}_{fm}}{k_{s,\,\mathrm{eff}}}\left(T_{fm} - T_\infty\right) = 0 \tag{13}$$

where the first term represents the net conduction heat transfer into a *dz* element and the second term represents the convection heat transfer from the solid phase of the foam within the element to the fluid. The convection heat transfer coefficient is determined as described in Section 2.4. Equation (13) may be simplified by defining an excess temperature, $\theta_{fm} \equiv T_{fm}\left(z\right) - T_\infty$, yielding

$$\frac{d^2\theta_{fm}}{dz^2} - m_{fm}^2\theta_{fm} = 0 \qquad \text{where} \qquad m_{fm}^2 = \frac{\alpha_v \bar{h}_{fm}}{k_{s,\,\mathrm{eff}}}$$

(14)

Equation (14) is applied from the interface between the fin and foam (at $z = t/2$) to the plane midway between two adjacent solid fins (at $z = (S\text{-}t)/2$). The thermal boundary conditions associated with these two planes are (*i*) a yet-to-be-determined radially dependent base temperature, $\theta_{fm,\mathrm{b}}(r) = T_{fm,\mathrm{b}}(r, z = t/2) - T_\infty$, and (*ii*) adiabatic conditions at $z = (S\text{-}t)/2$ due to symmetry. When solved under these conditions, the *z*-direction heat flux at the base of the axial foam segment and the associated thermal resistance per unit base area are

$$q''_{fm} = m_{fm} k_{fm,\,\mathrm{eff}} \tanh\left(m_{fm}\frac{S-t}{2}\right)\theta_{fm,b}(r) \tag{15a}$$

and

$$R''_{fm} = \left[m_{fm} k_{fm,\,\mathrm{eff}} \tanh\left(m_{fm}\frac{S-t}{2}\right)\right]^{-1} \tag{15b}$$

The thermal resistance R''_{fm} is utilized in the resistance network of Fig. 1(c). The remaining two thermal resistances are associated with (*i*) the contact between the fin and solid phase of the foam, $R''_{t,c-ff}$, and (*ii*) the convection from the exposed surface of the fin

$$R''_{\mathrm{conv},fn} = \frac{1}{\varepsilon \bar{h}_{fn}} \tag{16}$$

which allows the equivalent overall heat transfer coefficient to be written as

$$U = \varepsilon \bar{h}_{fn} + \left\{R''_{t,c-ff} + \left[m_{fm} k_{s,\,\mathrm{eff}} \tanh\left(m_{fm}\frac{S-t}{2}\right)\right]^{-1}\right\}^{-1} \tag{17}$$

Quantification of $R''_{t,c-ff}$ and $\bar{h}_{fm}$ is described in the next section.

2.4. Determination of α_v, $\bar{h}_{fm}$, $\bar{h}_{fn}$, $\bar{h}_{\mathrm{cyl}}$, $R''_{t,c-b}$, *and* $R''_{t,c-ff}$

Values of various parameters introduced in the preceding sections depend on the porous medium and operating conditions of interest. The medium employed in the experiments (described in Section 3) is an open-cell, high-porosity aluminum foam (Duocel® Al 10-44) with

a nominal pore size of 10 pores per inch (PPI) and a measured porosity of $\varepsilon = 0.941$. The characteristic pore size, D_p, is determined as a function of the pore density, expressed in terms of PPI or pores per meter (PPM), and the volume porosity, ε, as in Eq. (18a) [33]. The characteristic diameter of the metal fibers of the foam, D_f, is determined by taking the difference between the average unit cell length, D_c (which includes both fibers and pores), and D_p, as shown in Eq. (18b)

$$D_p = \frac{1}{PPI(or\ PPM)}\left(1 - 2\sqrt{\frac{1-\varepsilon}{3\pi}}\right);\ D_f = D_c - D_p \tag{18a;18b}$$

The surface area per unit volume of foam, (also known as the specific surface area) is determined from the values of D_p and D_f as [33]

$$\alpha_v = \frac{3\pi D_f}{D_p^2} \tag{19}$$

The area-averaged heat transfer coefficient between the solid and fluid phases of the foam is determined by an experimentally derived correlation [28]

$$\overline{Nu}_{D_f} = \frac{\bar{h}_{fm} D_f}{k_f} = 0.039 Re_{D_f}^{0.8} Pr^{0.4} \tag{20}$$

in which D_f is the length scale in both the Reynolds and Nusselt numbers, and the average pore velocity

$$u_p = u_\infty \left[\frac{S}{\varepsilon(S-t)} \frac{\pi r_2^2}{\left(\pi r_2^2 - \pi r_1^2\right)}\right] \tag{21}$$

is utilized in calculating the Reynolds number. The velocity u_∞ is the average air velocity immediately upstream of the array through the projected area $2r_2NS$.

To the authors' knowledge there are no existing correlations that describe the convection heat transfer coefficients for the exposed fin and cylinder surfaces in the configuration presented here. However, for similar geometries without the presence of foam, it has been shown that by approximating the fins and cylindrical segments as flat plates and plain cylinders, respectively, analytically determined coefficients are in close agreement with those determined by detailed numerical modeling [23]. Accordingly, a correlation for the area-averaged heat transfer coefficient associated with a flat plate attached to a porous medium experiencing forced convection [34]

$$\overline{Nu}_{L_{fn}} = \frac{\bar{h}_{fn} L_{fn}}{k_f} = 1.128\left(Re_{L_{fn}} Pr\right)^{1/2} \tag{22}$$

is used to approximate $\bar{h}_{fn}$. The characteristic length of the fin, L_{fn} (=$2r_2$), and the average pore velocity are used in the Reynolds and Nusselt numbers.

Similarly, the convection heat transfer coefficient associated with the exposed surface of the cylindrical segment between adjacent fins (at $r = r_1$), $\bar{h}_{\text{cyl}}$, is determined using a correlation for a cylinder that is embedded in a porous medium [34]

$$\overline{Nu}_{D_1} = \frac{\bar{h}_{\text{cyl}} D_1}{k_f} = 1.015\left(Re_{D_1} Pr\right)^{1/2} \tag{23}$$

The characteristic length used in calculating the Reynolds and Nusselt numbers is the base cylinder diameter, $D_1 = 2r_1$ and the average pore velocity is again used in calculating the Reynolds number.

Values of the thermal contact resistances $R''_{t,c-b}$ and $R''_{t,c-ff}$ are determined as follows. For the metal foams considered here, the contact resistances have been shown to depend on (*i*) the method of manufacture [35], (*ii*) the normal pressure on the interface between the foam and solid [36], and (*iii*) the possible presence of a bonding agent [32]. Values of the contact resistances are taken from experimental measurements from De Jaeger et al. [32], as explained in Section 3.2.

2.5. Calculation procedure

Calculation of R_{ff}, given by Eq. (7), proceeds as follows. First, values of $k_{fm,\text{eff}}$ and α_v are determined using Eqs. (11) and (19), respectively. The area-averaged convection heat transfer coefficient for the foam ($\bar{h}_{fm}$) is calculated via Eq. (20), which is followed by calculation of R''_{fm} using Eq. (15b). The area-averaged convection heat transfer coefficient for the exposed fin surfaces ($\bar{h}_{fn}$) is determined using Eq. (22), which allows for the calculation of $R''_{\text{conv},fn}$ using Eq. (16). These two thermal resistances (as well as the potential contact resistance $R''_{t,c-ff}$) may be combined to determine U using Eq. (17). Equation (10) is then employed to determine $k_{fn,\text{eff}}$. The thermal resistance of the fin with attached foam (R_{fn}) may subsequently be determined using Eq. (4). Equation (23) is then employed to determine $\bar{h}_{\text{cyl}}$, which in turn allows for the calculation of

$R_{\text{conv,cyl}}$ using Eq. (5). Finally, the array thermal resistance is determined using Eq. (6) or Eq. (8) for a single unit pitch or Eq. (7) (or equivalent if a contact resistance $R''_{t,c-b}$ is important) for an array of N unit pitches. Finally, the total array heat transfer rate may be found by using the relation $q_{\text{tot}} = \theta_b/R_{ff}$.

3. Experiments

Experiments were performed to validate the analytical model of Section 2.

3.1. Experimental apparatus

The experiments were conducted using the flow channel described in Stark et al. [23]. Air is drawn through the tunnel's main channel of cross sectional width (W_{ch} = 100 mm) and height (H_{ch} = 120 mm), along a length of L_{ch} = 1.2 m. The air cools a fin-foam array consisting of two equal unit-pitches, as shown in Fig. 2(a). Thermal energy is transported to the base of the fin-foam array by an electrically heated heat pipe (HP) of cylindrical cross section. The heat is dissipated to the air drawn through the channel and fin-foam array.

The copper-H_2O, sintered-wick HP (Enertron HP-HD06DI17500BA) is positioned vertically in a heavily insulated HP carrier which is attached to the bottom of the channel, as detailed in Fig. 3(a) of Stark et al. [23]. The cylindrical HP is of diameter D_{hp} = 6 mm and length L_{hp}= 175 mm. Physical and effective properties, as well as additional geometric dimensions, are reported elsewhere [23,37-38]. Within the HP carrier (a detailed description of which may be found in [37]) is a cylindrical heat spreader constructed of aluminum (Al 2024-T4; k_{hs} = 121 W/m·K) that surrounds the evaporator section of the HP (of length L_e = 50.8 mm). The spreader has an inner diameter of 6.05 mm, an outer diameter of 25.4 mm, and a height of $L_{hs} = L_e$. A 0.05 mm wide gap between the heat spreader and the HP is filled with thermal paste (Artic Silver 5; k_{tp} = 8.7 W/m K). An adhesive-backed electrical patch heater (McMaster 35765K634) [37] energized by a DC power supply (Dr. Meter HY3005F-3) is employed to provide thermal energy to the exterior of the heat spreader. The rate of joule heating within the patch heater is measured by a voltmeter (AMPROBE AM-510; accuracy ±0.8% of reading +1 LSD; resolution 10 mV) and an ammeter (FLUKE 77 IV; accuracy ±1.5% of reading +2 LSD; resolution 1 mA).

The HP condenser section (of length L_c = 51.4 mm) is placed at the center of the composite fin-foam array, consisting of two unit pitches (S = 26.2 mm) with an outer square dimension of L_{fn} = 100 mm. (The array is similar to the square foam-only array described in detail in Stark et al. [23].) Each pitch consists of two blocks of aluminum foam (10 PPI Duocel® Al 10-44) of thickness 12.7 mm attached to an aluminum fin (Al 3003-h14 ; k_{fn} = 159 W/m K) of thickness t = 0.8 mm, as shown in Fig. 2(a). The foam blocks have a measured porosity of ε = 0.941 and are attached to a threaded aluminum insert made of the same alloy as the heat spreader that is described in detail in Stark et al. [23]. The solid inserts have threaded outer diameters of r_1 = 25.4 mm (UNC 1-8 threads [39]) and inner diameters of 6.05 mm. An undersized hole (of diameter 5 mm) is drilled through the center of the foam, which the insert is then screwed into, crushing the foam into the screw threads in order to minimize the thermal contact resistance between the inserts and foam. The 0.05 mm gaps between the inserts and the HP are packed with Artic Silver thermal paste. The thermal paste is also applied to the interface between the fin and foam prior to assembly. Closed-cell styrofoam blocks (of outer dimension $L_i = L_{fn}$ = 100 mm, $L_{i,t}$ = 55 mm, and $L_{i,b}$ = 14.2 mm, k_i = 0.033 W/m K) are employed to ensure that the air flow is directed entirely through the fin-foam array, as well as to provide further thermal insulation.

A detailed description of the data acquisition systems associated with measurement of local temperatures and bulk channel velocities (including instrumentation, calibration, and validation) may be found in [23, 37].

3.2. Experimental data analysis

A resistance network affiliated with the experimental measurements is shown in Fig. 2(b). For a particular experiment the heat rate (q), the average channel velocity (u_{ch}), the upstream air temperature (T_∞), and the temperature of the thermocouples in the heat spreader (T_{tc}) are measured directly. (Note that the experimentally measured heat rates are corrected to account for parasitic heat losses which were found to be small, approximately 5 percent of the electrical power dissipated by the patch heater, and independent of the channel air velocity [23]). Values of five of the six resistances in the network of Fig. 2(b) are as follows.

Conventional conduction analysis is used to calculate the resistance posed by the aluminum heat spreader, yielding R_{hs} = 0.019 K/W [23]. The same methodology is employed to determine the resistance of the thermal paste located between the heat spreader and the

evaporator section of the HP ($R_{tp,e}$ = 0.003 K/W). Previous work by Sharifi et al. [38] has shown that the complex heat and mass transfer phenomena associated with the HP used here may be reduced to a single resistance, R_{hp} = 0.22 K/W which exists between the outer walls of the evaporator ($\overline{T_e}$) and condenser ($\overline{T_c}$) sections of the HP. At the condenser section, heat is conducted through another layer of thermal paste (with resistance $R_{tp,c}$ =0.0029 K/W) and then through the aluminum inserts (with resistance $R_{in,r}$ = 0.036 K/W) until it reaches the base of the composite fin-foam array at $r = r_1$. The thermal resistances of the experimental apparatus between (*i*) the location corresponding to T_{tc} and (*ii*) the base of the array have a sum of R_{app} = $R_{hs}+R_{tp,e}+R_{hp}+R_{tp,c}+R_{in,r}$ = 0.70 K/W.

The sixth resistance of Fig. 2(b), $R_{ff,sq}$, is determined using the analysis of Section 2.5, which is augmented by a recently developed semi-analytical method [23] to account for the usage of foam and fins with a square (instead of circular) planform in the experiments. Following the circular-to-square conversion procedure of Stark et al. [23], $R_{ff,sq}$ is ultimately expressed in a form similar to the annular array resistance of Eq. (7) as

$$R_{ff,sq} = \left[N \left(R_{fn,sq}^{-1} + R_{\text{conv,cyl}}^{-1} \right) \right]^{-1} \tag{24}$$

where

$$R_{fn,sq} = \frac{1}{2U\left(L_{fn}^2 - \pi r_1^2\right)\eta_{fn,sq}} \tag{25}$$

and

$$\eta_{fn,sq} = \frac{1 - e^{-2\pi m_{fn} L_{fn}}}{\dfrac{K_0\left(m_{fn}L_{fn}\right)}{\eta_{fn}} + \left[1 - K_0\left(m_{fn}L_{fn}\right)\right]\dfrac{A_{fn,sq}}{\left(\eta A\right)_{fn}}} \tag{26}$$

where N is the number of unit pitches in the array, $A_{fn,sq} = L_{fn}^2 / 4 - r_1^2$, and η_{fn} is determined by using Eq. (3) with r_2 replaced by $L_{fn}/2$. Note that $\overline{h}_{\text{cyl}}$ is calculated as in Eq. (23), but the value of A_{cyl} used in Eq. (5) is modified to account the larger surface area due to the threading and the pore velocity is

$$u_p = u_\infty \left[\frac{S}{\varepsilon\left(S - t\right)} \frac{L_{fn}^2}{\left(L_{fn}^2 - \pi r_1^2\right)} \right] \tag{27}$$

The value of $R''_{t,c-ff}$ (= 0.00125 m^{2}K/W) is taken from De Jaeger et al. [32], and is associated with a thermal paste placed between a metal foam and flat, solid surface. The value of $R''_{t,c-b}$ is set to zero, because the fin is a continuous solid at $r = r_1$, as evident Fig. 2. For the experimental conditions investigated here, the value of $R_{ff,sq}$ is between 50% and 75% that of R_{app}.

The temperature of the channel air increases appreciably (defined as an increase in the bulk temperature relative to θ_b that exceeds 5%) in the experiments. Accordingly, a log mean temperature difference (LMTD) is employed when calculating the heat transfer rate across $R_{ff,sq}$, leading to [23]

$$q = \left(T_{tc} - T_{\infty}\right) \frac{1 - e^{\frac{1}{\dot{m}c_{p,f} R_{ff,sq}}}}{R_{\text{app}} - \left(R_{\text{app}} + \frac{1}{\dot{m}c_{p,f}}\right) e^{\frac{1}{\dot{m}c_{p,f} R_{ff,sq}}}} \tag{28}$$

where $\dot{m}$ is the air mass flow rate and $c_{p,f}$ is the specific heat of the of the channel air. Note that flow work, which may be significant for large velocities and pressure drops [40] is not included in the analysis. Using measured values of T_{tc} and T_{∞}, along with known values of R_{app} and predicted values of $R_{ff,sq}$, predicted values of q can be obtained with Eq. (28) and will be compared to the corresponding measured heat rates. Since $R_{ff,sq} \approx R_{\text{app}}$, the values of q predicted using Eq. (28) are sensitive to the value of $R_{ff,sq}$ predicted with the model developed in this study.

4. Results and discussion

4.1. Comparison of measured and predicted heat transfer rates

To validate the model, predictions using Eq. (28) were compared with experimentally measured heat rates for three average velocities (u_{∞} = 0.4, 1.7, and 3.0 m/s) as shown in Fig. 3. Four excess temperatures, ranging from $8 \lesssim \theta = T_{tc} - T_{\infty} \lesssim 21$°C, were specified for each velocity with air properties evaluated at a temperature of $(T_b + T_{lm})/2$. The uncertainty in the measured heat rates (excess temperatures) is approximately ±3% (±1%) of the reported values while the average deviation of the predictions from the experimental measurements is less than 3%, with the largest discrepancies occurring for the lowest velocity cases. The relatively good agreement between the measurements and predictions confirms the efficacy of the proposed analytical model for the conditions considered here.

4.2. Parametric simulations

Once validated, the model can be exercised to determine the dependence of predicted heat rates to key parameters. Fins and foams of circular shape are considered with base case dimensions similar to those of the experiments. Specifically, N = 1, S = 26.2 mm, t = 0.8 mm, r_1 = 12.7 mm, and r_2 = 50 mm. Base case properties of the foam, fin, and air, as well as $R''_{t,c-ff}$ and $R''_{t,c-b}$ are the same as for the experimental comparisons of Section 4.1. Predicted heat rates are based on T_∞ = 25°C and T_b = 60°C, while Eq. (28) is again used to account for the increase in the air temperature as it flows through the foam. Various average air velocities are considered for each case.

4.2.1. Sensitivity to contact resistances $R''_{t,c-ff}$ *and* $R''_{t,c-b}$

Figure 4(a) shows the dependence of the heat rate on the average air velocity and the contact resistance between the fin and foam, $R''_{t,c-ff}$, with the thermal resistance at the base of the fin set to $R''_{t,c-b}$ = 0. Base case dimensions are used. For each value of $R''_{t,c-ff}$, the heat rate becomes larger as the air velocity increases, as expected. The dependence of the heat rate to $R''_{t,c-ff}$ is also as expected, with the smallest heat rates corresponding to $R''_{t,c-ff}$ = 1 m^{2}K/W for which heat transfer to the air occurs primarily from the fin and cylinder surfaces that are not in direct contact with the solid phase of the foam.

The dependence of the heat rate on both $R''_{t,c-ff}$ and $R''_{t,c-b}$ is reported in Fig. 4(b) for which $R''_{t,c-b}$ is arbitrarily set equal to $R''_{t,c-ff}$. The largest heat rates correspond to $R''_{t,c-b} = R''_{t,c-ff}$ = 0, and are identical those associated with the $R''_{t,c-ff}$ = 0 case of Fig. 4(a). In contrast, extremely small values of q are associated with $R''_{t,c-b} = R''_{t,c-ff}$ = 1 m^{2}K/W reflecting the fact that heat transfer to the air occurs almost exclusively from the cylinder surface at r_1 that is not in direct contact with the solid phase of the foam.

Figure 4(c) shows the dependence of the heat rate on $R''_{t,c-ff}$ in more detail. For any air velocity, the predicted heat rates exhibit both upper (at small $R''_{t,c-ff}$) and lower (at large $R''_{t,c-ff}$) limits, with a gradual transition between the two limiting heat rates. When $R''_{t,c-ff}$ is small, the corresponding thermal resistance of Fig. 1(c) is negligible, and the fin heat loss is dominated by R''_{fm} and $R''_{\mathrm{conv},fn}$. In contrast, when $R''_{t,c-ff}$ is large, the fin loses heat primarily through $R''_{\mathrm{conv},fn}$. Since $R''_{\mathrm{conv},fn}$ decreases as the air velocity is increased, the transition between the large and small heat rates shifts to smaller $R''_{t,c-ff}$ at higher air velocities. When $R''_{t,c-ff}$ and $R''_{t,c-b}$ are increased simultaneously the small heat rates are reduced relative to those of Fig. 4(c), as expected, and are reported in Fig. 4(d).

4.2.2. Sensitivity to array radius r_2/r_1

The dependence of the heat rate to r_2/r_1 is shown in Fig. 5(a) for various u_∞, where r_2/r_1 is varied by changing r_1. As evident, for each velocity there is a value of $r_2/r_1 = (r_2/r_1)_{\max}$ which yields a maximum predicted heat rate. For $r_2/r_1 > (r_2/r_1)_{\max}$, the relatively small base areas of the array (and corresponding lower surface efficiencies) limit performance. For $r_2/r_1 < (r_2/r_1)_{\max}$, the lack of sufficient convective surface area within the foam reduces performance. In the limiting case of $r_2/r_1 = 1$, heat transfer occurs only from the cylindrical surface at $r_2 = 50$ mm and its rate is relatively small. As u_∞ is increased, the convection heat transfer will increase and the surface efficiency of the array will decrease, resulting in decreasing values of $(r_2/r_1)_{\max}$.

Similar comparisons are presented in Fig. 5(b) for which r_1 is fixed. In general, increasing r_2/r_1 will increase the convective surface area within the foam, resulting in larger heat rates. In the limiting case of $r_2/r_1 = 1$ heat transfer occurs only from the inner cylindrical surface at $r_1 = 12.7$ mm, and for any value of r_2 its rate is smaller than the corresponding rate of Fig. 5(a).

4.2.3. Sensitivity to fin thickness t

The impact of varying the ratio of foam to fin thicknesses on the heat rate is shown in Fig. 6(a) where $(S-t)/t$ is changed by varying the fin thickness, t. For a given average air velocity, u_∞, increasing t (decreasing $(S-t)/t$), simultaneously increases the pore velocity and

reduces the radial conduction resistance of the array. Hence, q is shown to increase at small values of $(S\text{-}t)/t$. However, the model breaks down when the foam thickness is at or below the characteristic pore diameter, $(S-t)/t = D_p/t \leq 2.7$ (for the foam and fin used in the experiments). For foam-to-fin ratios of $(S-t)/t \gtrsim 3$, the heat rate is relatively insensitive to increases in the fin thickness due to the offsetting effects of (*i*) enhanced radial conduction in the solid fin and (*ii*) reduced surface area of the foam available for convection heat transfer to the air.

The dependence of the heat rate on $(S-t)/t$ and u_p is reported in Fig. 6(b). As evident, $q \rightarrow 0$ as $(S-t)/t \rightarrow 0$ regardless of the pore velocity, since (*i*) the air temperature quickly approaches the value of T_b as it flows through the array and (*ii*) less fluid is available for cooling. As noted in Fig. 6(b), the heat rate becomes relatively insensitive to the fin thickness for $(S-t)/t \gtrsim 3$.

5. Comparison of fin, foam, and composite fin-foam arrays

Predicted heat rates for the combined fin-foam array are now compared with rates associated with (*i*) a bare cylinder, (*ii*) an annular fin array, and (*iii*) a foam-only annular array. Comparisons are made employing the dimensions, materials, and temperatures of Section 4.2, but with the fin replaced by foam for the foam-only case, and with the foam removed for the fin array case. Heat transfer from the bare cylinder corresponds to convection from a cylinder in crossflow, where the convection heat transfer coefficient is determined using the correlation of Sparrow et al. [41]. It has been shown that heat transfer from finned cylinders may be modeled as a combination of transfer from plain cylinders (as in the previous case) and flat plates [42], and this approach is taken here. Predicted heat rates for the foam-only case are made using the methodology developed by Stark et al. [23].

Predicted heat transfer rates from the combined fin-foam array exceed those of the other configurations, as shown in Fig. 7(a) and in more detail in Fig. 7(b). Heat rates from the foam array are the next largest, followed by those of the fin array. As anticipated, the bare cylinder is affiliated with the smallest heat rates. Heat rates for the various configurations can be normalized to those of the fin array case, and are shown in Fig. 8(a). For the velocity range $0.1 \leq u_\infty \leq 10$ m/s, the predicted heat rates for the combined fin-foam array (foam array) are, on average, 4.8 (3.8) times larger than those associated with the fin array. In contrast, predicted heat rates for the bare cylinder are ~78% less than those of the fin array. Alternatively, the resistance associated

with the various configurations may be normalized relative to those of the fin array and are reported in Fig. 8(b) where each resistance is defined as $(T_b - T_{lm})/q$.

6. Conclusions and recommendations

Novel, analytical expressions have been developed for the thermal efficiency and thermal resistance of a composite annular array, consisting of periodic layers of open-cell metal foam and metal fins attached concentrically to a base cylinder, subjected to convective cooling (or heating). Heat rates predicted by the model are compared to experimentally measured rates associated with an array of square outer dimension (where the methodology developed in Stark et al. [23] is used to extend the annular model), in order to validate the model and demonstrate its usage. Parametric simulations were performed to assess the sensitivity of the heat rate to the array's geometrical configuration, contact resistances, and the air velocity. Finally, predictions associated with (*i*) a bare cylinder, (*ii*) an annular fin array, and (*iii*) a foam-only annular array were compared to those of the composite fin-foam array configuration, demonstrating its superior thermal performance.

The analytical model makes use of multiple assumptions which may impact the accuracy of its predictions. For example, approximation of the foam as a continuum is invalid for cases in which certain geometrical dimensions are smaller than the characteristic pore diameter (e.g., at small values of r_2/r_1 or $(S-t)/t$). Multidimensional effects may become significant for relatively large unit pitch values ($S/(r_2-r_1)$), fin thicknesses ($t/(r_2-r_1)$) or for large variations of the air temperature and velocity as it flows through the foam. Inaccuracies may arise from the prediction of convection heat transfer coefficients for the exposed surfaces of the fin and cylinder, which are approximated as Darcy flow across a flat plate and plain cylinder [34], respectively. Large pressure drops within the air may invalidate the assumption of a constant property fluid, and buoyancy effects could become significant at smaller air velocities.

Although the model performs well in predicting the experimental measurements reported here, further work is required to check its validity over a broad range of composite array dimensions, array materials, fluids used as a coolant, and operating conditions. In addition, an investigation of the tradeoffs between (*i*) reducing the thermal resistance of such arrays and (*ii*) increasing the fan power needed to force the air through the arrays is warranted. Although there are numerous opportunities to further investigate the thermal behavior of composite fin-foam

arrays, the results presented here clearly indicate that improved performance can be easily achieved by combining the beneficial aspects of metal foams and solid metal fins in a hybrid annular array configuration.

Acknowledgments

This material is based upon work supported by the National Science Foundation under Grant Nos. 1435131 (University of Kansas) and 1435233 (University of Connecticut).

References

[1] C.Y. Zhao, Review on thermal transport in high porosity cellular metal foams with open cells, International Journal of Heat and Mass Transfer 55 (2012) 3618–3632.

[2] I. Ghosh, How good is open-cell metal foam as a heat transfer surface, ASME Journal of Heat Transfer 131 (2009) 101004-1-8.

[3] L. Tadrist, M. Miscevic, O. Rahli, F. Topin, About the use of fibrous materials in compact heat exchangers, Experimental Thermal and Fluid Science 28 (2004) 193-199.

[4] K. Nawaz, Metal Foams as novel Materials for Air-Cooling Heat Exchangers, Master thesis, University of Illinois at Urbana-Champaign, Urbana, IL, 2011.

[5] A.A. Bhattacharya, R.L. Mahajan, Finned metal foam heat sinks for electronics cooling in forced convection, ASME. Journal of Electronic Packaging 124 (3) (2002) 155-163.

[6] H. Pokharna, A.A. Bhattacharya, Enhanced Heat Exchanger, Intel Corporation, US Patent No. 6958912 B2, 2005.

[7] S.S. Feng, M. Shi, Y. Li, T.J. Lu, Pore-scale and volume-averaged numerical simulations of melting phase change heat transfer in finned metal foam, International Journal of Heat and Mass Transfer 90 (2015) 838-847.

[8] A. Andreozzi, N. Bianco, M. Iasiello, V. Naso, Numerical study of metal foam heat sinks under uniform impinging flow, Journal of Physics; Conference Series, 34th UIT Heat Transfer Conference 796 (1) (2016) 1-9.

[9] S.S. Feng, J.J. Kuang, T. Wen, T.J. Lu, K. Ichimiya, An experimental and numerical study of finned metal foam heat sinks under impinging air jet cooling, International Journal of Heat and Mass Transfer 77 (2014) 1063-1074.

[10] A.A. Bhattacharya, R.L. Mahajan, Metal foam and finned metal foam heat sinks for electronics cooling in buoyancy-induced convection, ASME Journal of Electronic Packaging 128 (3) (2005) 259-266.

[11] C.T. DeGroot, D. Gateman, A.G. Straatman, The effect of thermal contact resistance at porous-solid interfaces in finned metal foam heat sinks, ASME Journal of Electronic Packaging 132 (4) (2010) 041007-041007-7.

[12] H. Seyf, M. Layeghi, Numerical analysis of convective heat transfer from an elliptic pin fin heat sink with and without metal foam insert, ASME Journal of Heat Transfer 132 (7) (2010) 071401-071401-9.

[13] D. Hernon, A. Lyons, S. Krishnan, M. Hodes, Al. O'Loughlin, Monolithic Structurally Complex Heat Sink Designs, Alcatel-Lucent USA Inc., US Patent No. 0299148, 2013.

[14] H. Kim, Heat Transfer Fin for Heat Exchanger, US Patent Application No. 0296008, 2005.

[15] D. Berukhim, A. Leishman, V. Avanessian, Mixed Carbon Foam/Metallic Heat Exchanger, Boeing, US Patent No. 9279626, 2012.

[16] A. Faghri, Heat Pipe Science and Technology, Second ed., Global Digital Press, 2016.

[17] A.A. El-Nasr, S.M. El-Haggar, Effective thermal conductivity of heat pipes, Heat and Mass Transfer 32 (1-2) (1996) 97-101.

[18] H. Shabgard, M.J. Allen, N. Sharifi, S.P. Benn, A. Faghri, T.L. Bergman, Heat pipe heat exchangers and heat sinks: opportunities, challenges, applications, analysis, and state of the art, International Journal of Heat and Mass Transfer 89 (2015) 138-158.

[19] A. Faghri, T.L. Bergman, Reviews of Advances in Heat Pipe Analysis and Numerical Simulation, Numerical Simulation of Heat Exchangers: Advances in Numerical Heat Transfer, Volume V, edited by W.J. Minkowycz, E.M. Sparrow, J.P. Abraham, J.M. Gorman, Taylor & Francis Group, Boca Raton, 2017, 173-212.

[20] C. T'Joen, P. De Jaeger, H. Huisseune, S. Van Herzeele, N. Vorst, M. De Paepe, Thermo-hydraulic study of a single row heat exchanger consisting of metal foam covered round tubes, International Journal of Heat and Mass Transfer 53 (16) (2010) 3262–3274.

[21] A. Chumpia, K. Hooman, Performance evaluation of single tubular aluminium foam heat exchangers, Applied Thermal Engineering 66 (1) (2014) 266-273.

[22] A. Chumpia, K. Hooman, Performance evaluation of tubular aluminum foam heat exchangers in single row arrays, Applied Thermal Engineering 83 (2015) 121-130.

[23] J.R. Stark, R. Prasad, T.L. Bergman, Experimentally validated analytical expressions for the thermal efficiencies and thermal resistances of porous metal foam-fins, International Journal of Heat and Mass Transfer 111 (2017) 1286-1295.

[24] M. Odabee, K. Hooman, H. Gurgenci, Metal foam heat exchangers for heat transfer augmentation from a cylinder in cross-flow, Transport in Porous Media 86 (3) (2011) 911-923.

[25] T.M. Jeng, S.C. Tzeng, Heat transfer measurement of the cylindrical heat sink with sintered-metal-bead-layers fins and a built-in motor fan, International Communications in Heat and Mass Transfer 59 (2014) 136-142.

[26] T.L. Bergman, A.S. Lavine, Fundamentals of Heat and Mass Transfer, Eighth ed., Wiley, Hoboken, 2017.

[27] V.V. Calmidi, R.L. Mahajan, The effective thermal conductivity of high porosity fibrous metal foams, ASME Journal of Heat Transfer 121 (2) (1999) 466-471.

[28] S.H. Park, T.H. Kim, J.H. Jeong, Experimental investigation of the convective heat transfer coefficient for open-cell porous metal fins at low Reynolds numbers, International Journal of Heat and Mass Transfer 100 (2016) 608-614.

[29] T.M. Jeng, S.C. Tzeng, Y.H. Hung, An analytical study of local thermal equilibrium in porous heat sinks using fin theory, International Journal of Heat and Mass Transfer (49) (11–12) (2006) 1907-1914.

[30] T. Dixit, I. Ghosh, An experimental study on open cell metal foam as extended heat transfer surface, Experimental Thermal and Fluid Science 77 (2016) 28-37.

[31] V.V. Calmidi, R.L. Mahajan R.L., Forced convection in high porosity metal foams, ASME Journal of Heat Transfer 122 (3) (2000) 557-565.

[32] P. De Jaeger, C. T'Joen, H. Huisseune, B. Ameel, S. De Schampheleire, M. De Paepe, Assessing the influence of four bonding methods on the thermal contact resistance of open-cell aluminum foam, International Journal of Heat and Mass Transfer 55 (21) (2012) 6200-6210.

[33] V.V. Calamidi, Transport Phenomenon in High Porosity Fibrous Metal Foams, PhD thesis, University of Colorado, Boulder, CO, 1997.

[34] D.A. Nield, A. Bejan, Convection in Porous Media, Third ed., Springer, New York, 2006.

[35] P. De Jaeger, C. T'Joen, H. Huisseune, B. Ameel, S. De Schampheleire, M. De Paepe, Assessing the influence of four cutting methods on the thermal contact resistance of open-cell aluminum foam, International Journal of Heat and Mass Transfer 55 (21–22) (2012) 6142-6151.

[36] E. Sadeghi, S. Hsieh, M. Bahrami, Thermal conductivity and contact resistance of metal foams, Journal of Physics D: Applied Physics 44 (12) (2011) 125406:1-7.

[37] J.R. Stark, N. Sharifi, T.L. Bergman, A. Faghri, An experimentally verified numerical model of finned heat pipes in crossflow, International Journal of Heat and Mass Transfer 97 (2016) 45-55.

[38] N. Sharifi, J.R. Stark, T.L. Bergman, A. Faghri, The influence of thermal contact resistance on the relative performance of heat pipe-fin array systems, Applied Thermal Engineering 105 (2016) 46-55.

[39] E. Oberg, Machinery's Handbook, 29th ed., Industrial Press, New York, 2012, 1815-1867.

[40] G. Koltsakis, O. Haralampous, C. Depcik, J.C. Ragone, Catalyzed diesel particulate filter modeling, Reviews in Chemical Engineering 29 (1) (2013) 1-61.

[41] E.M. Sparrow, J.P. Abraham, J.C.K. Tong, Archival correlations for average heat transfer coefficients for non-circular and circular cylinders and for spheres in crossflow, International Journal of Heat and Mass Transfer 47 (24) (2004) 5285-5296.

[42] J.R. Stark, T.L. Bergman, Prediction of convection from a finned cylinder in cross flow using direct simulation, turbulence modeling, and correlation-based methods, Numerical Heat Transfer, Part A: Applications 71 (3) (2017) 1-18.

Figure captions

Fig. 1. Description of the annular analytical domain. (a) overall domain, (b) annular control volume energy balance, (c) thermal resistance network for overall heat transfer coefficient.

Fig. 2. Experimental setup. (a) detail of the heat pipe and fin-foam, (b) thermal resistance network.

Fig. 3. Experimentally measured and predicted heat rates for a square fin-foam array under various ambient velocity and thermal conditions. Error bars on the experimental data points are of approximately the same size as the symbols and are not shown.

Fig. 4. Influence of thermal contact resistance on predicted heat rates for an annular geometry. (a) q versus u_∞ for $R''_{t,c-ff}$ = 0, 10^{-5}, 10^{-4}, 10^{-3}, 10^{-2}, 10^{-1}, and 1 m^{2}K/W ($R''_{t,c-b} = 0$), (b) q versus u_∞ for $R''_{t,c-b} = R''_{t,c-ff}$ = 0, 10^{-5}, 10^{-4}, 10^{-3}, 10^{-2}, 10^{-1}, and 1 m^{2}K/W, (c) q versus $R''_{t,c-ff}$ ($R''_{t,c-b} = 0$) for u_∞ = 0.01, 0.1, 1, and 10 m/s, (d) q versus $R''_{t,c-b} = R''_{t,c-ff}$ for u_∞ = 0.01, 0.1, 1, and 10 m/s.

Fig. 5. Influence of r_2/r_1 on predicted heat rates. (a) inner radius r_1 is varied, (b) outer radius r_2 is varied.

Fig. 6. Influence of foam-to-fin thickness on predicted heat rates. (a) for various u_∞, (b) for various u_p.

Fig. 7. Predicted heat rates for equal lengths of a (*i*) bare cylinder, (*ii*) finned cylinder, (*iii*) foam array, and (*iv*) composite fin-foam array versus u_∞. (a) for $0 \le u_\infty \le 10$ m/s, (b) for $0 \le u_\infty \le 0.5$ m/s.

Fig. 8. Predicted heat transfer rates and thermal resistances normalized to the fin array case. (a) heat rate ratios for $0 \le u_\infty \le 10$ m/s, (b) thermal resistance ratios for $0 \le u_\infty \le 10$ m/s.

Figures

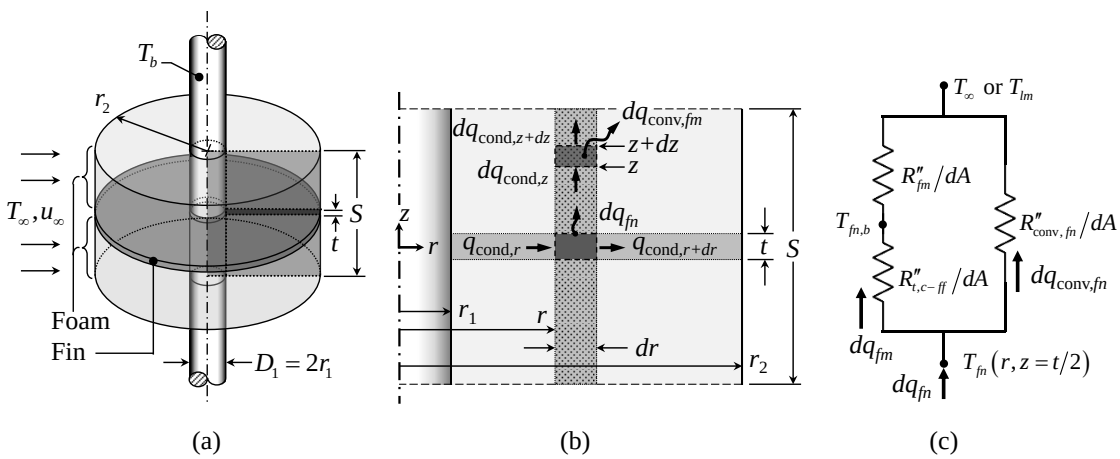

(a) (b) (c)

Fig. 1

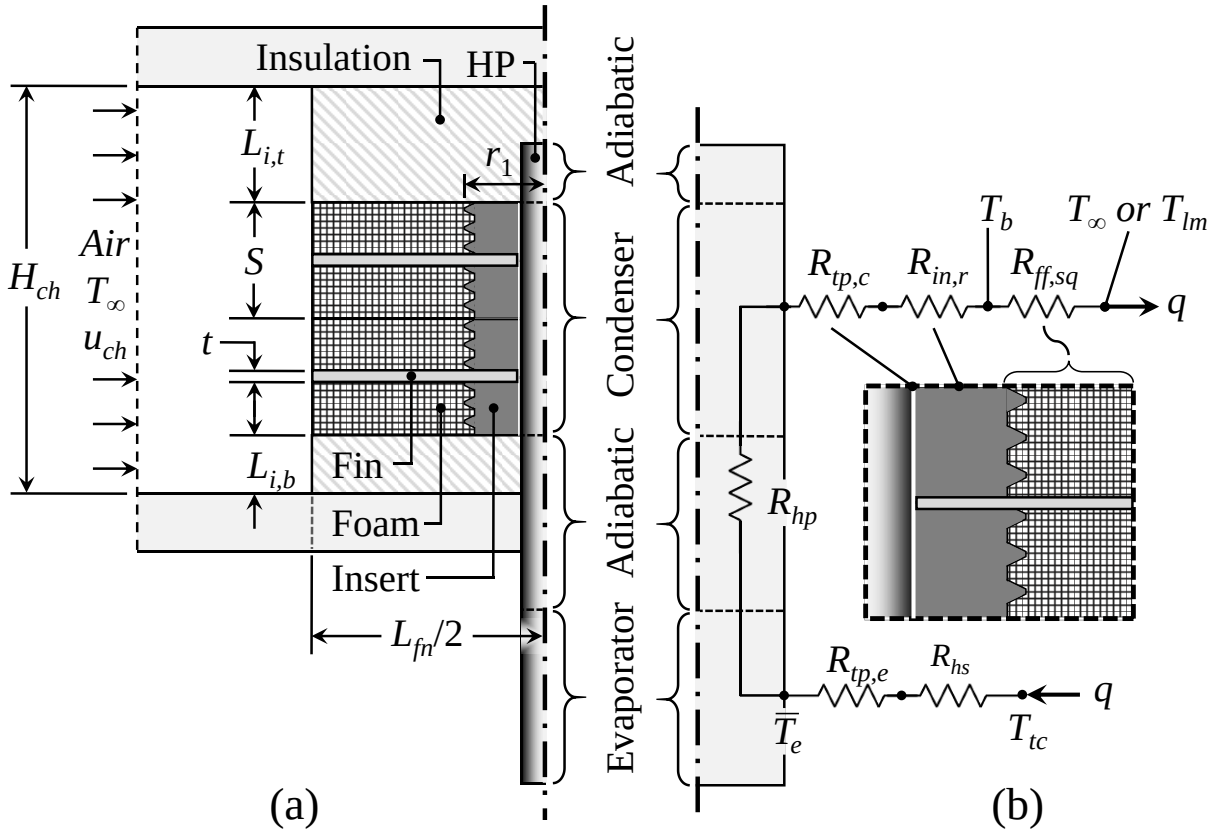
Insulation
HP
Adiabatic
$L_{i,t}$
r_1
Air
T_∞
u_{ch}
H_{ch}
S
t
Condenser
$L_{i,b}$
Fin
Foam
Insert
Adiabatic
$L_{fn}/2$
Evaporator
(a)
$R_{tp,c}$
$R_{in,r}$
T_b
$R_{ff,sq}$
T_∞ or T_{lm}
q
R_{hp}
$R_{tp,e}$
R_{hs}
q
$\overline{T}_e$
T_{tc}
(b)

Fig. 2

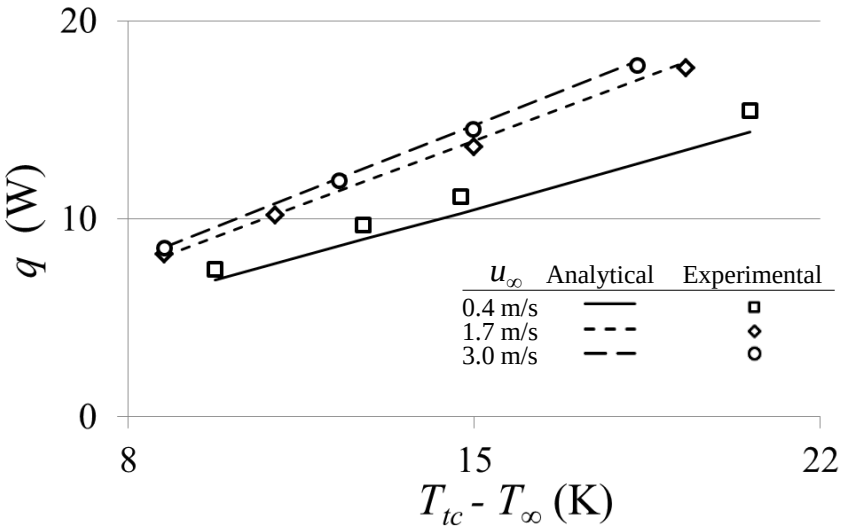
20
10
0
8
15
22
q (W)
T_tc - T_∞ (K)
u_∞
Analytical
Experimental
0.4 m/s
1.7 m/s
3.0 m/s

Fig. 3

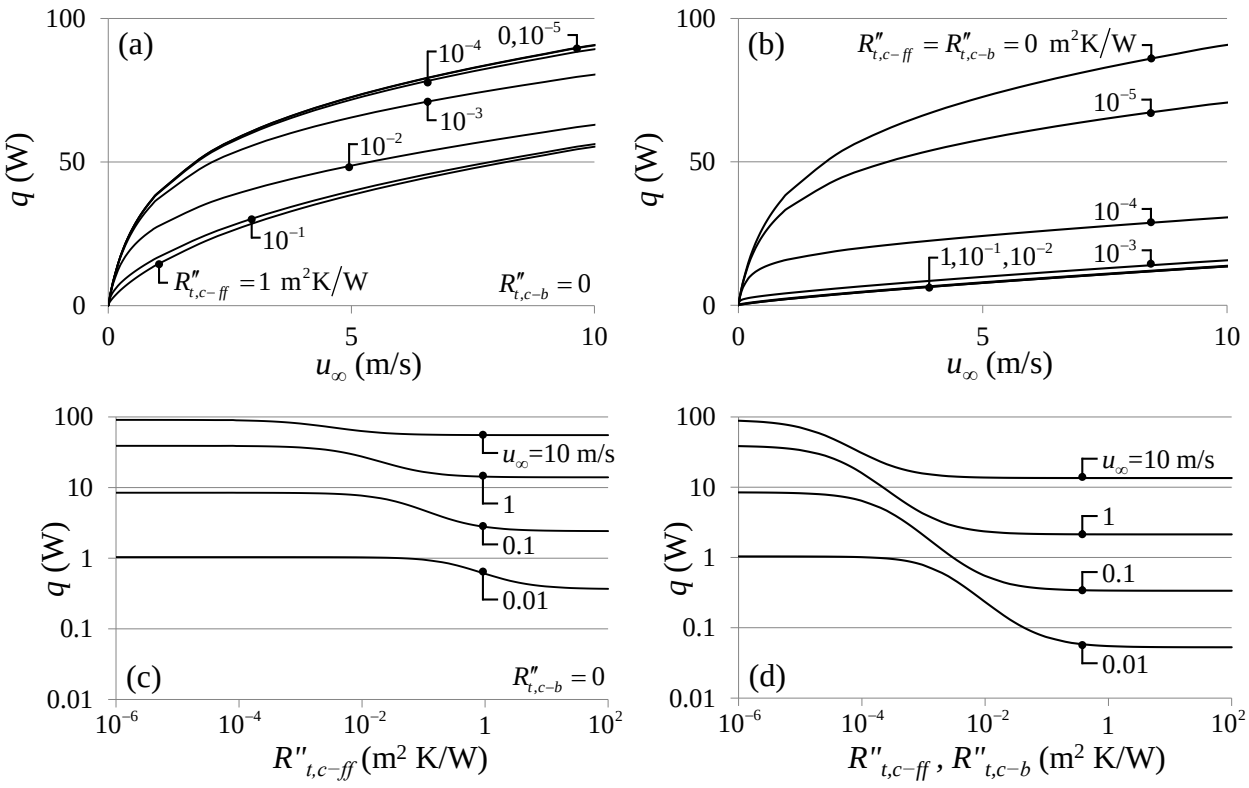
(a)
(b)
(c)
(d)
q (W)
u∞ (m/s)
R″t,c−ff (m² K/W)
R″t,c−ff , R″t,c−b (m² K/W)
R″t,c−ff = 1 m²K/W
R″t,c−b = 0
R″t,c−ff = R″t,c−b = 0 m²K/W
0,10⁻⁵
10⁻⁴
10⁻³
10⁻²
10⁻¹
1,10⁻¹,10⁻²
u∞=10 m/s
1
0.1
0.01

Fig. 4

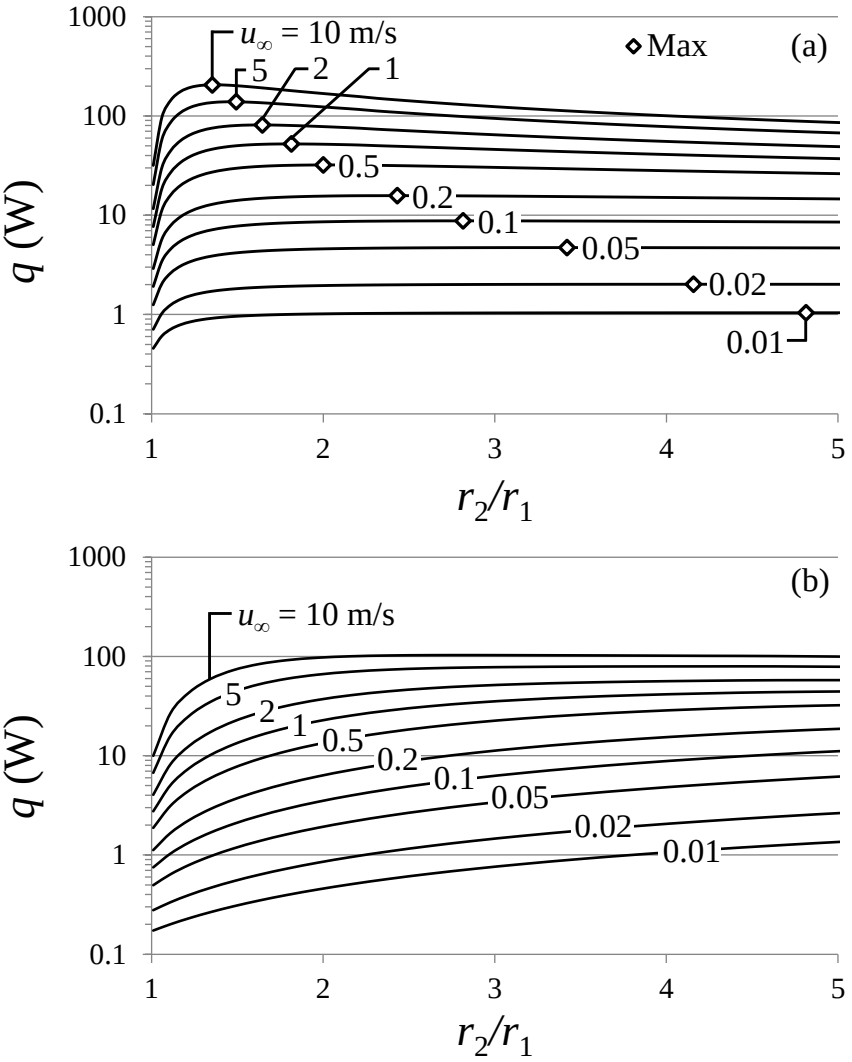
1000
100
10
1
0.1
q (W)
u_∞ = 10 m/s
5
2
1
0.5
0.2
0.1
0.05
0.02
0.01
Max
(a)
1
2
3
4
5
r_2/r_1
(b)
u_∞ = 10 m/s
5
2
1
0.5
0.2
0.1
0.05
0.02
0.01
r_2/r_1

Fig. 5

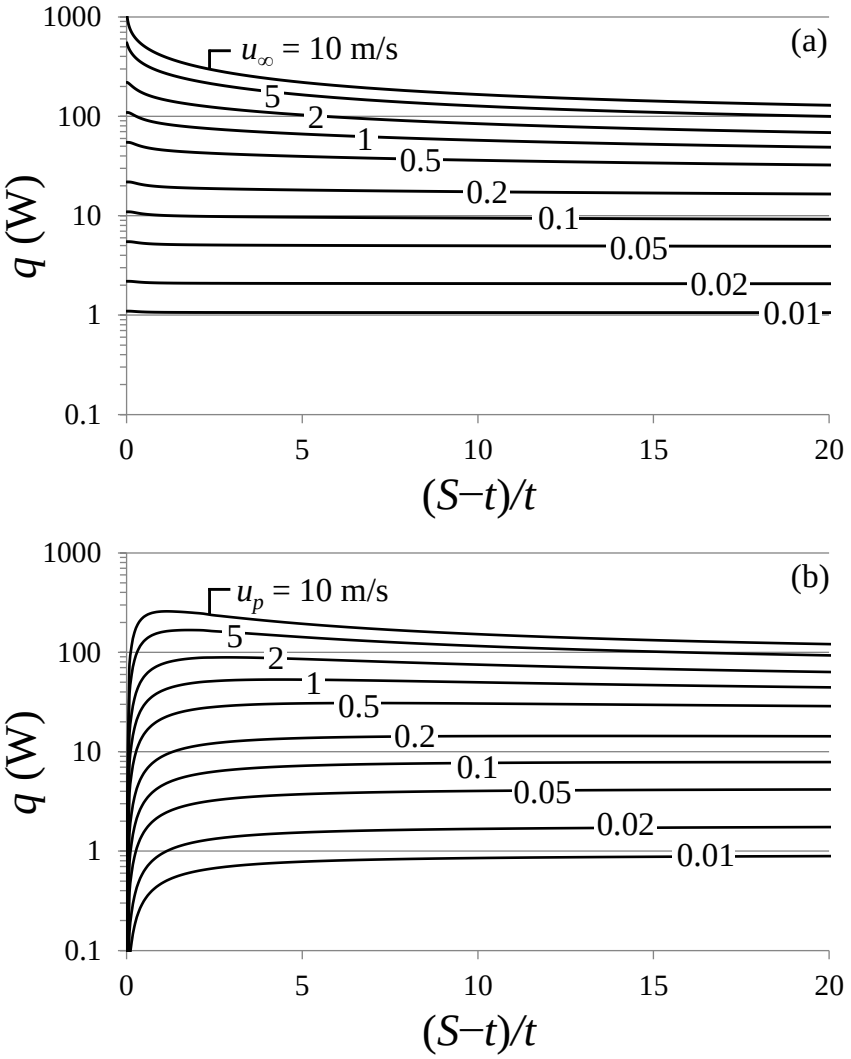
(a)
u_∞ = 10 m/s
5
2
1
0.5
0.2
0.1
0.05
0.02
0.01
1000
100
10
1
0.1
q (W)
0
5
10
15
20
(S−t)/t
(b)
u_p = 10 m/s
5
2
1
0.5
0.2
0.1
0.05
0.02
0.01
1000
100
10
1
0.1
q (W)
0
5
10
15
20
(S−t)/t

Fig. 6

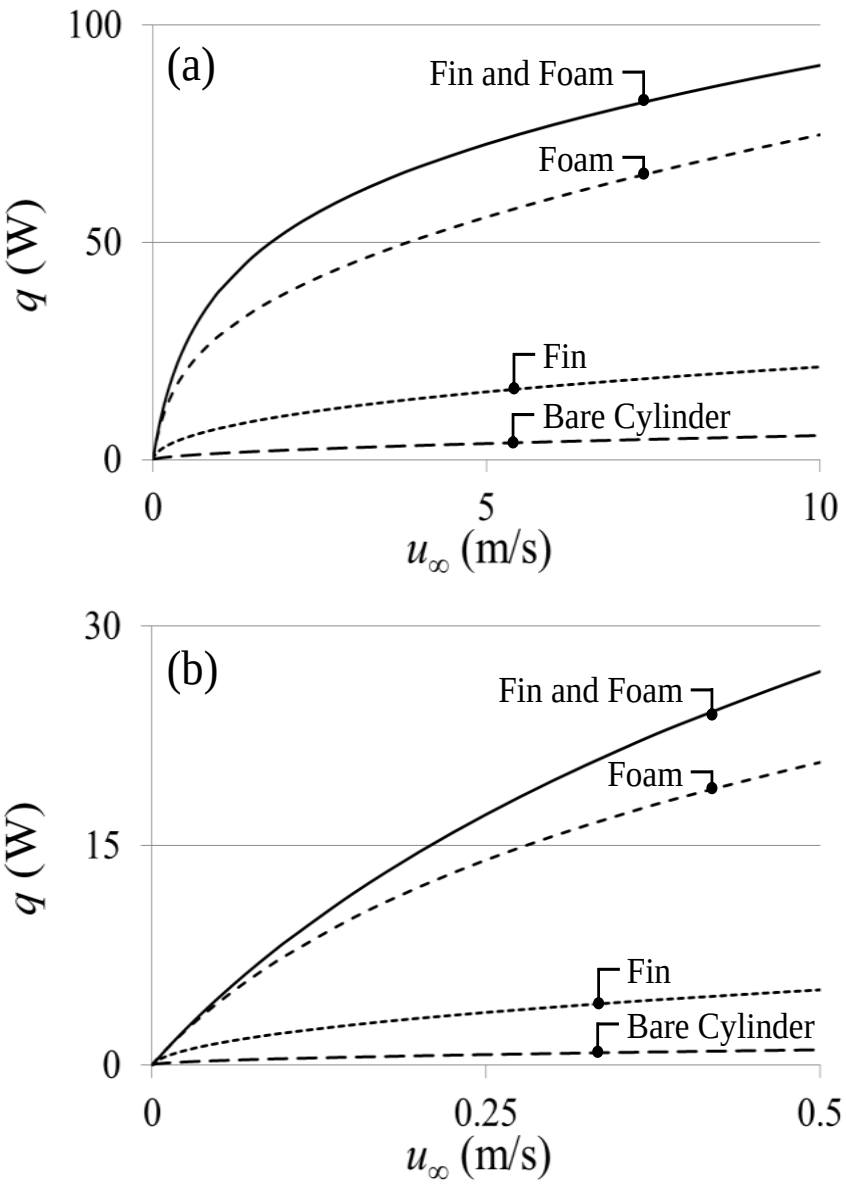
100
(a)
Fin and Foam
Foam
50
q (W)
Fin
Bare Cylinder
0
0
5
10
u∞ (m/s)
30
(b)
Fin and Foam
Foam
15
q (W)
Fin
Bare Cylinder
0
0
0.25
0.5
u∞ (m/s)

Fig. 7

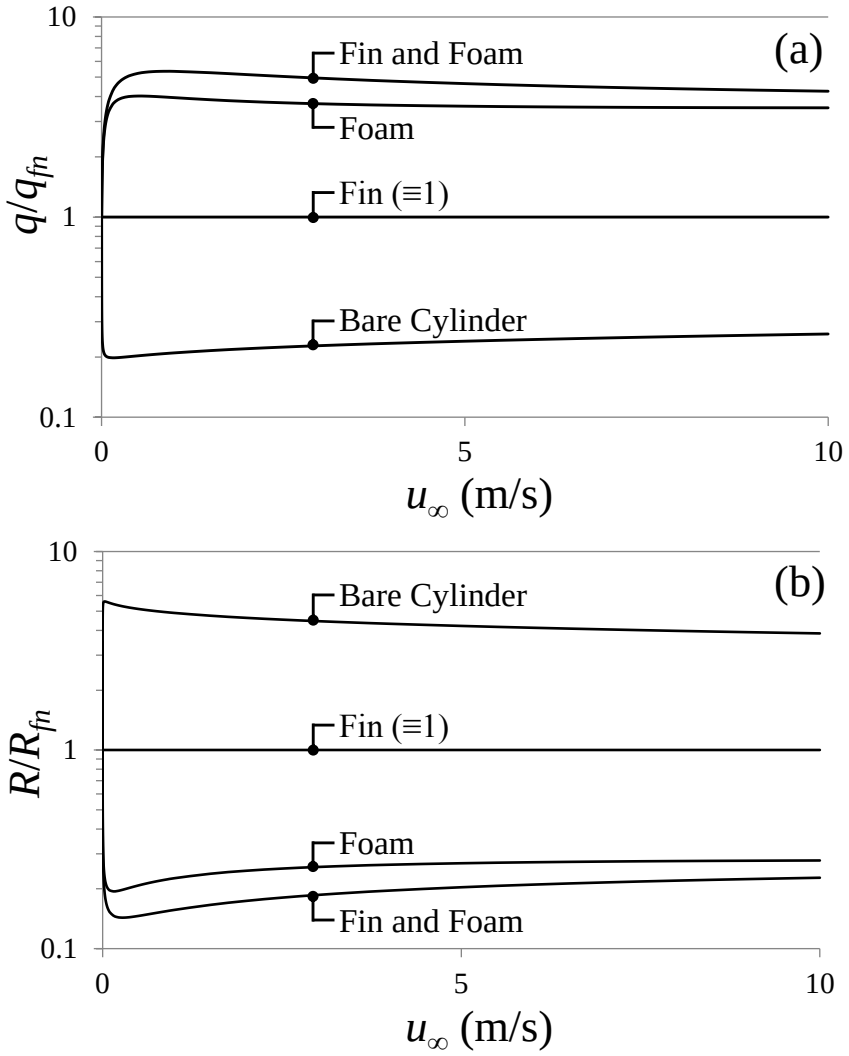
10
1
0.1
0
5
10
(a)
Fin and Foam
Foam
Fin (≡1)
Bare Cylinder
q/q_fn
u_∞ (m/s)
10
1
0.1
0
5
10
(b)
Bare Cylinder
Fin (≡1)
Foam
Fin and Foam
R/R_fn
u_∞ (m/s)

Fig. 8

Paper P5

Title:

The influence of thermal contact resistance on the relative performance of heat pipe-fin array systems

Authors:

Nourouddin Sharifi

John R. Stark

Theodore L. Bergman

Amir Faghri

Journal:

Applied Thermal Engineering

Applied Thermal Engineering 105 (2016) 46–55

Contents lists available at ScienceDirect

Applied Thermal Engineering

journal homepage: www.elsevier.com/locate/apthermeng

Research Paper

The influence of thermal contact resistance on the relative performance of heat pipe-fin array systems

Nourouddin Sharifi [a,*], John R. Stark [a], Theodore L. Bergman [a], Amir Faghri [b]

[a] Department of Mechanical Engineering, The University of Kansas, 1530 W. 15th Street 3138, Lawrence, KS 66045, USA
[b] Department of Mechanical Engineering, The University of Connecticut, 191 Auditorium Road, Storrs, CT 06269-3139, USA

HIGHLIGHTS

- Impact of contact resistances on finned-heat pipes (HPs) is investigated.
- Two configurations: (i) HP-heat sink and (ii) HP-fins are considered.
- Influence of contact resistance on heat transfer within the HP is shown.
- Tradeoff between (i) low overall system resistance and (ii) range of operation is quantified.

ARTICLE INFO

Article history:
Received 9 March 2016
Revised 6 May 2016
Accepted 20 May 2016
Available online 21 May 2016

Keywords:
Heat pipe
Fin arrays
Contact resistance
Design tradeoff

ABSTRACT

Externally-finned heat pipes (HPs) using individual fins (a HP-fin configuration) or a finned heat sink (HP-heat sink) are subject to thermal contact resistances at the HP-fin or HP-heat sink interfaces. A detailed HP model is used to quantify the influence of the contact resistances on the heat transfer and fluid flow within the HP, as well as on the overall heat transfer rate. For similar area-averaged contact resistance values, the HP-heat sink typically provides a lower overall thermal resistance than the HP-fin configuration. Under off-design operating conditions, however, the HP-heat sink option can underperform the HP-fin geometry. A thermal resistance model is also developed and its predictions compare qualitatively to those of the HP model. It is shown that the overall resistance of the HP-fin configuration is proportional to the number of fins in the array that are subject to a contact resistance. Using the detailed model it is also demonstrated that the order in which the fins (fins without versus fins with contact resistances) are placed within the array has little effect on the overall thermal resistance of the HP system.

Published by Elsevier Ltd.

1. Introduction

Heat pipes (HPs) are devices that transfer heat more effectively than high thermal conductivity media of the same physical dimensions [1,2]. Heat transfer within HPs is characterized by various thermal resistances, including the small thermal-resistance processes of evaporation (within the HP evaporator section) and condensation (in the HP condenser section) at the vapor–liquid interfaces of an internal working fluid. Applications of HPs have been reviewed [3–15], and in many practical situations the limiting system-level thermal resistances are associated with the flow of single-phase fluids *external* to the HP's condenser or evaporator sections. The larger external thermal resistance will typically be on the condenser end of the HP if, for example, air is used as the coolant and a flowing liquid heats the HP evaporator section. External arrays of fins, foils, and porous metallic foams have been added to HPs to reduce the overall system thermal resistances [16–29].

Two- and 3D models of HPs that account for the complexity of transient, conjugate heat transfer phenomena, including phase change of the HP working fluid, have been developed [27,28, 30–35]. Recently, Stark et al. [36] presented a detailed, experimentally-verified model capable of predicting the performance of a HP system involving fins that are attached to the condenser (cold) section of the HP. The 3D, transient mixed convection of air through the fin array was predicted by both direct simulation and use of a shear stress turbulence model, and the predictions of external convection were coupled to those of a 2D model that accounted for the pertinent heat transfer phenomena within the HP. It was shown that 3D effects within the HP did not significantly influence the performance of a HP-fin array system similar to that of interest in this study, justifying use of the 2D HP model.

* Corresponding author.
E-mail address: nourouddin.sharifi@ku.edu (N. Sharifi).

http://dx.doi.org/10.1016/j.applthermaleng.2016.05.121
1359-4311/Published by Elsevier Ltd.

Nomenclature

c_p	specific heat (J/kg K)
g	gravitational acceleration (m/s^2)
h	convection coefficient (W/m^2 K)
h_{fg}	latent heat (J/kg)
k	thermal conductivity (W/m K)
L	length (m)
m	fin constant (1/m)
m''	local mass flux (kg/s m^2)
N	number of fins
p_{sat}	vapor pressure (Pa)
Q	heat rate (W)
R	thermal resistance (K/W)
R''	thermal resistance per unit area (m^2 K/W)
r, z	coordinate directions (m)
S	fin pitch (m)
T	temperature (K)
t	thickness (m)
U	heat pipe centerline vapor velocity (m/s)
V	air velocity (m/s)

Greek symbols

θ	reduced temperature (°C)
μ	dynamic viscosity (Pa s)
ρ	density (kg/m^3)

Superscripts

--	average
~	no contact resistance

Subscripts

a	adiabatic, axial
b	heat sink base
c	condenser, contact
e	evaporator
eff	effective
f	fin
fc	corrected fin radius
hp	heat pipe
r	radial, ratio
t	thermal
v	vapor
v–wi	vapor–wick interface
w	wall
wi	wick
w–wi	wall–wick interface
∞	ambient

In practice, thermal contact resistances will exist at the interface between the exterior surface of a HP and the roots of individually-mounted, external fins (or the base of a finned heat sink). The magnitudes of these resistances depend on the manner in which the HP and fins (or the finned heat sink) are bonded. A wide range of thermal contact resistance values have been reported for finned-tube heat exchangers [37–41], a geometrical configuration similar to the finned-HP of interest here.

The specific objective of this study is to quantify the effect of thermal contact resistances on the performance of a vertical HP system using two approaches: (i) a detailed 2D numerical HP model that accounts for the effects of fin conduction and external convection (the fins are populated along the HP condenser section) and (ii) a thermal resistance network analysis. As will be shown and as expected, the presence of contact resistances decreases the performance of either the HP-fin or HP-heat sink configurations. However, it will also be demonstrated that the preferred system configuration (HP-fin versus HP-heat sink) is influenced by the presence of thermal contact resistances under certain operating conditions. This study represents, to the authors' knowledge, the first in depth investigation of how contact resistances modify heat transfer phenomena within the HP of such systems, and how they impact the range of conditions over which a HP-fin array system may successfully operate.

2. Numerical models

Two numerical models, a detailed HP model and a thermal resistance model, will be used to investigate the influence of thermal contact resistances on the performance of an externally-finned HP. Again, the fins are either directly attached to the HP (HP-fin) or incorporated in a heat sink whose base is in contact with the HP (HP-heat sink).

2.1. HP model

Fig. 1 shows a vertical HP-heat sink assembly that includes N annular fins incorporated into a heat sink of base thickness t_b. A second configuration (HP-fin, not shown) involves annular fins that are attached directly to the exterior surface of the HP at $r = r_{hp}$ (i.e., $t_b = 0$). In either configuration, the length of the HP, $L_{hp} = L_e + L_a + L_c$, includes an evaporator section (of length L_e), an adiabatic section (of length L_a) and a condenser section (of length L_c). Radially, the HP includes a vapor region ($0 \leqslant z \leqslant L_{hp}$; $0 \leqslant r \leqslant r_v$), a porous wick

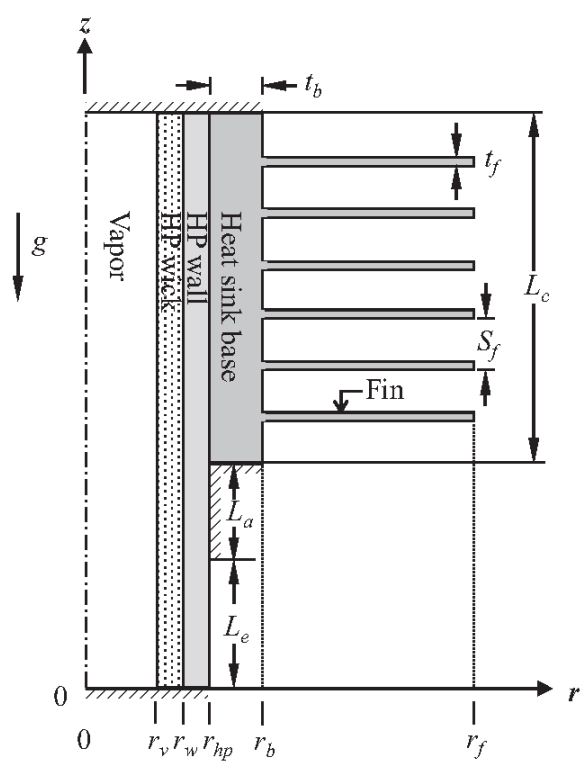

Fig. 1. Computational domain and fin array (HP-heat sink configuration).

($0 \leqslant z \leqslant L_{hp}$; $r_v < r \leqslant r_w$), and a solid wall ($0 \leqslant z \leqslant L_{hp}$; $r_w < r \leqslant r_{hp}$). The computational domain includes the entire HP, as well as the base of the heat sink (for $t_b = 1$ mm). The influence of convection from the un-finned regions of the heat sink (or from the HP between individually-mounted fins), as well as conduction within and convection from the fins, is described by application of appropriate boundary conditions applied at $r = r_b$ (or $r = r_{hp}$) as will be discussed shortly.

Axisymmetric, 2D flow of the HP working fluid and axisymmetric heat transfer within the HP and fins is assumed, while thermal radiation is assumed to be negligible. The HP wick is taken to be saturated with the liquid phase of the HP working fluid, and advection effects within the wick are not included in the governing energy equations [42]. Buoyancy forces are accounted for in the vapor phase of the HP working fluid. Until the HP capillary limit (calculated using the technique in [1]) is reached, the wick is assumed to provide sufficient capillary pressure, in conjunction with gravitational forces, to transport the HP working fluid from the condenser to the evaporator section of the HP. A detailed description of the lengthy governing equations of the HP model, including conservation of mass, momentum and energy, is available elsewhere [33].

A uniform and constant temperature, T_e, is applied to the exterior of the HP ($r = r_{hp}$) along its evaporator section. In addition to the adiabatic section of the HP, the end caps ($z = 0, L_{hp}$) and the bottom (and top) horizontal surfaces of the heat sink base are assumed to be adiabatic. Convection occurs at the un-finned regions of the heat sink (or from the exposed HP for the HP-fin configuration). For the HP-heat sink configuration the convection losses are described by

$$-k_w \left.\frac{\partial T}{\partial r}\right|_{z,r=r_b} = \overline{h_w}[T(z, r = r_b) - T_\infty] = \overline{h_w}\theta(z, r = r_b) \tag{1a}$$

where $\overline{h_w}$ is the area-averaged convection heat transfer coefficient on the base of the heat sink. The heat sink base is also cooled by radial conduction to the roots of each of the N annular fins of thickness t_f and outer radius r_f. Fin analysis [43] is used to generate an effective heat transfer coefficient, that is applied at $r = r_b$, so that

$$\begin{aligned} -k_w \left.\frac{\partial T}{\partial r}\right|_{z,r=r_b} &= \overline{h_{\text{eff}}}\theta(z, r = r_b) = \frac{\theta(z, r = r_b)}{R''_f} \\ &= \overline{h_f}\left[\frac{2}{t_f m} \times \frac{K_1(mr_b)I_1(mr_{fc}) - I_1(mr_b)K_1(mr_{fc})}{K_0(mr_b)I_1(mr_{fc}) + I_0(mr_b)K_1(mr_{fc})}\right] \\ &\quad \times \theta(z, r = r_b) \end{aligned} \tag{1b}$$

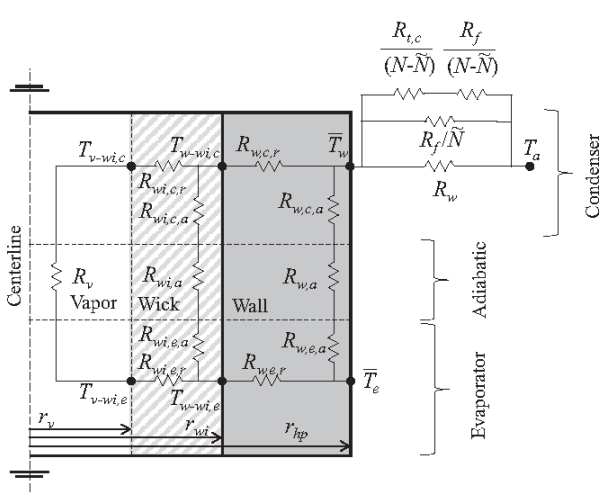

Fig. 2. Thermal resistance network (HP-fin configuration).

where $r_{fc} = r_f + t_f/2$ is used to account for convection from all exposed fin surfaces, and $m = \sqrt{2\overline{h_f}/k_f t_f}$. The parameter $\overline{h_f}$ is the area-averaged convection heat transfer coefficient associated with

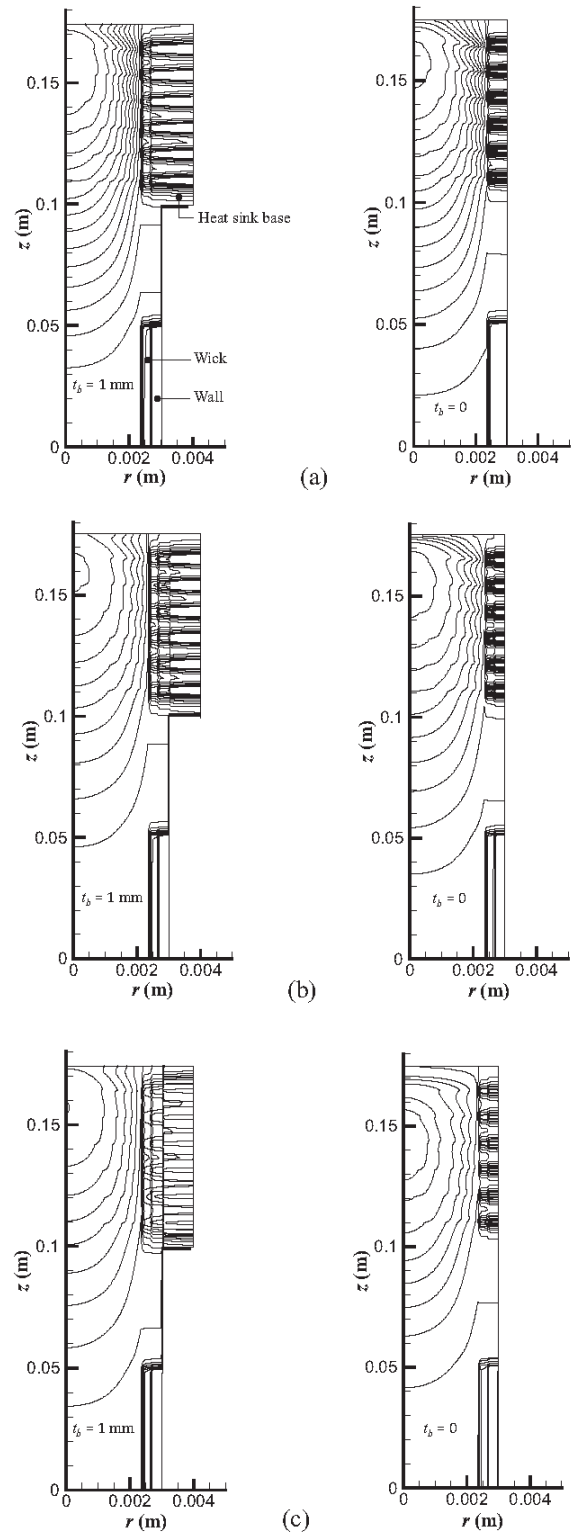

Fig. 3. Temperature distributions for $t_b = 1$ mm (left), $t_b = 0$ (right) with $T_e = 60$ °C: (a) $R''_{t,c} = 0$, (b) $R''_{t,c} = 10^{-5}$ m^2 K/W, (c) $R''_{t,c} = 10^{-4}$ m^2 K/W.

the top, bottom and tips of the fins, while I_0 (K_0) and I_1 (K_1) are modified, zero-order and first-order Bessel functions of the first (second) kind. Potential thermal contact resistance is considered at the HP-heat sink interface. The preceding analysis may be modified slightly and applied to the HP-fin configuration, but with Eqs. (1a) and (1b) applied at $r = r_{hp}$ and thermal contact resistances $R''_{t,c}$ specified at the roots of each fin which are added in series with the fin resistances R''_f defined in Eq. (1b).

The values of $\overline{h_w}$ and $\overline{h_f}$ have been obtained for a geometrically-similar configuration with the same operating conditions considered here through use of an experimentally-verified, (3D, elliptic, including buoyancy effects) shear stress model of the air flow within the fin array [36]. Values of the area-averaged contact resistances for either the HP-heat sink or HP-fin configurations, $R''_{t,c}$, are based on data from the literature, as will be discussed later.

Equations (1) through (12) of [33], specification of an initial, uniform temperature of 27 °C and zero velocities everywhere, along with the preceding boundary conditions complete the 2D HP model description. Note that, although the problem is steady in the mean, initial conditions are specified because the HP code accounts for the transient response before a steady state is reached, providing a unique pressure distributions within the HP [33]. The finite volume approach of Patankar [44] is used to discretize the governing equations. Convergence is assumed when residual mean square values less than 10^{-6} are achieved across all of the dependent variables for heat transfer and flow inside the HP. The solutions are deemed to be grid independent. Specifically, a grid of 190×76 ($z \times r$) yields predictions of overall heat transfer rates within 0.5% of those attained with a grid of 240×96 ($z \times r$) and the coarser grid was used here. Note that 12, 8, and 4 control volumes were included through the thickness of each fin in the grid sensitivity study. Predicted local temperatures using 8 and 12 control volumes in each fin are nearly identical, and 8 control volumes were used here. A typical computation time required for one simulation is 1 h on a 3.5 GHz, 16 GB Ram computer. Additional details are available in [36].

2.2. Thermal resistance model, HP-fin configuration

To quickly sort design options, it is desirable to develop thermal resistance models (TRMs) for HP systems, and the TRM developed here is similar to those described in [5,45,46]. However, the current model accounts for N individual fins and potential contact resistances at the N HP-fin interfaces. A similar model could be developed for the HP-heat sink configuration.

The thermal resistance network for a finned HP with N individual fins is shown in Fig. 2. To consider the potential for variability in thermal contact resistances from fin-to-fin, which could result due to damage during operation, for example, $\tilde{N}$ of the N fins are specified to have no thermal contact resistance at their roots. The remaining $N - \tilde{N}$ fins are subject to a thermal contact resistance, $R_{t,c}$.

As shown in Fig. 2, four individual thermal resistances are applied to the exterior of the HP condenser section to account for the presence of all N fins. The bottom exterior resistance shown, R_w, is associated with convection from the exposed surface of the HP to the ambient fluid (air). For fins having no contact resistance at their base, a parallel path for heat loss from the HP condenser section is through the $\tilde{N}$ fins, represented by a single thermal resistance $R_f/\tilde{N}$ where R_f is the thermal resistance of one fin. Heat loss through the $N - \tilde{N}$ fins subject to a contact resistance and is represented by the top heat flow path consisting of the contact and fin resistances in series.

The thermal resistance associated with the HP working fluid vapor, R_v, is due to evaporation occurring at the HP wick–vapor interface, the pressure drop and associated temperature change of the vapor as it flows upward in the HP, and condensation at the vapor–wick interface [1,5,45,46]. Flow of the HP working fluid vapor also redistributes the temperature distribution within the HP vapor, as will be discussed in conjunction of Fig. 3. The value of R_v is typically small and, in the limiting case, is equal to zero.

3. Results and discussion

3.1. Geometrical parameters and operating conditions

Results are presented for two HP-fin configurations involving $N = 6$ annular fins, each of thickness $t_f = 0.97$ mm and pitch $S_f = 10.8$ mm. As noted previously, the fins are either (i) individually attached to the HP condenser wall of length L_c, or (ii) are part of a cylindrical heat sink of base thickness $t_b = r_b - r_{hp} = 1$ mm and length L_c. The mass of the two configurations is specified to be identical, with $r_f = 53.42$ mm (51.67 mm) for the individual fin (heat sink) case.

The copper–water HP (modeled after an Enertron HP-HD06DI17500BA) and aluminum fins, as well as pertinent thermophysical properties and HP dimensions, are taken from [36] and are listed in Table 1. As in the reference, the upstream velocity of air in crossflow through the fin array is $V = 1.5$ m/s, and the air temperature is $T_\infty = 25$ °C. The heat transfer coefficient for the bare (unfinned) portion of the exposed HP condenser wall (at $r = r_{hp}$) is $\overline{h_w} = 51.5$ W/m^2 K, while that of the exposed surfaces of the fins is $\overline{h_f} = 19.5$ W/m^2 K. Both values are taken from [36].

Table 1
Thermophysical properties and pertinent dimensions.

	HP working fluid	HP wall	HP wick (sintered powder of porosity 0.4 [47])	Heat sink
Material	Water [1]	Copper [43]	Copper saturated with water (effective properties) [1]	AL 3003-h14 [48]
Density, ρ (kg/m^3)	996.6 (liquid)	8933	5758.44	2730
Thermal conductivity, k (W/m K)	0.6132 (liquid) 0.01932 (vapor)	401	200.8	159
Specific heat, c_p (J/kg K)	4181 (liquid) 1882 (vapor)	385	647.78	893
Viscosity, μ (Pa s)	8614×10^{-7} (liquid) 91.74×10^{-7} (vapor)			
Latent heat, h_{fg} (kJ/kg)	2434.9			
Vapor pressure, p_{sat} (Pa)	4352			
Dimensions (mm)		$L_e = 50.8$ $L_a = 49.2$ $L_c = 75$ $r_v = 2.35$ $r_{hp}-r_w = 0.3$ [47]	$r_w-r_v = 0.35$ [47]	In text

For cases involving a base thickness of $t_b = 1$ mm the value of $\overline{h_w}$ is determined by correcting the $t_b = 0$ value through application of the Hilpert correlation [43] to account for the larger radius, $r = r_b > r_{hp}$. After implementing the correction, the convection coefficient associated with the exposed portions of the heat sink base is $\overline{h_w} = 44.3$ W/m^2 K. Since the exposed areas of the fins for the $t_b = 0$ and $t_b = 1$ mm configurations are nearly identical, the value of $\overline{h_f} = 19.5$ W/m^2 K is applied to both the HP-heat sink and HP-fin configurations.

Finned tubes are typically formed by expanding the tube radius (e.g. by introducing high pressure oil within the tubes) to form a snug fit between the tube and individual, intermittently-spaced fins. Various fabrication methods lead to thermal contact resistances per unit area ($R''_{t,c}$) ranging from 0 to 10^{-4} m^2 K/W [37–41]. Here, $R''_{t,c}$ values of 0, 10^{-5} and 10^{-4} m^2 K/W are specified for both (i) individual fins that are attached directly to the HP and (ii) the heat sink base-HP interface. Since the heat sink base-HP contact area is larger than the fin base-HP contact area, the contact resistances (K/W) for the $t_b = 1$ mm configuration are smaller than those associated with the $t_b = 0$ configuration. Specifically, for $R''_{t,c} = 10^{-5}$ m^2 K/W, $R_{t,c} = 0.007$, 0.547 and 0.091 K/W for (i) the heat sink base-HP interface, (ii) the interface between a single fin and the HP, and (iii) $N = 6$ fins acting in parallel, respectively. For $R''_{t,c} = 10^{-4}$ m^2 K/W the corresponding resistances are $R_{t,c} = 0.070$, 5.47 and 0.911 K/W.

3.2. Detailed HP model predictions

Steady-state temperature distributions within the HP (and in the $t_b = 1$ mm thick base of the heat sink) are shown in Fig. 3. The predictions are associated with a uniform HP evaporator temperature of $T_e = 60$ °C and contact resistances of 0, 10^{-5} and 10^{-4} m^2 K/W. Isotherms are drawn at intervals of 0.1 K over the range 330.5 K $\leqslant T \leqslant$ 333 K. For either the $t_b = 0$ or $t_b = 1$ mm configurations, the fins (not shown) impact the temperature distributions within the HP wall, wick, and working fluid. Specifically, the fins depress local temperatures within the HP wall, wick, and working fluid (and in the heat sink base). As evident from inspection of the isotherm distributions within the HP vapor, overall temperature differences along the HP are reduced as thermal contact resistances are increased, as expected.

Axial HP wall temperature distributions for the $t_b = 0$ and $t_b = 1$ mm configurations at $0 \leqslant L \leqslant L_{hp}$, $r = r_{hp}$ are presented in Fig. 4. For either the $t_b = 0$ or 1 mm configuration the fins induce appreciable thermal depressions in the condenser section of the HP wall in a manner similar to that described in [36] for a HP-fin configuration with no contact resistance. Because of thermal buffering attributed to the heat sink base, temperature depressions are always larger for the individual fin configuration ($t_b = 0$) relative to those associated with the based heat sink ($t_b = 1$ mm). As expected, magnitudes of the local depressions are reduced as $R''_{t,c}$ is increased. As suggested in the discussion of Fig. 3, the average temperature drop along the HP wall ($\Delta T = T_e - \overline{T_c}$) decreases as the thermal contact resistances are increased. Specifically, $\Delta T = 3.19$, 3.17 and 3.07 K for the heat sink ($t_b = 1$ mm) case with no, low, and high thermal resistances. For the individual fin ($t_b = 0$) configuration, $\Delta T = 3.04$, 2.84 and 1.94 K for no, low, and high thermal resistances.

Mass fluxes of the liquid phase HP working fluid (water) are reported in Fig. 5; local *radial* mass fluxes at the vapor-wick interface (m''_r, $r = r_v$; LHS of Fig. 5) and local *axial* fluxes averaged over the wick cross-sectional area (m''_a, $r_v \leqslant r \leqslant r_w$; RHS of Fig. 5) are shown. Inspection of the radial fluxes in the HP evaporator section (negative radial mass fluxes), shows that overall mass transfer

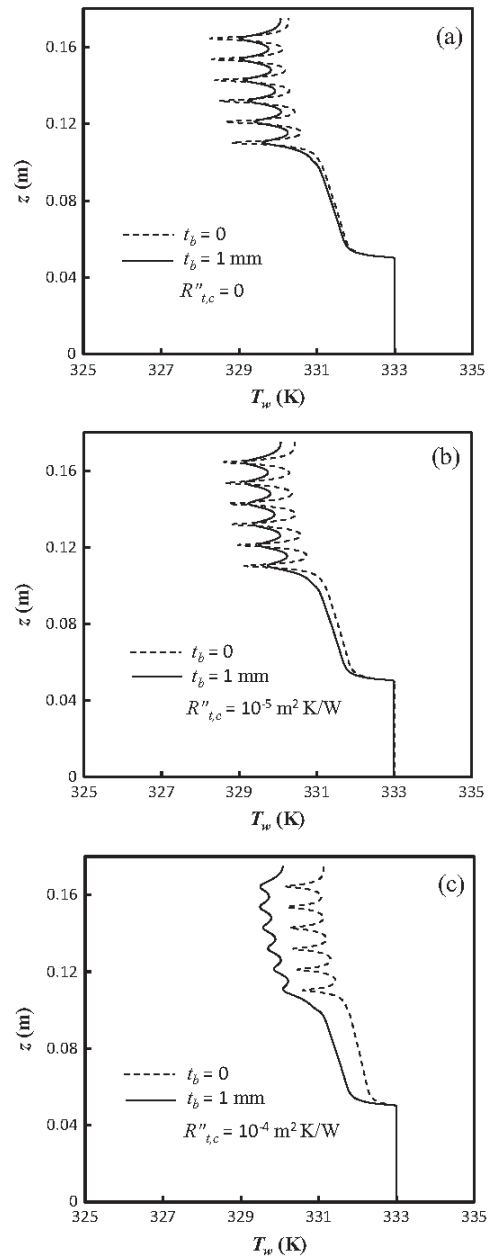

Fig. 4. Heat pipe wall temperatures: (a) $R''_{t,c} = 0$, (b) $R''_{t,c} = 10^{-5}$ m^2 K/W, (c) $R''_{t,c} = 10^{-4}$ m^2 K/W.

rates (and as will be shown, overall heat rates) are reduced as thermal contact resistances are increased. Variations in the radial mass fluxes within the condenser section (positive mass fluxes) are more sensitive to the thermal contact resistance for the HP-fin configuration than for the HP-heat sink configuration, as expected from consideration of the thermal depressions shown in Fig. 4.

Axial mass fluxes within the HP wick (RHS of Fig. 5) are zero at $z = 0$ and L_{hp}, as required. Downward mass fluxes are increased from the top of the HP until the HP adiabatic section is reached, reflecting the condensation of the HP working fluid in the overlaying sections of the HP. The waviness evident in the axial mass flux distributions in the condenser section is associated with the high local radial mass fluxes in the vicinity of each fin root. The axial

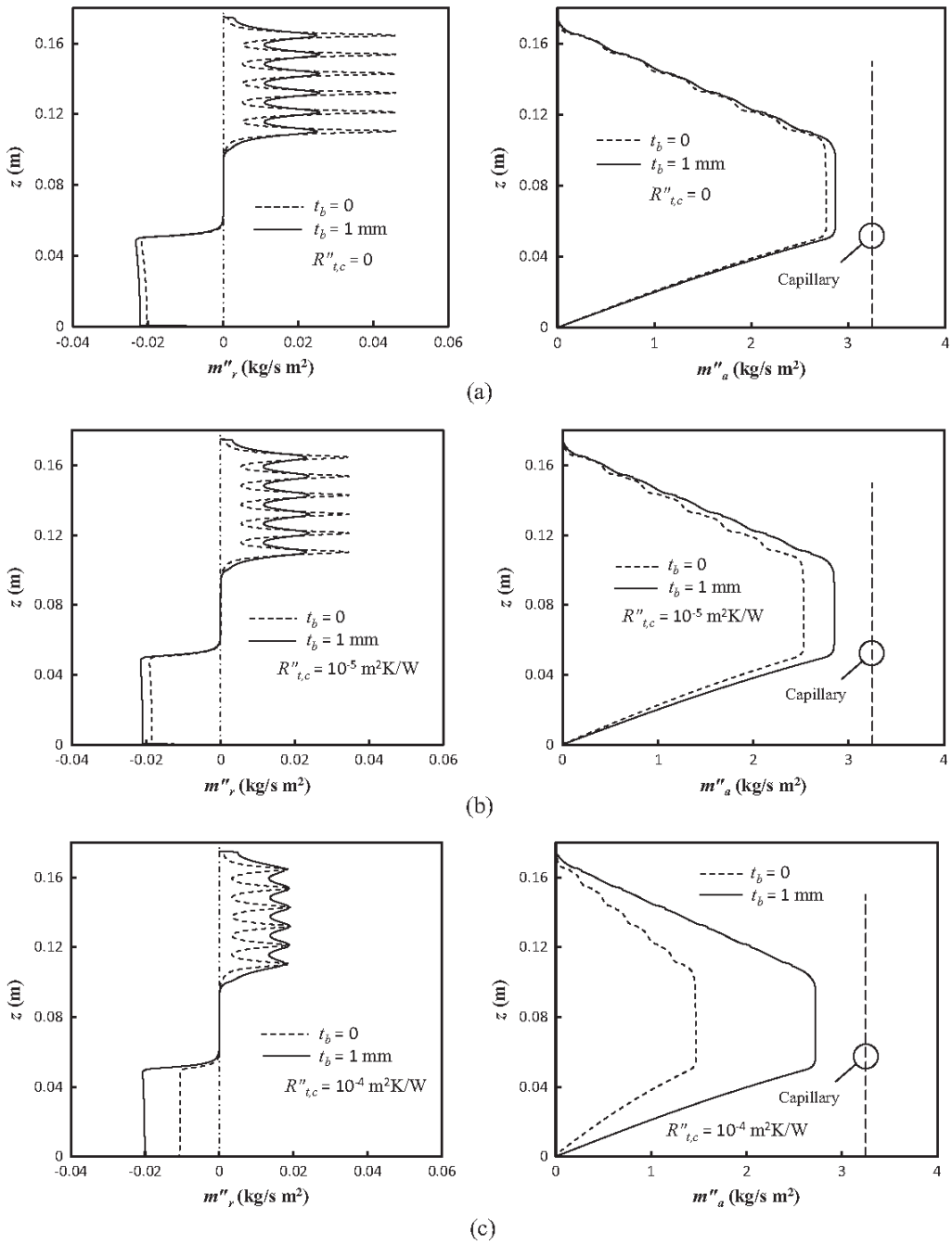

Fig. 5. Local mass flux along the HP at the vapor–wick interface (left) and within the wick (right): (a) $R''_{t,c} = 0$, (b) $R''_{t,c} = 10^{-5}$ m^2 K/W, (c) $R''_{t,c} = 10^{-4}$ m^2 K/W.

mass flux is reduced from its maximum value in the HP adiabatic section to zero at $z = 0$ as water evaporates radially inward in the HP evaporator section. The influence of the thermal contact resistance on the axial mass flux is more pronounced for the individual fin ($t_b = 0$) cases, as expected from the preceding discussion. Axial vapor velocities along the centerline of the HP are reported in Fig. 6. Peak vapor velocities are small relative to the sonic limits for HPs [1], and are reduced with increasing contact resistances.

Although the HP sonic limit is far from being reached, other limitations are important. For example, the capillary limit (~44 W) can be calculated for the HP considered here using procedures described in [1]. Since the same HP is used in either system, this capillary limit applies to both the HP-heat sink and the HP-fin configurations. The maximum axial mass flux associated with the capillary limit is identified by a vertical line in Fig. 5 (RHS). As evident, the HPs operate just below the capillary limit for all of the cases considered so far, but may reach the limit as different operating conditions (e.g. increased evaporator temperatures) are encountered.

Overall heat transfer rates are shown in Fig. 7 (LHS). As evident in Fig. 7a, minor differences exist between the heat rates for the two physical configurations ($t_b = 0$ and 1 mm) when contact

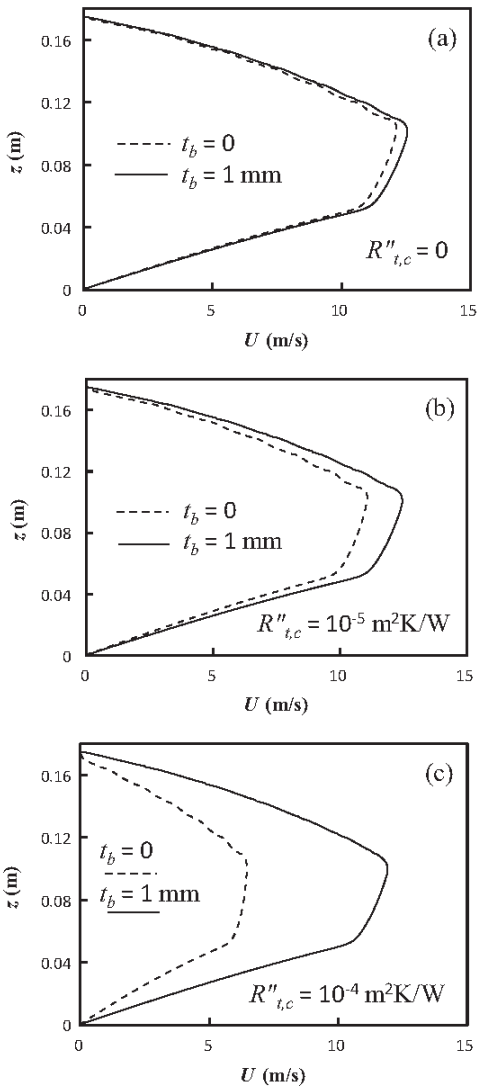

Fig. 6. Heat pipe centerline vapor velocities: (a) $R''_{t,c}$ = 0, (b) $R''_{t,c}$ = 10^{-5} m^2 K/W, (c) $R''_{t,c}$ = 10^{-4} m^2 K/W.

resistances are non-existent. Both the HP-heat sink and HP-fin configurations exhibit reduced heat rates as the thermal contact resistance is increased (LHS of Fig. 7a–c). As expected, the HP-heat sink (t_b = 1 mm) performance is not as sensitive to $R''_{t,c}$ as that of the individual fin configuration (t_b = 0).

In all cases reported in Fig. 7 (LHS), Q increases as the evaporator temperature is increased until a capillary limit is reached, corresponding to a critical evaporator temperature. Prior to reaching its capillary limit, the HP-heat sink configuration out-performs the HP-fin geometry because of its smaller overall contact resistance (K/W). When the capillary limit is reached, phase change within the HP is curtailed, and it transitions to operation in a conduction mode. Therefore, heat rates at evaporator temperatures exceeding critical values are predicted based on the assumption of stagnant HP gas and liquid phases. These heat rates are small relative to rates associated with the properly-operating HP. A similar effect is evident for the t_b = 0 configuration.

Although no HP would be designed to operate beyond its capillary limit, the HP-fin configuration (t_b = 0) could potentially provide superior performance relative to the HP-heat sink geometry in situations for which there might be, for example, an excursion in HP evaporator temperatures beyond expected or design values. In other words, a tradeoff exists between (i) achieving a low HP-fin array system thermal resistance and (ii) broadening the range of conditions for which the HP (and, therefore, the HP-fin array system) can operate. This tradeoff ultimately depends on the magnitude of thermal contact resistances between the HP and the fin array and is quantified in terms of a dimensionless heat rate ratio involving the heat sink (t_b = 1 mm) and individual fin array (t_b = 0) configurations

$$Q_r = Q(t_b = 1\ \text{mm})/Q(t_b = 0) \tag{1}$$

Consider an excursion in the HP evaporator temperature from its design value. The dependence of Q_r on the evaporator temperature is shown on the RHS of Fig. 7. Except for a narrow window at $T_e \approx 68$ °C, $Q_r \approx 1$ for $R''_{t,c}$ = 0 (Fig. 7a). In contrast, for the largest contact resistance considered here (Fig. 7c), the dimensionless heat ratio is large ($Q_r \approx 2$) until the capillary limit is reached for the HP-heat sink configuration (t_b = 1 mm). When the critical evaporator temperature is reached for the t_b = 1 mm configuration, the heat rate ratio suddenly decreases to a small value ($Q_r \approx 0.06$) until a second capillary limit is exceeded for the HP-fin geometry ($T_e \approx 100$ °C in Fig. 7c) after which Q_r increases to a value of approximately unity as both HP configurations operate in the conduction mode. Hence, the HP-heat sink (t_b = 1 mm case) offers superior performance relative to the HP-fin configuration (t_b = 0) under expected operating conditions (or when the HPs of both configurations are operating beyond their respective critical evaporator temperatures). However, the HP-fin configuration is superior to the HP-heat sink option over a potentially large intermediate range of T_e, corresponding to operation between the two critical temperatures. Hence, thermal contact resistances affect not only the HP heat rates, but can influence the choice of whether to use a based heat sink or individual fins in finned HP devices.

3.3. TRM predictions

The individual resistances shown in Fig. 2 are defined and quantified in Table 2 or described in [5]. Unique to the finned HPs considered here, thermal contact resistances at the root of each fin are determined using $R''_{t,c}$ = 0 or 10^{-4} m^2 K/W. The thermal resistance associated with the HP working fluid vapor, R_v, has been estimated using a novel, iterative technique recently developed [36]; the thermal resistance associated with this particular HP under similar operating conditions is R_v = 0.092 K/W.

Predicted overall heat rates are presented in Fig. 8 for $0 \leqslant \tilde{N} \leqslant N = 6$. Again, $\tilde{N}$ is the number of fins that are unaffected by a contact resistance. Note that for $1 \leqslant \tilde{N} \leqslant N - 1 = 5$, multiple overall heat rates exist for each value of $\tilde{N}$. For example, for $\tilde{N} = 1$, the single fin with no contact resistance could be placed at any of 6 different locations in the fin array, resulting in 6 unique heat rates (differences in the heat rates are expected, since each fin is exposed to a unique root temperature, as is evident upon consideration of Fig. 4). However, it was found that the largest differences in the heat rates predicted by the HP model correspond to placement of all of the zero-contact resistance fins at the top of the array versus placement of the same fins at the bottom of the array. The upper bounds (HPUB) and lower bounds (HPLB) of heat rates predicted by the detailed HP model are shown in Fig. 8, along with predictions of the TRM.

As evident in Fig. 8, the heat rate decreases nearly linearly as the number of fins suffering from contact resistances ($N - \tilde{N}$) increases. Predictions of the HP model are confined to a narrow window defined by their upper and lower bounds. Predictions of the TRM

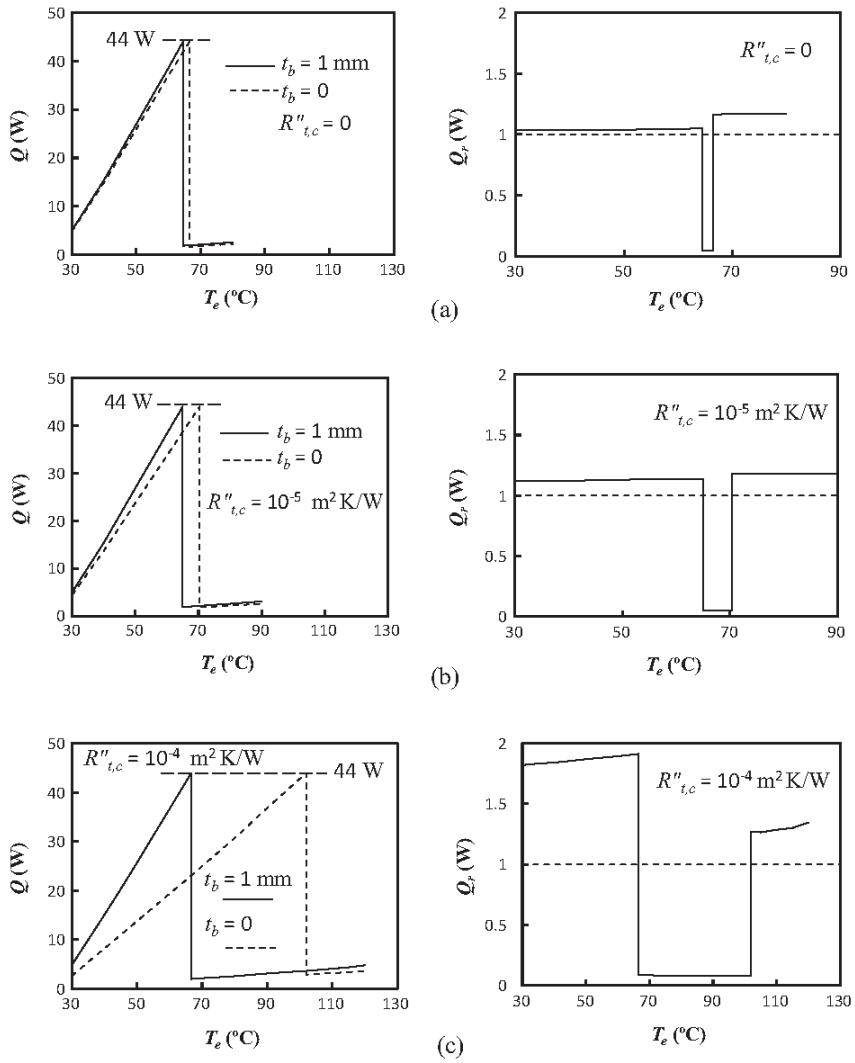

Fig. 7. Heat rates (left) and heat rate ratios (right): (a) $R''_{t,c} = 0$, (b) $R''_{t,c} = 10^{-5}$ m² K/W, (c) $R''_{t,c} = 10^{-4}$ m² K/W.

are in qualitative agreement with those of the HP model. Quantitatively, the TRM predictions are within 18 ($\tilde{N} = 0$) to 25 percent ($\tilde{N} = 6$) of the HP model predictions when $R_v = 0$. When $R_v = 0.092$ K/W, the TRM predictions are within 12 percent of those of the HP model over the entire range of $\tilde{N}$. Specification of an arbitrary, yet reasonable value of $R_v = 0.22$ K/W results in TRM predictions (not shown in Fig. 8) that are within 3.5 percent of the detailed HP predictions over the entire range of $\tilde{N}$, with an average discrepancy of less than 1.9 percent.

4. Conclusions and recommendations

A detailed HP model has been used to quantify the influence of external contact resistances on the heat transfer and fluid flow within a finned HP, as well as on the overall heat transfer rate of the HP-fin array system. For the same area-averaged contact resistance values, a HP-heat sink configuration provides lower overall thermal resistance than a HP-individually finned configuration under design conditions. However, the HP-fin option can significantly outperform the HP-heat sink configuration if the HP capillary limit is accounted for during off-design operation. The thermal resistance model has quantified the magnitude of various resistances within the system, and has provided predictions that compare favorably to those of the HP model. The overall heat rate of the HP-fin configuration is proportional to the number of fins in the array that are not subject to a contact resistance at the HP-fin interface. It was also found that the order in which the fins (fins with no versus fins with contact resistances) are placed within the fin array has little effect on the overall thermal resistance of the HP system considered here.

The modeling approach used here neglects three-dimensional phenomena and possible variability of contact resistances that might occur on a fin-by-fin basis, such effects could also be included in future studies. Constriction resistances [43] within the HP wall and heat sink base, as evidenced by the compacted isotherms in the vicinities of the fin roots, may be important to quantify and include in future refinements of the TRM model. The utilization of multiple HP-fin array configurations in large systems including the effects of contact resistances could also be considered in future investigations of finned HPs and HP systems.

Table 2
Thermal resistance descriptions, formulae, and values.

Thermal resistance	Description	Formula [43]	Value (K/W)
Adiabatic section			
$R_{w,a}$	Axial conduction in wall	$\frac{L_a}{k_w \pi (r_{hp}^2 - r_{wi}^2)}$	22.8
$R_{wi,a}$	Axial conduction in wick	$\frac{L_a}{k_{wi} \pi (r_{wi}^2 - r_v^2)}$	44.1
Condenser section			
$R_{w,c,a}$	Axial conduction in wall	$\frac{0.5L_c}{k_w \pi (r_{hp}^2 - r_{wi}^2)}$	17.4
$R_{w,c,r}$	Radial conduction in wall	$\frac{\ln\left(\frac{r_{hp}}{r_{wi}}\right)}{2\pi k_w L_c}$	0.00056
R_w	Convection resistance between air and exposed condenser wall	$\frac{1}{h_w 2\pi r_{hp}(L_c - Nt_f)}$ [a]	14.9
R_f	Thermal resistance for 1 fin	Analytical annular fin analysis [b]	4.76
$R_{t,c}$	Contact resistance for 1 fin	$\frac{R''_{t,c}}{2\pi r_{hp} t_f}$ [c]	5.47
$R_{wi,c,a}$	Axial conduction in wick	$\frac{0.5L_c}{k_{wi} \pi (r_{wi}^2 - r_v^2)}$	33.6
$R_{wi,c,r}$	Radial conduction in wick	$\frac{\ln\left(\frac{r_{wi}}{r_v}\right)}{2\pi k_{wi} L_c}$	0.00147
Evaporator section			
$R_{w,e,r}$	Radial conduction in wall	$\frac{\ln\left(\frac{r_{hp}}{r_{wi}}\right)}{2\pi k_w L_e}$	0.00082
$R_{w,e,a}$	Axial conduction in wall	$\frac{0.5L_e}{k_w \pi (r_{hp}^2 - r_{wi}^2)}$	11.8
$R_{wi,e,r}$	Radial conduction in wick	$\frac{\ln\left(\frac{r_{wi}}{r_v}\right)}{2\pi k_{wi} L_e}$	0.00216
$R_{wi,e,a}$	Axial conduction in wick	$\frac{0.5L_e}{k_{wi} \pi (r_{wi}^2 - r_v^2)}$	22.8
Vapor region			
R_v	Vapor thermal resistance	$\frac{0.5L_e + L_a + 0.5L_c}{k_v \pi r_v^2}$ [d]	0.092

[a] $h_w = 51.54 \frac{W}{m^2\,K}$ [36].

[b] From Eqs. (3.96) and (3.97) [43], and $h_f = 19.5 \frac{W}{m^2\,K}$ [36].

[c] $R''_{t,c} = 10^{-4} \frac{m^2\,K}{W}$.

[d] $k_v = 70{,}000 \frac{W}{m\,K}$ [36].

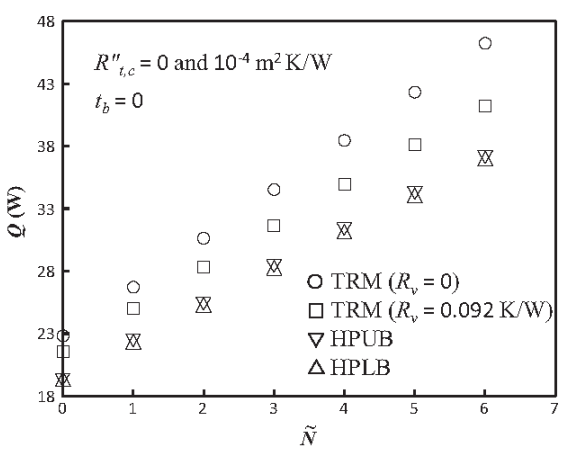

Fig. 8. Overall heat rate dependence on the number of fins with no thermal contact resistance, as predicted by the HP and TRM models.

Acknowledgement

This material is based upon work supported by the National Science Foundation under Grant Nos. 1435131 (University of Kansas) and 1435233 (University of Connecticut).

References

[1] A. Faghri, Heat Pipe Science and Technology, Taylor and Francis, Washington, DC, 1995.
[2] D.A. Reay, P.A. Kew, R.J. McGlen, Heat Pipes: Theory, Design, and Applications, Sixth ed., Elsevier, Oxford, 2014.
[3] X. Chen, H. Ye, X. Fan, T. Ren, G. Zhang, A review of small heat pipes for electronics, Appl. Therm. Eng. 96 (2016) 1–17.
[4] D. O'Connor, J.K.S. Calautit, B.R. Hughes, A review of heat recovery technology for passive ventilation applications, Renew. Sustain. Energy Rev. 54 (2016) 1481–1493.
[5] H. Shabgard, M.J. Allen, N. Sharifi, S.P. Benn, A. Faghri, T.L. Bergman, Heat pipe heat exchangers and heat sinks: opportunities, challenges, applications, analysis, and state of the art, Int. J. Heat Mass Transf. 89 (2015) 138–158.
[6] M.S. Naghavi, K.S. Ong, M. Mehrali, I.S. Badruddin, H.S.C. Metselaar, A state-of-the-art review on hybrid heat pipe latent heat storage systems, Energy Convers. Manage. 105 (2015) 1178–1204.
[7] C.W. Chan, E. Siqueiros, J. Ling-Chin, M. Royapoor, A.P. Roskilly, Heat utilisation technologies: a critical review of heat pipes, Renew. Sustain. Energy Rev. 50 (2015) 615–627.
[8] B. Orr, A. Akbarzadeh, M. Mochizuki, R. Singh, A review of car waste heat recovery systems utilising thermoelectric generators and heat pipes, Appl. Therm. Eng. 101 (2016) 490–495.
[9] A. Faghri, Heat pipes: review, opportunities and challenges, Front. Heat Pipes 5 (1) (2014).
[10] K.S. Ong, Review of heat pipe heat exchangers for enhanced dehumidification and cooling in air conditioning systems, Int. J. Low-Carbon Technol. (2014) 1–8.
[11] W. Srimuang, P. Amatachaya, A review of the applications of heat pipe heat exchangers for heat recovery, Renew. Sustain. Energy Rev. 16 (2012) 4303–4315.
[12] A. Mardiana-Idayu, S.B. Riffat, Review on heat recovery technologies for building applications, Renew. Sustain. Energy Rev. 16 (2) (2012) 1241–1255.
[13] A. Faghri, Review and advances in heat pipe science and technology, J. Heat Trans. 134 (12) (2012) 123001-1–123001-18.
[14] H.N. Chaudhry, B.R. Hughes, S.A. Ghani, A review of heat pipe systems for heat recovery and renewable energy applications, Renew. Sustain. Energy Rev. 16 (4) (2012) 2249–2259.
[15] M. Mochizuki, T. Nguyen, K. Mashiko, Y. Saito, T. Nguyen, V. Wuttijumnong, A review of heat pipe application including new opportunities, Front. Heat Pipes 2 (1) (2011) 1–15.
[16] S. Almsater, W. Saman, F. Bruno, Performance enhancement of high temperature latent heat thermal storage systems using heat pipes with and without fins for concentrating solar thermal power plants, Renew. Energy 89 (2016) 36–50.
[17] J. Choi, M. Jeong, Compact, lightweight, and highly efficient circular heat sink design for high-end PCs, Appl. Therm. Eng. 92 (2016) 162–171.

[18] S. Tiari, S. Qiu, Three-dimensional simulation of high temperature latent heat thermal energy storage system assisted by finned heat pipes, Energy Convers. Manage. 105 (2015) 260–271.
[19] S. Tiari, S. Qiu, M. Mahdavi, Numerical study of finned heat pipe-assisted thermal energy storage system with high temperature phase change material, Energy Convers. Manage. 89 (2015) 833–842.
[20] D.J. Malan, R.T. Dobson, F. Dinter, Solar thermal energy storage in power generation using phase change material with heat pipes and fins to enhance heat transfer, Energy Proc. 69 (2015) 925–936.
[21] A. Khalifa, L. Tan, A. Date, A. Akbarzadeh, Performance of suspended finned heat pipes in high-temperature latent heat thermal energy storage, Appl. Therm. Eng. 81 (2015) 242–252.
[22] Y. Ye, L.H. Saw, Y. Shi, A.A.O. Tay, Numerical analyses on optimizing a heat pipe thermal management system for lithium-ion batteries during fast charging, Appl. Therm. Eng. 86 (2015) 281–291.
[23] M.F. Remeli, L. Tan, A. Date, B. Singh, A. Akbarzadeh, Simultaneous power generation and heat recovery using a heat pipe assisted thermoelectric generator system, Energy Convers. Manage. 91 (2015) 110–119.
[24] C.A. Chung, Y.-Z. Chen, Y.-P. Chen, M.-S. Chang, CFD investigation on performance enhancement of metal hydride hydrogen storage vessels using heat pipes, Appl. Therm. Eng. 91 (2015) 434–446.
[25] M.J. Allen, T.L. Bergman, A. Faghri, N. Sharifi, Robust heat transfer enhancement during melting and solidification of a phase change material using a combined heat pipe-metal foam or foil configuration, J. Heat Trans. 137 (2015) 102301-1–102301-12.
[26] M.J. Allen, N. Sharifi, A. Faghri, T.L. Bergman, Effect of inclination angle during melting and solidification of a phase change material using a combined heat pipe-metal foam or foil configuration, Int. J. Heat Mass Transf. 80 (2015) 767–780.
[27] H. Shabgard, A. Faghri, T.L. Bergman, C.E. Andraka, Numerical simulation of heat pipe-assisted latent heat thermal energy storage unit for dish-stirling systems, J. Sol. Energy Eng. 136 (2014) 021025-1–021025-12.
[28] N. Sharifi, T.L. Bergman, M.J. Allen, A. Faghri, Melting and solidification enhancement using a combined heat pipe, foil approach, Int. J. Heat Mass Trans. 78 (2014) 930–941.
[29] A. Faghri, T.L. Bergman, N. Sharifi, M.J. Allen, H. Shabgard, J.S. Breit, Energy storage and thermal management using phase change materials in conjunction with heat pipes and foil, foams, or other porous media, US Patent Application No 0284020 A1, 2014.
[30] M. Mahdavi, S. Qiu, S. Tiari, Numerical investigation of hydrodynamics and thermal performance of a specially configured heat pipe for high-temperature thermal energy storage systems, Appl. Therm. Eng. 81 (2015) 325–337.
[31] M. Mahdavi, S. Qiu, Mathematical modeling and analysis of steady state performance of a heat pipe network, Appl. Therm. Eng. 91 (2015) 556–573.
[32] N. Sharifi, A. Faghri, T.L. Bergman, C.E. Andraka, Simulation of heat pipe-assisted latent heat thermal energy storage with simultaneous charging and discharging, Int. J. Heat Mass Trans. 80 (2015) 170–179.
[33] N. Sharifi, S. Wang, T.L. Bergman, A. Faghri, Heat pipe-assisted melting of a phase change material, Int. J. Heat Mass Trans. 55 (2012) 3458–3469.
[34] B. Xiao, A. Faghri, A three-dimensional thermal–fluid analysis of flat heat pipes, Int. J. Heat Mass Trans. 51 (11–12) (2008) 3113–3126.
[35] J. Rice, A. Faghri, Analysis of porous wick heat pipes, including capillary dry-out limitations, J. Thermophys. Heat Trans. 21 (3) (2007) 475–486.
[36] J.R. Stark, N. Sharifi, T.L. Bergman, A. Faghri, An experimentally verified numerical model of finned heat pipes in crossflow, Int. J. Heat Mass Trans. 97 (2016) 45–55.
[37] K. Merlin, D. Delaunay, J. Soto, L. Traonvouez, Heat transfer enhancement in latent heat thermal storage systems: comparative study of different solutions and thermal contact investigation between the exchanger and the PCM, Appl. Energy 166 (2016) 107–116.
[38] K. Nakaso, H. Mitani, J. Fukai, Convection heat transfer in a shell-and-tube heat exchanger using sheet fins for effective utilization of energy, Int. J. Heat Mass Trans. 82 (2015) 581–587.
[39] D. Taler, P. Ocło, Thermal contact resistance in plate fin-and-tube heat exchangers, determined by experimental data and CFD simulations, Int. J. Therm. Sci. 84 (2014) 309–322.
[40] J. Jeong, C.N. Kim, B. Youn, A study on the thermal contact conductance in fin-tube heat exchangers with 7 mm tube, Int. J. Heat Mass Trans. 49 (2006) 1547–1555.
[41] J.W. Sheffield, R.A. Wood, H.J. Sauer Jr., Experimental investigation of thermal conductance of finned tube contacts, Exp. Therm. Fluid Sci. 2 (1989) 107–121.
[42] Y. Cao, A. Faghri, Transient two-dimensional compressible analysis for high-temperature heat pipes with pulsed heat input, Num. Heat Trans. Appl. 18 (4) (1990). 483-50.
[43] T.L. Bergman, A.S. Lavine, F.P. Incropera, D.P. Dewitt, Fundamentals of Heat and Mass Transfer, seventh ed., Wiley, Hoboken, 2011.
[44] S.V. Patankar, Numerical Heat Transfer and Fluid Flow, McGraw-Hill, New York, 1980.
[45] Z.J. Zuo, A. Faghri, A network thermodynamic analysis of the heat pipe, Int. J. Heat Mass Trans. 41 (1998) 1473–1484.
[46] H. Shabgard, T.L. Bergman, N. Sharifi, A. Faghri, High temperature latent heat thermal energy storage using heat pipes, Int. J. Heat Mass Trans. 53 (15–16) (2010) 2979–2988.
[47] https://www.enertron-inc.com/online-store/heatpipe.aspx (communications with Enertron company).
[48] http://www.scribd.com/doc/36719273/Aluminum-3003-H14#scribd.